



**HAL**  
open science

# Dynamical spin injection and spin to charge current conversion in oxide-based Rashba interfaces and topological insulators

Paul Noel

► **To cite this version:**

Paul Noel. Dynamical spin injection and spin to charge current conversion in oxide-based Rashba interfaces and topological insulators. Mesoscopic Systems and Quantum Hall Effect [cond-mat.mes-hall]. Université Grenoble Alpes, 2019. English. NNT : 2019GREAY062 . tel-02619764

**HAL Id: tel-02619764**

**<https://theses.hal.science/tel-02619764v1>**

Submitted on 25 May 2020

**HAL** is a multi-disciplinary open access archive for the deposit and dissemination of scientific research documents, whether they are published or not. The documents may come from teaching and research institutions in France or abroad, or from public or private research centers.

L'archive ouverte pluridisciplinaire **HAL**, est destinée au dépôt et à la diffusion de documents scientifiques de niveau recherche, publiés ou non, émanant des établissements d'enseignement et de recherche français ou étrangers, des laboratoires publics ou privés.

## THÈSE

Pour obtenir le grade de

### **DOCTEUR DE LA COMMUNAUTE UNIVERSITE GRENOBLE ALPES**

Spécialité : **Physique de la matière condensée**

Arrêté ministériel : 25 mai 2016

Présentée par

**Paul NOËL**

Thèse dirigée par **Jean-Philippe ATTANÉ, UGA** et  
codirigée par **Laurent VILA, CEA**

préparée au sein du **Laboratoire Spintronique et Technologie  
des Composants (SPINTEC)**  
et de **l'École Doctorale de Physique de Grenoble**

## **Dynamical spin injection and spin to charge current conversion in oxide-based Rashba interfaces and topological insulators**

Thèse soutenue publiquement le « **14/11/2019** »,  
devant le jury composé de :

**Mme, Stefania, PIZZINI**

Directrice de recherche, Institut Néel, Présidente du jury

**Mr, Michel, VIRET**

Chercheur CEA Saclay, laboratoire SPEC, Rapporteur

**Mr, Pietro, GAMBARDELLA**

Professeur, ETH Zurich, Department of materials, Rapporteur

**Mr, Abdelmadjid, ANANE**

Enseignant-Chercheur, Université Paris-Sud, Examineur

**Mr, Dafiné, RAVELOSONA**

Directeur de recherche, C2N, Examineur

**Mr, Manuel, BIBES**

Directeur de recherche, CNRS Thales, Membre invité





# Table of contents

<b>Introduction</b>	<b>6</b>
<b>1 Spin current to charge current interconversion by spin orbit coupling</b>	<b>12</b>
1.1 Spin currents and charge currents . . . . .	12
1.1.1 Characteristic lengths . . . . .	12
1.1.2 Two currents model . . . . .	14
1.2 Spin Hall Effect . . . . .	16
1.2.1 Intrinsic Spin Hall Effect . . . . .	17
1.2.2 Extrinsic Spin Hall Effect . . . . .	18
1.3 Rashba-Edelstein Effect at surfaces and interfaces . . . . .	20
1.3.1 Rashba two dimensional electron gases and Topological surface states . . . . .	20
1.3.2 Direct and inverse Rashba-Edelstein Effect . . . . .	23
<b>2 Spin pumping by ferromagnetic resonance</b>	<b>29</b>
2.1 Ferromagnetic Resonance . . . . .	29
2.1.1 Landau-Lifschitz-Gilbert equation . . . . .	29
2.1.2 Ferromagnetic resonance conditions . . . . .	31
2.2 FMR: a powerful magnetometry tool . . . . .	36
2.2.1 Broadband FMR: frequency dependence . . . . .	36
2.2.2 FMR in cavity: angular dependence at X-band . . . . .	38
2.3 Spin transfer via spin pumping by ferromagnetic resonance . . . . .	45
2.3.1 Origin of the spin injection . . . . .	46
2.3.2 Spin current expression . . . . .	48
2.3.3 Evaluation of spin charge interconversion efficiency . . . . .	51
2.4 Disentangling ISHE/IEE from spurious effects . . . . .	55
2.4.1 Spin pumping ISHE/IEE angular dependence . . . . .	55
2.4.2 Spin Rectification Effects . . . . .	56
2.4.3 Thermal effects? . . . . .	61
<b>3 Spin Hall effect in heavy metals and Alloys</b>	<b>64</b>
3.1 Spin Hall effect in pure metals: Pt, Ta and W . . . . .	64
3.1.1 Positive or negative spin hall angle? . . . . .	65
3.1.2 Stacking order dependence . . . . .	66
3.2 A possible thermal contribution? . . . . .	67
3.2.1 Lack of Universal method to evaluate the thermal related effects . . . . .	68
3.2.2 Spin Pumping experiment . . . . .	69
3.2.3 Temperature increase and spin signal: a different timescale . . . . .	70



3.2.4	Differences in the timescale: further evidences . . . . .	71
3.3	Spin Hall Effect in Au based alloys . . . . .	75
3.3.1	Sample fabrication . . . . .	75
3.3.2	Methods . . . . .	76
3.3.3	Spin diffusion length and spin Hall angle in AuW . . . . .	77
3.3.4	Spin diffusion length and spin Hall angle in AuTa . . . . .	79
<b>4</b>	<b>Rashba Edelstein effect at oxide heterointerfaces</b>	<b>82</b>
4.1	A two dimensional electron gas at the surface of STO . . . . .	82
4.1.1	A 2DEG with appealing properties for spintronics . . . . .	83
4.1.2	STO\Al: no need of LAO . . . . .	84
4.1.3	STO 2DEG: a complex bandstructure . . . . .	87
4.2	Spin to charge conversion in STO\Al\Py structure . . . . .	90
4.2.1	Mapping to the bandstructure . . . . .	90
4.2.2	Role of the insulating barrier . . . . .	94
4.2.3	Spin to charge interconversion at room temperature . . . . .	96
4.3	Ferroelectricity in STO: non volatile switching of the IEE . . . . .	97
4.3.1	Ferroelectric STO? . . . . .	98
4.3.2	Remanent modulation of the spin to charge conversion . . . . .	101
4.3.3	Modulation of the 2DEG by ferroelectricity . . . . .	105
4.3.4	Possible memory and logic applications . . . . .	109
<b>5</b>	<b>Edelstein effect in topological insulators</b>	<b>112</b>
5.1	An efficient spin to charge conversion in strained HgTe . . . . .	112
5.1.1	Tensile strained HgTe on CdTe: a 3D topological insulator . . . . .	113
5.1.2	Sample preparation . . . . .	115
5.1.3	Spin to charge conversion: role of the HgCdTe barrier . . . . .	115
5.1.4	Spin to charge conversion: role of the HgTe thickness . . . . .	119
5.2	$Sb_2Te_3$ : a sputtered deposited topological insulator material . . . . .	123
5.2.1	Sputtering: an industry compatible process . . . . .	123
5.2.2	High quality thin films . . . . .	124
5.2.3	Magnetotransport: Weak Antilocalization . . . . .	127
5.2.4	Spin to charge interconversion . . . . .	131
	<b>Conclusion</b>	<b>134</b>
	<b>Acknowledgment</b>	<b>139</b>
	<b>Bibliography</b>	<b>142</b>
	<b>A FMR cavity: Brucker MS5 loop gap</b>	<b>164</b>
	<b>B Offset signal associated with the temperature increase</b>	<b>167</b>

<b>C</b>	<b>Change of the magnetic properties of the ferromagnet with the applied power</b>	<b>170</b>
<b>D</b>	<b>Gate voltage dependence of the ferromagnetic resonance lineshape in STO \CFB</b>	<b>176</b>
<b>E</b>	<b><math>Sb_2Te_3</math> ultrathin films and stoichiometry</b>	<b>179</b>

# Introduction

During the last fifty years the available processing power has evolved exponentially, thanks to the aggressive scaling down of transistors down to 10 nm or less<sup>1</sup>. This exponential downscaling has been accompanied by an exponential decrease of the power consumption and of the manufacturing costs, as well as an increase of the available processing power, following what is known as Moore's law<sup>2</sup>. While still valid today, this exponential scaling is now approaching physical limits<sup>3</sup>. In order to limit the power consumption of information and communication technology, that now represents more than 4% of the worldwide power consumption<sup>4</sup>, and to promote novel computing schemes for better processing capabilities, new routes need to be explored. Beyond the scaling down of transistors and improved architectures, the field of spin-electronics or spintronics appears as a particularly appealing path in the quest of an electronic beyond Moore's law.

Thanks to the intimate interaction of the electronic and magnetic structures with spin currents, spintronics allow novel ways to process information and store data. The remanence associated with magnetization and the ability to switch it in hundreds of picoseconds makes it possible to obtain fast non-volatile devices. Moreover, it allows reducing the energy needed for information storage, as the data remain stored in absence of any power input. Spintronics also open novel routes for processing units, including logic in memory architectures or majority gate circuits<sup>5,6</sup>.

## From Conventional spintronics

Although efforts on the understanding of various spin effects such as the Anomalous Hall Effect or the Anisotropic Magnetoresistance have been made since the 1950's<sup>7</sup> the birth of modern spintronics is usually associated with the independent discovery of the giant magnetoresistance (GMR) by the groups of Albert Fert and Peter Gr undberg in 1988<sup>8,9</sup>. This magnetoresistive effect appears in ferromagnetic/normal metal/ferromagnetic (FM/NM/FM) layers, and allows to obtain different levels of resistance depending on the relative magnetization direction of the two ferromagnetic layers<sup>10</sup>. Therefore, the resistance of this structure is sensitive to an external magnetic field. This effect permitted the development of a wide variety of sensors, such as read-heads for hard-disk drives. Those all metallic GMR devices were further replaced by magnetic tunnel junctions where the non magnetic metallic layer is an insulator<sup>11</sup>. In these junctions the tunnelling magnetoresistance (TMR) can reach hundreds of percent, compared to some dozens of percent for GMR devices<sup>12</sup>. Thanks to this higher change of resistance, magnetic tunnel junctions allow a better sensitivity and are now widely used as the reading head of Hard Drive disks<sup>13</sup>.

However, magnetic tunnel junctions are not only passive devices, operating as variable resistors sensitive to the magnetic field: they can also work as active devices. In 1996 Slonczewski<sup>14</sup> and Berger<sup>15</sup>

predicted the existence of the spin transfer torque (STT). This mechanism relies on the angular momentum conservation: a flux of angular momentum, known as a spin current, can be transferred from one ferromagnetic layer to the other, thus exerting a torque on the magnetization. This torque can lead the magnetization to precess<sup>16</sup>, it can induce domain wall motion<sup>17</sup>, or even lead to the switching of the ferromagnetic layer<sup>18</sup>. Using a ferromagnetic material as a source of spin current allows to write information by reversing the magnetization of a free layer, and it also allows to read the magnetization direction using the TMR. This property has been used to develop a type of non-volatile magnetic random access memory (MRAM) known as spin transfer torque MRAM (STT-MRAM)<sup>19</sup>. These MRAMs are now reaching industrial scale production. They can be easily embedded in CMOS technology, are way faster than NAND Flash, and have a higher cyclability than phase change memories. Moreover, when compared with SRAM and DRAM, they are comparable in terms of speed, but their non-volatility allows lowering the total power consumption<sup>20</sup>. In addition the STT can be used to induce magnetization precession. This leads to the development of magnetic oscillators for wireless communication, high frequency logic, or filters<sup>21</sup>.

Using a ferromagnetic layer has been the first method to obtain spin currents, allowing to modify the magnetization state of an adjacent layer using spin transfer torque. However, in recent years, an alternative way to manipulate spin currents has been proposed.

## **Towards spinorbitronics**

An emerging field of spintronics, called spin-orbitronics, exploits the interplay between charge and spin currents enabled by the spin-orbit coupling (SOC) in non-magnetic systems. It is sometimes called “spintronics without magnetic materials“, as the spin current source is not a ferromagnetic material anymore. This promising way to obtain and detect spin currents has been first proposed by Dyakonov and Perel in 1971<sup>22</sup> and was later experimentally demonstrated<sup>23;24;25;26;27</sup>. By harnessing the spin orbit coupling, it is indeed possible to obtain spin-charge current interconversion through two effects known as the spin Hall effect (SHE) in the bulk of the material<sup>28</sup> and the (Rashba-) Edelstein Effect (EE) in surfaces and interfaces<sup>29</sup>. In both cases, thanks to the spin orbit coupling a flow of current produces a transverse spin density, which can diffuse as a spin current in an adjacent material. The obtained spin current is transverse to the charge current and free of any charge current, which is why it is usually called a pure spin current. Conversely, it is possible to detect a charge current using the reciprocal (inverse) mechanisms, known as the Inverse Spin Hall and Inverse Edelstein Effects (ISHE and IEE). Both the SHE and EE can be used as a source of spin current or spin accumulation, and as a spin current detector.

In 2012, Michel Dyakonov, who first predicted the existence of the SHE, asked about the spin Hall Effect “What is it good for?“(in terms of applications). His answer at that time could be summarized as “probably nothing“<sup>30</sup>. However, the spin currents originating from the SHE and EE have been eventually found to be large enough to allow magnetization switching in SOC material\FM bilayers<sup>31</sup>. This effect is known as the spin orbit torque (SOT), a torque on the magnetization originating from the spin orbit interaction. After the demonstration of current-induced magnetization

reversal, the efforts of most of the spintronics community shifted towards these SOTs, with experiments such as current-induced magnetization switching<sup>32</sup> or magnetization oscillations<sup>33</sup>, and current-induced domain walls<sup>34</sup> or Skyrmion motion<sup>35;36</sup>. Experiments on SOT have been first performed using Platinum<sup>31;37</sup> and soon after high resistive phase of Ta and W<sup>32;38;39</sup>. Now a strong challenge lies in the understanding and the use of Rashba interfaces<sup>40;41;42</sup> and topological insulators<sup>43;44</sup> for future improvements in SOT devices.

## Foreseen Spinorbitronics Applications

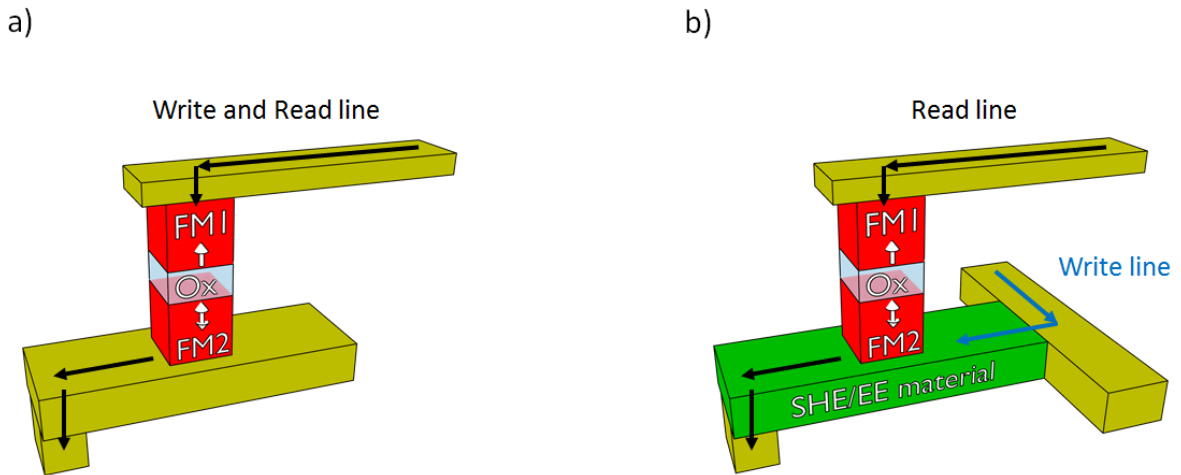


FIG. 1: Schematic representation of a) Spin Transfer Torque MRAM and of b) Spin Orbit Torque MRAM.

Following the discovery of the spin orbit torques and the ability to switch magnetization with an in-plane current, a growing interest for Spin Orbit Torques Magnetic Random Access Memory (SOT-MRAM) emerged<sup>45</sup>. But other applications of the spin orbit interaction also appeared recently. For example THz emitter based on the ultra fast spin charge current conversion<sup>46</sup> outperforms the best semiconductor THz emitters at a fraction of the cost. The reverse conversion, *i.e.*, the ability to detect spin currents allows to obtain large output signals<sup>47</sup> and can be useful for spin-logic applications such as the recently proposed Magneto Electric Spin Orbit Logic (MESO logic) by Intel<sup>48</sup>. All these applications rely on an highly efficient spin current to charge current interconversion.

The MRAM technology emerging today on the industrial scale is the spin transfer torque MRAM technology. Such a technology relies on the reading of the magnetization state by tunneling magnetoresistance and the writing by spin transfer torque. Nonetheless, it still suffers problems of density and reliability on the long term. As the writing path and the reading path are shared on a 2 terminal STT MRAM it is possible to switch the magnetization during the reading process. Moreover the insulating MgO barrier is particularly thin and can be damaged by the high current density going through it during the writing as seen in figure 1.a<sup>49;50</sup>. Such drawbacks are not present in the so called SOT MRAM. In such a 3-terminal MRAM the writing and reading path are separated, therefore the MgO barrier is not damaged during the writing process, and the thickness of the MgO can be higher. This

increases the device reliability<sup>45</sup>. Moreover, the total current density and power is lower than in their STT counterparts and the writing speed is faster<sup>37;51</sup>. The switching is performed by the spin accumulation due to either SHE or EE, the writing path is therefore composed of a spin to charge current conversion layer below the free magnetic layer as seen on figure 1.b. The fact that SOT MRAMs possess 3 terminals instead of 2 nonetheless limits the density, but it could be particularly useful in applications for which a high density is not needed but where reliability and high performances are importants, for instance for cache memory<sup>52</sup>. For now on, the main drawback of SOT MRAMs is that the switching is not field free, and that a small magnetic field is required to switch the magnetization, even though recent demonstrations of field free switching were performed<sup>38;53</sup>.

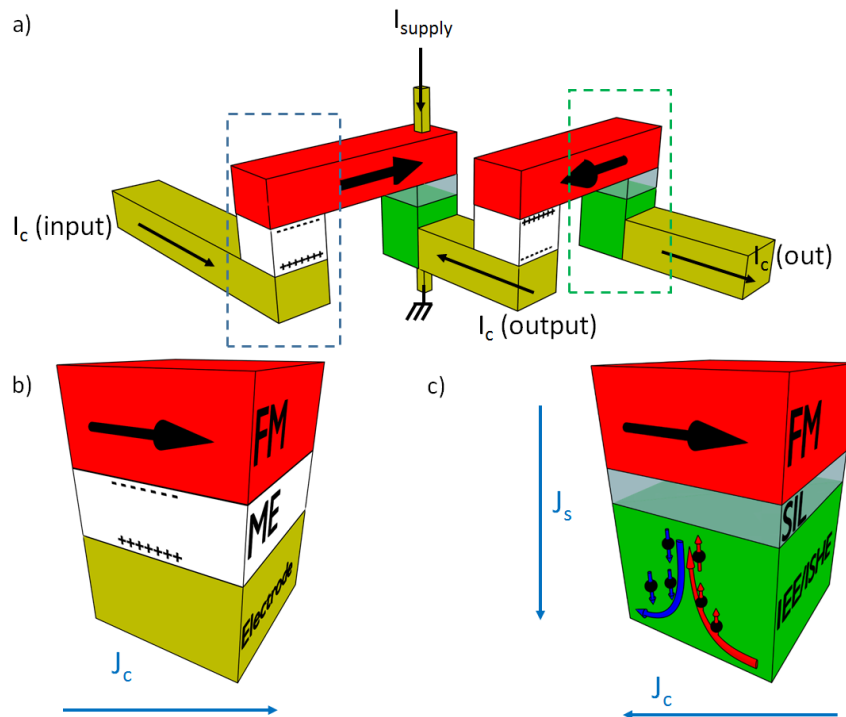


FIG. 2: Schematic representation of the MESO logic. a) Low-voltage-charge-based MESO interconnect with cascaded logic gates. Two inverters are chained together to form an interconnect. b) Operating mechanism for a magnetoelectric (ME) material. A ferromagnet is coupled via exchange/strain to the magnetoelectric material and can be switched. c) Operating mechanism for spin-to-charge conversion using a high-SOC material (SO). A spin injection layer (SIL) is used where needed by the materials interfaces. Spins are injected from the ferromagnet (FM) and a charge current is generated in the SO layer by ISHE or IEE. Small red and blue arrows indicate up and down spins, injected from the magnet.

The spin orbit related conversion effects could also lead to the development of new spintronics devices, beyond MRAMs. For instance, in figure 2.a we can see the complete structure of two cascaded MESO logic devices. Each part is composed of a ferromagnetic material FM which can be switched by the magnetoelectric coupling with an adapted magnetoelectric element (ME), providing that a high enough voltage is applied. The magnetoelectric coupling between the ferromagnetic material (FM) and the ME element –typically a ferroelectric or piezoelectric material– allows to obtain the complete

switching of the ferromagnetic layer as depicted in figure 2.b. The second part of the device is composed of an IEE/ISHE material, possibly separated by a spacer spin injection layer (SIL) from the ferromagnet, and is the Spin Orbit part of the device (SO). Through efficient spin charge conversion the magnetization of the FM can therefore be read as seen in figure 2.c. If the output voltage is high enough it can lead to the magnetoelectric switching of the next connected Magnetoelectric layer, thus allowing the cascaded gates to function. In that case, not only the efficient conversion is important but also the high resistivity. Regarding the fact that the main interest of this device for the Spin Orbit part is to obtain an output power as high as possible, and an output voltage as high as possible, this device would require a material with a high resistivity and a high conversion efficiency.

This beyond CMOS logic could possibly lead to the development of low power and memory-in logic devices. More importantly it is less sensitive to the resistivity of the interconnects: it is thus possible to use interconnects of high resistivity, which is not possible with conventional MOSFETs, thus limiting the transistors density. If optimized, according to Intel, it should permit to achieve “progressive miniaturization, reduced switching energy, improved device interconnection and ultra low standby power“ compared to CMOS logic. However, there is still a long way to go to obtain materials that offers the possibility to have a competitive MESO logic.

## Measure the spin to charge current conversion

Spin orbit coupling is therefore not anymore only a curiosity for physicists, it is emerging as an useful mechanism for electronics and optronics applications. But there is still the need to reach a better understanding of the mechanisms at stake in the spin-charge conversion processes. These mechanisms are inherently set by the transport properties of the SOC material but are far from being completely explained.

There are several important parameters needed to obtain an efficient switching through SOT as well as a large spin signal detection. The first evident one is the conversion efficiency, and the spinorbitronics community is actively looking for materials possessing the highest possible conversion rates. In this context it is important to develop an accurate metrology tool of the spin–charge interconversion to detect conversion in the bulk of the material, and at surfaces and interfaces. Amongst the large number of possible techniques, such as for instance spin-torque ferromagnetic resonance (ST-FMR)<sup>54</sup>, optical detection<sup>55</sup>, electrical detection<sup>56:57</sup>, or second harmonic detection<sup>58</sup>, I choose during my PhD to use the spin pumping by ferromagnetic resonance measurement (SP-FMR). The SP-FMR technique allows to evaluate the spin to charge current conversion efficiency in a large variety of materials while most other techniques are dedicated to the direct conversion from charge to spin such as ST-FMR and second harmonic. Moreover, using the SP-FMR technique instead of more conventional electrical detection techniques there is no need to nanopattern devices using costly E-beam lithography. The SP–FMR could also take advantage of previous developments in the experimental technique within the laboratory<sup>40:59:60:61:62</sup>

This manuscript starts with an introductory chapter on the spin dependent transport, with a specific

focus on the spin to charge interconversion mechanisms due to the spin-orbit interaction. In particular, we present the Spin Hall Effect, which occurs in the bulk of materials, and the Edelstein Effect, which occurs in interfaces and surfaces. In a second chapter we describe the spin pumping by ferromagnetic resonance technique, explaining why it is an useful and accurate metrology tool, and how to perform a good measurement. In the third chapter we describe the measurement of the spin to charge conversion using spin pumping in heavy metals and Au-based alloys that offer high conversion efficiencies. We also present a technique to eliminate possible spurious effects associated with temperature gradients. In the fourth chapter we will explore the possibility offered by the two-dimensional electron gas at the surface of  $SrTiO_3$  to tune conversion effects with a gate or spontaneous electric polarization, and how this high conversion is intimately related to the bandstructure of  $SrTiO_3$ . Finally, in the fifth chapter, we will present some results on spin to charge current conversion in the topological insulators  $HgTe$  and  $Sb_2Te_3$ , evidencing that this novel class of material shows large and promising conversion efficiencies.



# Spin current to charge current interconversion by spin orbit coupling

Conventional spintronics and its applications rely on the possibility to inject spin currents using a ferromagnetic layer and to detect it using a second one using either Giant Magnetoresistance (GMR)<sup>8;9</sup> or Tunnel Magnetoresistance (TMR)<sup>11</sup>. Tunnel junctions composed of two ferromagnetic metals separated by an insulating MgO thin film, used as read-head in Hard Disk Drive, and in non-volatile Spin Transfer Torque MRAMs (STT-MRAMs)<sup>63</sup> are at the heart of conventional spintronic applications. Such a spin injection and detection is permitted thanks to the spin polarization of the ferromagnetic material and to the spin-filtering of the MgO barrier. Ferromagnetic materials allowing efficient spin to charge current interconversion, leading to high TMR ratio, efficient STT-switching and high thermal stability are therefore needed for these applications.

Nonetheless, spin injection and detection is not limited to ferromagnetic materials, and an efficient spin to charge current interconversion can be obtained by harnessing the spin-orbit coupling. This can be done in a large variety of non-magnetic materials including heavy metals<sup>61;64;65</sup>, metals or oxides heterointerfaces<sup>40;66</sup> and the so-called topological insulators<sup>43;67;68</sup>. These materials could allow novel spintronics applications including Spin Orbit Torque-MRAM<sup>31;51;45</sup> which possess a higher reliability than their STT counterparts, the recently proposed Magneto-electric Spin Orbit Logic (MESO Logic) by Intel<sup>48</sup>, and optical applications in the THz range<sup>46</sup>.

In this chapter, we will first give a definition of the spin and charge currents, then we will describe the mechanisms involved in the spin to charge current interconversion through spin-orbit coupling, including the Spin Hall Effect and the Rashba Edelstein Effect. Finally we will describe the possible applications of spin-charge interconversion using Spin Orbit coupling.

## 1.1 Spin currents and charge currents

### 1.1.1 Characteristic lengths

For relatively high temperature above few Kelvins the motion of electrons in a medium is diffusive and is thus deeply related to scattering processes. These scattering mechanisms can be of various types, from scattering due to defects or impurities to scattering related to the electron-phonon interaction. The Drude model describes the transport of electron in a medium, the characteristic length (time) between two scattering events is known as the mean free path  $l_e$  (relaxation time  $\tau_e$ ). These two quantities can be linked by the so-called Fermi velocity  $v_F$  which is the velocity of electrons close to the Fermi level:

$$l_e = v_F \tau_e \quad (1.1)$$

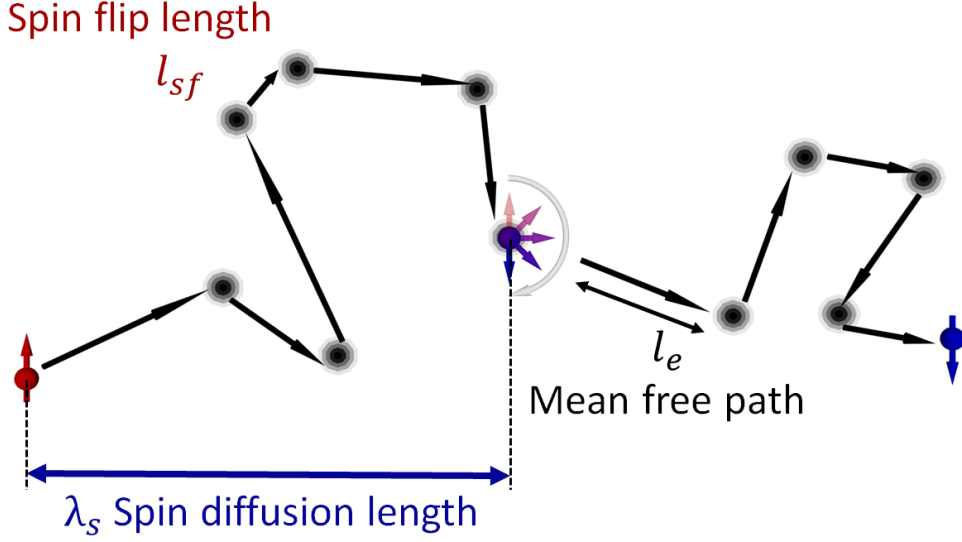


FIG. 1.1: Schematic representation of the electron and spin diffusions. One electron of a given spin is subjected to several scattering events, eventually leading to a flip of the spin. The characteristic lengths are represented, the mean free path  $l_e$ , the spin flip length  $l_{sf}$  and the spin diffusion length  $\lambda_s$ .

To obtain a complete description of electron motion, Drude model needs to be extended to account for the spin of the electron. For the sake of simplicity we will describe only the Elliot-Yafet mechanism<sup>69;70</sup> that is valid in most transition metals as evidenced for Pt<sup>71</sup>. Similarly to the charge, during these scattering events, it is also possible for the spin of the electron to change its direction. Some of the scattering events preserve the spins, and some do not preserve it. Therefore the diffusion mechanisms do not only affect the movement of the charge in the medium but also its spin. The characteristic length travelled between these changes of the spin direction is known as the spin flip length  $l_{sf}$ . These scattering events occur on average every  $\tau_{sf}$ , the spin flip time. There is a loss of spin information due to the change of the spin direction, and the transport of spin information is easier in material with a long  $l_{sf}$ <sup>72</sup>. The spin flip time and spin flip length are linked via the Fermi velocity:

$$l_{sf} = v_F \tau_{sf} \quad (1.2)$$

The transport of the spin is thus governed by both the scattering of the electron and the spin flip. The spin diffusion length  $\lambda_s$  is the geometric mean of the spin flip length  $l_{sf}$  and mean free path  $l_e$ :

$$\lambda_s = \frac{1}{\sqrt{3}} v_F \sqrt{\tau_{sf} \tau_e} \quad (1.3)$$

the  $\frac{1}{\sqrt{3}}$  prefactor takes into account the fact that the scattering mechanism is occurring in three dimensions.

Depending on the nature of the main scattering process and of the properties of the material/impurities the spin diffusion length can vary consequently. For example, it is of several hundreds of nanometers in light metals such as Cu or Al<sup>73</sup>, while it is of only some nanometers in Pt or Ta<sup>61;74</sup>. Most of the materials with high spin orbit coupling, are known for their short spin diffusion length.

## 1.1.2 Two currents model

Let's now define the spin and charge currents which are at the heart of spintronic mechanisms. The charge current density is defined as the flux of charges transferred through a surface  $S$ :

$$J_c = \frac{e}{S} \frac{dN}{dt} \quad (1.4)$$

with  $N$  the total number of charges. The spin up (down) current density can therefore be defined as a flux of spin up (down) angular momentum through a surface  $S$ . This leads to the following definition:

$$J_{\uparrow(\downarrow)} = \frac{\hbar}{S} \frac{dN_{\uparrow(\downarrow)}}{dt} \quad (1.5)$$

with  $N_{\uparrow(\downarrow)}$  the number of charges of spin up (down). Strictly speaking, charge and spin currents have thus different units. In the following and in order to simplify the expressions, we will consider the spin current and charge current to be in the same unit, by multiplying the spin current by the Josephson constant  $\frac{2e}{\hbar}$ . The charge current and spin current can thus be written as:

$$\text{Charge current: } J_c = J_{\uparrow} + J_{\downarrow} \quad (1.6)$$

$$\text{Spin current: } J_s = J_{\uparrow} - J_{\downarrow} \quad (1.7)$$

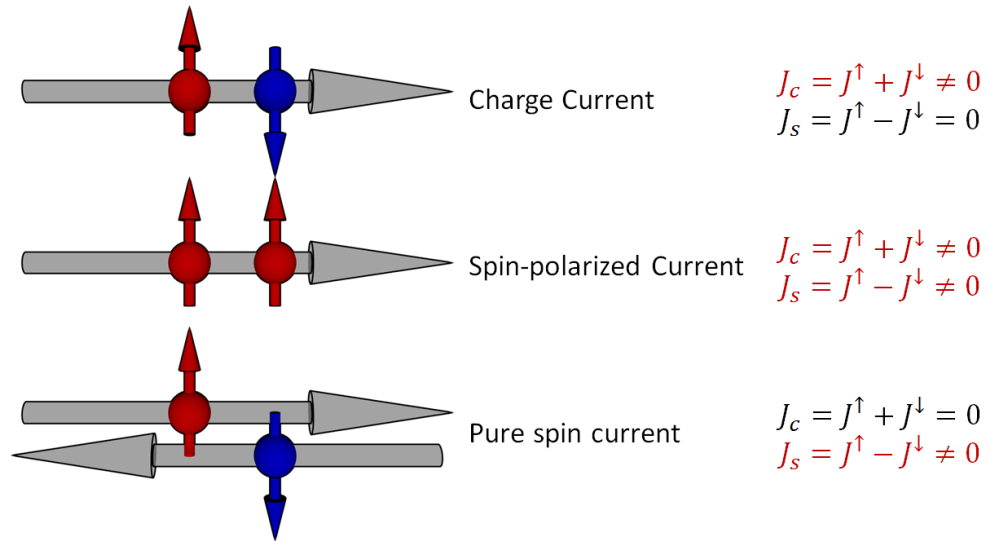


FIG. 1.2: Schematic representation of a pure charge current, of a spin polarized current and of a pure spin current.

The current can be either a pure charge current with no net flow of angular momentum, a polarized current when there are both a flow of charges and angular momentum and even a pure spin current if there is no net flow of charges but only of angular momentum as depicted in figure 1.2. Contrary to the charge current, that is defined by a direction and an intensity, the spin current should in general be written as a tensor including the current direction but also the spin direction<sup>30;75</sup>. This tensorial definition would nonetheless not be needed in the following of this manuscript as in most cases we will consider spins along a single direction.

It is to be noted that contrary to the charge current, the spin current is non-conservative. Indeed, the scattering events can modify the electron direction or its velocity but its charge is preserve. On the contrary, the electron spin information can be lost during spin-flip events. Therefore the motion of spins can not be described by the standard diffusion equation of electrons but by spin dependent diffusion equations, described using the Valet-Fert model<sup>76;77</sup>.

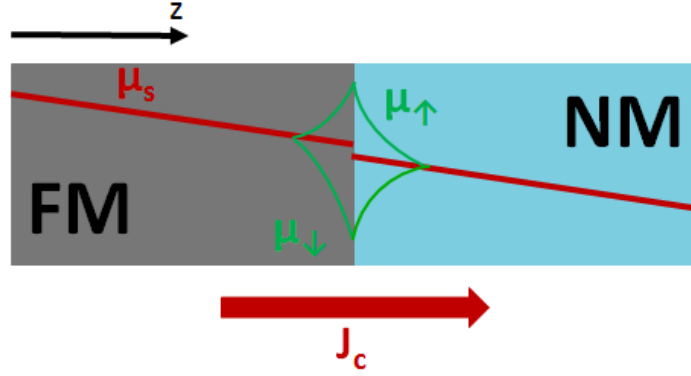


FIG. 1.3: Schematic representation of the geometry of the 1D Ferromagnetic (FM)/non magnetic (NM) interface. Charge current is injected along the  $z$  direction. Electrochemical potential for each spin population and the weighted average one are shown.

Assuming a 1D Ferromagnetic/non magnetic interface along  $z$  as shown in figure 1.3 we have the following equations:

$$\frac{1}{\sigma_{\uparrow}} \frac{\partial J_{\uparrow}}{\partial z} = 2 \frac{\mu_s}{\lambda_{\uparrow}^2} \quad \text{and} \quad \frac{1}{\sigma_{\downarrow}} \frac{\partial J_{\downarrow}}{\partial z} = 2 \frac{\mu_s}{\lambda_{\downarrow}^2} \quad (1.8)$$

$$J_{\uparrow} = \frac{\sigma_{\uparrow}}{e} \frac{\partial \mu_{\uparrow}}{\partial z} \quad \text{and} \quad J_{\downarrow} = \frac{\sigma_{\downarrow}}{e} \frac{\partial \mu_{\downarrow}}{\partial z} \quad (1.9)$$

With  $e$  the electron charge,  $\sigma_{\uparrow(\downarrow)}$  the electrical conductivity,  $\mu_{\uparrow(\downarrow)}$  the electrochemical potential  $\lambda_{\uparrow(\downarrow)}$  the spin diffusion length for each spin population.  $\mu_s$  is the weighted average of the electrochemical potential of up and down spins governing the transport process. It is to be noted that in a non magnetic material the spin diffusion length and spin conductivity of spin up and down should be the same, while they are different in a ferromagnetic material.

Combining equations 1.8 and 1.9 allows to determine the spin diffusion equation at a Ferromagnetic/non magnetic interface:

$$\frac{\partial^2 \mu_s}{\partial z^2} = \frac{\mu_s}{\lambda_s^2} \quad (1.10)$$

$$\frac{\partial^2 (\sigma_{\uparrow} \mu_{\uparrow} + \sigma_{\downarrow} \mu_{\downarrow})}{\partial z^2} = 0 \quad (1.11)$$

Where  $\lambda_s$  is the spin diffusion length introduced previously, with  $\frac{1}{\lambda_s^2} = \frac{1}{\lambda_{\uparrow}^2} + \frac{1}{\lambda_{\downarrow}^2}$ . Therefore the  $z$  dependence of the spin current in the normal metal can be obtained by solving the differential equation 1.10 and 1.11. An example of the profile of the electrochemical potential is shown in figure 1.3 when charge current is injected along the  $z$  direction. Spin accumulation arises at the ferromagnetic/normal

metal interface and disappears over the spin diffusion length in the normal metal.

While charge current can be easily produced and detected in conventional electronics, it is not the case of spin currents. Production and detection of spin current with efficient interconversion process from spin to charge or charge to spin is therefore needed for energy efficient spintronics. By harnessing the spin orbit interaction, it is indeed possible to convert spin current to charge current and oppositely charge current to spin current. There are two known mechanisms: the Spin Hall Effect in the bulk of materials and the Rashba Edelstein Effect in the surfaces or interfaces. In the following we will describe these two mechanisms.

## 1.2 Spin Hall Effect

The Spin Hall effect is a spin orbit related effect that allows the charge to spin (direct effect) or spin to charge (inverse effect) current conversion, in absence of any ferromagnetic material. It was first described by Mikhail Dyakonov and Vladimir Perel in 1971<sup>75:22</sup>, and the inverse Spin Hall Effect, the conversion from spin current to charge current, was observed for the first time during the 70's and 80's in semiconductors by the group of Solomon in Ecole Polytechnique<sup>78</sup> and by the group of Fleisher at the Ioffe Institute<sup>23:24</sup>.

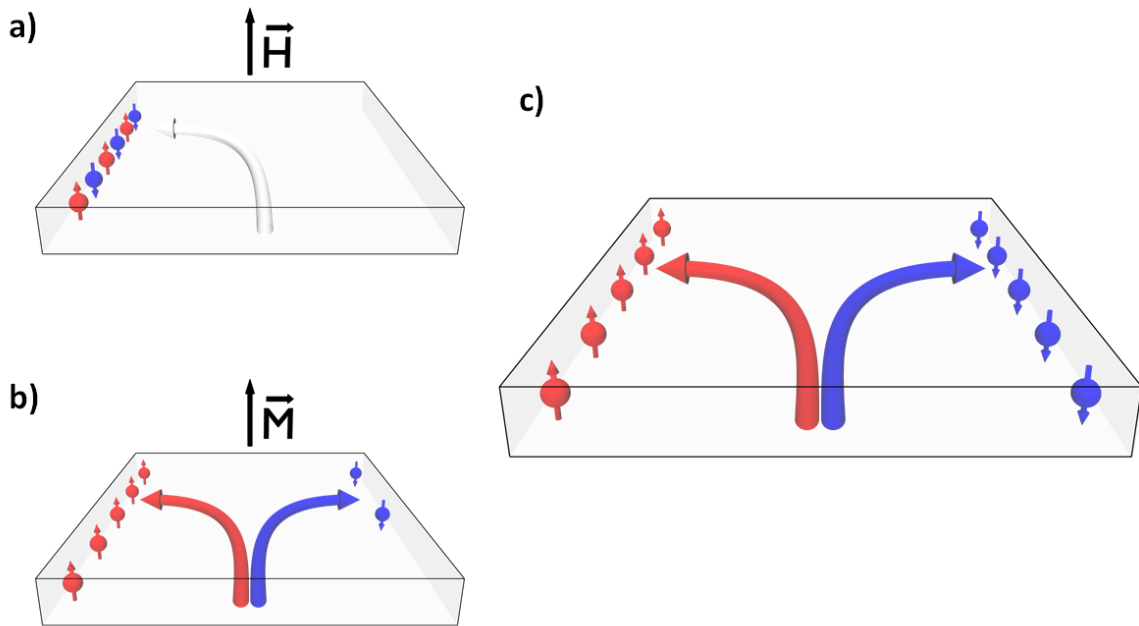


FIG. 1.4: Schematic representation of the different Hall effects: a) Ordinary Hall Effect, b) Anomalous Hall Effect and c) Spin Hall Effect.

The name of Spin Hall effect was introduced by Hirsch in 1999<sup>28</sup>, by analogy to the ordinary Hall Effect. The direct spin Hall Effect was later measured in 2004 in semiconductor GaAs by Kerr rotation microscopy<sup>25</sup>, and was detected in metals only in 2006 in Aluminum<sup>27</sup> and Platinum<sup>26</sup>. Since its detection at room temperature and its possible applications in electronics it attracted a large interest. During the last decade a large number of spin Hall Effect materials including heavy metals<sup>57</sup>, alloys<sup>64</sup>,

and semiconductors<sup>79</sup> were discovered unravelling the existence of Spin Hall in a large variety of materials...

While in the ordinary Hall effect an accumulation of charge is obtained transverse to the electric and magnetic field, in the spin Hall effect an accumulation of spins is obtained in a paramagnetic material in absence of magnetic field. The ordinary Hall effect is due to the deflection of carriers moving along an electric field by a magnetic field. This effect is well known to be caused by the Lorentz force, and leads to a charge accumulation resulting in a Hall voltage. But there is no net spin accumulation because the number of spin up and down is the same. The anomalous Hall effect is the result of spin-dependent deflection of carrier motion in a ferromagnetic material, which produces both a spin accumulation at the edges and a Hall voltage<sup>7</sup>. The spin Hall effect is also caused by spin-dependent deflection of carriers. As the number of deflected spin up and down is the same it produces no Hall voltage but gives rise to a spin accumulation<sup>80</sup>. All these mechanisms are associated with a non zero non-diagonal term of the resistivity tensor  $\rho_{xy}$ . In fig 1.4 we present these three different mechanisms.

The conversion efficiency for the spin to charge current interconversion, *i.e.* the figure of merit of a Spin Hall Effect material is called the Spin Hall Angle  $\theta_{SHE}$ . It is a quantity without unity that links the produced charge current to the injected spin current:

$$J_c^{\vec{I}SHE} = \theta_{SHE} \vec{J}_s \times \vec{\sigma} \quad (1.12)$$

where  $\vec{\sigma}$  is the spin polarization unit vector. In this formula the Josephson constant is already accounted in the expression of  $J_s$ . The spin Hall angle can thus be defined as the non-diagonal part of the resistivity tensor, the spin Hall resistivity,  $\rho_{xy} = \rho_{SHE}$  divided by the diagonal one  $\rho_{xx}$ . It is to be noted that this definition is similar to the Anomalous Hall Angle:  $\theta_{SHE} = \frac{\rho_{SHE}}{\rho_{xx}}$

As this value is intimately related to the spin orbit interaction high efficiency is expected to occur in heavy metals such as Pt<sup>26</sup>, Ta<sup>32</sup> or W<sup>39</sup>, and alloys containing heavy metals impurity such as CuBi<sup>64</sup>, AuW<sup>60</sup> or AuPt<sup>81</sup>.

Similarly to the case of AHE, the SHE has two different contributions, an intrinsic and an extrinsic one. The intrinsic contribution is related to the anomalous velocity of the carriers, and the extrinsic contribution is related to skew or side-jump scattering on impurities in presence of spin orbit coupling. In the following we will describe these mechanisms and their dependences on the resistivity of the SHE material.

### 1.2.1 Intrinsic Spin Hall Effect

The intrinsic contribution to the Spin Hall Effect exists even in absence of any impurity on which scattering could occur. This contribution is insensitive to the scattering time  $\tau$  and originates from the band structure. The electrons obtain an anomalous contribution to their velocity (non-diagonal resistivity is non zero and spin dependent) related to the so-called Berry Curvature linking the band-structure to the anomalous velocity in presence of an electric field<sup>82;83</sup>. The fig 1.5.a presents the

intrinsic mechanism where electrons of different spins are deflected in two different directions in presence of an electric field due to the anomalous velocity of electrons.

Platinum is a very well known material in the field of spinorbitronics and have a dominating intrinsic spin Hall Effect contribution. The expected scaling of the intrinsic Spin Hall Effect contribution with the resistivity is that the anomalous resistivity  $\rho_{SHE}$  is proportional to the square of the longitudinal resistivity  $\rho_{xx}$ . It is to be noted that the spin Hall Angle in highly resistive Pt is thus higher than their low resistivity counterparts, as shown by Sagasata et al<sup>71</sup>.

## 1.2.2 Extrinsic Spin Hall Effect

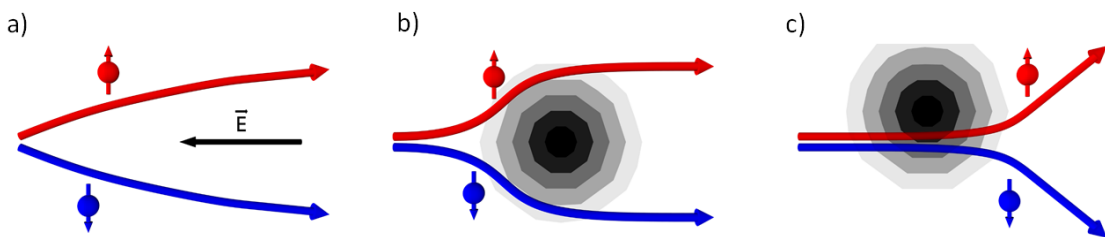


FIG. 1.5: Schematic representation of the different spin hall effect mechanisms a)intrinsic Spin Hall Effect b) Side-jump scattering and c) Skew scattering.

The spin dependent deflection of carriers due to impurities has been vastly discussed (for more than 50 years) in order to understand the microscopic origin of the Anomalous Hall Effect (AHE) in ferromagnetic metals and paramagnetic materials containing ferromagnetic impurities<sup>84</sup>. Two possible scattering mechanisms leading to the spin dependent deflections were identified, the skew and the side jump scattering contribution. They were first described by Smit (skew scattering)<sup>85</sup> and Berger (side-jump scattering)<sup>86</sup> as possible explanations to the non diagonal term of the resistivity in the case of the AHE. The scattering events on impurities with spin orbit coupling are thus one of the possible origin of AHE in ferromagnets and SHE in paramagnets. By modifying the number of impurity it is then be possible to tune the spin Hall angle.

The skew scattering mechanism is related to the asymmetric scattering due to the spin orbit coupling on the impurity, leading to a change of the k vector direction before and after the scattering event. The fig 1.5.c presents the skew scattering mechanism, where electrons of different spins are deflected in two different directions with different k vectors in presence of impurities with strong spin-orbit coupling. Such a mechanisms of skew scattering for the Spin Hall Effect was first experimentally demonstrated by Niimi et al. in CuIr<sup>87</sup> and CuBi<sup>64</sup> and described by Levy and Fert<sup>88</sup>. The side-jump scattering contribution is associated with a scattering of different nature. Close to the impurity with strong spin orbit coupling the electron is deflected in opposite direction when entering and leaving the proximity of the impurity due to the opposing electric field contribution. This leads the electron to preserve its k vector but to a deflection to the left (right) depending on its spin as seen in Fig1.5.b. The extrinsic side-jump mechanism has been only recently unambiguously observed in NiCu for AHE<sup>89</sup> and AuTa for SHE<sup>90</sup>.

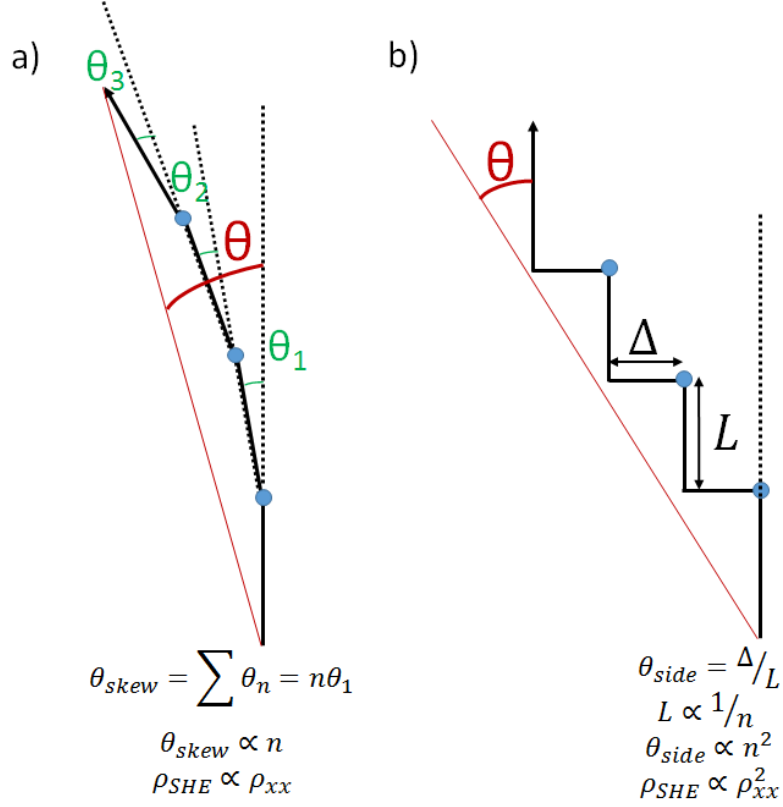


FIG. 1.6: Schematic representation of the a) skew and b) side jump scattering and link with number of scattering events from geometry.

In a dilute alloy the resistivity increases linearly with the concentration of impurity due to the linear increase of the number of scattering events<sup>91</sup>. As shown in figure 1.6.a from simple geometry the spin Hall resistivity  $\rho_{SHE}$  is in the case of the skew scattering proportional to the number of scattering events and thus to the longitudinal resistivity  $\rho_{xx}$ . This thus makes the spin Hall angle independent of the resistivity, and thus to the alloying concentration as shown for example in CuIr<sup>87</sup>. The extrinsic side jump scattering contribution as can be seen in figure 1.6.b has a different resistivity dependence:  $\rho_{SHE}$  is proportional to the square of the longitudinal resistivity, and the spin Hall Angle is thus proportional to the resistivity  $\rho_{xx}$ <sup>90</sup>.

The scattering contributions are generally interesting as they allow to increase the spin hall angle in a cheap light metal material which can be mixed with an expensive heavy metal compound as Pt or Ir. Nonetheless large alloying concentration can not be reached for most of alloys and formation of clusters occur. Regarding all these contributions intrinsic or extrinsic, we obtain the following link between Spin Hall Angle and resistivity:

$$\theta_{SHE} = (C_{intrinsic} + C_{side-jump})\rho_{xx} + C_{skew} \quad (1.13)$$

The sum of these different mechanisms would allow to increase the spin Hall Angle as a function of resistivity. It is to be noted that alloying with an impurity that allows to obtain a large side-jump contribution compared to a skew scattering one is more interesting for applications as it allows to



obtain large spin Hall angles with low resistivity and could increase the power efficiency for SOT for example. Nonetheless choosing the right impurity in order to obtain a large side jump contribution is not straightforward. The observation of the intrinsic contribution of Au in AuW alloys and of a large side-jump contribution in AuTa are described in Chapter III. Results about SHE in structures with Pt will also be presented.

## 1.3 Rashba-Edelstein Effect at surfaces and interfaces

The Rashba Edelstein effect has been first theoretically described in the eighties and early nineties<sup>92;93;29</sup>. It is also sometimes called the (Inverse) Spin Galvanic effect as it was first probed using polarized radiations in the pioneering work of Ganichev et al. in 2002<sup>94</sup>. Such an effect has been widely studied in semiconductor structures<sup>94;95;96</sup>, but it can also be observed in metallic heterostructures such as Ag/Bi<sup>40</sup> or oxide heterointerfaces such as STO/LAO<sup>66</sup> in the so-called Rashba interfaces and also in surface states of Topological insulator<sup>43;67;68</sup>.

The very peculiar properties of surfaces and interfaces could lead to larger spin to charge conversion efficiencies than Spin Hall Effect and are associated with very specific band-structure properties. In the next part we will describe these specific properties and how they can be associated with a large conversion efficiency.

### 1.3.1 Rashba two dimensional electron gases and Topological surface states

The spin charge interconversion phenomenon by Spin Hall Effect occurs in the bulk of the material. Nonetheless the conversion can also occur in surface states or in interface states of some materials, as long as they possess some specific properties. It is well known that surfaces of solids or interfaces of heterostructures behave differently from the bulk in various ways because the surrounding environment of the atom is different from one in the volume.

In the bulk of a solid the free electron is moving in a periodic solid with both inversion symmetry  $E(\uparrow, \vec{k}) = E(\uparrow, -\vec{k})$  and time reversal symmetry  $E(\uparrow, \vec{k}) = E(\downarrow, -\vec{k})$ . This thus leads to the spin degeneracy  $E(\uparrow, \vec{k}) = E(\downarrow, \vec{k})$ , where  $\uparrow$  ( $\downarrow$ ) are the spin up (down) and  $\vec{k}$  the k-vector. In that case the dispersion curve of free electrons of effective mass  $m^*$  is spin degenerate  $E(k) = \hbar^2 k^2 / 2m^*$  as can be seen in figure 1.8.a The experimentally observed dispersion of free electrons by means of Angle-resolved photoemission spectroscopy (ARPES) in light metals such as Copper<sup>97</sup> correspond well to this description.

However when the inversion symmetry is broken either by a surface or an interface the spin degeneracy is lifted, which leads to some change in the electron dispersion. This was first described by Yurii Bychkov and Emmanuel Rashba and is thus called the Bychkov-Rashba or Rashba effect<sup>92</sup>. It is to be noted that in crystals with lack of inversion symmetry, in the bulk of polar or ferroelectric materials the spin degeneracy can also be lifted. This is the case of GeTe<sup>99</sup> or BiTeI<sup>100</sup>, though in the following we will only focus on Rashba effect arising at surfaces or interfaces. In presence of

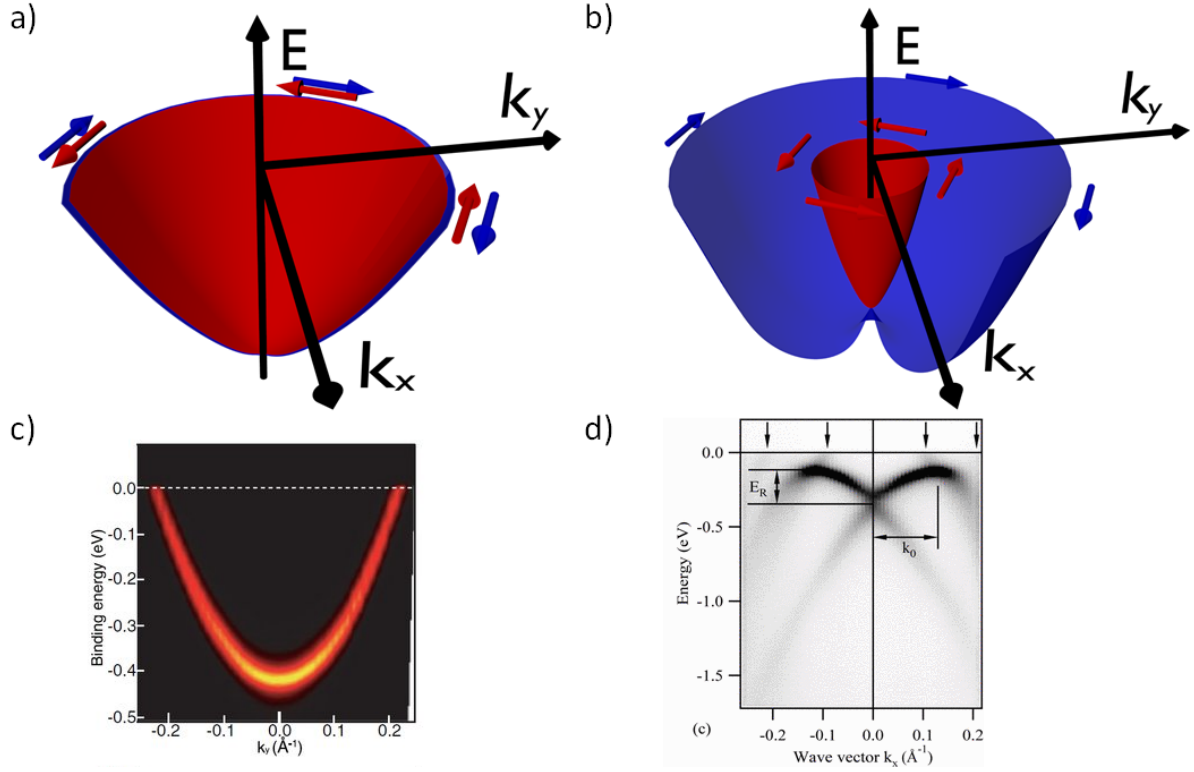


FIG. 1.7: Schematic representation of nearly free carriers with or without Rashba spin splitting. In a) Bands with spin degeneracy typical for bulk of materials without breaking of inversion symmetry or interfaces with lack of spin orbit coupling. b) Bands with a spin degeneracy lifted by a strong Rashba interaction at a Rashba interface with spin orbit coupling. c) Nearly free electron dispersion curve of Cu(111) measured by ARPES. Because of the small spin orbit coupling in Cu ( $Z=29$ ) spin splitting is not visible d) Dispersion of Bi/Ag interface measured by means of ARPES with giant spin splitting of the bands. Figure c) and d) are extracted from reference<sup>97</sup> and<sup>98</sup>

inversion symmetry breaking an electron moving in a surface or interface experiences an electric field  $\vec{E}_z$  perpendicular to the surface and an effective magnetic field  $B_{eff}$  therefore a splitting of the band happen. Such an effect can be described by the Rashba Hamiltonian  $H_R$ :

$$H_R = \alpha_R(\vec{e}_z \times \vec{k}) \cdot \underline{S} \quad (1.14)$$

where the Rashba constant  $\alpha_R$  describes the strength of the Rashba interaction.  $\vec{e}_z$  is the unit vector oriented perpendicular to the surface,  $\vec{k}$  is the electron momentum and  $\underline{S}$  is the Pauli matrices that gives the spin of the electron.  $\alpha_R$  is proportionnal to  $\lambda E_z$  where  $\lambda$  is the spin orbit constant. In absence of Rashba field ( $\alpha_R = 0$ ), bands of opposite spins are degenerate as schematized in figure 1.8.a. This is the case for the surface of light metals as Cu, where despite the existence of broken inversion symmetry at the surface the splitting is weak due to the lack of strong spin orbit coupling.

In presence of broken inversion symmetry (at interfaces or surfaces) and of a strong spin orbit interaction the Rashba interaction is sizable. This thus gives rise to a splitting of bands of different spins that is larger when the  $\alpha_R$  value is larger, as can be seen in figure 1.8.b The dispersion equation for

such bands is<sup>92</sup>:

$$E_{\pm}(k) = \frac{\hbar^2 k^2}{2m^*} \pm \alpha_R k \quad (1.15)$$

As experimentally observed by ARPES in figure 1.8.d, a large splitting of the bands can be obtained at the Silver-Bismuth interface<sup>98</sup>, where a large Rashba parameter is obtained. This is due to both a large spin orbit coupling in Bismuth and electric field due to the interface. More importantly, as can be seen from the Rashba Hamiltonian it is clear that the spin  $\vec{S}$ , the k-vector  $\vec{k}$  and the perpendicular to the plane  $\vec{e}_z$  are all perpendicular to each other to have a maximal contribution of the Rashba Hamiltonian. This leads the spin to lie in the plane perpendicular to  $\vec{k}$ , a phenomenon known as the spin momentum locking.

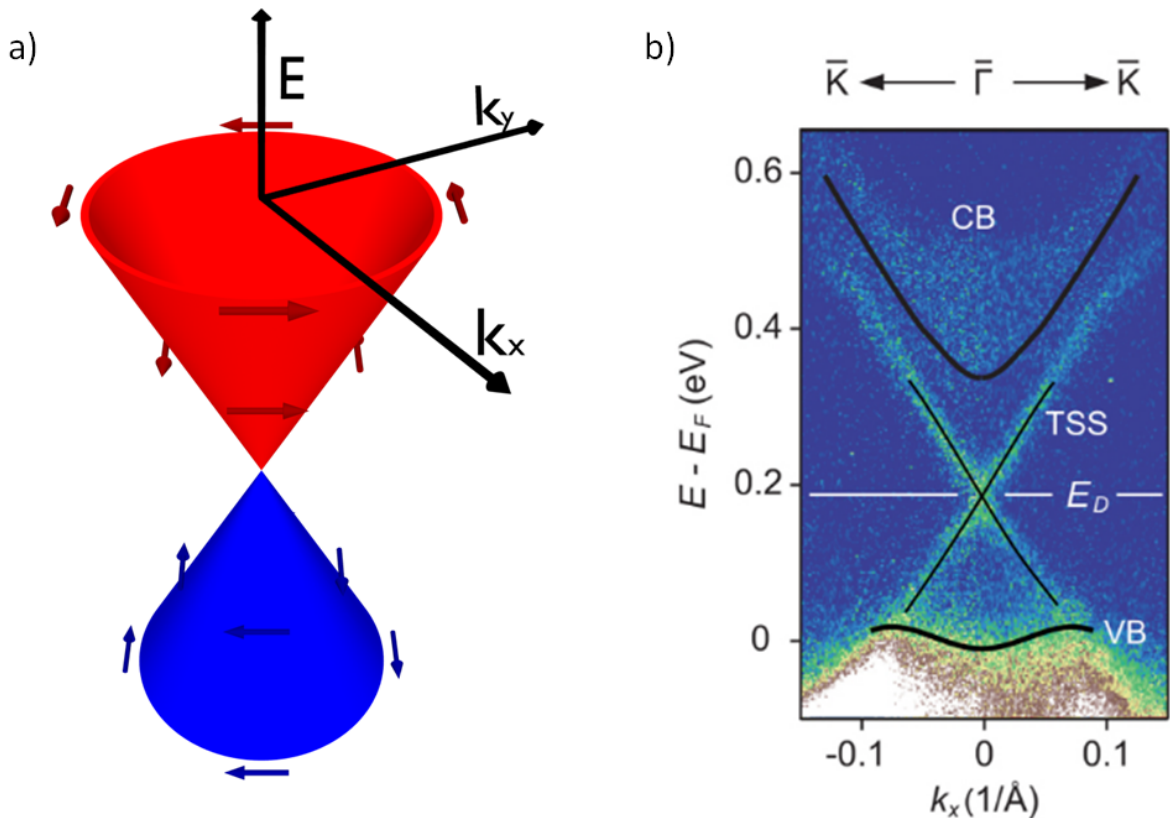


FIG. 1.8: Topological surface States. a) Schematic representation of the dispersion relation of Topological surface states with a Dirac cone exhibiting the spin momentum locking. b) Angle Resolved photoemission spectroscopy of  $Sb_2Te_3$ , linear dispersion of in-gap states from reference<sup>101</sup>.

Beyond Rashba interfaces, surfaces of 3D Topological insulators are attracting a growing interest in spintronics. Topological insulators are a recently discovered class of materials that possess a bulk band gap (insulators) but conductive surfaces known as topological surface states. They are named 3D topological insulators because they are insulating in the bulk (3D) but conductive in the surface. They were first described in 2007 by Fu, Kane and Mele<sup>102:103</sup>, and since then a large number of topological insulators or related materials as Weyl Semimetals or Topological Semimetals have been discovered. This includes  $BiSb$ <sup>104</sup>,  $Bi_2Se_3$ <sup>105</sup>,  $Bi_2Te_3$ <sup>106</sup>,  $Sb_2Te_3$ <sup>107</sup>, but also  $HgTe$ <sup>108</sup> or  $\alpha - Sn$ <sup>109</sup>. In fact

this kind of material is not so uncommon and according to recent calculations 11% of all material in nature are topological insulators<sup>110</sup>.

The topological surface states of TIs are Dirac like states with spin momentum locking<sup>111</sup>. These surface states can be described by the following Hamiltonian:

$$H_R = \pm \hbar v_f (\vec{e}_z \times \vec{k}) \cdot \underline{S} \quad (1.16)$$

With  $v_f$  the Fermi velocity. The sign  $\pm$  describe the change of chirality below and above the Dirac point. Schematics of the Energy dispersion of the surface states is shown in figure 1.9.a and an ARPES measurement of  $Sb_2Te_3$ <sup>101</sup> with the Dirac-like dispersion can be seen in figure 1.9.b. Due to the large number of different systems the complete description of the bandstructure of a Topological insulator is complex and out of the scope of this manuscript<sup>112</sup>.

When the Fermi level lies in the gap and cross only the topological surface states the Fermi Contour resembles the one of Rashba interfaces. Spin to charge current interconversion can thus be described similarly in both Topological Insulators and Rashba interfaces. We would like to mention here that as topological insulators are materials with high spin orbit coupling the SHE could occur in their bulk when the fermi level is crossing a bulk band. Moreover Rashba splitting can also occur at their surfaces as is observed in  $Bi_2Se_3$ <sup>113</sup>. In the following we would not focus anymore on the Rashba Hamiltonian and on the topological surface states but on how this specific bandstructure and more particularly spin momentum locking can be harnessed to obtain spin charge interconversion with possibly high efficiency.

### 1.3.2 Direct and inverse Rashba-Edelstein Effect

Let us now focus on what happens when charge current is injected in these materials. Due to the strong similarities between the bandstructures of Rashba interfaces and topological insulators we will present both of them simultaneously. Figure 1.9.a shows the Fermi surface of a Rashba interface in absence of any current, with two Fermi contours of opposite chiralities one clockwise and the other one counter clockwise. Figure 1.9.c shows the Fermi surface of the surface state of a Topological insulator, which is indeed very similar to the one of Rashba except that there is only one chirality.

When a current density  $\vec{j}$  is injected in the plane of the sample along -x, there is an electric field in the same direction with  $\vec{j} = \sigma \vec{E}$  with  $\sigma$  the electrical conductivity. Therefore a Coulomb force  $\vec{F}_{Coul}$  acts on the electron in the material with  $\vec{F}_{Coul} = q \vec{E}$  where q is the charge of the carrier. By applying Newton's second law  $\vec{F}_{Coul} = \frac{d\vec{p}}{dt}$  where  $\vec{p}$  is the momentum, and as  $\vec{p} = \hbar \vec{k}$  injecting a charge current during a time  $\Delta t$  induces a shift of the Fermi surface.

This shift  $\Delta \vec{k}$  of the contour is given by:

$$\Delta \vec{k} = \frac{\Delta t q \vec{j}}{\sigma \hbar} \quad (1.17)$$

In real systems, in presence of scattering, for times longer than electron scattering  $\tau$  the electric field

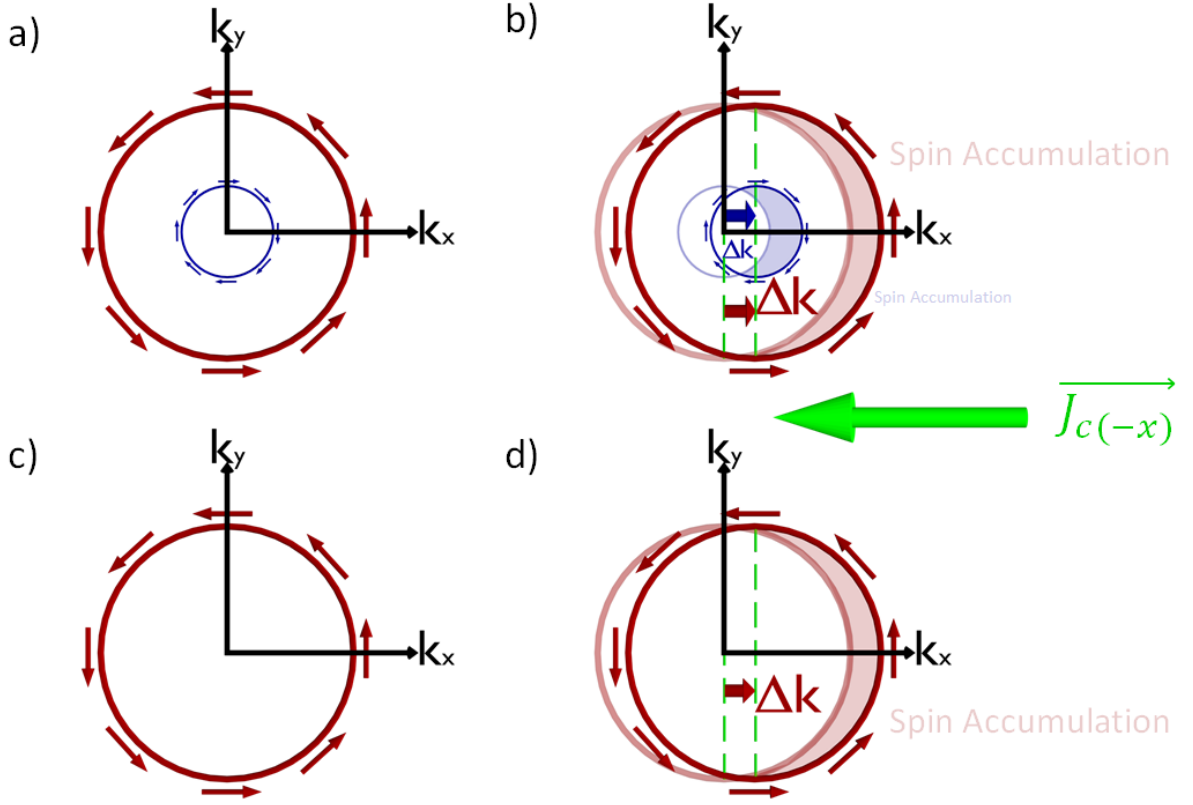


FIG. 1.9: Schematic representation of the Direct Edelstein Effect: a) Fermi contours in a Rashba interface with no charge current b) Fermi Contours in a Rashba interface. When a charge current is injected along  $-x$  the Fermi contour is shifted. This gives rise to a spin accumulation, the two contours of opposite helicities partially compensating each others c) Fermi Contour in a Topological surface State with no charge current d) Fermi Contour in a Topological Surface State when a charge current is injected along  $-x$  the contour is shifted which leads to a spin accumulation.

is not affecting the Fermi contour anymore, as the momentum of the electron is randomized<sup>114</sup>. As  $\tau$  is short typically of the order of fs in metals and up to ps in semiconductors, in the permanent regime:

$$\vec{\Delta k} = \frac{\tau q \vec{j}}{\sigma \hbar} \quad (1.18)$$

This shift is independent on  $\vec{k}$  and thus leads to a rigid shift of the Fermi contour, as depicted in figure 1.9.d. for the topological surface states. When two contours are present, as in the case of Rashba interfaces, both contours are shifted (cf 1.9.b). This more complex case has been fully treated by Miron and Gambardella<sup>115</sup>. In the case presented in figure 1.10, the carriers are electron ( $q = -e$ ) as the shift is opposite to the direction of the current. Due to this shift of the Fermi contour  $\vec{\Delta k}$  there is a spin accumulation that arises in both the Rashba and Topological insulator case. In the case of Rashba interfaces, as there are two contours of opposite helicities, the total spin accumulation is reduced. They might also have a different relaxation time  $\tau$ .

From a charge current a spin accumulation is obtained and charge to spin conversion is thus achieved.

If this spin accumulation can relax to an adjacent material, a spin current will flow towards the adjacent material. This effect is known as the direct Edelstein effect, that was first predicted by V.M. Edelstein in 1990<sup>29</sup>. The conversion from a 2D charge current to a 3D spin current is defined as the inverse of a length  $q_{EE}$ <sup>116</sup> with:

$$q_{EE} = \frac{J_s^{3D}}{J_c^{2D}} \quad (1.19)$$

The ratio between the escaping 3D spin current and the injected 2D charge current. This value needs to be maximized to obtain the largest conversion possible.

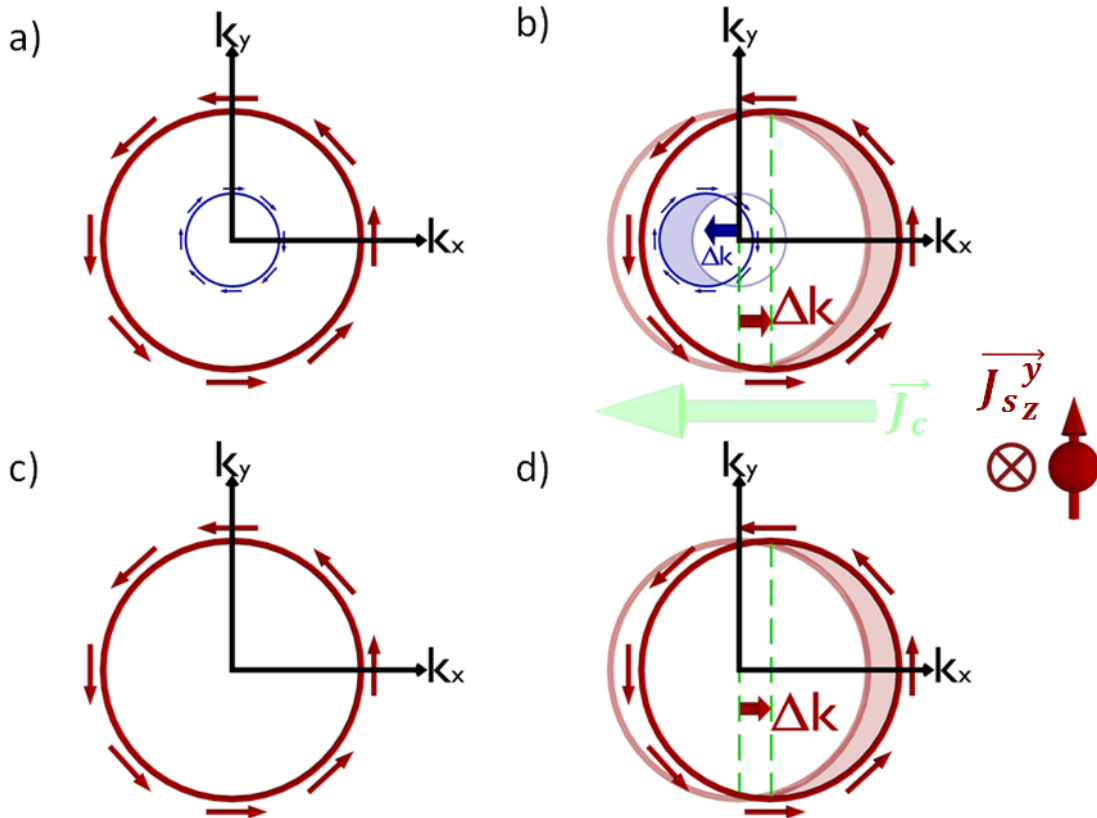


FIG. 1.10: Schematic representation of the Inverse Edelstein Effect: a) Fermi Contours in a Rashba interface with no spin current injection. b) Fermi Contours in a Rashba interface. When a spin current is injected along  $z$  with the spin direction along  $y$  the Fermi contour is shifted giving rise to a non-zero  $\Delta k$  and thus a charge current. The two contours of opposite helicities partially compensate each others. c) Fermi Contour in a Topological surface State with no spin current injection d) Fermi Contour in a Topological Surface State when a spin current is injected along  $z$  with spin along  $y$ . The Fermi contour is shifted, giving rise to a non-zero  $\Delta k$ , and thus to a charge current.

Let us now focus on the reciprocal effect, the inverse Edelstein effect. In figure 1.10.a and c, the Fermi Surface of a Rashba interface and of a Topological insulator are represented in absence of spin current. When a spin current is injected perpendicular to the surface, due to an out of equilibrium spin density



$\langle \delta S \rangle$  the Fermi surface is shifted by  $\vec{\Delta k}$ . Due to this shift and with equation (1.17) a charge current is obtained as shown in figure 1.10.b and d. A three dimensional spin current injected perpendicular to the surface is converted into a two dimensional charge current, and spin to charge conversion is obtained. The conversion efficiency is defined as a length, the inverse Edelstein length  $\lambda_{IEE}$ <sup>40</sup>:

$$\lambda_{IEE} = \frac{J_c^{2D}}{J_s^{3D}} \quad (1.20)$$

The ratio between the resulting 2D charge current to the injected 3D spin current.

### Calculation of Spin to charge conversion efficiency: case of topological insulator

Calculation of the inverse Edelstein length in a topological insulator has been done by Fert and Zhang by using the spinor Boltzmann equation<sup>117</sup>. In this model they showed that assuming no effect due to the interface  $\lambda_{IEE} = v_F \tau = l_e$  which means that the inverse Edelstein length should be equal to the mean free path. The sign of  $\lambda_{IEE}$  would depend on the type of carrier involved and the chirality of the contour. In this part we propose to calculate this from the shift of the Fermi contour with respect to the out of equilibrium spin density

For a single contour as in the case of topological surface states. The out of equilibrium spin density is equal to the total number of spins injected during the relaxation time  $\tau$ :

$$\langle \delta S \rangle = \frac{\tau J_s^{3D}}{q} \quad (1.21)$$

For small shifts of the contour  $\Delta k \ll k_F$  where  $k_F$  is the k-vector at equilibrium, the total spin density corresponds to the surface occupied by electrons of a given spin, and can be written as:

$$\langle \delta S \rangle \approx 2\pi k_F \Delta k \quad (1.22)$$

As shown previously in equation (1.17), the link between  $\Delta k$  and charge current  $J_c^{2D}$  leads to:

$$\langle \delta S \rangle = \pm \frac{k_F \tau e J_c^{2D}}{\sigma \hbar} \quad (1.23)$$

The sign depends on the chirality of the contour (clockwise or counter-clockwise) and the kind of carrier involved (electrons or holes). In the following, and for the sake of simplicity we will consider the absolute value of  $\langle \delta S \rangle$ . The expression of the Fermi wave vector is given by  $k_F = e v_F \tau / \mu \hbar$  and the one of conductivity by  $\sigma = n e \mu$ <sup>118</sup>. Moreover in a 2DEG system the carrier density  $n$  is linked to the Fermi wave vector  $n = 2\pi k_F^2$ , we obtain:

$$\langle \delta S \rangle = \frac{J_c^{2D}}{q v_F} \quad (1.24)$$

Combining equation 1.20, 1.21 and 1.24 we obtain the expression of the inverse Edelstein length for a unique Fermi contour, *i.e.* in the case of a topological insulator:

$$\lambda_{IEE} = v_F \tau = l_e \quad (1.25)$$

which is a similar result as the one of Fert and Zhang<sup>117</sup>

## Calculation of Spin to charge conversion efficiency: case of Rashba interface

In presence of two contour with opposite helicities in Rashba interfaces, the conversion is partially compensated by the contour of opposite chirality. The spin density of the majority contour  $\delta S_+$  and of the minority contour  $\delta S_-$  needs to be accounted for the evaluation of the total spin density:  $\langle \delta S \rangle = \delta S_+ + \delta S_-$  as well as the total current production  $J_c^{2D} = J_+ + J_-$ . These two contours have different relaxation time  $\tau_{\pm}$ , and Fermi wavevector  $k_{F\pm}$ , but the same Fermi velocity in the free electron approximation. This thus make the calculation similar but longer than in the case of a single contour. By using results from Gambardella and Miron<sup>115</sup> and also of Rojas-Sanchez *et.al*<sup>40</sup>, one can obtain at the first order in  $\alpha_R$ :

$$\begin{aligned} k_{F+} - k_{F-} &= \frac{2m^*}{\hbar^2} \alpha_R \\ \delta S_{\pm} &= \pm \frac{m^*}{2e\hbar k_{F\pm}} J_{\pm} \\ J_c^{2D} &= \frac{q\alpha_R}{\hbar} \langle \delta S \rangle \end{aligned} \quad (1.26)$$

Using the previous equations and equation 1.20 and 1.21, the inverse Edelstein length in the case of a Rashba interface is thus of:

$$\lambda_{IEE} = \frac{\alpha_R \tau}{\hbar} \quad (1.27)$$

Its sign will also depends on the chirality of the contour and type of carriers at the Fermi level.

It is noteworthy that in both cases, the larger the electron scattering time  $\tau$ , the larger the conversion efficiency. Materials which offer long scattering time with small Spin Orbit Coupling, and thus small Rashba spin splitting, offers possibly larger conversion efficiencies than those with a large Spin Orbit but a short relaxation time. It is indeed the case as Ag/Bi, an interface with one of the largest Rashba constant but a short electron relaxation time, gives a smaller conversion efficiency than the STO/LAO system, which possess a small Rashba constant but a particularly long relaxation time at low temperature<sup>66</sup>.

Also, the direct contact with a metal might be detrimental for the conversion because of the possible relaxation channel towards the highly conductive material. It was shown recently that the transmission rate across the interface gives a non-zero contribution to the transport relaxation, and thus plays a major role in the conversion efficiency. A choice of a proper interface is therefore needed to improve the conversion efficiency<sup>119</sup>. The fact that the conversion efficiency is sensitive to the mean free path emphasize that the Edelstein effect has a different origin than the intrinsic Spin Hall Effect, which is connected to the anomalous velocity and often insensitive to the relaxation time<sup>82</sup>.

To compare IEE and ISHE efficiency it is needed to find a similar figure of merit. Indeed, the conversion through ISHE converts a 3D spin current into a 3D charge current so that the conversion efficiency  $\theta_{SHE}$  is dimensionless. In the case of IEE, the conversion is from a 3D spin current, to a 2D charge current. Thus the conversion efficiency is a length  $\lambda_{IEE}$ , as depicted in figure 1.12. As in a SHE material the spin to charge current conversion occurs on a typical thickness of the order of the spin



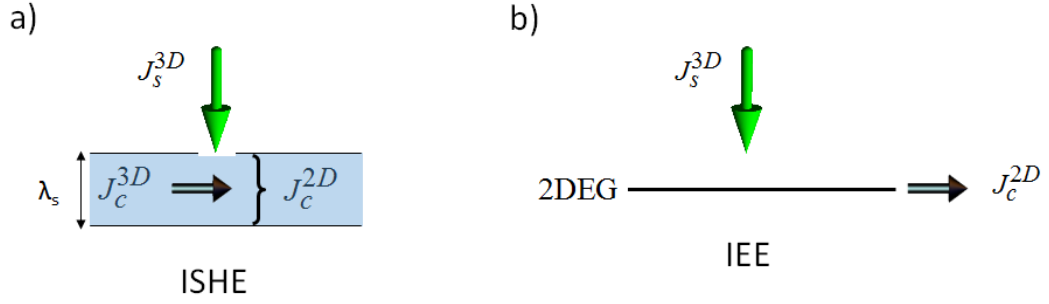


FIG. 1.11: a) Conversion of a 3D spin current in a 3D charge current in an ISHE material b) Conversion of a 3D spin current in a 2D charge current charge current in an IEE material.

diffusion length  $\lambda_s$ , the equivalent 2D charge current would be  $J_c^{2D} = \lambda_s J_c^{3D}$ . In that case the effective conversion length for SHE material  $\lambda^*$  is the product of the spin hall angle by the spin diffusion length:

$$\lambda^* = \theta_{SHE} \lambda_s \quad (1.28)$$

Materials in which Spin Hall Effect or Edelstein Effect occur can possibly allow increased spin charge interconversion efficiency. This could lead to novel spinorbitronics applications as novel magnetic RAM or beyond CMOS logic devices as presented in the introduction.

Spin to charge interconversion by harnessing the spin orbit interaction can be obtained by various means, as explained in this chapter it can be obtained through spin Hall Effect or Edelstein Effect in a large variety of materials. It also extends the field of spintronics beyond ferromagnetic materials. This conversion is intimately related to the bandstructure, impurity nature, spin orbit strength...etc. For applications and also to understand the deep physics of the spin charge interconversion a method of accurate evaluation of this conversion is needed. In the next chapter we will describe how spin pumping by ferromagnetic resonance allows to probe the spin to charge current conversion.

## Spin pumping by ferromagnetic resonance

The first pioneering works on the effect of the ferromagnetic resonance on an adjacent paramagnetic material were performed in the late 80's by Silsbee and Monod<sup>120</sup>. Spin pumping by ferromagnetic resonance was then further developed in the late 2000's mostly within Saitoh, Rezende, Van Wees and Hoffmann groups<sup>26;121;122;123</sup> and became since then a widely used technique in the field of spin-orbitronics. Based on the theoretical work of Tserkovnyak, Brataas and coworkers<sup>124</sup> this technique allows to extract the figure of merit of the spin to charge current conversion, *i.e.*, the spin Hall angle, the inverse Edelstein length and the spin diffusion length in a wide variety of materials including heavy metals, semiconductors, organic materials, Rashba interfaces and topological insulators. The main interest of such a technique is its compatibility with a large variety of systems and that it does not require nano-patterning by E-beam lithography contrary to lateral spin valves.

In this chapter we will first describe the ferromagnetic resonance mechanism and present this powerful magnetometry tool. Then we will present the FMR spin pumping theory developed by Tserkovniak, Brataas *et al.* and explain how to disentangle the ISHE/IEE related effects from other spurious effects unrelated to spin charge current interconversion. We will present some results in order to show how to obtain the spin to charge current conversion efficiency and the spin diffusion length. This chapter has been written to present the experimental technique and was extended to be a guide to perform an accurate Ferromagnetic resonance and spin pumping measurements.

## 2.1 Ferromagnetic Resonance

The first theoretical description of the precession of the magnetization in a ferromagnet was proposed by Lev Davidovitch Landau and Evgeny Mikhailovich Lifshitz in 1935<sup>125</sup>. A modification of the Landau-Lifschitz equation was then proposed by Thomas Gilbert in 1955 including a magnetization damping term (the so-called Gilbert damping term)<sup>126</sup>. Later in 1996 Slonczewski expanded the model to account for the spin transfer torque phenomena<sup>14</sup>. In this part we will focus on the Landau-Lifschitz-Gilbert equation (LLG equation) and give the resonance conditions. Note that in the following the formulas are in SI units and could differ slightly from the literature results that are usually in CGS units.

### 2.1.1 Landau-Lifschitz-Gilbert equation

The description of the link between the magnetization  $\vec{M}$  of norm  $M_s$ , the saturation magnetization of the FM, and the effective applied magnetic field  $H_{eff}$  is given by:

$$\frac{d\vec{M}}{dt} = -\frac{g\mu_B}{\hbar}\mu_0 \vec{M} \times \vec{H}_{eff} \quad (2.1)$$

Where  $g$  is the Landé  $g$  factor with  $2 < g < 2.2$  in a Ferromagnetic material,  $\mu_B$  is the Bohr magneton,  $\hbar$  is the reduced Planck constant and  $\mu_0$  is the vacuum permeability. This equation is known as the Landau-Lifschitz equation<sup>125</sup> and describe the motion of magnetization around an affective magnetic field. Here  $\vec{H}_{eff}$  is the effective magnetic field accounting for the external magnetic field  $\vec{H}_0$ , the demagnetizing field  $\vec{H}_D$ , and the anisotropy field  $\vec{H}_k$ :

$$\vec{H}_{eff} = \vec{H}_0 + \vec{H}_D + \vec{H}_k \quad (2.2)$$

We won't demonstrate here how this equation is obtained but in the following we will give some phenomenological explanation from a micromagnetic point of view<sup>127</sup>. The magnetic moment  $\vec{\mu}$  of a ferromagnetic material tends to align to an applied external magnetic field  $\vec{H}_{ext}$ . The effective magnetic field  $\vec{H}_{eff}$  felt by the magnetic moment will thus exert a torque  $\vec{\tau}$  on the magnetization:

$$\vec{\tau} = \vec{\mu} \times \mu_0 \vec{H}_{eff} \quad (2.3)$$

The torque exerted by the external field is by definition the derivative of the angular momentum  $\vec{J}$ :

$$\vec{\tau} = \frac{d\vec{J}}{dt} \quad (2.4)$$

And the magnetic moment and angular momentum are linked through the gyromagnetic ratio  $\gamma = \frac{g\mu_B}{\hbar}$ :

$$\vec{\mu} = -\gamma \vec{J} \quad (2.5)$$

Considering the whole magnetic volume, we can replace atomic magnetic moment by the magnetization  $\vec{M}$  and the equation is thus similar to the Landau-Lifschitz equation. This equation describe the uniform precessional equation of motion of the magnetization around the magnetic field, and is usually referred as the Larmor precession.

This equation of motion is nonetheless incomplete, indeed it is dissipationless and implies a perpetual precession of the magnetization which is not compatible with real system where angular momentum is lost. Several processes can lead to a loss of angular momentum including electron-phonon scattering, electron-magnon scattering, or magnon-phonon scattering<sup>127</sup>. Regarding the complexity to describe these various phenomenom and their different origin a phenomenological damping term  $\lambda$  was introduced by Landau and Lifschitz in the equation 2.1<sup>125</sup>. It describes the damped precession of the magnetization due to the loss of angular momentum:

$$\frac{d\vec{M}}{dt} = -\mu_0\gamma \vec{M} \times \vec{H}_{eff} - \lambda \vec{M} \times (\vec{M} \times \vec{H}_{eff}) \quad (2.6)$$

This equation can be used when the damping is small, but does not describe the magnetization motion well for large damping values, especially in thin films. That's why in 1955 Thomas Gilbert proposed another description of the damping that depends on the derivative of the magnetization vector<sup>126</sup>. The dissipation is similar to a 'viscous' force, whose components are proportional to the time derivatives of the magnetization and is written  $\alpha$ :

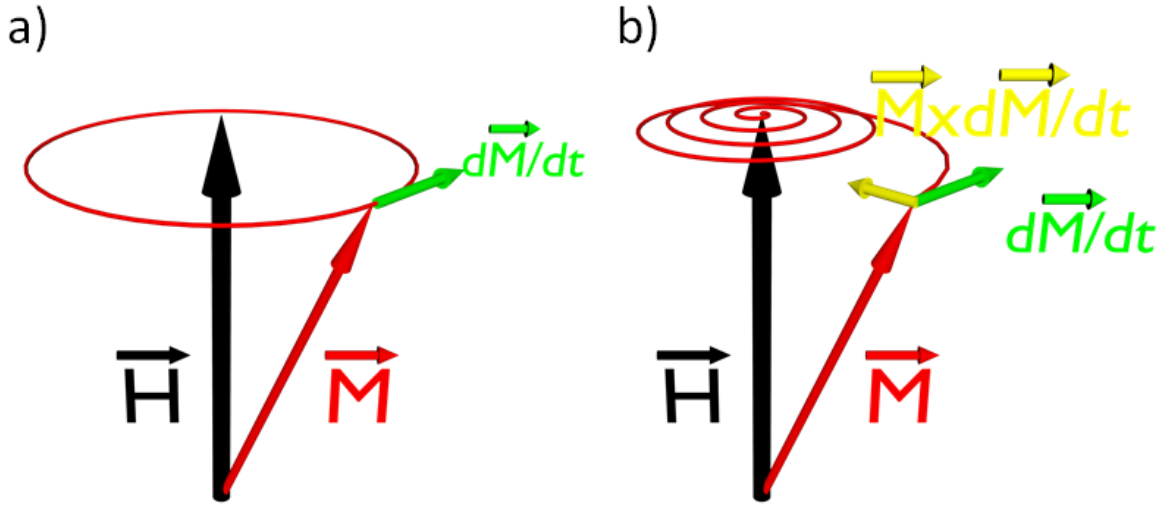


FIG. 2.1: Magnetization dynamics: a) Without damping and b) with Gilbert damping.

$$\frac{d\vec{M}}{dt} = -\mu_0\gamma \vec{M} \times H_{eff} + \frac{\alpha}{M_s} \vec{M} \times \frac{d\vec{M}}{dt} \quad (2.7)$$

Where  $\alpha$  is the dimensionless Gilbert damping parameter and  $M_s$  is the saturation magnetization. The equation 2.7 known as the Landau-Lifshitz-Gilbert equation (LLG) describe the magnetization dynamics. Note in both formula the presence of the vacuum permeability  $\mu_0$ , this is to have all formulas in SI units, notably to keep the magnetic fields  $H$  in A/m. In figure 2.1 we show the magnetization precession dynamics around an effective field in presence or absence of damping. In the presence of Gilbert damping, the magnetization has a spiral motion within a time scale of  $(1/\alpha\gamma\mu_0 H_{eff})$  and tends to align with the applied magnetic field.

The resonance appears when an excitation is periodically applied to the system at a given frequency known as the resonance frequency  $f_{res}$ . At this frequency the system oscillates with a larger amplitude than at other frequencies. Obtaining the resonance conditions consists in solving the equation of motion and determine the maximum of motion under the given experimental conditions. In the following we will solve the LLG magnetization equation of motion in the presence of an external DC field  $H_{DC}$  and a small radiofrequency field  $h_{rf}$  acting as a periodic excitation. A typical setup to obtain the ferromagnetic resonance is composed of an electromagnet allowing to apply large DC field and a source of radiofrequency field which can be either a stripline or an Electron Paramagnetic Resonance (EPR) cavity. The resonance is then measured by the change in the absorption of the microwave energy at resonance. A scheme of the typical FMR geometry is shown in figure 2.2, we will describe later in this chapter the differences between the strip-line and the cavity setups.

## 2.1.2 Ferromagnetic resonance conditions

In order to simplify the resolution and to avoid unnecessary long calculations we will solve only the undamped Landau-Lifshitz equation and will then extend this results to the case obtained when the

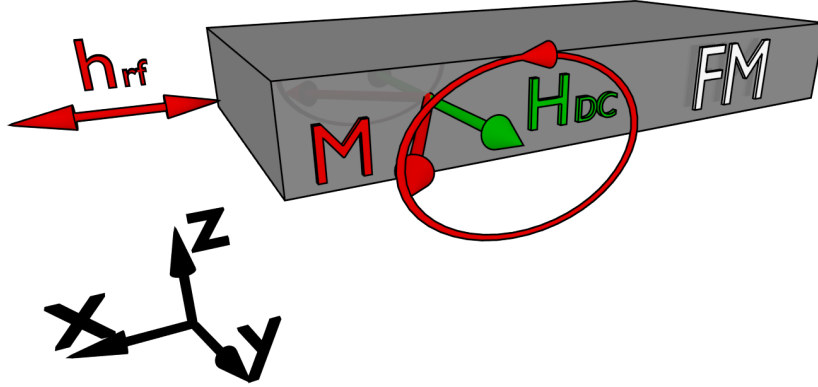


FIG. 2.2: Ferromagnetic material FM which magnetization is precessing under action of both an rf magnetic field at resonance frequency and a DC magnetic field

damping is non-zero. The complete solution to the LLG equation can be found elsewhere, for example in “Magnetization Oscillations and Waves“ by Gurevich and Melkov<sup>127</sup> and in Michael Farle’s review on the ferromagnetic resonance in thin films<sup>128</sup>. We will use the geometry of the figure 2.2 in the following part.

The total magnetization  $\vec{M}_{tot}$  and field  $\vec{H}_{tot}$  can be written as:

$$\vec{M}_{tot} = \vec{M}_0 + \vec{m}(r,t) \quad \vec{H}_{tot} = \vec{H}_{eff} + \vec{h}(r,t) \quad (2.8)$$

where  $\vec{h}(r,t)$  ( $\vec{H}_{eff}$ ) and  $\vec{m}(r,t)$  ( $\vec{M}_0$ ) are the dynamic (static) component of the magnetic field and magnetization. In a typical FMR setup the AC exciting field is small compared with the DC field and thus  $\vec{h}(r,t)$  and  $\vec{m}(r,t)$  can be addressed as a perturbation to the total magnetic field and magnetization. This means that the precession cone angle is small and thus in the coordinate system of fig 2.2:

$$\left\| \vec{h}(r,t) \right\| \ll \left\| \vec{H}_{eff} \right\| \quad \left\| \vec{m}(r,t) \right\| \ll \left\| \vec{M}_0 \right\| \quad \vec{H}_{eff} = H_{eff} \vec{y} \quad \vec{M}_0 = M_0 \vec{y} \quad (2.9)$$

By introducing  $\vec{M}_{tot}$  and the field  $\vec{H}_{tot}$  to the LLG equation, with the small precession cone angle conditions, we have the following equation in the first order approximation :

$$\frac{d \vec{m}(r,t)}{dt} = -\mu_0 \frac{g\mu_B}{\hbar} (M_0 \vec{y} \times \vec{h}(r,t) + \vec{m}(r,t) \times H_{eff} \vec{y}) \quad (2.10)$$

We will solve this equation by introducing  $\vec{m}$  and  $\vec{h}$  in the frequency domain  $\vec{m}(w) e^{i(wt)}$  and  $\vec{h}(w) e^{i(wt)}$  in order to linearise the equation (2.10):

$$i\omega \vec{m} = -\mu_0 \frac{g\mu_B}{\hbar} \vec{y} \times (M_0 \vec{h} - H_{eff} \vec{m}) \quad (2.11)$$

Then we can project this equation onto the axes of the coordinate system of the figure (2.2):

$$\begin{aligned} i\omega m_x &= \mu_0 \frac{g\mu_B}{\hbar} (M_0 h_z - H_{eff} m_z) \\ i\omega m_y &= 0 \\ i\omega m_z &= \mu_0 \frac{g\mu_B}{\hbar} (-M_0 h_x + H_{eff} m_x) \end{aligned} \quad (2.12)$$

We can also link the magnetization and the external magnetic field by using the Polder susceptibility tensor<sup>129</sup>  $\vec{m} = \overleftrightarrow{\chi} \vec{h}$  and which is defined as:

$$\overleftrightarrow{\chi} = \begin{pmatrix} \chi' & i\chi'' \\ -i\chi'' & \chi' \end{pmatrix} \quad (2.13)$$

The equations 2.12 and 2.13 directly leads to:

$$\chi' = \frac{M_0 H_{eff} \left(\frac{g\mu_B}{\hbar}\right)^2}{\left(\frac{g\mu_B}{\hbar}\right)^2 H_{eff}^2 - \omega^2}; \chi'' = \frac{\omega M_0 \left(\frac{g\mu_B}{\hbar}\right)}{\left(\frac{g\mu_B}{\hbar}\right)^2 H_{eff}^2 - \omega^2} \quad (2.14)$$

The resonance is then obtained when the response to the excitation is the largest, *i.e.*, when the susceptibility is the largest:

$$\omega_{res} = \left(\frac{g\mu_B}{\hbar}\right) \mu_0 H_{eff} \quad (2.15)$$

Equation (2.15) is different from the well known Kittel formula<sup>130</sup>, indeed here we did not take into account the link between  $\vec{H}_{eff}$  and the magnetic field through the demagnetizing field. The effective field  $H_{eff}$  is the sum of the applied field, demagnetizing field and anisotropy field as defined in the equation 2.2. In an ellipsoid –in a thin film– the demagnetizing field and anisotropy field are related to the magnetization through the demagnetizing tensor  $\vec{H}_D = \overleftrightarrow{N} \vec{M}_{tot}$ :

$$\vec{H}_D = \begin{pmatrix} N_x & 0 & 0 \\ 0 & N_y & 0 \\ 0 & 0 & N_z \end{pmatrix} \begin{pmatrix} m_x \\ M_s \\ m_z \end{pmatrix} \quad (2.16)$$

By solving the linearised LLG equation in the case of an infinite film with the field in the plane of the field, which is relevant for the experiments we have  $N_x = N_y = 0$  and  $N_z = 1$ . When accounting for the damping and the demagnetizing field the complete expression of the imaginary part of the Polder susceptibility  $\chi''$  associated with the absorption of power<sup>131</sup> can be written as:

$$\chi'' = \frac{-\alpha \left(\frac{\omega}{\gamma}\right) \mu_0 M_s \left( (\mu_0 M_s + \mu_0 H_0 + \mu_0 H_k)^2 + \left(\frac{\omega}{\gamma}\right)^2 \right)}{\left( \mu_0^2 (M_s + H_0 + H_k) * (H_0 + H_k) - \left(\frac{\omega}{\gamma}\right)^2 \right)^2 + \left( \alpha \left(\frac{\omega}{\gamma}\right) (\mu_0 M_s + 2(\mu_0 H_0 + \mu_0 H_k)) \right)^2} \quad (2.17)$$

Therefore the resonance condition is obtained when the susceptibility is maximized, so when:

$$\omega_{res} = \frac{g\mu_B}{\hbar} \mu_0 \sqrt{(M_s + H_0 + H_k)(H_0 + H_k)} \quad (2.18)$$

This is the well-known Kittel formula. The position of the  $\mu_0$  constant can be different from the original Kittel formula with magnetic fluxes in Tesla instead of magnetic fields in A/m, here  $M_s$ ,  $H_0$  and  $H_k$  are all in A/m.

The power absorbed in the ferromagnetic material is described by  $\chi''$ <sup>131</sup> and close to the FMR at a fixed frequency it has a Lorentzian lineshape:

$$\chi'' = \frac{A_{sym}\Delta H^2}{\Delta H^2 + (H_{eff} - H_{res})^2} \quad (2.19)$$

With  $A_{sym}$  the amplitude of the Lorentzian,  $\Delta H$  the half width at half maximum equal to  $\mu_0\Delta H = \frac{\alpha\omega}{\gamma}$  and the absorbed power can then be written  $P_{abs} = \omega\chi''h_{rf}^2$ . The amplitude of this Lorentzian is inversely proportional to the Gilbert damping  $\alpha$  and proportional to the square of the rf magnetic field.

Note that in general a lineshape asymmetry can be observed. This asymmetry has been recently associated with eddy currents generated by the time varying magnetic field<sup>132;133;134</sup>. The phase shift between the rf magnetic field and the eddy current-induced field will thus distort the resonance shape. The measured lineshape is therefore not perfectly symmetric and has an anti-Lorentzian (dispersive) contribution

$$\chi'' = A_{sym} \frac{\Delta H^2}{\Delta H^2 + (H_{eff} - H_{res})^2} - B_{asym} \frac{\Delta H(H_{eff} - H_{res})}{\Delta H^2 + (H_{eff} - H_{res})^2} \quad (2.20)$$

Note that the asymmetric part can be large when measuring FMR using striplines with a strong out of plane component of the radiofrequency field on large samples with a thick conductive layer in contact with the ferromagnet<sup>134</sup>. Nonetheless it is negligible when using small samples, especially in cavity with an homogeneous radiofrequency field in the plane of the sample<sup>133</sup>. In that case equation 2.19 describe well the absorption spectrum.

To increase the signal over noise ratio FMR measurement are usually performed using a lock-in technique either by modulating the frequency or the field. In the case of the setups described in this manuscript the field modulation was used. Therefore the shape of the measured FMR is not a Lorentzian but the derivative of a Lorentzian as seen in figure 2.3 for the resonance of a 20nm thick Permalloy film (NiFe 20nm) deposited on Silicon. The complete expression accounting for a non-zero asymmetric part is given by the following expression and was used to fit the derivative FMR lines in the entire manuscript:

$$\frac{d\chi''}{dH} = -2A_{sym} \frac{\Delta H^2(H_{eff} - H_{res})}{(\Delta H^2 + (H_{eff} - H_{res})^2)^2} + 2B_{asym} \frac{\Delta H(H_{eff} - H_{res})^2}{\Delta H^2 + (H_{eff} - H_{res})^2} - B_{asym} \frac{\Delta H}{\Delta H^2 + (H_{eff} - H_{res})^2} \quad (2.21)$$

The fit follows perfectly the FMR line as seen in fig 2.3, from this fitting we could extract the resonance field  $H_{res}$ , the half width at half maximum  $\Delta H$  and the peak to peak linewidth  $\Delta H_{pp}$  defined as the interval between the extrema of the derivative. We have  $\mu_0\Delta H_{pp} = \frac{2}{\sqrt{3}}\Delta H$ , this leads to the link between  $\Delta H_{pp}$  and the Gilbert damping:

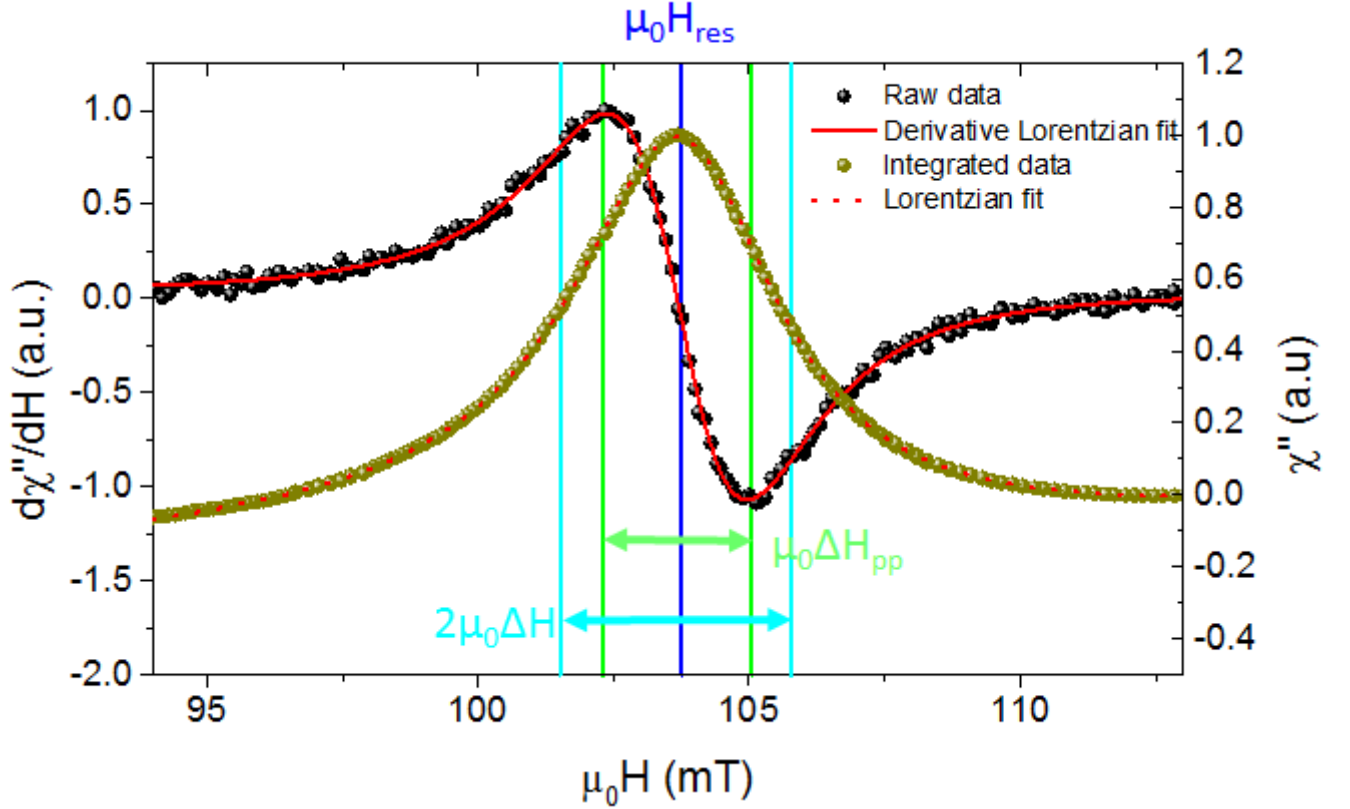


FIG. 2.3: Derivative of the absorption at resonance in a NiFe20nm deposited on Si and integrated signal measured at a frequency of 10GHz in a field modulated FMR setup. Both fits were obtained using equation (2.20) and (2.21) the fitting parameters are  $\mu_0\Delta H = 2.24 \pm 0.01\text{mT}$ ;  $\mu_0\Delta H_{pp} = 2.59 \pm 0.01\text{mT}$  and  $\mu_0H_{res} = 103.8 \pm 0.2\text{mT}$

$$\mu_0\Delta H_{pp} = \frac{2}{\sqrt{3}} \frac{\alpha\omega}{\gamma} \quad (2.22)$$

To account for the disorder in the sample the so called inhomogeneous broadening  $\Delta H_0$  can be introduced. In a polycrystal all the crystals are not perfectly similar, they don't have the exact same orientation, anisotropy and magnetization leading to a crystallite dependent resonance field and thus they don't resonate at the exact same field which lead to a linewidth enhancement<sup>135</sup>. When the field is applied in plane in samples with a good homogeneity  $\mu_0\Delta H_0$  is of the order of 0.1mT, this is for example the case in Permalloy of CoFeB thin films. The FMR is thus also a good tool to measure the homogeneity of a polycrystal<sup>136</sup>. When accounting for the inhomogeneous broadening we obtain equation 2.23:

$$\mu_0\Delta H_{pp} = \frac{2}{\sqrt{3}} \frac{\alpha\omega}{\gamma} + \mu_0\Delta H_0 \quad (2.23)$$

Therefore from the Ferromagnetic resonance measurements it is possible to obtain the dynamic and static properties of a ferromagnetic material including  $M_s$ , anisotropies and damping by using the Kittel formula (equation 2.18) and the Gilbert damping (equation 2.23). It is to be noted that equation 2.23 is incomplete, indeed a wide variety of effects including two-magnon scattering and non Gilbert damping phenomenon as slow and fast relaxer impurities<sup>137;127</sup> can increase the total linewidth of the



FMR. Nonetheless these effects are non-negligible only in some very specific cases, in particular in YIG at low temperature or impurity doped NiFe in the case of slow relaxer<sup>138;139</sup>, or epitaxial ultra-thin film for the 2-magnon scattering<sup>140;141</sup>.

## 2.2 FMR: a powerful magnetometry tool

Ferromagnetic resonance is a spectroscopy technique that has been widely used to probe the magnetic properties of ferromagnets. As other resonance methods it is a very highly sensitive spectroscopy technique and is extremely precise to measure anisotropy in magnetic thin films<sup>142</sup>, dynamical properties of ferromagnets<sup>143</sup>, and defects in magnetic thin films<sup>136</sup>. In this part we will emphasize the possibility offered by the ferromagnetic resonance to determine the main properties static and dynamic properties of ferromagnetic materials.

### 2.2.1 Broadband FMR: frequency dependence

A broadband FMR measurement setup allows to measure the ferromagnetic resonance on a wide frequency range using a broadband microwave source. Typically such a measurement is performed using a Vector Network Analyser (VNA) to inject microwave power into a microstripline and detect the change in the microwave output power as a function of the magnetic field.

The broadband FMR measurement relies on the use of a microstripline. A microstripline is constituted of one signal wire separated from ground plate by a dielectric material (substrate) as seen in fig 2.4.a. This stripline is used to convey microwave-frequency signals and contrary to a waveguide there exists no cutoff frequency and signal of various frequencies can be conveyed. When a microwave frequency signal is injected in the signal wire, the electromagnetic wave goes along the signal line, an rf electric field  $e_{rf}$  from the signal wire to the ground plates will appear and an rf magnetic field  $h_{rf}$  perpendicular to the direction of propagation of the wave and to the electric field will arise. Therefore by injecting a microwave signal in a microstripline it is possible to obtain a radiofrequency field  $h_{rf}$  as shown in figure 2.4.b. If a sample is placed close to the signal line in the presence of a DC magnetic field it is thus possible to obtain the ferromagnetic resonance as described in the previous part. Moreover regarding the broad frequency of the signal that can be injected in the microstripline the frequency dependence of the FMR can be obtained and it is possible to use equations 2.18 and 2.23.

The typical setup to measure broadband FMR is to use a vector network analyzer (VNA) and is usually called VNA-FMR<sup>144</sup>. The VNA supply a microwave power at a given frequency in the signal line, the power  $P_{in}$  enter the stripline, a part of this power  $P_{abs}$  is absorbed within the stripline and by the sample and the output power  $P_{out} = P_{in} - P_{abs}$  is measured using the detector of the VNA. The external DC magnetic field  $H_{DC}$  is swept and at the ferromagnetic resonance the absorbed power  $P_{abs} = \omega\chi''h_{rf}^2 + C^{ste}$  will increase and thus the output power detected by the VNA will decrease, it is therefore possible to measure the ferromagnetic resonance using a VNA-FMR setup. Nonetheless this is not the FMR broadband setup used in spintec, indeed such a measurement relies on a direct

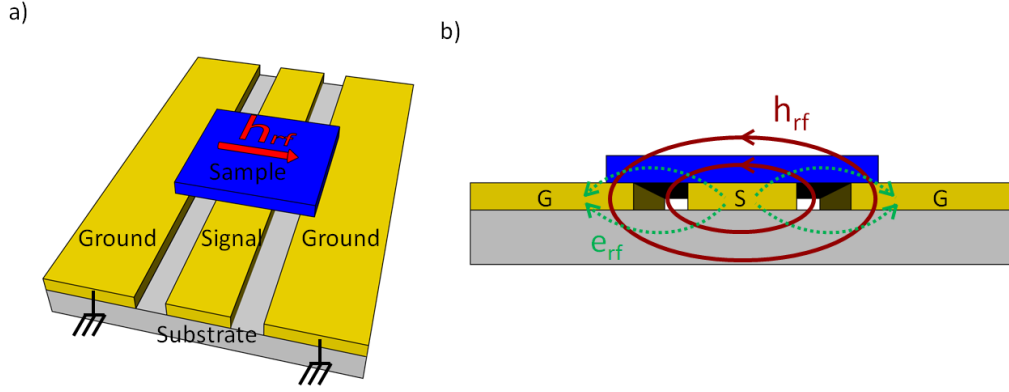


FIG. 2.4: Schematic representation of a microstripline. a) The different part constituting the microstripline with sample on the signal line with FM layer facing the line. b) Direction of the rf magnetic field and electric field when a microwave signal is conveyed in the signal line.

measurement of the absorbed rf power using a VNA, it does not benefit from the increased signal over noise ratio permitted by using the lock-in technique and relies on a full microwave line that is more fragile and harder to handle for non-trained user than coaxial cable.

The lock-in amplifier FMR (LIA-FMR) setup that is used is described in figure 2.5. Similarly to the case described above a power source (from a VNA or any other power source) is supplied in the signal line, and the output signal is detected by a broadband diode detector that will output an electrical signal  $V_{diode} \propto P_{out}$ . Modulation coils are powered at the reference frequency provided by the lock-in amplifier (low frequency compared to the rf) and the electrical signal output by the diode is connected to the signal input of the lock-in. Therefore the signal measured is the derivative of the diode voltage with respect to the field and is thus proportional to the derivative of the absorbed power allowing the measurement of the FMR and taking advantage of the lock-in technique to enhance the signal over noise ratio. The magnetic field is measured using a Gaussmeter (not shown here for clarity). It is to be noted that the sample needs to be small enough to be subjected to an uniform DC field and be uniformly excited by the rf magnetic field. We typically use sample of 0.4mm\*2.4mm that are small enough to avoid these problems but are still large enough to obtain a signal that can be easily measured and fitted. Using these small samples also allows to reduce the asymmetric contribution to the FMR compared to larger samples<sup>134</sup>.

An example of a typical broadband FMR measurement and the extraction of the main ferromagnetic properties of a 20nm thick Permalloy film deposited on Si is provided in fig 2.6. The ferromagnetic resonance spectrum is measured for different frequency as seen in figure 2.6.a. The derivative of the Lorentzian is obtained from 4.0 to 24.0GHz. It is possible to obtain the resonance field  $H_{res}$  and the peak to peak linewidth  $\Delta H_{pp}$  as a function of frequency. The extracted values are then fitted using the Kittel formula given in equation 2.18, and the link between damping and peak to peak linewidth in equation 2.23. As can be seen in figure 2.6.b and 2.6.c from these fitting it is possible to extract some of the magnetic properties of the magnetic layer. In particular from this fit we can obtain the g-factor,  $g = 2.10 \pm 0.02$ , the saturation magnetization  $M_{seff} = 807 \pm 18kA/m$ , the uniaxial anisotropy

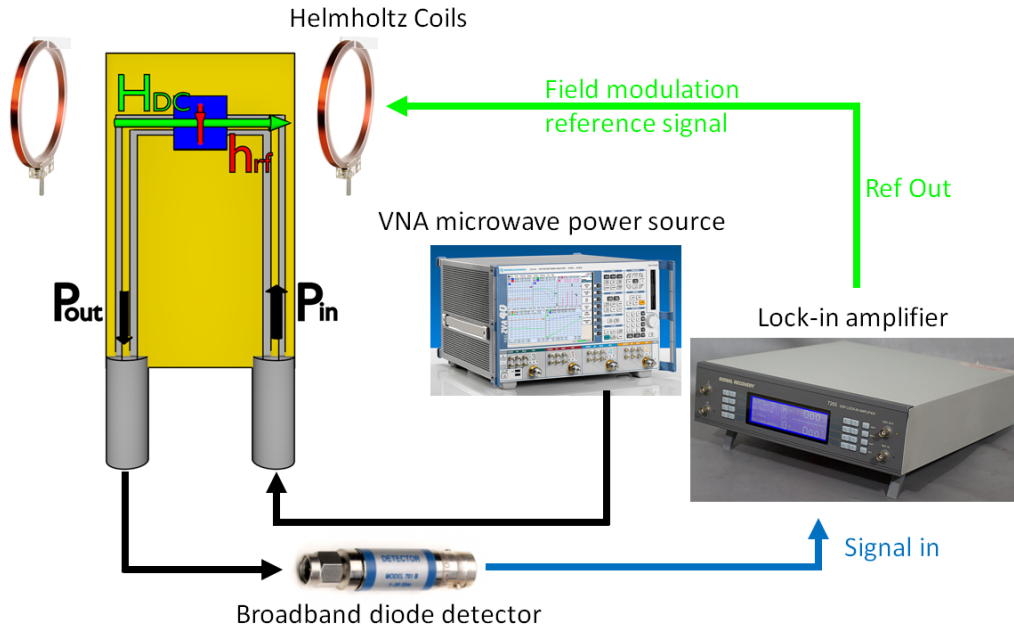


FIG. 2.5: Schematic representation of a Typical LIA-Broadband FMR setup and its main elements.

$\mu_0 H_k = -0.8 \pm 0.3 \text{ kA/m}$ , the Gilbert damping  $\alpha = 0.00636 \pm 0.00003$  and the inhomogeneous broadening  $\mu_0 \Delta H_0 = 0.09 \pm 0.01 \text{ mT}$ . These extracted values are typical of a 20nm thick Permalloy thin film deposited on Silicon and are in line with results published in literature<sup>60;145</sup>.

## 2.2.2 FMR in cavity: angular dependence at X-band

The ferromagnetic resonance can also be obtained using a resonant cavity. The only main disadvantage of a cavity is that it is needed to work at a fixed frequency, the cavity resonance frequency. For data presented in this manuscript we used a MS5 loop gap resonator at X-band around 9.75GHz operating in a pseudo  $TE_{102}$  mode. A complete description of the MS5 loop-gap resonator and its differences and advantages compared with a rectangular or cylindrical cavity are given in appendix A. The results described in this section can be obtained in any resonant cavity at X-band. The advantages of using a cavity are numerous including the considerably larger field that can be obtained, or the high signal to noise ratio. More importantly it is easier to make electrical detection of the FMR and the rf magnetic and electric field direction and amplitude are very well defined.

The two last points are particularly important for spin pumping FMR measurements that will be described later on in this thesis, nonetheless it seems to be at the cost of the frequency dependence and thus determination of  $M_s$ ,  $H_k$  and  $\alpha$ . We will show now that it is possible to obtain all these parameters from an out of plane angular dependence of the FMR performed in cavity, and show that the obtained results are similar to the one obtained through broadband FMR with the example of an archetypal Platinum/Permalloy sample.

The ferromagnetic resonance can be obtained using a resonant cavity, for this purpose a brucker EPR 300E setup was used. This setup is very similar to the stripline setup, only the rf source and detec-

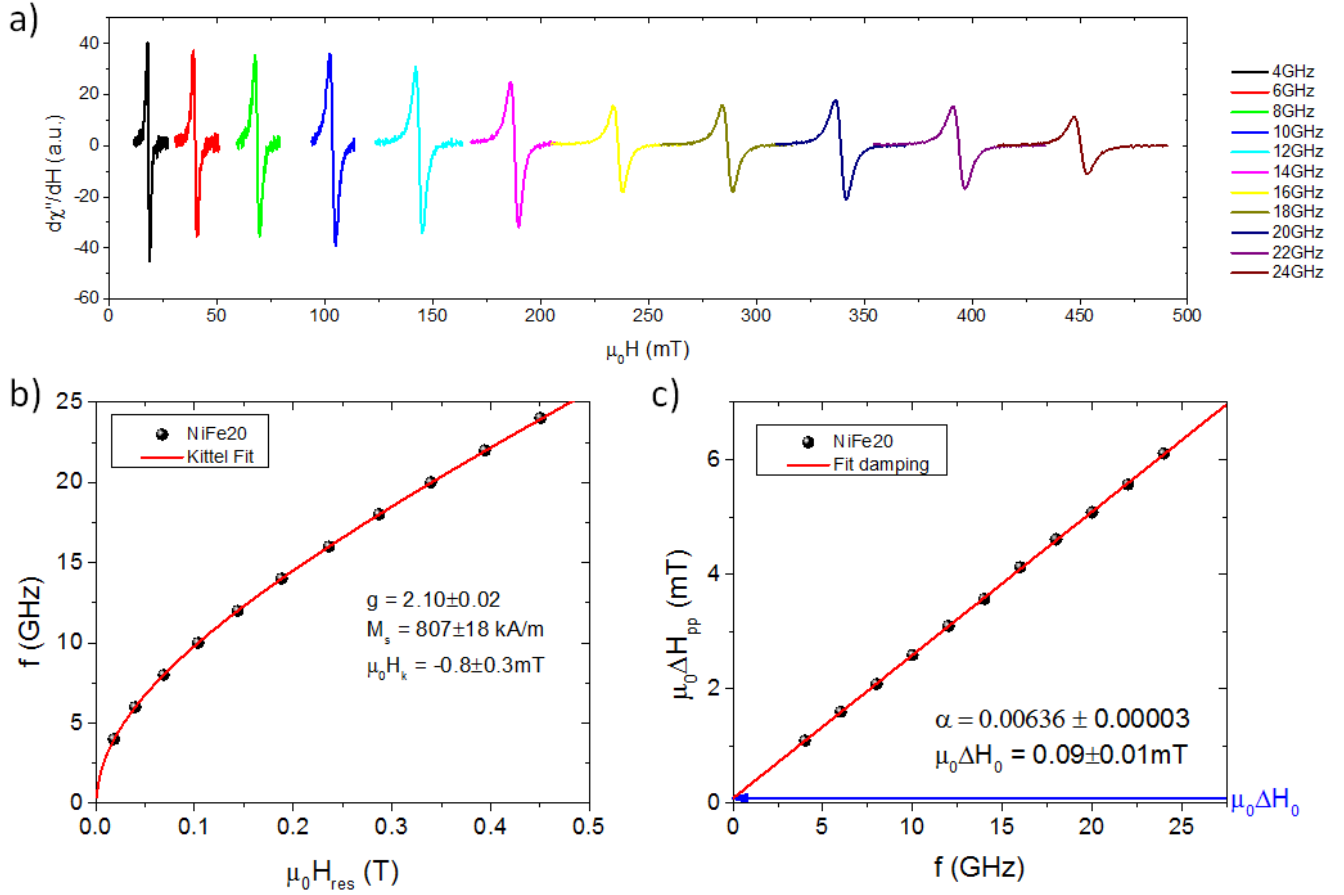


FIG. 2.6: Typical results obtained from a broadband FMR measurement. a) The FMR signals obtained at different frequencies. b) The resonance fields and c) the peak to peak linewidths obtained from the raw data shown in a) and fitted using equation 2.18 and 2.23 respectively.

tion method is different. As seen in figure 2.7 the sample is positioned in a cavity in the gap of the Electromagnet. The radiofrequency source which is typically a Gunn diode emits a wave which is directed towards a circulator. Through this circulator the signal is directed toward the cavity. Due to this incident electromagnetic radiation, at the resonant frequency of the cavity, electromagnetic power is entering the cavity giving rise to a radiofrequency electric and magnetic field. Part of this power is absorbed in the cavity the rest is reflected towards the circulator and then goes through the circulator towards the microwave detector. At the ferromagnetic resonance the power absorbed in the cavity increases leading to a reduce power directed towards the detector and allowing to measure the resonance. It is thus needed to couple the cavity before the measurements so that the power absorbed out of resonance is the same as the power reflected towards the detector. Similarly to the case of the stripline measurement, field modulation is obtained using Helmholtz coils to allow better sensitivity of the setup using a lock-in detection. Therefore the obtained signal is very similar to the one of the stripline technique and is fitted using equation 2.21.

The samples that we use for measurements in cavity are the same as the ones we use for the broadband and are typically of  $0.4\text{mm} \times 2.4\text{mm}$ . These samples are glued on a PCB which has two copper lines that allows us to detect the resonance electrically and measure ISHE or IEE as described in the

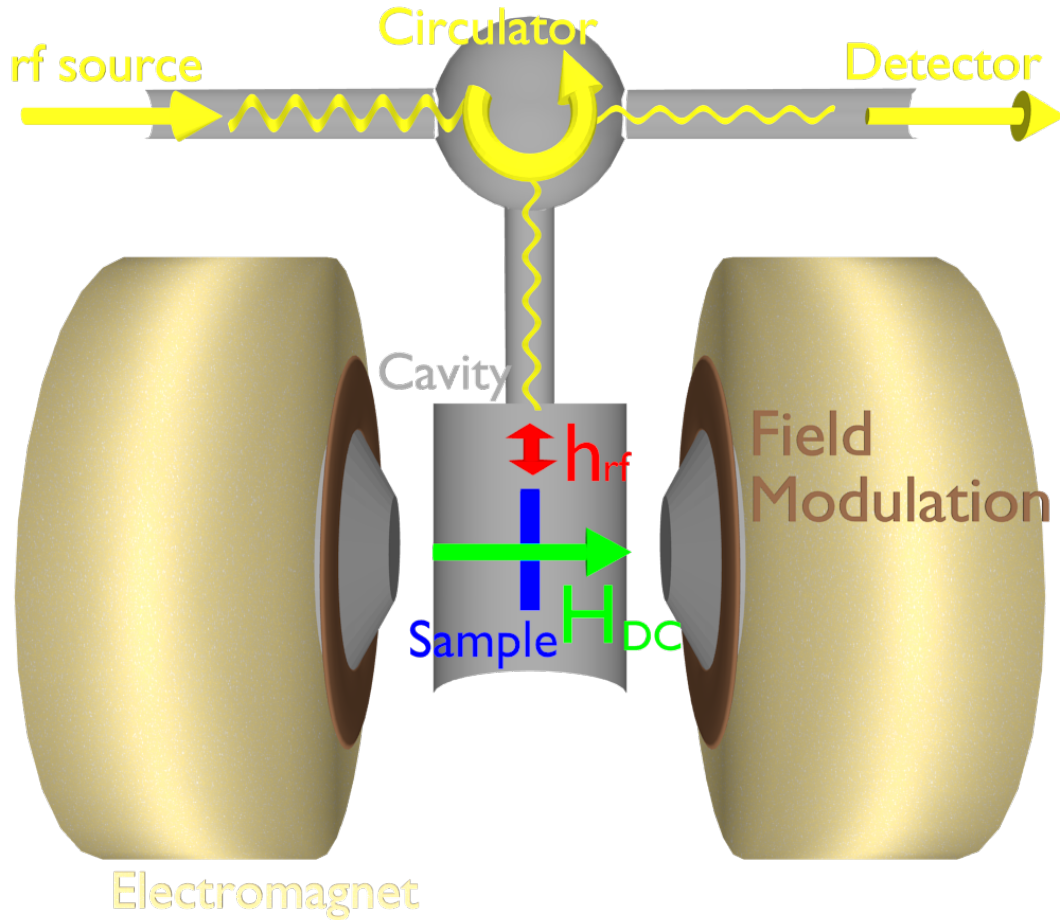


FIG. 2.7: Schematic representation of the measurement of FMR using a resonant cavity.

following sections. The sample is positioned in the center of the cavity where the rf magnetic field  $h_{rf}$  is maximum as seen in fig 2.8a). When inserted in the cavity the sample is not aligned with the DC magnetic field  $H_{DC}$  and the angle between the normal of the sample and the DC field is written  $\theta_H$ , this angle can be modified using a goniometer. The sample is not visible within the cavity but it is very easy to align it in the plane of the DC field ( $\theta_H = \pm 90^\circ$ ) or perpendicular to it ( $\theta_H = 0^\circ$ ). For an in plane magnetized ferromagnet the resonance field minimum is obtained in the plane, and the resonance field maximum perpendicular to the plane<sup>146</sup>.

After aligning the sample in a known direction a full set of angular dependence can be performed as seen in figure 2.8b) for a Pt(10nm)/Permalloy(20nm). The main changes occurring as a function of the out of plane angle are the change of the resonance field from a minimum at  $\pm 90^\circ$  to a maximum at  $0^\circ$  and the change of the linewidth with the angle. By fitting the FMR signal using equation 2.21 we can extract the resonance field and peak to peak linewidth as seen on figure 2.8c) and d). The angular dependence of the linewidth shows a complex pattern, it is maximum close to  $\pm 15^\circ$ , minimum at  $\pm 90^\circ$  and a local minimum is observed at  $0^\circ$ . The angular dependence of both the linewidth and the resonance field can allow us to obtain the magnetic properties of the ferromagnet. To do so we will

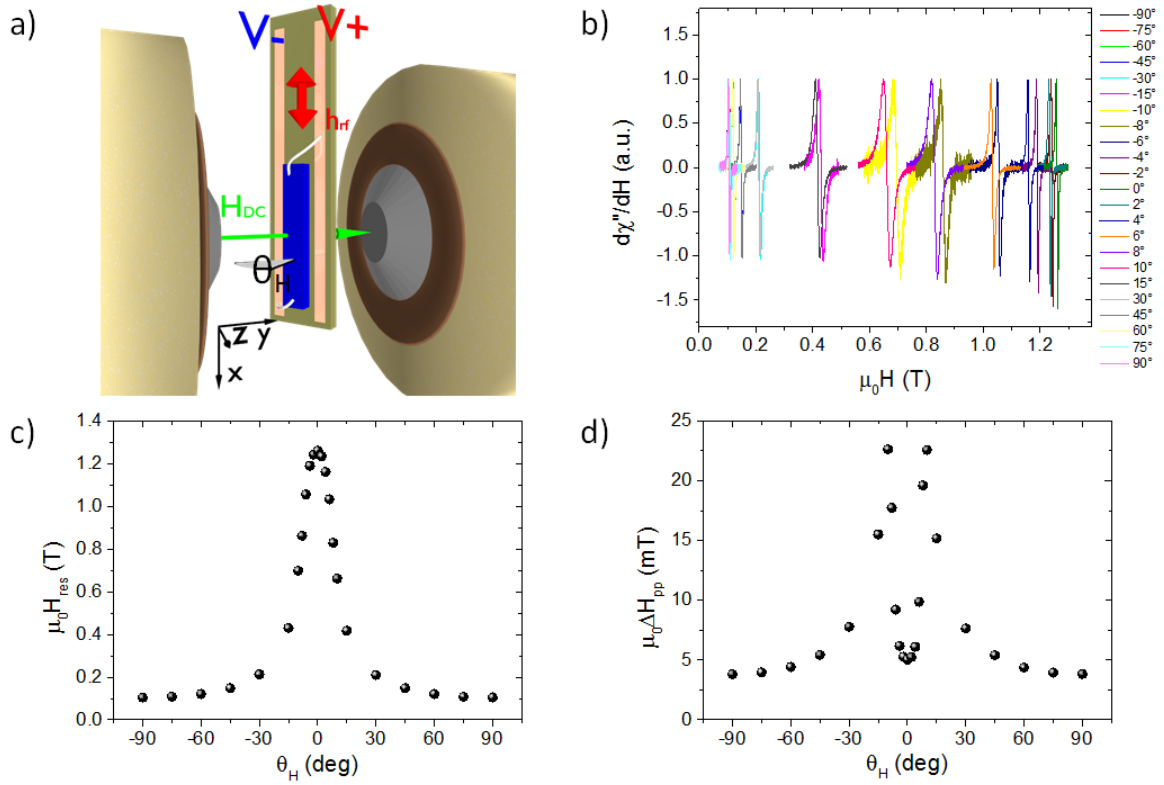


FIG. 2.8: FMR measurement in the out of plane configuration. a) Schematic representation of the experimental setup where  $\theta_H$  is the angle between the normal of the sample and the DC field direction as defined in the main text. The electrical contacts are shown here to describe more accurately the setup. b) Resonance obtained for various angle  $\theta_H$  of a Permalloy 20nm-Platinum 10nm sample, from the fitting of these data c) the resonance field and d) the peak to peak linewidth are extracted.

use the same method as the one previously described by Rojas Sanchez *et al.*<sup>59</sup>.

First of all it is needed to fit the angular dependence of the resonance field, as seen in section 2.1.2 the conditions to obtain the resonance depends on the demagnetizing field and thus the exact direction of the magnetization is needed. To obtain the resonance condition for every angle we will thus use the Smit-Beljers equation<sup>135;147;59</sup> that gives the resonance condition in a ferromagnetic film from minimization of the free energy density  $F$  similarly to Stoner Wolfarth model:

$$\left(\frac{\omega}{\gamma}\right)^2 = \frac{1}{\mu_0 M_s^2 \sin^2 \theta} \left[ \frac{\partial^2 F}{\partial \theta^2} \frac{\partial^2 F}{\partial \phi^2} - \left( \frac{\partial^2 F}{\partial \theta \partial \phi} \right)^2 \right] \quad (2.24)$$

Where  $\theta$  ( $\phi$ ) is the polar (azimuthal) magnetization angle. The derivative are evaluated at the equilibrium angles  $\theta_M$  and  $\phi_M$  ie when the direction of the magnetization gives  $\partial F / \partial \theta = \partial F / \partial \phi = 0$ . In the case of the out of plane angular dependence only the polar angle is modified. The free energy density  $F$  can be written as the sum of the Zeeman energy (for a uniformly magnetized system), the demagnetization energy and the uniaxial anisotropy energy:

$$F = -\mu_0 \vec{M} \cdot \vec{H} + \frac{\mu_0}{2} M_s^2 \cos^2 \theta_M + K_u \cos^2 \theta_M \quad (2.25)$$



Where  $K_u$  denoted the perpendicular uniaxial anisotropy energy,  $K_u = \frac{\mu_0 H_u M_s}{2}$ , with  $H_u$  the anisotropy field. Considering the small in-plane crystalline anisotropy in Permalloy thin film compared with the demagnetizing field  $M_s$  contribution from in-plane anisotropy is negligible.  $\vec{M}$  and  $\vec{H}$  can be written for out of plane angular dependence in the yz plane:

$$\begin{aligned}\vec{M} &= M[\sin(\theta_M)\cos(\phi_M)\vec{x} + \sin(\theta_M)\sin(\phi_M)\vec{y} + \cos(\theta_M)\vec{z}] \\ \vec{H} &= H_{DC}[\sin(\theta_H)\vec{y} + \cos(\theta_H)\vec{z}]\end{aligned}\quad (2.26)$$

This leads to the expression of the free energy density:

$$F = -\mu_0 M_s H_{DC}(\sin(\theta_M)\sin(\phi_M)\sin(\theta_H) + \cos(\theta_M)\cos(\theta_H)) + \frac{\mu_0}{2}(M_s + H_u)M_s \cos^2 \theta_M \quad (2.27)$$

From the conditions of vanishing of the derivatives in equations 2.24 and expression 2.27 of the free energy density we obtain the equilibrium point:

$$\begin{aligned}2H_{DC}\sin(\theta_M - \theta_H) &= M_{seff}\sin(2\theta_M) \\ \phi_M &= \pi/2\end{aligned}\quad (2.28)$$

Where  $M_{seff}$  is the effective magnetization accounting for the anisotropy  $M_{seff} = M_s + H_u$ . The Smit Beljers formula can now be written as:

$$\left(\frac{\omega}{\gamma}\right)^2 = \mu_0^2 [H_{DC}\cos(\theta_M - \theta_H) - M_{seff}\cos^2(\theta_M)][H_{DC}\cos(\theta_M - \theta_H) - M_{seff}\cos(2\theta_M)] \quad (2.29)$$

With field and magnetization in A/m. From equation 2.29 we can therefore extract the effective magnetization, anisotropy and g factor (gyromagnetic ratio) from the out of plane angular dependence and extract from equation 2.28 the link between the DC field angle and the magnetization angle. Using this formula in the case of the Permalloy-Platinum thin film and as seen in figure 2.9.a we obtain a saturation magnetization of 730kA/m and a g-factor of 2.108. This result is in good agreement with the FMR broadband measurement performed on the same field as seen in figure 2.9.c. Using the Kittel formula to fit the raw data the obtained g-factor is of  $2.109 \pm 0.003$  and saturation magnetization is of  $721 \pm 3$  kA/m. Therefore it is not needed to perform a broadband FMR measurement to extract the static magnetization parameters, it can also be obtained from angular dependence. Combining both methods allows a more accurate estimation of the magnetic properties. Our setup reaches a B field of 1.45T which allows to obtain FMR out of the plane for ferromagnets with effective magnetization below 1MA/m which includes Permalloy, Nickel, and some stoichiometry of CoFeB.

Let's now show how to evaluate the damping from the change of the peak to peak linewidth as a function of the polar angle. There are several contribution to the linewidth as previously mentioned, among them the Gilbert damping, and inhomogeneous broadening. As seen previously for Permalloy thin film the contribution of inhomogeneous broadening to the linewidth is small compared to the total linewidth at 10GHz, this is further confirm by the broadband measurement in figure 2.9.d. The Gilbert damping contribution to the linewidth as a function of the magnetization angle and the DC field angle is given by:

$$\mu_0 \Delta H_{Gilbert} = \frac{\frac{2\alpha\omega}{\sqrt{3}\gamma}}{\cos(\theta_H - \theta_M)} \quad (2.30)$$

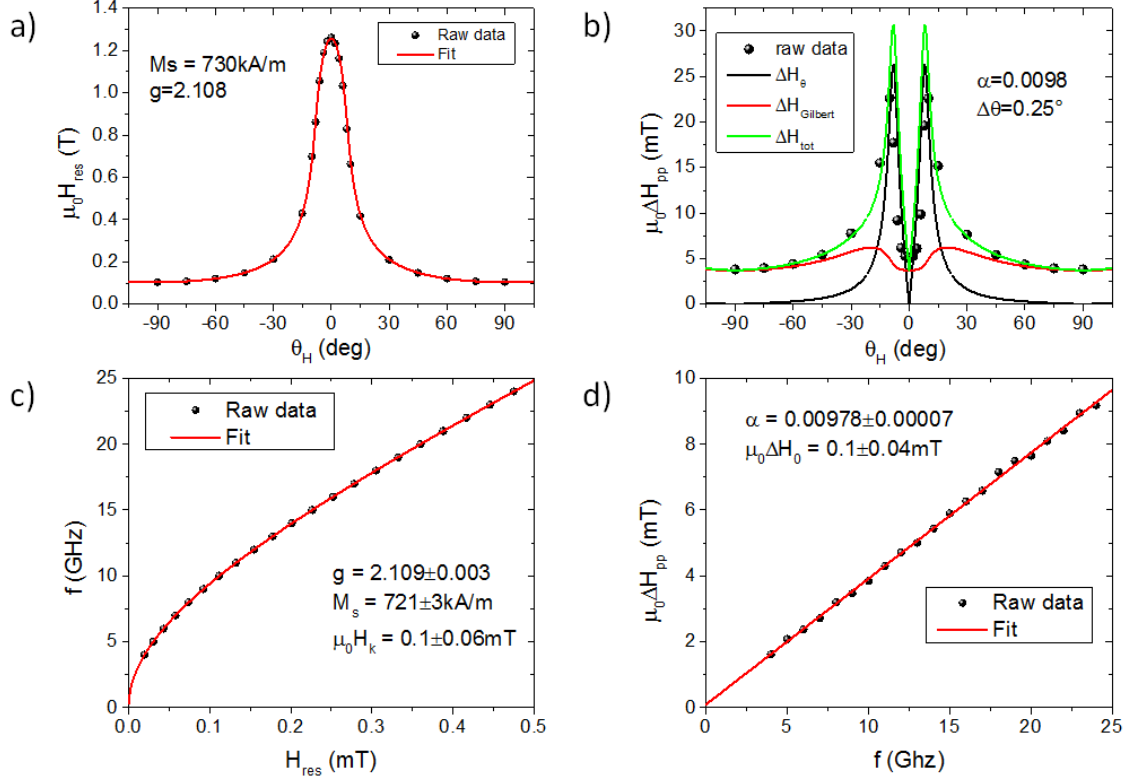


FIG. 2.9: Extraction of the magnetic properties of a Permalloy 20nm-Platinum 10nm from out of plane angular dependence of a) the resonance field and b) peak to peak linewidth. c) and d) shows Broadband FMR measurement and fitting results for the same sample.

By using the magnetization angle extracted from the previous fit it is possible to plot the angular dependence of  $\Delta H_{Gilbert}$ , as seen in figure 2.9.b. While the linewidth can be well fitted in the  $[\pm 90^\circ; \pm 45^\circ]$  angular range it fails to fit the linewidth close to the perpendicular to the plane direction. Indeed the linewidth does not depend only on the Gilbert damping.

Two magnon scattering contribution can also give rise to an enhancement of the linewidth, the two magnon contribution arises in presence of inhomogeneities on large scale and is typically observe in epitaxial thin film<sup>141</sup>. Nonetheless in the Permalloy thin film this contribution can be considered as negligible, indeed the two magnon mechanism is not operative when the magnetization is perpendicular to the film surfaces<sup>148</sup>. The linewidth perpendicular to the plane should be smaller than the in plane one as in Zakeri *et al.*<sup>140</sup>. This is not what we have obtained experimentally. This is in good agreement with literature where two magnon scattering is usually considered as negligible permalloy films thicker than 5nm<sup>145</sup>.

The other expected contribution arises from the inhomogeneous linewidth that is due to spatial inhomogeneity of effective magnetization and orientation of the crystallites. There is indeed a spread of surface orientation of the crystallite in a polycrystalline thin film as Permalloy therefore  $\theta_H$  would vary from grain to grain and the linewidth would represent the envelope of the distribution of tilted grains<sup>135</sup>. We plot the angular dependence for  $M_{seff} = 740 \text{ kA/m}$  and  $g = 2.108$  as seen in figure



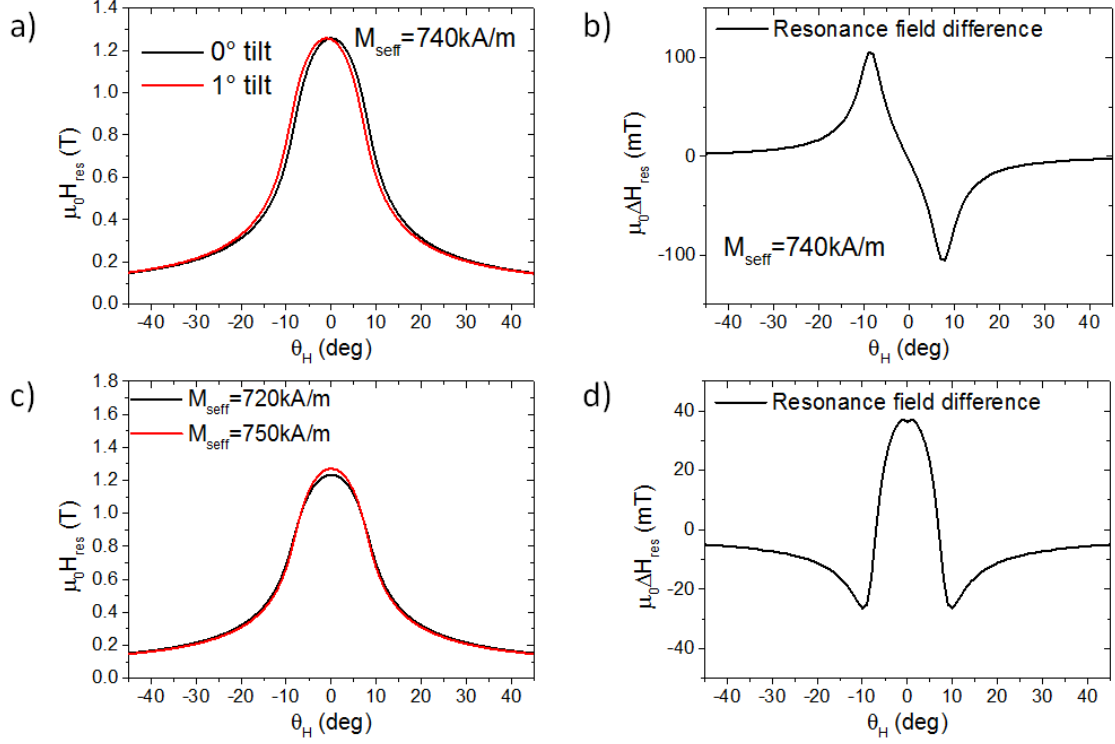


FIG. 2.10: Origin of the inhomogeneous linewidth. a) Shift of the resonance field in presence of ferromagnetic crystals with identical effective magnetization but crystal direction tilted by  $0^\circ$  and  $1^\circ$ . b) Difference of the resonance field for these two tilted crystals as a function of the out of plane angle. c) Angular dependence of the resonance field for crystal of different effective magnetization of  $720$  kA/m,  $750$  kA/m. d) Difference of the resonance field for these two crystals as a function of the out of plane angle

2.10.a with no tilt and a small  $1^\circ$  tilt. The difference in the angular dependence of the resonance field is clearly noticeable and is maximum at around  $\pm 8^\circ$  and minimum close to  $0^\circ$  as seen in figure 2.10.b this is qualitatively similar to what is observed experimentally in Permalloy-Platinum as seen in figure 2.8.b. For small tilt angles this contribution  $\Delta H_\theta$  is proportional to the spread of orientation of the crystals  $\Delta\theta$  and to the derivative of the resonance field with the angle, *i.e.*, proportional to the change of resonance field with the tilt angle. It can therefore be expressed as

$$\mu_0 \Delta H_\theta = \mu_0 \Delta\theta \frac{dH_{res}}{d\theta_H} \quad (2.31)$$

Inhomogeneities of the effective magnetization from crystal to crystal would also lead the resonance field to vary spatially. As seen in figure 2.10.c for two crystallites of slightly different effective magnetization  $M_{seff} = 720$  kA/m and  $M_{seff} = 750$  kA/m while the resonance field is nearly identical in the plane of the sample as seen in figure 2.10.d the difference has two local extrema at around  $\pm 10^\circ$  and is maximum in the perpendicular to the plane configuration  $0^\circ$ . Experimentally we observed no maximum in the linewidth in the perpendicular configuration but instead a local minimum, which is not compatible with a strong contribution of effective magnetization inhomogeneity. The slight difference between the in plane and perpendicular to the plane linewidth is indeed related to effective magnetization inhomogeneity. In fact this contribution is further reduced due to the so-called ex-

change narrowing contribution as the Permalloy crystals are small and strongly coupled by exchange field with each other<sup>135</sup>. For large crystals when exchange narrowing is not effective it is possible to observe several resonance peaks<sup>136</sup>, the out of plane resonance is thus a good measurement of the magnetic inhomogeneities in a ferromagnetic thin film.

Therefore the two main contributions to account to fit the angular dependence of the peak to peak linewidth in Permalloy-Platinum and in polycrystalline ferromagnetic thin film are the Gilbert damping contribution  $\Delta H_{Gilbert}$  and the inhomogeneous linewidth due to crystallites misorientation  $\Delta H_{\theta}$ :

$$\mu_0 \Delta H_{tot} = \mu_0 \Delta H_{Gilbert} + \mu_0 \Delta H_{\theta} = \frac{\frac{2\alpha\omega}{\sqrt{3}\gamma}}{\cos(\theta_H - \theta_M)} + \mu_0 \Delta\theta \frac{dH_{res}}{d\theta_H} \quad (2.32)$$

Using equation 2.32 it is possible to fit the angular dependence of the peak to peak linewidth in figure 2.9.b with  $\alpha = 0.0098$  which is similar to damping extracted from broadband FMR and  $\Delta\theta = 0.25^\circ$  typical for permalloy thin film. We have therefore shown that from out of plane angular dependence, using the Smit-Beljers equation and linewidth angular dependence we can extract the main magnetic properties of a ferromagnetic thin film and that the obtained values are nearly identical to the one obtained by broadband FMR. These two methods and all the above formulas will be used several times in this manuscript.

Ferromagnetic resonance apart from obtaining the static and dynamic properties of a ferromagnetic thin film also allows to evaluate the spin to charge current interconversion using a technique called spin pumping by ferromagnetic resonance. In the following part we will describe the spin transfer mechanism at the ferromagnetic resonance and how to evaluate the injected spin current at resonance using the magnetic properties determined by using the same FMR setup.

## 2.3 Spin transfer via spin pumping by ferromagnetic resonance

The spin to charge interconversion mechanisms such as ISHE and IEE can be studied by various techniques including lateral spin valves and other related nanodevices<sup>27;57;47</sup>, second harmonic measurements<sup>58</sup>, ST-FMR<sup>54</sup>, Longitudinal Spin Seebeck effect<sup>149</sup> etc. One of this technique is know as spin pumping by ferromagnetic resonance where spin injection is performed using the magnetization precession at the ferromagnetic resonance. The spin injection at resonance was first demonstrated in the pioneering works of Silsbee and Johnson in the 80's<sup>120</sup> and were followed by the development of the spin pumping theory by Tserkovniak, Brataas *et al.*<sup>124;150;151;152</sup> and Mizukami *et al.*<sup>153</sup> in 2002. These experimental and theoretical works were describing the enhancement of the damping associated with the spin injection at resonance. This is only in 2006 that Saitoh *et al.*<sup>26</sup> and Costache *et al.*<sup>122</sup> demonstrated the possibility to use this technique to inject a spin current and detect the spin to charge current conversion in Platinum. The spin pumping by ferromagnetic resonance technique is since then a widely used method to detect spin to charge current conversion and to determine the spin hall angles and inverse Edelstein lengths.

In this part we will first describe the origin of the spin current injection using Tserkovniak and Brataas

theory of spin pumping, then we will give the expression of the injecting spin current and converted charge current and how to measure it through electrical detection of the FMR.

### 2.3.1 Origin of the spin injection

Spin injection by means of spin pumping by ferromagnetic resonance can be considered as the reciprocal effect to the spin torque. If a spin current is injected from an adjacent layer towards a ferromagnetic material, it will transfer angular momentum to the ferromagnetic layer through s-d exchange. Then the magnetization is put out of equilibrium and start to precess and can even be switched if enough angular momentum is transferred. This is the process involved in the switching of spin torque MRAMs. This phenomenon has been first described by Berger and Slonczewski in 1996<sup>14</sup>, and to describe it a torque term  $\vec{\tau}_{Sloncz}$  is added to Landau-Lifschitz-Gilbert equation:

$$\frac{d\vec{M}}{dt} = -\gamma\mu_0 \vec{M} \times \vec{H}_{eff} + \frac{\alpha}{M_s} \vec{M} \times \frac{d\vec{M}}{dt} + \vec{\tau}_{Sloncz} \quad (2.33)$$

Which is known as the Landau-Lifschitz-Gilbert-Slonczewski equation. Such a torque is analogous to a torque in classical mechanics. Reciprocally if the magnetization of the ferromagnetic layer is precessing angular momentum will be lost in the adjacent layer. Magnetization precession will lead to a transfer of a spin current  $\vec{J}_{s,pump}$  from the ferromagnetic material (FM) towards the adjacent non-magnetic material (NM). This can be summarized as ‘‘A spin current can exert a finite torque on the ferromagnetic order (figure 2.11.a), and, vice versa, a moving magnetization vector loses torque by emitting a spin current (figure 2.11.b)’’ as stated by Tserkovnyak and coauthors<sup>124</sup>.

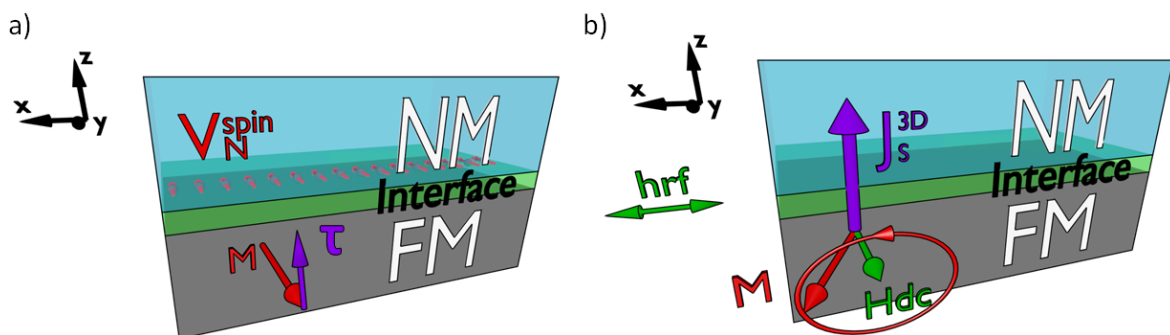


FIG. 2.11: a) In presence of a spin accumulation at the interface a torque  $\vec{\tau}$  is exerted on the magnetization of the FM layer that will be put out of equilibrium. b) When the rf magnetic field leads the magnetization to precess at resonance, a part of the angular momentum is loss towards the adjacent layer corresponding to a spin current injection  $\vec{J}_s$  towards the NM.

Therefore spin pumping by ferromagnetic resonance is related to a loss phenomenon and thus to the damping parameter. To account for this extra damping contribution  $\Delta\alpha$  related to spin pumping the LLG equation needs to be modified. The total damping is the sum of the Gilbert damping of the FM material with no adjacent layer, the reference damping  $\alpha_{ref}$ , and of the extra-damping  $\Delta\alpha$  due to spin pumping<sup>152</sup>. The LLG equation is now written:

$$\frac{d\vec{M}}{dt} = -\gamma\mu_0 \vec{M} \times \vec{H}_{eff} + \frac{\alpha_{ref}}{M_s} \vec{M} \times \frac{d\vec{M}}{dt} + \frac{\Delta\alpha}{M_s} \vec{M} \times \frac{d\vec{M}}{dt} \quad (2.34)$$

The value of the extra damping can be obtained by measuring two samples with and without an adjacent layer. In that case the sample without adjacent layer is known as the reference layer of damping  $\alpha_{ref}$ , and the damping with adjacent layer has a total damping  $\alpha_{tot} = \alpha_{ref} + \Delta\alpha$ . This emphasize the importance of a good estimation of the damping and thus importance of the previous part of the manuscript.

In figure 2.12 one can see the damping enhancement in Py(20nm)/Pt(10nm) ( $\alpha = 0.00978 \pm 0.00005$ ) compared to Py(20nm)/Si ( $\alpha = 0.00636 \pm 0.00003$ ). It is to be noted that in the case of Pt spin memory loss at the interface is non-negligible and should in general be accounted in the damping enhancement to measure the exact amount of spin current that is injected at resonance<sup>154</sup>. For the sake of simplicity we will neglect spin memory loss in this sample. In the following we will focus on this well-known Py/Pt sample to explain how to measure spin pumping FMR signal and evaluate the spin hall angle.

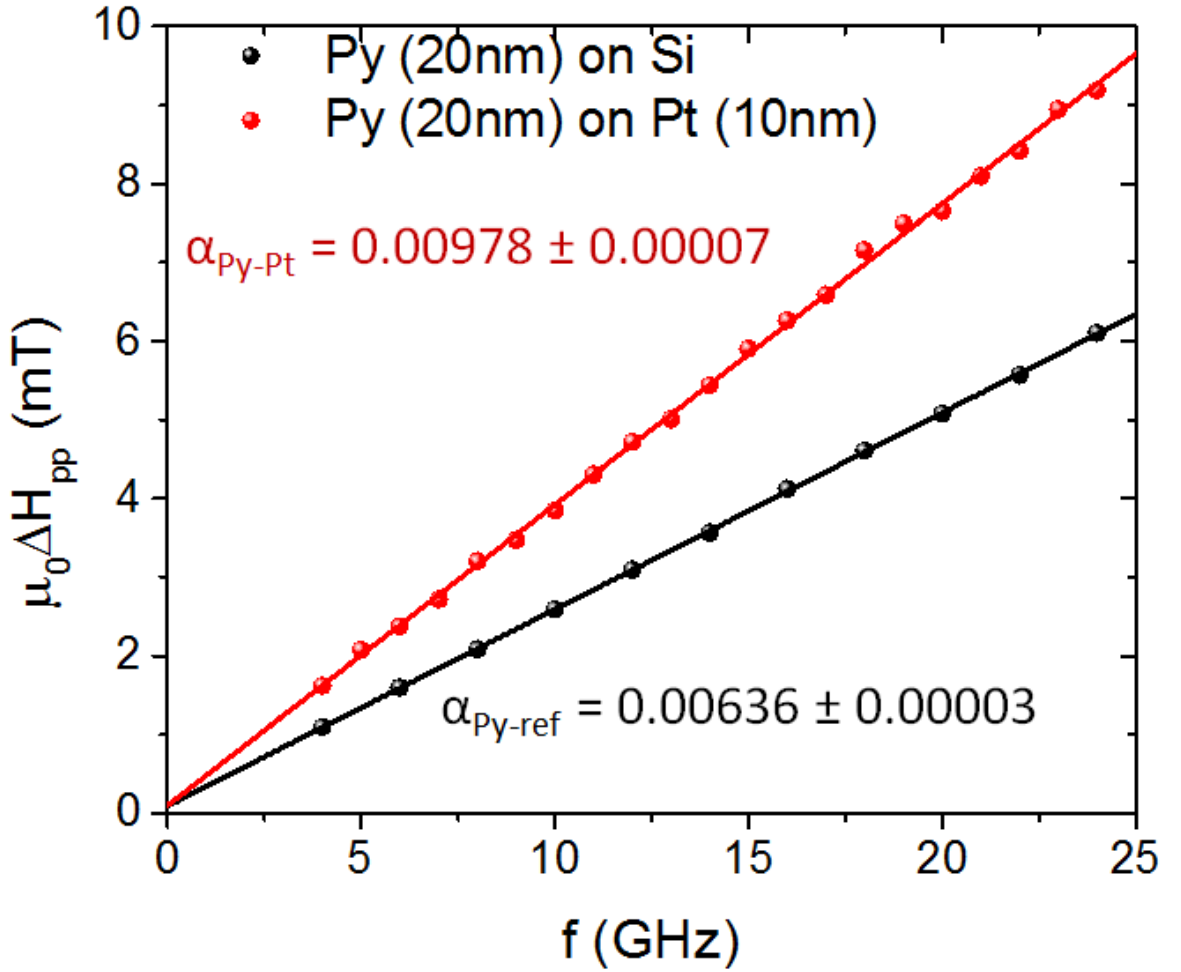


FIG. 2.12: Damping measurement of two samples of Permalloy (20nm) one deposited on a thin film of Pt of 10nm and the other one deposited on Silicon. Total increase of the damping due to spin pumping in Platinum is of  $\Delta\alpha = 0.00342 \pm 0.00008$

### 2.3.2 Spin current expression

Efficiency of the injection is related to the coupling between the ferromagnetic material and the non magnetic material. A large loss of angular momentum – a large damping increase– is associated with an efficient spin current injection via spin pumping. The model of Tserkovnyak, Brataas and coauthors on the spin pumping FMR spin injection link the enhancement of the damping and instantaneous spin pumping current  $J_{s,0}^{pump}$  through the equations<sup>151;150</sup>:

$$\begin{aligned} \vec{J}_{s,0}^{pump} &= \frac{\hbar}{4\pi} \frac{Re(g^{\uparrow\downarrow})}{M_s^2} \vec{M} \times \frac{d\vec{M}}{dt} \left( \frac{2e}{\hbar} \right) \\ \Delta\alpha &= \frac{g\mu_B}{4\pi M_s t_{FM}} Re(g^{\uparrow\downarrow}) \end{aligned} \quad (2.35)$$

where  $g^{\uparrow\downarrow}$  is known as the spin mixing conductance which express the global spin transmission, and  $t_{FM}$  is the thickness of the ferromagnetic layer. From equations 2.35 one can see that the instantaneous spin current injection is perpendicular to both the magnetization and the derivative of the magnetization. The spin current generated at the interface would then lead to the build-up of a spin accumulation inside the adjacent NM layer. In the case of Py/Pt using value extracted in the previous sections:  $\Delta\alpha = 0.00342 \pm 0.00008$ ,  $g=2.109 \pm 0.003$ ,  $M_s = 721 \pm 3 \text{ kA/m}$  and  $t_{FM} = 20 \text{ nm}$  we obtain a spin mixing conductance  $g^{\uparrow\downarrow} = 32.1 \pm 0.9 \text{ nm}^{-2}$  which is comparable to previously obtained results in our group in Co/Pt and Py/Pt bilayers<sup>61</sup> and theoretical results of Liu *et al.*<sup>155</sup>.

In absence of the spin flip scattering or if the thickness of the NM material is short compared to the spin diffusion length ( $t_{NM} \ll \lambda_s$ ), the spin current is reflected at the NM/vacuum interface and then reabsorbed by the ferromagnet. In that case the net spin current through the interface is zero. Hence it is needed to account for the back-flow  $J_{s,0}^{back}$  to obtain the total spin current injected from the FM  $J_{s,0} = J_{s,0}^{pump} - J_{s,0}^{back}$ <sup>150</sup>. In the simplest model of back-flow with the source of decoherence in the NM only and for perfect reflections and transmission  $J_{s,0}^{back} = J_{s,0}^{pump} e^{-\frac{2t_{NM}}{\lambda_s}}$ . The factor of 2 emphasize the fact that the spin current go from the interface to the vacuum and then back from the vacuum to the interface. Due to this back-flow one can rewrite the injected spin current as follows<sup>156;157;158</sup>:

$$J_s = J_{s,0}^{pump} \left( 1 - e^{-\frac{2t_{NM}}{\lambda_s}} \right) \quad (2.36)$$

In general due to an imperfect reflection and transmission the factor is more than 2<sup>159</sup>.

Following equation (2.35) and (2.36) the damping enhancement is obtained for thin film of adjacent materials only when their thickness is close to the spin diffusion length which is typically of some nm in heavy metals as Pt or Ta but of some hundreds of nm in Cu as experimentally observed for example by Mizukami *et al.*<sup>153;160</sup>. The spin backflow into the ferromagnet reduces the damping and spin mixing conductance which are not only related to interface phenomenon but also to spin diffusion in the NM layer. To account for this we introduce the effective spin mixing conductance  $g_{eff}^{\uparrow\downarrow}$  in equation 2.35 with  $g_{eff}^{\uparrow\downarrow} \leq g^{\uparrow\downarrow}$ , which is equal to the spin mixing conductance in absence of backflow, if the NM layer is larger than spin diffusion length no backflow is expected and  $g_{eff}^{\uparrow\downarrow} = g^{\uparrow\downarrow}$ . Following equation (2.35) and (2.36) thickness dependence of the spin mixing conductance (or damping) can be

described by the decay of the spin accumulation in the NM material of thickness  $t_N$ :

$$g_{eff}^{\uparrow\downarrow} = g^{\uparrow\downarrow} \left(1 - e^{-\frac{2t_{NM}}{\lambda_s}}\right) \quad (2.37)$$

Therefore it is possible to measure the spin diffusion length from the enhancement of the damping or spin mixing conductance. Nonetheless due to large spin memory loss at the FM/Pt interface or proximity induced magnetism this technique do not hold well<sup>161</sup>. The spin diffusion length can be largely underestimated by using this technique in bilayers with Pt as shown for example by Rojas-Sanchez *et al.* and as can be seen in figure 2.13<sup>61</sup>. In general one should not use damping enhancement to evaluate the spin diffusion length accurately. Other more complex formula accounting for the spin memory, proximity induced magnetism or trilayers can be found in the literature<sup>161;162;163;164</sup>.

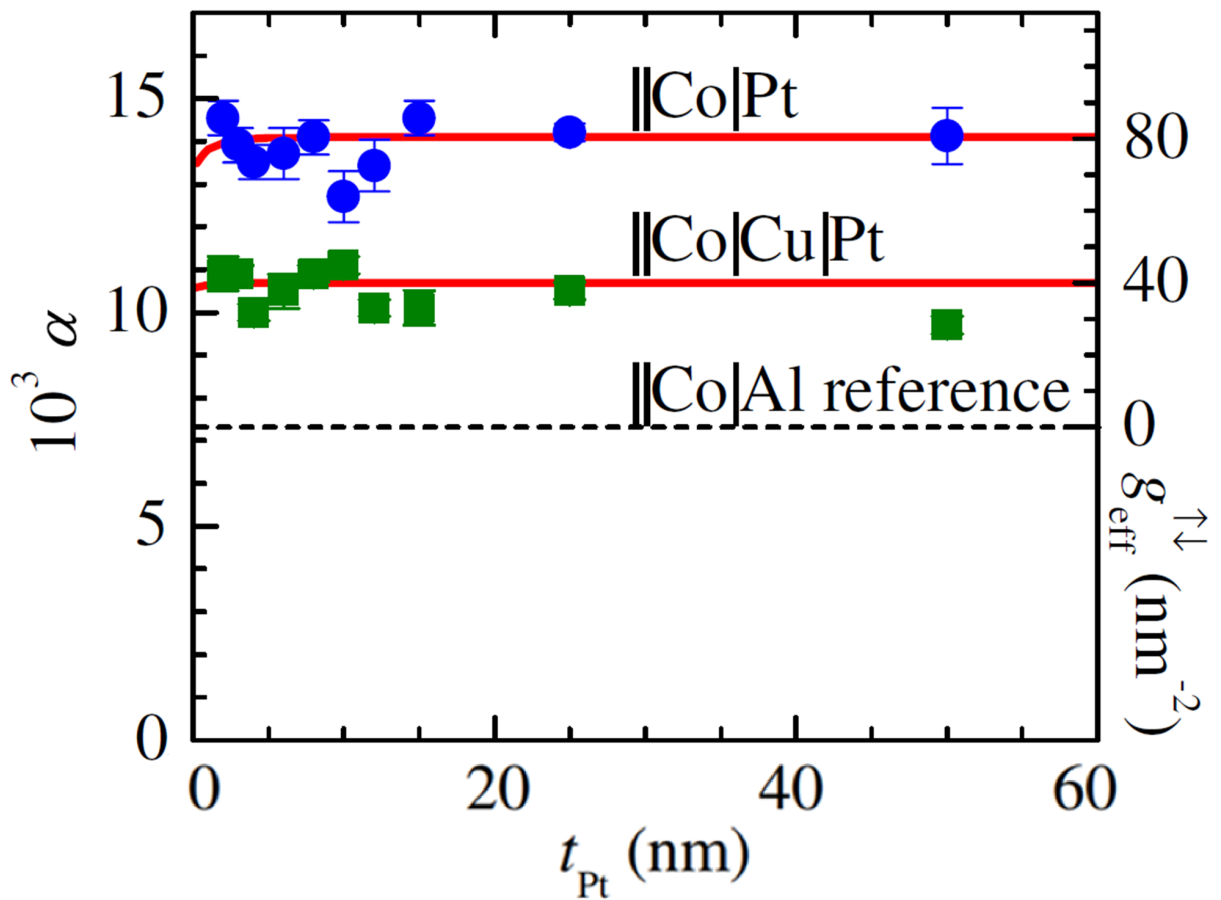


FIG. 2.13: Damping and spin mixing conductance as a function of Pt thickness for a Co\Pt and Co\Cu\Pt extracted from Rojas-Sanchez *et al.*<sup>61</sup>. One can see that the damping is nearly independent on the thickness of Pt, this is due to large SML at Co\Pt interface

It is to be noted that the expression of the spin pumping current of equation (2.35) is an instantaneous AC current while the measurement of the spin pumping signal rely on a DC current measurement. To obtain the component of the DC spin current value it is needed to integrate it over a full precession of the magnetization vector. The DC component of the generated spin current density along z is then:

$$J_{s,DC}^{pump} = \frac{\omega}{2\pi} \int_0^{2\pi} \frac{\hbar}{4\pi} \frac{Re(g_{eff}^{\uparrow\downarrow})}{M_s^2} \vec{M} \times \frac{d\vec{M}}{dt} \left( \frac{2e}{\hbar} \right) dt \quad (2.38)$$

As the only time dependent term is the magnetization it is needed to have an exact evaluation of the magnetization vector trajectory to evaluate accurately the DC spin current. This can be done by calculating all the magnetization components and then integrate over a full precession using equation (2.38). Such a calculation can be found in Costache *et al.*<sup>165</sup>. A more general expression for every direction of magnetization has been derived by Ando *et al.* in the coherent precession regime<sup>166;167</sup>. We will restrain the calculation to the small precession cone angle approximation in order to linearize the LLG equation and to homogeneously magnetized samples. To calculate magnetization component along x, y and z exact expression of Polder tensor in (2.13) and use of Resonance conditions for every angle (2.28) and (2.29) is needed. This leads to the following expression of  $M_x$  and  $M_z$ , the magnetization component along x and z:

$$M_x(t) = \frac{\mu_0 M_S h_{rf} \gamma \left[ 2\alpha\omega \cos(\omega t) + \left( \mu_0 M_s \gamma \sin^2(\theta_M) + \sqrt{(\mu_0 M_s \gamma \sin^2(\theta_M))^2 + 4\omega^2} \right) \sin(\omega t) \right]}{2\alpha\omega \sqrt{(\mu_0 M_s \gamma \sin^2(\theta_M))^2 + 4\omega^2}}$$

$$M_z(t) = \frac{\mu_0 M_S h_{rf} \gamma \cos(\omega t)}{\alpha \sqrt{(\mu_0 M_s \gamma \sin^2(\theta_M))^2 + 4\omega^2}} \quad (2.39)$$

From equations (2.38) and (2.39), and as the small precession angle approximation leads to  $\frac{dM_y}{dt} = 0$  the following expression of the spin current is obtained:

$$J_{S,pump} = \frac{Re(g^{\uparrow\downarrow}) \gamma^2 \hbar h_{rf}^2}{8\pi\alpha^2} \left( \frac{\mu_0 M_s \gamma \sin^2(\theta_M) + \sqrt{(\mu_0 M_s \gamma \sin^2(\theta_M))^2 + 4\omega^2}}{(4\pi M_s \gamma \sin^2(\theta_M))^2 + 4\omega^2} \right) \left( \frac{2e}{\hbar} \right) \quad (2.40)$$

The injected DC spin current is sometimes calculated as a function of the precession cone angle of magnetization as it is proportional to the area of magnetization trajectory. This has been done for example by Mosendz *et al.*<sup>168</sup> and Costache *et al.*<sup>165</sup>. This calculation leads to similar results and allows to compare magnetic materials with different damping (different precession cone angle) more easily<sup>169</sup>. It is important to point out the fact that as the injected spin current is proportional to the out of equilibrium magnetization due to the absorption of power. Therefore, the injected spin current is proportional to the absorption at resonance and the field dependence follows the Lorentzian shape of  $\chi''$

The injected spin current at resonance can be estimated using values extracted from FMR measurements as seen in previous sections including  $\alpha$ ,  $M_s$  and  $g^{\uparrow\downarrow}$ . For an in plane field ( $\sin(\theta_M) = 0$ ), we can easily calculate the injected spin current. Using previously measured value of  $M_s$ ,  $g^{\uparrow\downarrow}$ ,  $\alpha$  etc we obtained the value of the injected spin current for the NiFe/Pt sample described in the previous parts:  $J_{S,pump}^{NiFe/Pt} = 12.6 \pm 0.2 MA.m^{-2}.G^{-2}$ . Injected spin current is expressed in  $A.m^{-2}.G^{-2}$  to take into account the change of injected spin current as a function of the square of the rf field excitation. Using equation (2.40) we can also obtain the angular dependence of the ISHE signal that would be further described in the next sections of this chapter. Note that an AC spin current injection also occurs with



polarization along x. This injection is in principle much more efficient<sup>170</sup> but difficult to disentangle with inductive effects<sup>171;172</sup>.

### 2.3.3 Evaluation of spin charge interconversion efficiency

In the previous sections we showed that it is possible to inject spin current at the ferromagnetic resonance and to evaluate the spin current amplitude from the magnetic layer properties. To measure the spin to charge current conversion efficiency it is now needed to measure the produced charge current originating from the spin to charge current conversion.

#### Measurement of the charge current production:

It is possible to measure the voltage drop at resonance as shown in figure 2.14.a. Due to the infinite impedance of the voltmeter (some  $M\Omega$ ) compared to the sample (typically below  $1k\Omega$ ), the voltage drop is detected in open circuit conditions. As the spin current is injected from the NiFe ferromagnetic layer to the Pt layer with a polarization direction along y and is then converted into a charge current by ISHE in Pt there is a charge current flowing in the sample along the x direction. Due to that an electric field  $\vec{E}$  arises. In open circuit conditions such an electric field would generate a current that is equal in amplitude but opposite to the one due to inverse spin hall effect:

$$\vec{J}(x) = J_c(x) + \sigma \vec{E} \quad (2.41)$$

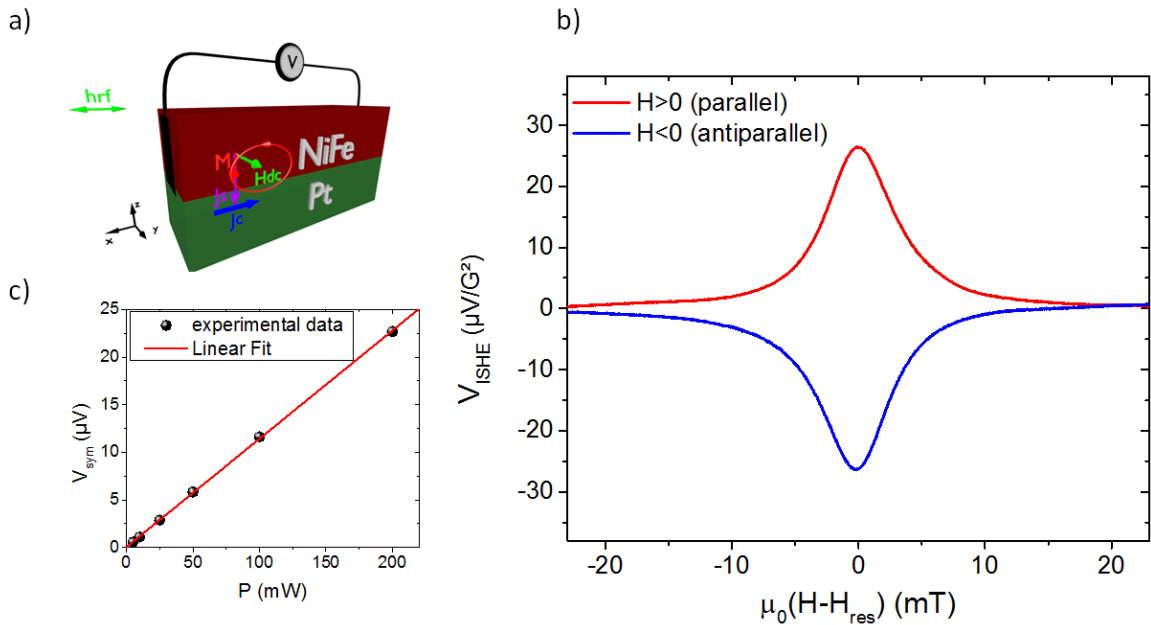


FIG. 2.14: a) Schematic representation of the spin pumping in a NiFe/Pt bilayer, at resonance spin current is injected from NiFe towards Pt. b) Typical spin pumping FMR voltage measured in open circuit normalized by  $h_{rf}^2$  in the parallel ( $H > 0$  in plane) and the antiparallel ( $H < 0$ ) in plane configuration and c) Spin pumping signal power dependence with linear fitting.

with  $\sigma$  the conductivity of the sample. For a sample with the geometry of a wire, which is typically the case of the  $W = 0.4mm \times L = 2.4mm$  sample that we use for spin pumping FMR measurement,



one can consider that  $\left\| \vec{E} \right\| = V_{sp}L$ . Therefore when measuring FMR and detecting voltage in open circuit at the same time due to spin injection and spin to charge conversion a measurable voltage drop arises due to ISHE or IEE as shown in figure 2.14.b. There are two main characteristic of the spin pumping ISHE/IEE signal. Firstly as the injected spin current follows the Lorentzian shape of  $\chi''$  the shape of the spin pumping signal is a Lorentzian. Secondly due to symmetry of the spin injection and the spin to charge conversion by means of ISHE or IEE the signal is reversed either by reversing the stacking order or by reversing the magnetic field<sup>167;173;174</sup>. These two main characteristics are indeed observed in NiFe/Pt. Following equation (2.41) one can calculate the total charge current production by simply using Ohm's law:

$$I_c = V_{sp}/R \quad (2.42)$$

Where R is the resistance of the sample measured independently, for the NiFe/Pt sample shown here it is of 58.8  $\Omega$ . One might notice that in figure 2.14.b the signal is given in  $\mu V/G^2$  instead of  $\mu V$ , this is to take into account the rf power dependence of the spin injection, indeed as seen in equation (2.40) the injected spin current and thus the spin pumping signal is proportional to  $h_{rf}^2$ . Therefore, the signal depends on the incident rf power and the cavity properties. In the case of the MS5 3loop–2gap cavity that we are using here we can determine the radiofrequency field amplitude directly from the cavity Q factor and microwave Power (see annex A for further details on the MS5 loop gap cavity):

$$h_{rf} = 0.2 \sqrt{\frac{PQ}{500}} \quad (2.43)$$

The total signal is linear with power (with  $h_{rf}^2$ ) as observed in NiFe/Pt as seen in figure 2.14.c. In the case of NiFe/Pt we measured a total charge current of 450  $nA/G^2$  similar to previous results of J-C Rojas Sanchez *et al.* on Co/Pt with comparable Pt thickness and resistivity<sup>61</sup>. Now that we have described methods to measure the injected spin current using FMR measurement and produced charge current by electrical detection of FMR it is possible to evaluate the spin to charge current conversion efficiency using the amplitude of the charge and spin currents.

### **Estimation of the conversion efficiency from the spin pumping FMR:**

As stated before the main interest of the spin pumping FMR method apart from accurately measuring the magnetic properties of ferromagnetic materials is to evaluate the spin Hall angle, the spin diffusion length or the inverse Edelstein length of a wide variety of materials. In the first chapter we described the link between the injected spin current and the detected charge current in the case of both the spin Hall effect and the inverse Edelstein effect.

Calculation of the inverse Edelstein length is the easiest one to obtain, assuming conversion from a 3D spin current completely absorbed at the interface/surface to a purely 2D charge current we directly have:

$$\lambda_{IEE} = \frac{J_c^{2D}}{J_{s,pump}^{3D}} = \frac{I_c}{W J_{s,pump}^{3D} \sin(\theta_M)} \quad (2.44)$$

with  $W$  the width of the sample. The effective conversion length  $\lambda^*$  in ISHE materials can also be calculated the same way.

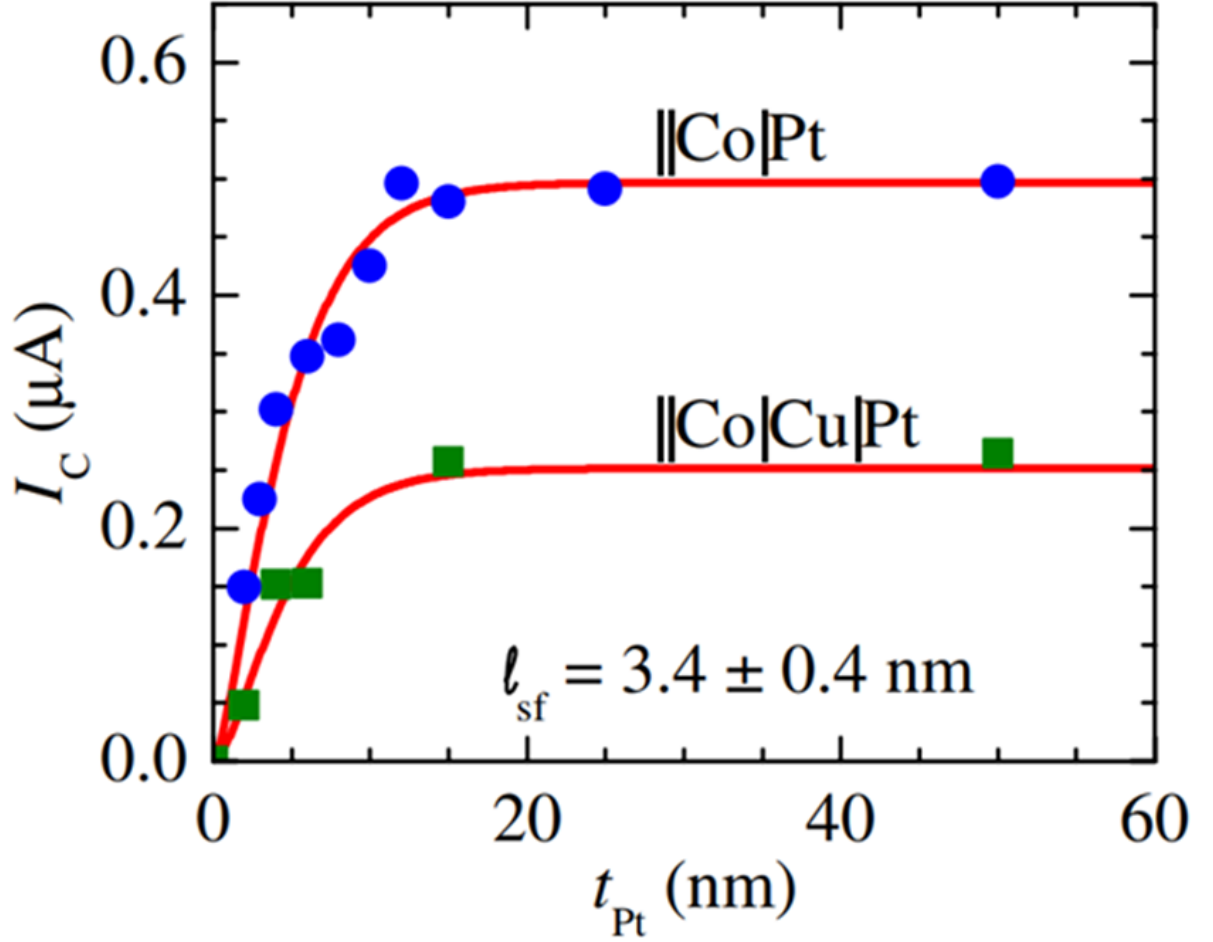


FIG. 2.15: Thickness dependence of the produced charge current obtained for Pt with a resistivity of  $17\mu\Omega.cm$ . The fitting yields to a spin diffusion length of 3.4 nm. This figure is extracted from J-C Rojas Sanchez et al. <sup>61</sup>.

In ISHE material the spin diffusion in the bulk of the samples needs to be accounted. Indeed the spin accumulation profile at the FM/NM interface follows a specific thickness dependence. Following the spin diffusion equations (1.10) and (1.11) it is possible to show that the spin current profile follows <sup>159;123;121</sup>:

$$J_s(z) = J_{s,pump} \frac{\sinh\left(\frac{(t_N-z)}{\lambda_s}\right)}{\sinh\left(\frac{t_N}{\lambda_s}\right)} \quad (2.45)$$

with  $t_N$  the thickness of the non-magnetic layer and  $J_{s,pump}$  the spin current density at the FM/NM interface due to spin pumping spin injection. Due to inverse spin Hall Effect this spin current is then converted into charge current with  $J_c^{ISHE}(z) = \theta_{SHE} \vec{J}_s(z) \times \vec{\sigma}$ . Therefore the total charge current  $I_c$  along x is obtained by integrating along the z direction:

$$I_c = W \int_0^{t_N} \theta_{SHE} \left( \vec{J}_s(z) \times \vec{\sigma} \right) \cdot \vec{x} dz \quad (2.46)$$

Using the expression of  $J_s(z)$  in equation (2.44) and by integrating with expression (2.45) we can directly obtain the expression of the charge current production as a function of the thickness of the film:

$$I_c = W\theta_{SHE}\lambda_s\sin(\theta_M)J_{s,pump}(\theta_M)\tanh\left(\frac{t_N}{2\lambda_s}\right) \quad (2.47)$$

This shows that the ISHE current production changes as a function of the thickness  $t_N$  of the ISHE material as  $\tanh\left(\frac{t_N}{2\lambda_s}\right)$ . This specific thickness dependence has already been observed by many in a large variety of ISHE materials<sup>158;175;159;121</sup> and is for example obtained in Pt as seen in figure 2.15, these data were extracted from Rojas Sanchez *et al.*<sup>61</sup>. From the fitting of the thickness dependence of the charge current production using equation (2.46) it is possible to estimate the spin diffusion length of the material. As the interface between the ferromagnetic layer and the non-magnetic layer can never be perfectly abrupt, to fit accurately the thinnest sample it is sometimes needed to account for the minimal thickness needed to obtain a continuous film (the interface roughness  $R_{ough}$ ). Using this fitting equation a spin diffusion length of  $3.4\pm 0.4$  nm is obtained for Pt sample with a resistivity of  $17 \mu\Omega.cm$ .

It is important to note that the measured spin signal is not directly proportional to  $\theta_{SHE}$  but to  $\theta_{SHE}\lambda_s$ . Due to that to extract properly the Spin Hall Angle from the spin pumping FMR measurement one should know the exact value of the spin diffusion length of its sample. For example in the case of Pt, value of the product  $\theta_{SHE}\lambda_s$  obtained by various group is quite similar but there is a strong variation from group to group for  $\theta_{SHE}$  and  $\lambda_s$ <sup>154</sup>. It was especially the case for the first spin pumping FMR measurements where the spin diffusion length was either extracted from the damping dependence on the thickness or from previously published results and not directly measured from the charge current production. In the case of the NiFe/Pt sample presented all along this chapter using the spin diffusion length obtained for a comparable resistivity<sup>61;71</sup> of  $3.4\pm 0.4$  nm for Pt we obtain a spin hall angle  $\theta_{SHE} = 2.9 \pm 0.5\%$  is evaluated. This value is smaller than the one obtained in reference<sup>61</sup> of  $\theta_{SHE} = 5.6 \pm 1\%$  when accounting for the spin memory loss. Indeed the spin memory loss induces a strong interfacial depolarization of the spin current injected in Pt by spin-pumping this can largely affects the ability to correctly extract the intrinsic spin Hall angle<sup>154;162</sup>. This effect is known to occur in NiFe/Pt samples<sup>176</sup>. So in general one should be careful when giving bulk value of the spin Hall angle and the spin diffusion length but should refer to effective value instead. As the spin memory loss is unavoidable conversion efficiency is always affected by it, in the following of the manuscript we will mention only the effective values of  $\theta_{SHE}$  and  $\lambda_{IEE}$ .

In the previous part we neglected other effects that can give rise to a non-zero DC voltage at resonance but they must not be neglected in general, we should carefully evaluate them for a proper estimation of the spin charge conversion efficiency. Here we will show how to disentangle the ISHE/IEE signal from other DC voltage at resonance.

## 2.4 Disentangling ISHE/IEE from spurious effects

The measurement of a voltage in open circuit is not sufficient to conclude on the fact that a spin to charge current conversion was detected. To clarify the nature of the signal several dependences needs to be performed. The easiest way is of course to obtain the specific thickness dependence of the inverse spin hall effect signal which is a specific signature of ISHE or to obtain the same spin signal with stacking inversion. The absence of signal in a reference sample without the non-magnetic material attached or separated by a thick insulating layer is also a strong evidence of the presence of the ISHE or IEE in an adjacent material. In general the angular dependence of the signal is the strongest evidence of the signal origin. In the following we will discuss the possible contributions to the signal including the ISHE/IEE signal and the spin rectification effects and how to disentangle them from symmetry arguments. We will also comment on possible thermal and spin-caloritronics effect that can arise at resonance.

### 2.4.1 Spin pumping ISHE/IEE angular dependence

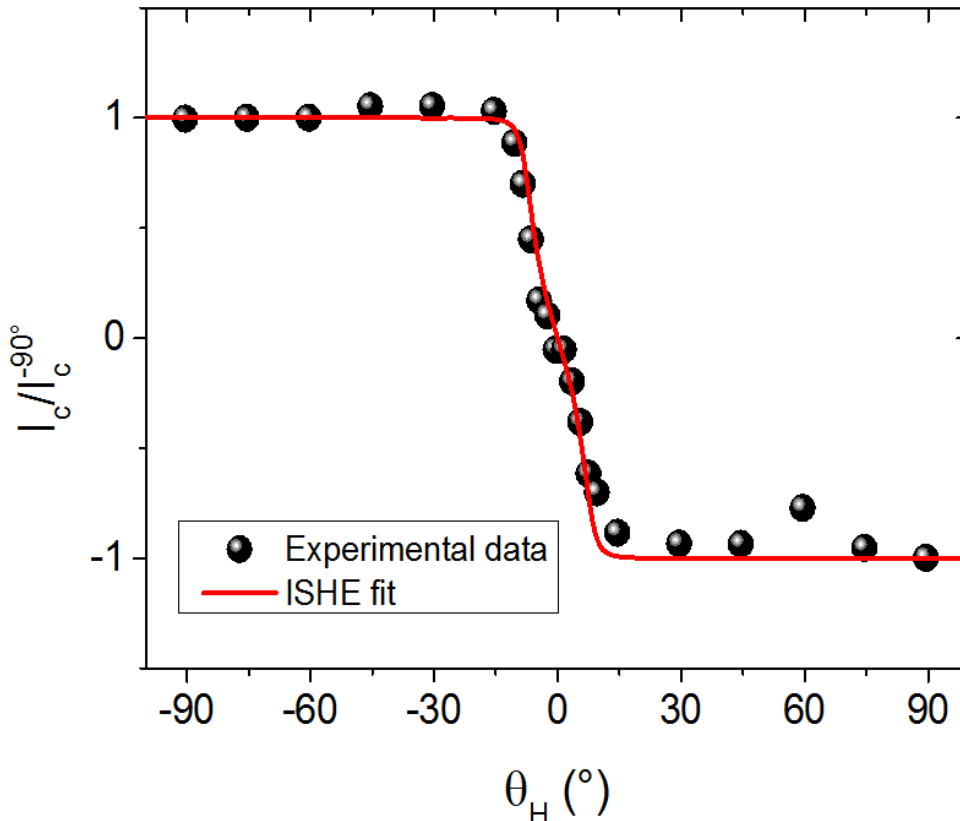


FIG. 2.16: Angular dependence of the ISHE signal calculated using equation 2.47 with the magnetic properties of NiFe/Pt given in the previous sections.

Both the spin pumping spin injection and the spin to charge conversion have a specific angular dependence on the magnetization or spin direction. Using the full expression of  $J_{s,pump}$  given in equation

(2.40) and expression (2.44) or (2.47) one can extract the angular dependence of the spin pumping ISHE and IEE signal:

$$I_c = I_c(-90^\circ) \sin(\theta_M) \left( \frac{\mu_0 M_s \gamma \sin^2(\theta_M) + \sqrt{(\mu_0 M_s \gamma \sin^2(\theta_M))^2 + 4\omega^2}}{(\mu_0 M_s \gamma \sin^2(\theta_M))^2 + 4\omega^2} \right) \quad (2.48)$$

Therefore by measuring the out of plane angular dependence of the spin pumping signal and combining it with the conventional FMR measurement allows to evaluate the magnetization properties of the ferromagnet to estimate  $J_{s,pump}$ , and also to check if the ISHE/IEE angular dependence is respected. Using the equation (2.29) to extract  $\theta_M$  it is possible to fit the obtained angular dependence of the charge current as seen in figure 2.16 in the case of NiFe/Pt. It is to be noted that the so-called self-induced spin hall effect could also give rise to a similar signal in a single layer of ferromagnetic material in presence of spatial dependences of the damping as shown by Tsukahara *et al.*<sup>177</sup>. The measured signal is indeed following well the expected angular dependence of the ISHE, nonetheless it is not the only contribution to DC voltage. The measured signal also includes the so-called spin rectification effects<sup>178;179</sup> and possibly thermal effects<sup>180</sup>.

## 2.4.2 Spin Rectification Effects

In a conducting ferromagnetic material the resistance is related to the magnetization direction through magnetoresistance effects such as the Anisotropic Magnetoresistance (AMR), or the Giant Magnetoresistance (GMR). When a current is flowing in the ferromagnet it is also possible to observe Hall effects such as the Anomalous Hall Effect (AHE) or the Planar Hall Effect (PHE). Due to the change of the magnetization direction at the ferromagnetic resonance, when a current is flowing in the ferromagnetic layer, the appearance of a non-zero voltage is expected. The electrical detection of the FMR due to the change of the sample resistivity has indeed been observed by many<sup>181;182;183;184;178</sup>. Nonetheless in the electrical detection of the spin pumping, the signal is measured in open circuit (without DC current). Naively one might think that no change of the voltage due to AMR, AHE or PHE at resonance is expected because no current is flowing in the sample.

As the magnetization is excited using a radio-frequency magnetic field  $h_{rf}$ , an electric field  $e_{rf}$  is also always present in the cavity. If this radio-frequency electric field is nonvanishing in the cavity at the sample level a radio-frequency induced current  $j_{rf}$  could flow in the ferromagnet. Therefore the presence of an electric field in the cavity can give rise to a change of the AC resistance at the GHz frequency at resonance. Nonetheless as we are measuring a DC signal it seems to be unimportant... **It is not!** The observation of a DC voltage at resonance in absence of any DC current has in fact already been observed in the late 50's and has been explained by Juretschke<sup>185</sup> and Egan in the 60's as can be seen in figure 2.17 extracted from measurements of Egan *et al.* published in 1963<sup>186</sup>. In Nickel plates both the detection of a DC voltage at resonance and the specific angular dependence in the in-plane geometry were observed and understood. These voltage were ascribed to magnetoresistance and Hall effects.

Let's take the simple example of AMR, following Ohm's law the AC and DC voltages can be written

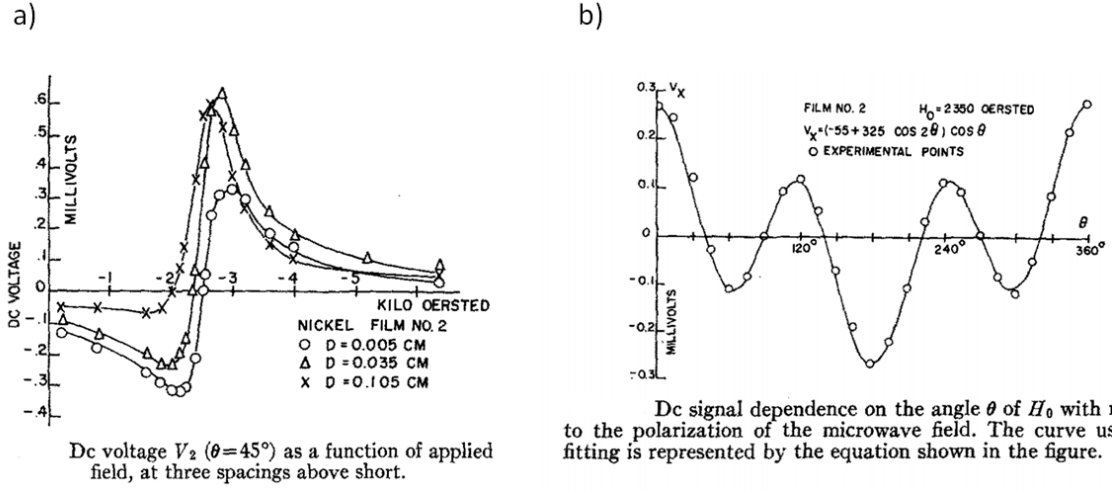


FIG. 2.17: DC voltage detection of SRE measured by Egan and Juretschke in 1963 in Nickel extracted from reference . Figure a) shows some signals measured in Nickel plates at a power of 500mW and figure b shows angular dependence in the plane and fitting of the data.

as:

$$V_{AC}(t) = R(t) \times I_{rf}(t) \quad (2.49)$$

$$V_{DC} = \langle V_{AC}(t) \rangle$$

Due to the change of resistance related to AMR, the resistance will change with the magnetization precession. It is written  $R(t) = R_0 + \Delta R_{AMR} \cos(\omega t)$  and the AC current flowing in the ferromagnetic material is given by  $I_{rf}(t) = I_{rf} \sin(\omega t + \psi)$  with  $\psi$  the dephasing between the magnetization precession and the AC current. Following equations 2.48 a non-zero DC voltage can arise and is given by:

$$V_{DC} = \frac{\Delta R_{AMR} I_{rf} \cos(\psi)}{2} \quad (2.50)$$

The origin of the spin-rectification effects can be summarized as follows: at the resonance field, the precessing magnetization induces a time varying resistivity of the ferromagnetic layer due to magneto-resistive or Hall effects. This change of resistivity combines with the radio-frequency induced current  $j_{rf}$  and give rise to a non-vanishing DC voltage. This voltage is sometimes called a photovoltage as it is due to microwave photons<sup>184</sup>. More than forty years after these reports, the spin pumping ISHE detection measurements were performed. As can be seen already in one of the first spin pumping ISHE measurement by Costache *et al.*<sup>165</sup> a non-zero DC voltage is observed even in absence of the adjacent ISHE layer. This signal has an angular dependence different from the one of ISHE. This effect is in fact similar to the one observed by Egan and Juretschke in Nickel.

To avoid a large contribution of the spin rectification effects (SRE) it is needed to choose carefully which cavity to use and where to place the sample. It is needed to position the sample at a position where the electric field  $e_{rf}$  is minimum to obtain a minimum of SRE and at a maximum of  $h_{rf}$  to obtain a maximum of ISHE/IEE signal. This position of the sample is known as the nodal plane. Such a position is found in the center of TE011 cylindrical and TE102 rectangular cavities which are common EPR cavity. All presented experiments in this manuscript were performed using a MS5

3loop-2gap resonator in a pseudo TE<sub>102</sub> mode with sample positioned in the center of the main gap. Using an MS5 loop gap has several advantages described in appendix A, this includes the fact that electric field is contained in the gap (far from the sample) while magnetic field is contained in the loop (at the sample position) and are thus well separated. Due to that parasitic SRE voltage is reduced and is less sensitive to decentering problem. In general cavity in a TE<sub>102</sub> mode are less sensitive to SRE than the one in the TE<sub>011</sub> mode due to a better separation of the electric and magnetic fields<sup>187</sup>. I would like to mention here that the MS5 resonator was sometimes called a cylindrical cavity in some publications<sup>188</sup>, while its shape is indeed cylindrical it is not a cylindrical TE<sub>011</sub> cavity.

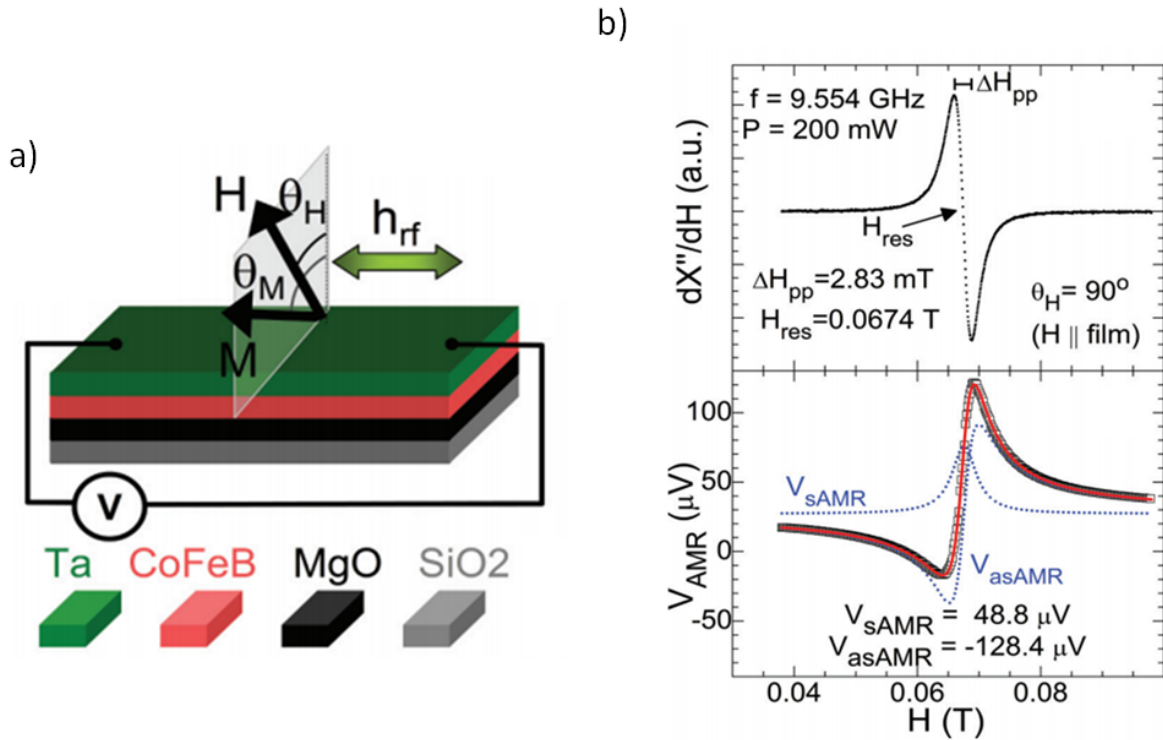


FIG. 2.18: DC voltage detection of AMR related spin rectification effect in CoFeB extracted from Rojas-Sanchez *et al.*<sup>59</sup>. Figure a) shows the stacking used for this study and figure b) shows electrical detection of FMR due to Spin rectification effect at resonance. Signal is a mixture of symmetric and asymmetric signal.

But even with a good positioning of the sample some SRE contribution can still give rise to a measurable DC voltage as no perfect placement of the sample is possible. The first method to separate the ISHE signal from the SRE signal were based on the separation of the symmetric and antisymmetric component of the electrically detected FMR<sup>26;123</sup>. On the one hand and as mentioned before ISHE/IEE spin pumping signal is purely symmetric because it is proportional to the FMR absorption intensity. On the other hand SRE is not because the spin precession phase shifts by  $\pi/2$  at resonance, and the signal should be antisymmetric<sup>123</sup>. Nonetheless this is true only for a microwave confined in a lossless resonator. In general due to dissipation by currents or losses in the sample or wiring the shift is not  $\pi/2$  and give rise to both a symmetric and asymmetric signal. This was observed for example by Rojas Sanchez *et al.* in thin film of CoFeB where both symmetric and antisymmetric contribution



coexists<sup>59</sup> (cf. figure 2.18.). So this technique while easy to use can be inaccurate and cause some misinterpretation especially when the signal is mostly antisymmetric. Note that when the signal is purely symmetric the spin rectification effects are generally negligible.

To disentangle accurately the ISHE/IEE signal from the SRE one it is needed to perform control measurements. At least it is needed to perform a measurement in the parallel and the antiparallel configuration. The signal should have a similar amplitude when normalized by the rf field and an opposite sign. From this measurement one can verify the good positioning of the sample in the nodal plane and the limited AC current in the sample. In general one should perform the complete angular dependence or measure a reference layer without the ISHE or IEE adjacent material<sup>40</sup>. In a various number of measurement geometry it is possible to separate the signal due to SRE from the signal due to ISHE with an angular dependence. This method was first developed by Costache *et al.* and Azevedo *et al.* in specific geometries<sup>165;121</sup> and further developed by other groups including Saitoh and Harder groups<sup>189;190;179</sup> for most of the other geometry. For a cavity in a TE102 mode and an out of plane FMR measurement in the geometry described in figure 2.8.a and 2.19.a the calculation of the SRE contribution has been done by Rojas Sanchez *et al.*<sup>59</sup> and Tsukahara *et al.*<sup>177</sup>. This measurement allows to effectively separate the ISHE/IEE contributions from the AMR and AHE one.

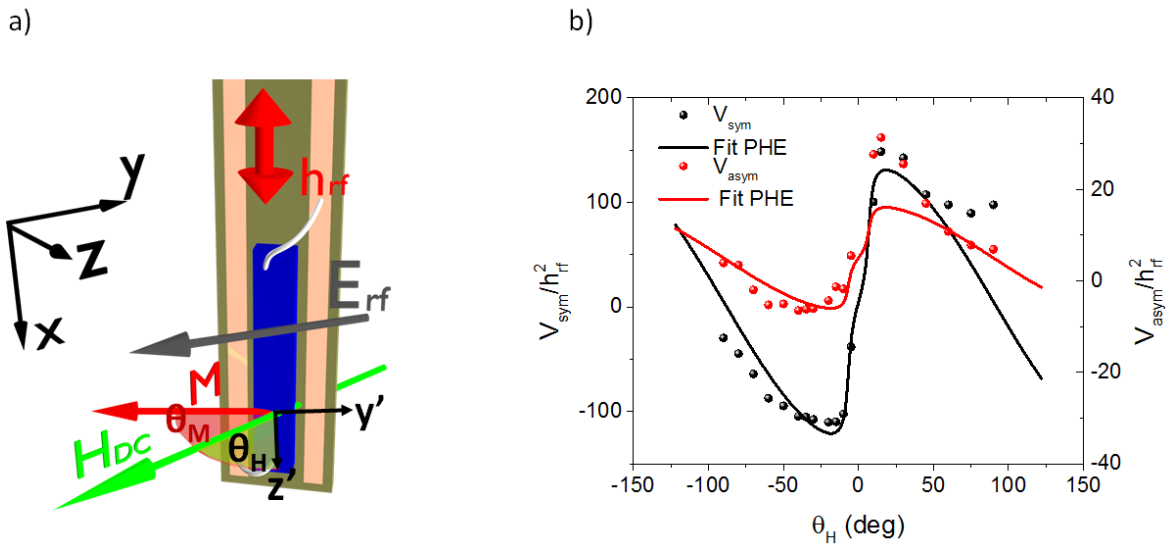


FIG. 2.19: a) Drawing of the experimental set-up with the definitions of the angles. b) Typical Out of plane angular dependence dominated by PHE fitted using equation , here observed in STOMgO(5nm) Permalloy (20nm)

To calculate the angular dependence of the spin rectification effects we have to follow the same method as Juretschke and Egan and use the generalized Ohm's law<sup>185;186</sup>. The sample is rotated out of the plane as depicted in figure 2.19.a. with  $\theta_H = 0^\circ$  when the DC magnetic field is perpendicular to the plane and  $\theta_H = \pm 90^\circ$  when the field is in the plane. As we are in open circuit conditions no DC current is supplied and only an AC current flows in the FM layer due to the non-vanishing rf field  $\vec{J} = \vec{j}_{rf}$  with  $j_{rf} = j_0 \cos(\omega t + \psi) \vec{y}'$ . The generalized Ohms law can then be written:



$$\vec{E} = \rho \vec{j}_{rf} + \frac{\Delta\rho}{M_s^2} (\vec{j}_{rf} \cdot \vec{M}) \vec{M} - R_H \vec{j}_{rf} \times \vec{M} \quad (2.51)$$

This take into account the magnetoresistance of all types  $\Delta\rho$  and Hall effects  $R_H$ . In ferromagnetic metals, with electrical contacts in the Hall configuration the largest contribution is the Planar Hall Effect (PHE). As shown by Rojas Sanchez *et al.* and Tsukahara *et al.*, using the geometry of the figure 2.19.a, the PHE contribution can be written:

$$V_{PHE} = -\frac{1}{2}\omega j_0 \rho_{AMR} \cos(\theta_M) \times \frac{\hbar\gamma \left[ 2\alpha\omega \cos(\psi) - \left( \mu_0 M_s \cos^2(\theta_M) + \sqrt{(\mu_0 M_s)^2 \gamma^2 \cos^4(\theta_M) + 4\omega^2} \right) \sin(\psi) \right]}{2\alpha\omega \sqrt{(\mu_0 M_s)^2 \gamma^2 \cos^4(\theta_M) + 4\omega^2}} \quad (2.52)$$

With  $\rho_{AMR}$  the change of resistivity due to AMR/PHE. It is to be noted that in the MS5 resonator or in a TE102 cavity the amplitude of the rf current amplitude  $j_0$  has an angular dependence due to the direction of the rf electric field inside the cavity or resonator as shown in annex A. In first approximation (in an unperturbated cavity)  $j_0$  change with the DC magnetic field angle as  $j_0 \propto \sin(\theta_H + \theta_E)$ , where  $\theta_E$  is the direction of the rf electric field in the cavity.

In absence of any ISHE or IEE, it is possible to detect the spin rectification effects contribution at resonance. It can be observed for example in Permalloy deposited on MgO/STO as seen in figure 2.19.b. The obtained angular dependence is different from the one of ISHE in particular there exists a signal maximum at angles close to the perpendicular to the plane orientation. The maximum position and amplitude will depend on the magnetic properties of the FM and the phase difference between the AC current and magnetization. To fit the data here we used a dephasing  $\phi$  of  $85^\circ$  and an angle  $\theta_E$  of  $90^\circ$ . Note that the symmetric and asymmetric parts of the electrical signal has similar angular dependence, this is expected as they are connected through the dephasing  $\phi$  that is ideally not angular dependent. In general the signal is also not well reversed when changing the magnetic field direction from the parallel configuration to the antiparallel configuration.

When the ISHE or IEE signal dominates the signal as in CFB(15nm)\NiCu(15nm) and Pt(10nm)\Permalloy(20nm) shown in figure 2.20, the angular dependence of the symmetric and asymmetric part of the signal are different and the symmetric signal is well fitted with an ISHE only contribution.

Now that we have shown that it is possible to differentiate spin rectification effects from ISHE or IEE signal in our geometry we would like to note here that other geometries allow to do this separation more easily, in particular by doing in plane angular dependence with rf magnetic field out of the plane<sup>158;162</sup>. In that case there exists well defined extinction of the SRE signal close to maximum values of the spin pumping signal. Unfortunately this geometry is not compatible with our cavity, due its limited sample access size it is difficult to enter a sample without breaking the bondings.

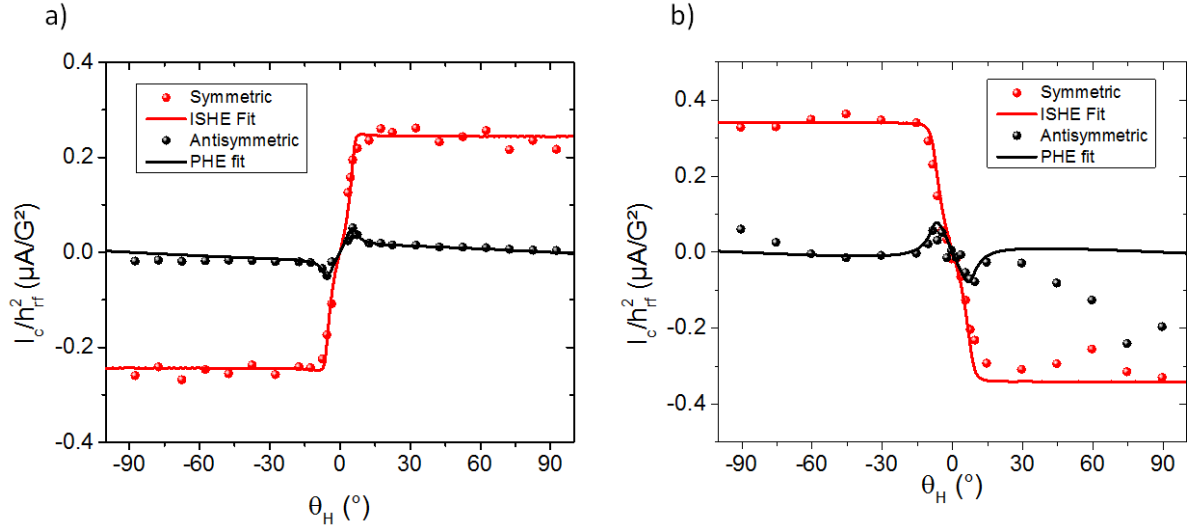


FIG. 2.20: Angular dependence of the symmetric and antisymmetric contribution to the electrically detected FMR in a) CFB(15nm)/NiCu(15nm) and b) Pt(10nm)/Permalloy(20nm). The symmetric contribution is perfectly fitted by ISHE angular dependence, while the antisymmetric contribution is well fitted by PHE angular dependence.

### 2.4.3 Thermal effects?

Not only spin rectification effects can complicate measurement of the spin pumping FMR signal. A temperature increase and thus a non-zero thermal gradient could arise at the ferromagnetic resonance, due to the energy absorption in the ferromagnetic layer. Such a thermal gradient could give rise to several thermoelectric and spin-caloritronics contributions, in particular the Anomalous Nernst Effect (ANE)<sup>191</sup> and the Spin Seebeck effect (SSE)<sup>149</sup>, that would add up to the spin pumping Inverse Spin Hall Effect signal. In this picture, the signal would thus be due to a combination of the ISHE signal, the spin rectification effects and thermal effects.

Regarding the geometry of the system due to an increase of the power absorption at resonance, the temperature of the ferromagnet should increase. Therefore, a thermal gradient along  $z$  would appear. Recent analysis of spin-pumping FMR results have even been based on the hypothesis that the observed signals are dominated by these thermal effects<sup>180;192</sup>. Figure 2.21.a depicts the dynamical spin injection process as described by Bratass *et al.*, the model that we extensively used in this chapter. As suggested by Yamanoi *et al.*, the additional dissipation at the ferromagnetic resonance could lead to the appearance of a voltage along the  $x$  direction<sup>180</sup>. The absorption at resonance would lead to a temperature increase of the ferromagnet, and thus to a thermal gradient perpendicular to the layers. This thermal gradient would lead to the injection of a pure spin current along  $z$  towards the non-magnetic material, converted by ISHE into an electric field along  $x$  through a process known as the longitudinal Spin Seebeck effect<sup>149</sup>. This possibility is described in figure 2.21.b. Due to the existence of a thermal gradient, the Anomalous Nernst Effect in the FM layer could also appear, and can give rise to an electric field along  $x$  as depicted in figure 2.21.c.

Among the main thermal contributions or spin caloritronics contribution that could give rise to a

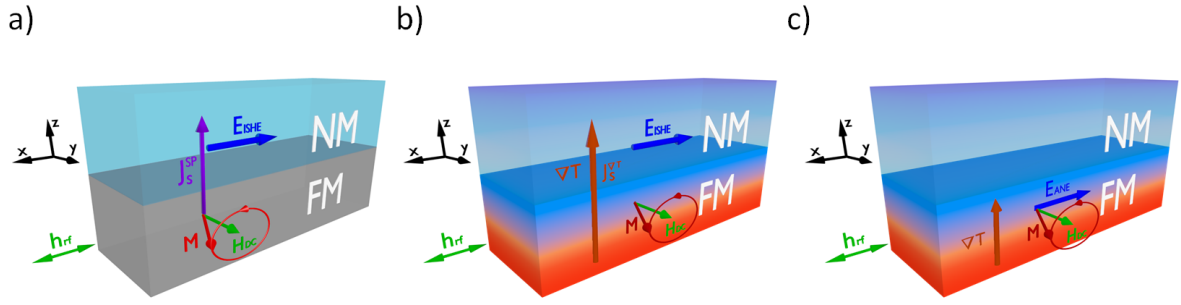


FIG. 2.21: Schematic representation of the possible spin injection mechanisms at the FMR and of thermal gradient related effects. a) Dynamical spin injection. Because of the magnetization precession, the spin current  $J_s^{sp}$  is injected from the FM layer towards the NM layer. An electromotive force  $E_{ISHE}$  arises along  $x$ , due to ISHE, which can be detected as a voltage in open circuit conditions. b) Spin injection due to the thermal gradient. At the ferromagnetic resonance the temperature of the FM layer increases creating a thermal gradient  $\nabla T$  along the  $z$  direction and thus a thermal spin current injection  $J_s^{\nabla T}$  this spin current is then converted into an electromotive force  $E_{ISHE}$ . c) Thermal gradient within the ferromagnet could give rise to an Anomalous Nernst related electromotive force  $E_{ANE}$ .

measurable signal there are contribution that are field independent (ordinary Seebeck Effect), field dependent (ordinary Nernst Effect), or magnetization dependent (spin Seebeck effect and anomalous Nernst effect). Therefore they have different angular dependences. As the ordinary Seebeck effect (OSE) has no field nor magnetization dependence it has no angular dependence. The ordinary Nernst effect (ONE) is proportional to the total magnetic field perpendicular to the thermal gradient so in the case of a thermal gradient along  $z$  it varies as  $\mu_0 H_{res} \sin(\theta_H)$ . And as both the spin Seebeck effect (SSE) and the anomalous Nernst effect (ANE) are proportional to the magnetization perpendicular to the thermal gradient they all vary as  $\sin(\theta_M)$ . The angular dependences of all these thermal contributions –normalized by the value in the plane– but also the one of the ISHE are given in figure 2.22. Note that we used the properties of the NiFe/Pt sample described in the previous sections.

It is therefore clear that angular dependence of the ISHE and some thermal related effects as ANE, SSE or even ONE are extremely close. Due to that, the out of plane angular dependence do not allow to disentangle accurately all the thermal contributions from the ISHE/IEE. It is needed to use a novel method and technique to verify that the thermal contribution is negligible.

Usually disentangling thermal from non-thermal effect is obtained based on modifications of the structure. Usually it is done by inserting a thick insulating barrier between the ferromagnet and the adjacent layer. In this case as spin injection is blocked but temperature gradient still exists only thermal related signal is expected to occur at resonance. Nonetheless it also prevents SSE to be observed and thus do not allow to evaluate signal related to SSE contribution. It also changes adjacent layer of the ferromagnetic layer and could modify the temperature profile and thus the measured thermal signal<sup>193</sup>. The other solution is to cap the ferromagnet with a metal of high thermal conductivity but low spin hall effect contribution as Cu or Au. This will modify the temperature profile and should thus modify the

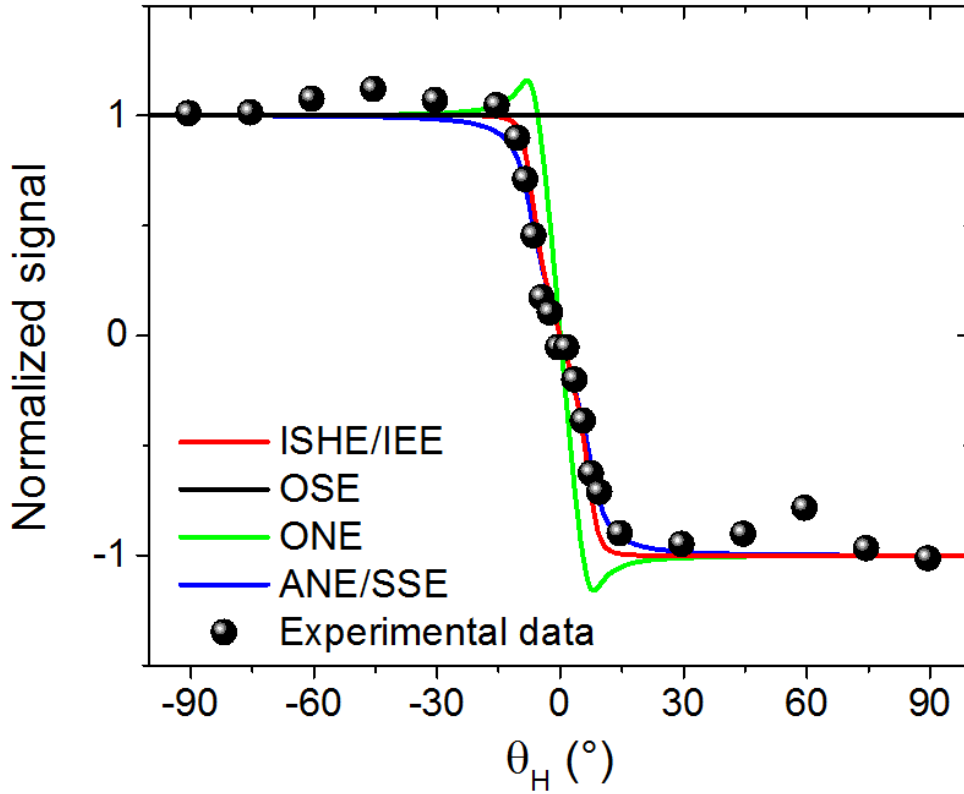


FIG. 2.22: Angular dependence of the possible thermal contributions including Ordinary Seebeck Effect (OSE), Ordinary Nernst Effect (ONE), Spin Seebeck effect (SSE) and Anomalous Nernst Effect (ANE) compared with ISHE and experimental data of a typical ISHE measurement

thermal gradients within the thin film. In absence of any modification of the signal with modification of the thermal gradient one can conclude on the absence of thermal effects<sup>194</sup>. Nonetheless this technique is not compatible with epitaxial ferromagnetic layers where the substrate is chosen for good epitaxy and capping layer is the ISHE/IEE material. Moreover it modifies the growth and resistance of the sample and possibly other magnetic properties making quantitative estimation more difficult. In the following chapter we propose a novel technique that is free of these problems and do not require the growth of control samples. It is based on the strong difference in the time dependence of the spin pumping spin current injection occurring in the nanosecond range and the temperature increase occurring in the second range.

Now that we have described the spin pumping FMR technique and the method to evaluate the spin current injection, the conversion efficiency and the spin diffusion length we will present experiments using this technique in metals and alloys, Rashba interfaces and topological insulators. We would also present a novel technique developed to evaluate the existence or absence of possible thermal contributions occurring at the ferromagnetic resonance. We will also present other results including magnetotransport or material characterizations that are important to understand the different phenomenon described in the manuscript.

## Spin Hall effect in heavy metals and Alloys

After the first experimental demonstrations of the Direct and Inverse Spin Hall Effects measurements in metals<sup>57;27;26</sup> a lot of research focused on increasing conversion efficiency in transition metals. Heavy metals, including in particular Pt, W and Ta, have attracted a broad interest in the spintronic community due to their large spin Hall angles<sup>31;39;32;61</sup> and their ability to induce PMA for example in Co based multilayers<sup>195</sup>. With intrinsic mechanisms the spin Hall angle is proportional to the resistivity of the heavy metal, in general large value of spin Hall angle are associated with high resistivity. As shown by Sagasta *et al.* the highest spin hall angles in Pt and Ta are obtained for large resistivities: 15% for  $70 \mu\Omega.cm$  in Pt<sup>71</sup> and 35% for  $650 \mu\Omega.cm$  in Ta<sup>196</sup>. A material with a large resistivity limits the maximum current density and increase the power needed for SOT applications (associated with an increase of the size of transistors)<sup>81</sup>. As mentioned in the first Chapter it is possible to use extrinsic mechanisms in alloys especially combining a large intrinsic and extrinsic side-jump contribution. This should allow to obtain large spin Hall angles while keeping the resistivity low.

In this chapter we will first present measurements on heavy metal to provide some examples of spin pumping FMR measurements with materials that possess positive and negative spin hall angles, with different ferromagnets and stacking order, to show the capability to measure the spin to charge conversion accurately in our experimental setup. Then we will look for a spin signal related to thermal effects in Platinum/Ferromagnet bilayers using bolometric measurements and finally we will evidence the large spin to charge current conversion obtained in Au based alloys by taking advantage of the side-jump contribution in AuTa.

### 3.1 Spin Hall effect in pure metals: Pt, Ta and W

The first studies performed on spin-pumping ISHE in metals were done in Pt, which has a positive Spin Hall Angle<sup>197</sup>. These studies were followed by others on Ta or W which have a negative spin Hall angle<sup>198;65</sup>. These three metals are particularly interesting because they allow to verify some general properties of the spin pumping signal in particular its sign. Similar measurements have already been performed by other groups for consistency check of the spin pumping FMR measurements<sup>198;65;199</sup>. Nonetheless there are criticisms on the possibility for spin pumping FMR technique to measure accurately spin to charge conversion due to spurious effects as thermal effects or spin rectification effects<sup>192</sup>, therefore it is important to bring to light these basic experiments before presenting any other results. Moreover knowing the sign of the spin signal for Pt (positive spin Hall angle) and Ta (negative spin Hall angle) allows to accurately determine the sign of the conversion of unknown systems.

### 3.1.1 Positive or negative spin hall angle?

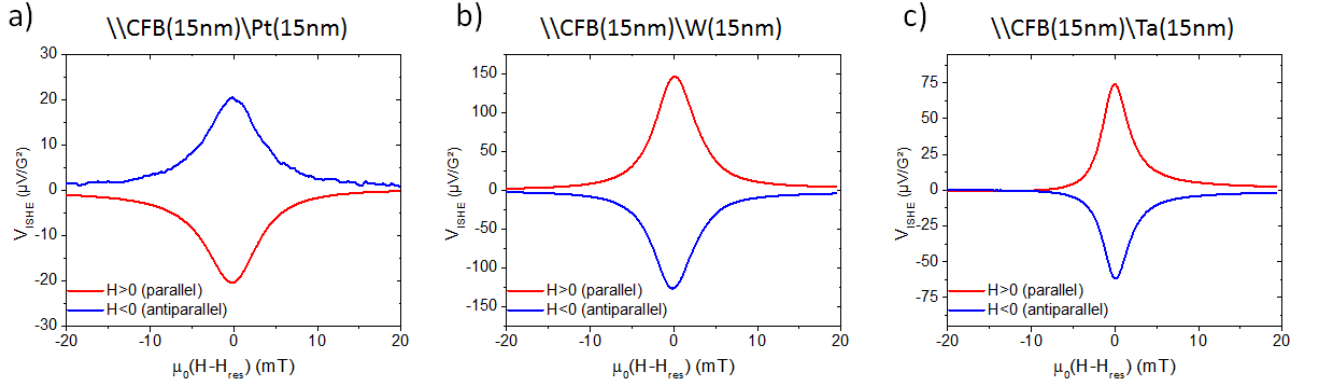


FIG. 3.1: Spin pumping ISHE signals measured in different bilayers in the parallel and antiparallel configurations using CoFeB as the ferromagnetic layer: a) CoFeB(15)\Pt(15) b) CoFeB(15)\W(15) and c) CoFeB(15)\Ta(15). Thicknesses are in nanometers.

The value of the spin Hall angles for Pt, W and Ta varies a lot in the literature, but there is a general agreement on the sign of the conversion. In particular an opposite sign between  $\theta_{SHE}^{Pt} > 0$  and  $\theta_{SHE}^{Ta}; \theta_{SHE}^W < 0$  was observed by various groups and by various means of measurements<sup>198;199;174;200;201</sup>. Therefore one can expect that the spin pumping signal obtained in Pt has a sign opposite to the one of Ta or W if the dominating signal is the one due to ISHE. As observed recently by Conca *et al.* in CoFeB\Pt, and CoFeB\Ta bilayers measured using a stripline, symmetric signal might have the same sign<sup>202</sup>. This is due to a large spin rectification contribution and it is only thanks to a careful evaluation of the angular dependence that they could obtain the right sign of ISHE for Pt and Ta.

As we are using a cavity we are less sensitive to spin rectification effects, especially when using CoFeB that has a small AMR/PHE and a high resistivity leading to smaller rf currents flowing in the ferromagnet for similar power. In figure 3.1 we show results of spin pumping measurements performed on CoFeB(15)\Pt(15), CoFeB(15)\W(15), and CoFeB(15)\Ta(15), all deposited by magnetron sputtering and measured with the same contact configuration. As can be seen in figure 3.1.a the signal in the parallel configuration as defined in chapter 2 is negative for CoFeB(15)\Pt(15) but is positive for both CoFeB(15)\W(15) and CoFeB(15)\Ta(15). Moreover the signal is reversed as expected in the antiparallel configuration and is fully symmetric around the resonance field. It is to be noted that the smaller voltage obtained by using Pt is due to the smaller resistivity of Pt ( $20\mu\Omega.cm$  at room temperature here) compared to those of both Ta and W (around  $140\mu\Omega.cm$ ). The sign obtained in these bilayers is in accordance with previous results and also the symmetry of the ISHE proposed by Schreier *et al.* for Pt<sup>197</sup>.

To confirm the sign of the effect and that such an accurate measurement can be extended to other ferromagnetic materials we have also performed similar measurements on bilayers with Permalloy, Cobalt and  $La_{0.7}Sr_{0.3}MnO_3$  (LSMO). On these samples a thin Pt film was deposited either by evaporation (for Permalloy) or sputtering (Co and LSMO). As can be seen in figure 3.2a,b and c the

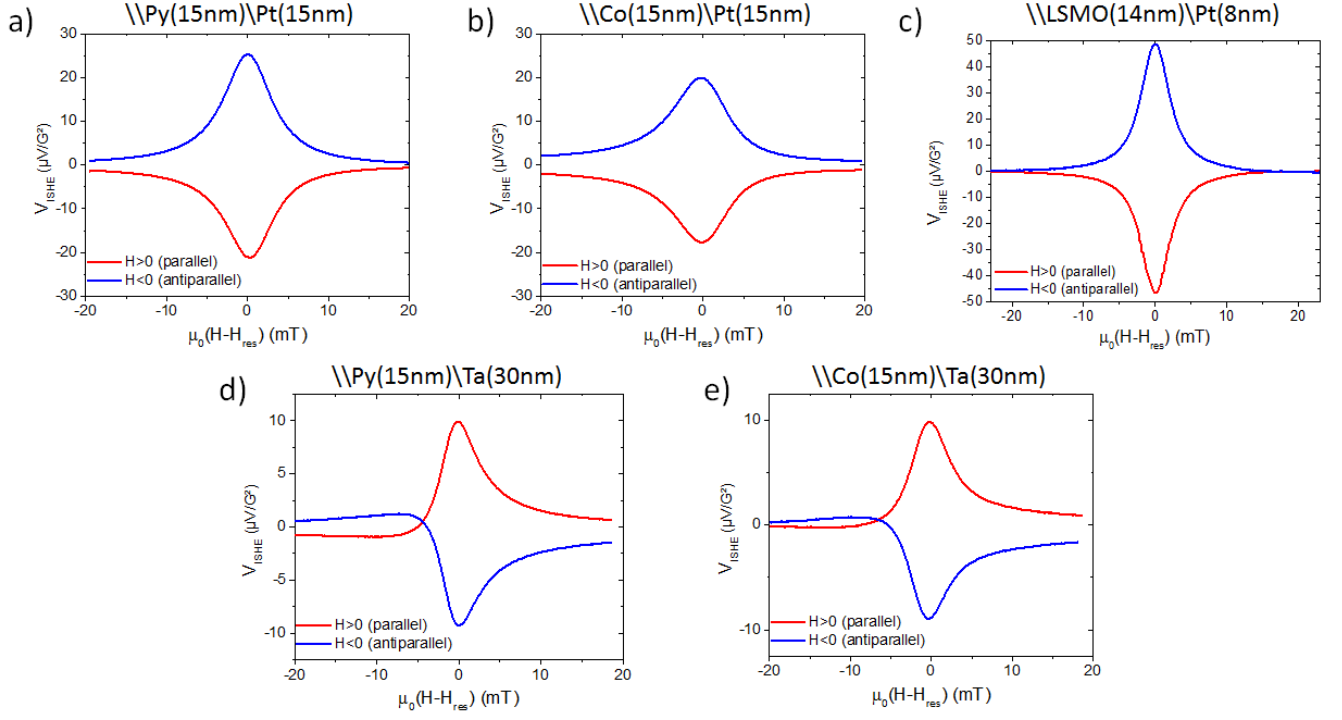


FIG. 3.2: Spin pumping ISHE signals measured using different ferromagnetic materials in a), b) and c) and Ta in d) and e). As the sign of the ISHE is independent on the FM material same sign is observed in association with Pt by using a) Permalloy, b) Cobalt, c) LSMO and also in association with Ta by using d) Permalloy or e) Cobalt

sign of the signal is the same as in  $CoFeB(15)\backslash Pt(15)$ . This shows that even when using Permalloy or Cobalt with a larger AMR/PHE and lower resistivity than in CoFeB, and thus possibly larger spin rectification effect, the signal is still largely dominated by the ISHE signal. By using Tantalum instead of Pt we can also observe the same sign change as in  $CoFeB(15)\backslash Ta(15)$  for both  $Py(15)\backslash Ta(30)$  and  $Co(15)\backslash Ta(30)$ , further confirming that the symmetric signal is mostly of ISHE nature. As can be seen in figure 3.2 d and e there is some antisymmetric contribution to the signal likely to be related to the spin rectification effect, on the contrary to  $CoFeB(15)\backslash Ta(15)$  which is perfectly symmetric. An angular dependence or a thickness dependence is in general needed to account for this non-zero contribution as mentioned in chapter 2.

### 3.1.2 Stacking order dependence

Apart from the sign of the ISHE positive for Pt and negative for Ta or W, it is important to check the stacking order dependence. By reversing the stacking order with a fixed magnetization direction the injected spin current  $\vec{J}_s$  is reversed, as seen in figure 3.3. This leads  $J_c^{ISHE}$  to be reversed and thus to a change in the sign of the detected ISHE signal following equation (1.12):

$$J_c^{ISHE} = \theta_{SHE} \vec{J}_s \times \vec{\sigma} \quad (3.1)$$

Therefore the spin pumping ISHE signal obtained in  $FM\backslash NM$  has to be of opposite sign to the one in  $NM\backslash FM$ . If the change of stacking order does not lead to further modifications of the interface



and of the resistivity, and if the ISHE signal dominates they should even have the same amplitude. This is the case for inverted structure of  $Py \backslash Pt$  and  $Pt \backslash Py$  using the same contact configuration as can be seen in figure 3.3 a) and b). The inverted sign obtained in these bilayers is therefore in accordance with previous results and also with the expected symmetry of the spin pumping FMR <sup>174;173</sup>. Therefore we can conclude that for a stacking order  $FM \backslash NM$  a negative (positive) spin pumping ISHE signal obtained in parallel (antiparallel) configuration corresponds to a positive spin Hall angle. For the opposite stacking order  $NM \backslash FM$  it would be the opposite sign due to opposite direction of the spin current injection. This shows the importance of the stacking order and the need to have a good reference with the same  $FM \backslash NM$  order to determine the sign of the conversion.

I would like to thank Juan-Carlos Rojas Sanchez and Fu Yu that performed similar measurements some years ago. Their results allow me to address easily the question of the sign of the spin hall angle or inverse Edelstein length by comparing the sign of the signal with the one of Pt and Ta with the same stacking order.

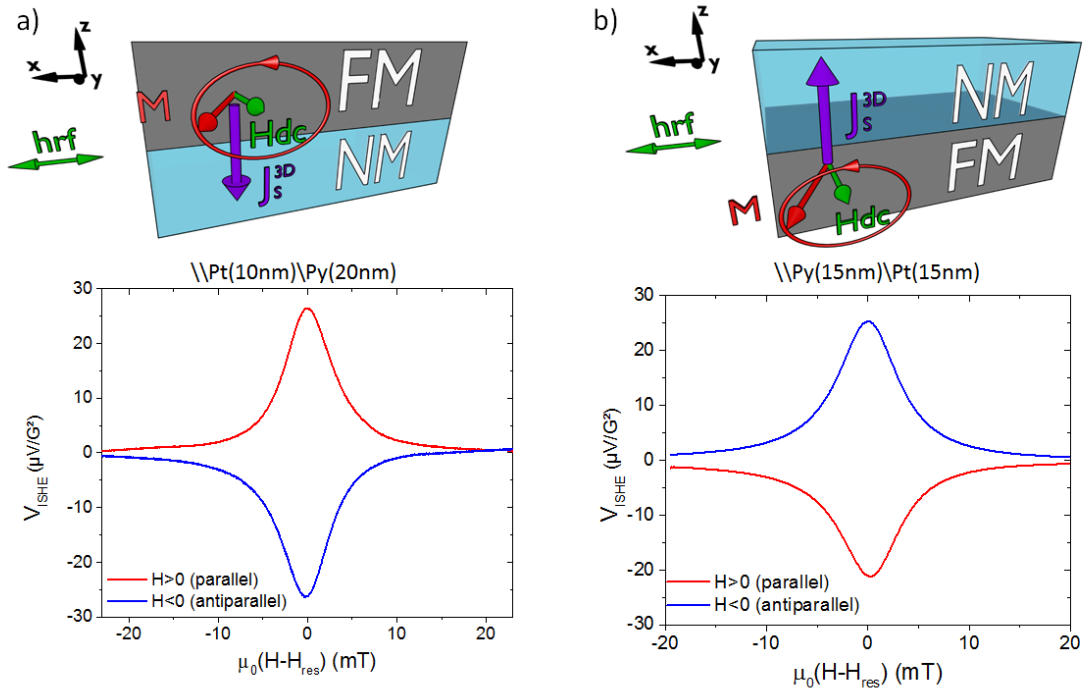


FIG. 3.3: Spin pumping ISHE signal measured using different stacking order with a) FM on top of NM and b) NM on top of FM. Due to inversion of stacking order the injected spin current is reversed and the spin signal too.

### 3.2 A possible thermal contribution?

Spin pumping by ferromagnetic resonance has been one of the most common technique to determine spin hall angles, Edelstein lengths or spin diffusion lengths of a large variety of materials. Nevertheless in recent years, rising concerns have appeared regarding the interpretation of these experiments, underlining that the signal could arise purely from thermoelectric effects <sup>192;203;204;180</sup>, rather than from



the spin-charge interconversion mechanism mentioned in the previous chapter. This would therefore prevent any accurate measurement. From the previous section it is clear that the sign change of the signal with Pt and Ta or the stacking inversion is not compatible with a dominating anomalous Nernst effect (ANE) contribution or Ordinary Seebeck effect (OSE) contribution however these effect might still contribute to the signal as well as Spin Seebeck Effect (SSE). It is therefore mandatory to evaluate this thermal contribution and to find a generic method to evaluate it, this is the goal of this section. The work described in the next section is available on arxiv and is entitled “Do thermal effect always contribute to spin pumping signal”<sup>205</sup>. It has been submitted to Physical Review Applied and is currently under review.

### 3.2.1 Lack of Universal method to evaluate the thermal related effects

There is no generic method to evaluate the presence or absence of thermal effects in spin pumping signals. As shown in the previous chapter angular dependences can not be unambiguously used in our experimental geometry. One idea could be to combine bolometry and spin pumping by ferromagnetic resonance measurements, and compare their timescale. Using *Pt\Py* and *LSMO\Pt* samples, we aim were able to demonstrate the absence of any measurable thermoelectric contribution such as the spin Seebeck and Anomalous Nernst effects.

Even for a widely studied material as Platinum the estimated values of spin diffusion length and spin Hall angle determined by different techniques spread over more than one order of magnitude, with spin diffusion lengths ranging from 1.2 nm<sup>206</sup> to 11 nm<sup>55</sup>, and spin Hall angles from 1.2%<sup>175</sup> to 38.7%<sup>163</sup>. This large discrepancy can be partially explained by differences in Pt resistivity<sup>71</sup> or accounted for by interface-related phenomena as spin memory-loss, but it still remains mostly unexplained<sup>154</sup>. In this particular context, concerns regarding the reliability of the SP-FMR technique have been pointed out. A thermal gradient could indeed arise at the ferromagnetic resonance, due to the energy absorption in the ferromagnetic layer<sup>192;204;180</sup>. Such a thermal gradient could give rise to several thermoelectric and spin-caloritronics contributions, in particular the ANE and the SSE, that would add up to the spin pumping ISHE signal. In this picture, the signal would thus be due to a combination of the ISHE signal, the spin rectification effects (SRE) and thermal effects.

While the separation of ISHE from SRE has already been vastly discussed and can be achieved from the angular dependence in different measurement geometries as shown in chapter 2, it is not straightforward to disentangle the ISHE signal from thermal effects. Here we propose to do disentangle thermal from non-thermal effects by comparing the timescale of the FMR spin injection mechanism and of the temperature related signal. We will perform measurements on two multilayers. The first one is a *Pt\Py* bilayer, archetypal of spin pumping ISHE experiments<sup>168;175;206;26</sup>, with a large ANE coefficient in Py<sup>207</sup>, and the second one is a *LSMO\Pt* bilayer, for which a high SSE contribution is expected<sup>208</sup>.

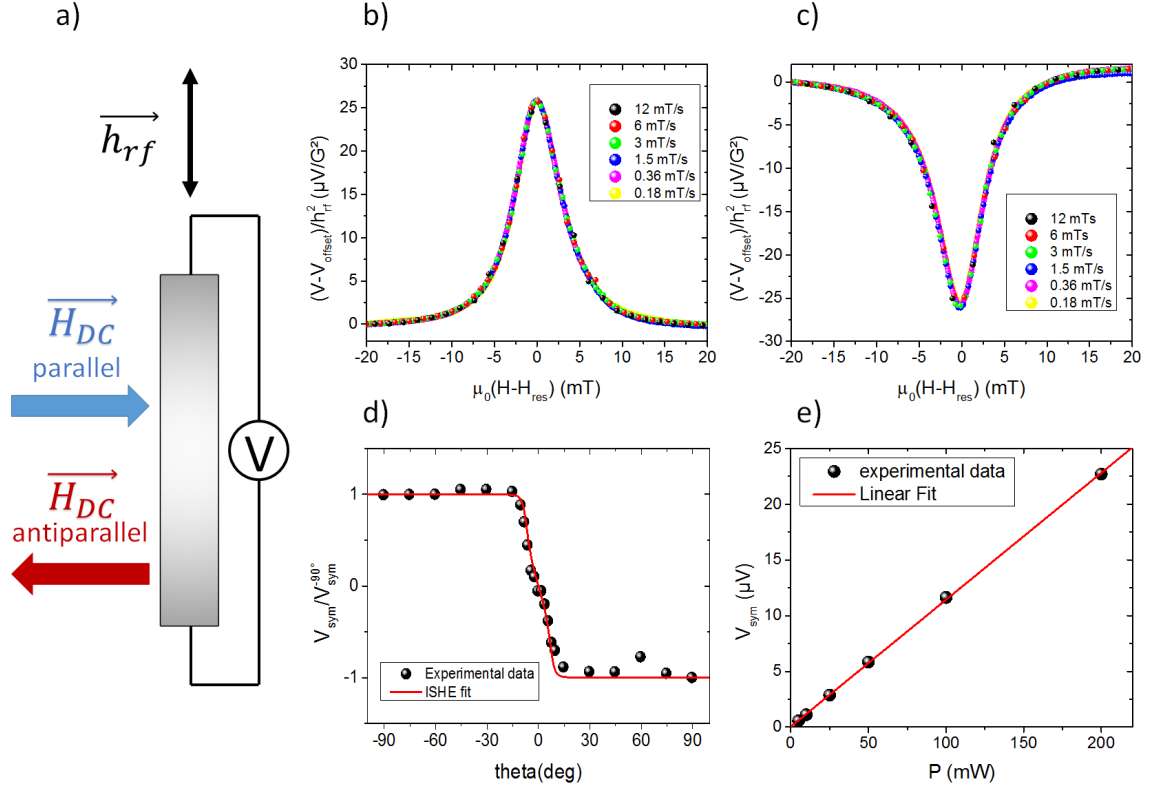


FIG. 3.4: a) Schematic representation of the measurement device used to detect spin pumping ISHE at resonance in the  $\text{SiO}_2 \backslash \text{Pt}(10) \backslash \text{Py}(20)$  sample (top view). b) Signal obtained in the in-plane parallel configuration for various sweeping rates, normalized by the square of the rf magnetic field  $h_{rf}^2$  for a power of 100 mW. c) Similar measurement in the in-plane antiparallel configuration. d) Out-of-plane angular dependence of the spin signal fitted using the ISHE angular dependence provided in chapter 2. e) Power dependence of the symmetric part of the signal as a function of the microwave power in the parallel configuration.

### 3.2.2 Spin Pumping experiment

The characteristic timescale of the FMR spin injection mechanism is the FMR precession period, which is of the order of the nanosecond. But the temperature increase timescale, the time needed to reach a thermal equilibrium, is of several seconds<sup>183:184</sup>: thermal and non-thermal effects have different dynamics. We thus propose a technique that can be adapted to any SP-FMR experiment to disentangle the two mechanisms, by measuring the time dependence of the spin pumping signal and of the temperature increase. We performed SP-FMR measurements on a  $\text{SiO}_2 \backslash \text{Pt}(10) \backslash \text{Py}(20)$  multilayer, on a  $2.4 \times 0.4 \text{ mm}^2$  structure. In fact this is the same sample as the one shown several times in the previous part. The amplitude of the rf magnetic field  $h_{rf}$  was determined by measuring the Q factor with the sample placed inside the cavity<sup>59</sup>.

We performed a FMR measurements at different sweeping rates, at a power of 100 mW. The scheme of the measurement is shown in figure 3.4.a, and consists in the measurement of the voltage at the ferromagnetic resonance in open circuit. As seen in figure 3.4.b and c in both the parallel and antiparallel configurations, the signal is fully symmetric and independent of the sweeping time. Regarding

the possible contribution of Spin Rectifications Effects in Py, the out-of-plane angular dependence has also been performed (cf. figure 3.4.d). The obtained symmetric signal can be fitted with the ISHE angular dependence model described in the previous chapter. This does not exclude the ANE or SSE but it demonstrates that the contribution of the spin rectification voltages are negligible. This also excludes any contribution of the Ordinary Seebeck effect, which would be field independent. The signal is also linear with the power up to 200 mW(cf. figure 3.4.e), indicating a negligible change of magnetization when increasing the power. The signal possesses the ISHE angular dependence, and there is no trace of thermal drift, which implies that if there is a thermal component to the signal, a steady state of thermal equilibrium has to be reached in a characteristic time well below one second.

### 3.2.3 Temperature increase and spin signal: a different timescale

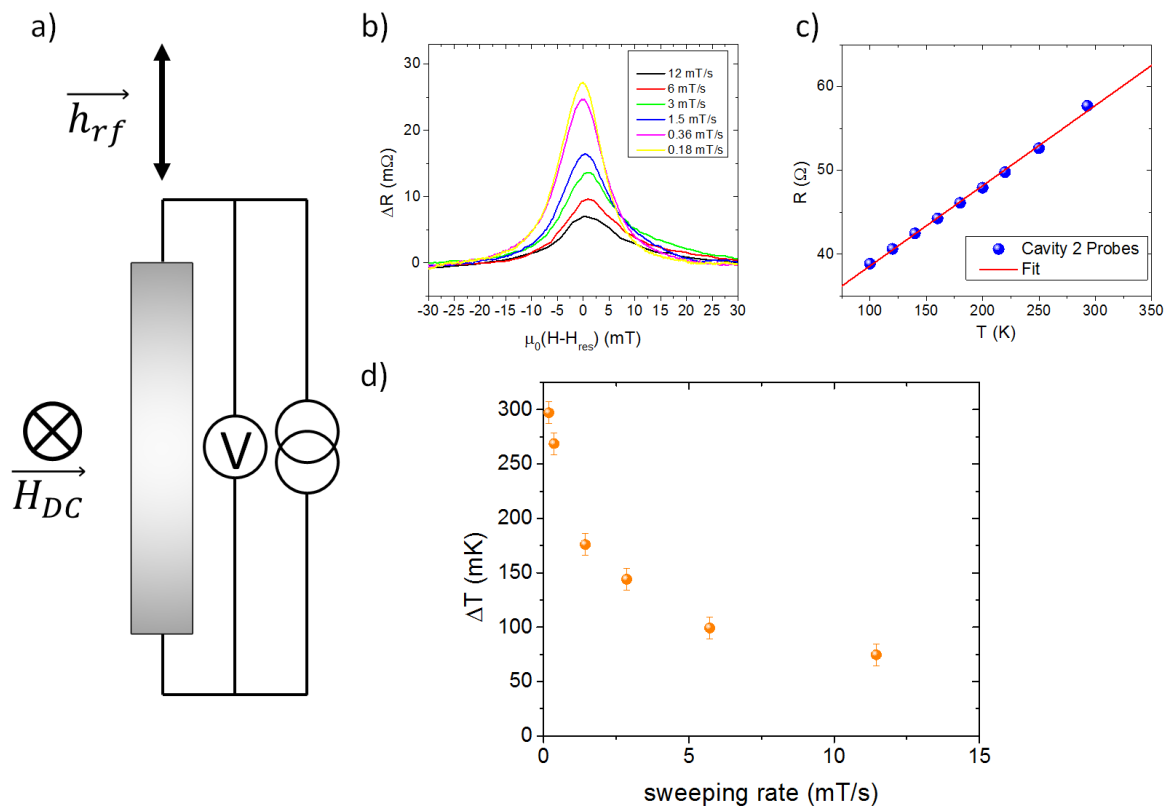


FIG. 3.5: a) Schematic representation of the measurement device used to detect a resistance change at resonance in the  $SiO_2/Pt(10)/Py(20)$  sample (top view). b) Change of the two-probe resistance around the resonance field, for various field sweeping rates (with the base resistance subtracted). c) Resistance of the sample as a function of the temperature, measured in a two-probe configuration on the same sample. The slope value is  $96 \pm 2m\Omega/K$ . d) Temperature change as a function of the sweeping rate, estimated from the increase of resistance at resonance.

Let us now evaluate this characteristic time. A temperature increase can occur at the ferromagnetic resonance, due to the increased microwave absorption<sup>183;184;204;198</sup>. To evaluate the time dependence of this effect, we adopt the measurement scheme shown in figure 3.5.a, where the field is applied out of plane to avoid ISHE or SRE voltage contribution. We used a fixed DC current of 1 mA, a fixed power

of 100 mW and we measured the change of resistance at resonance, known as the bolometric effect. As can be seen on figure 3.5.b we observe an increase of resistance at resonance; more importantly, this increase is highly dependent on the field sweeping rate. The resistance increases from  $7.2 \pm 1 m\Omega$  for a sweeping rate of  $12 mT/s$ , to  $28.5 \pm 1 m\Omega$  for a sweeping rate of  $0.18 mT/s$ . The result is in stark contrast with those shown in figure 3.4 where the signal is independent on the sweeping rate. The temperature increase characteristic time is thus of several seconds, as the time spent near resonance at a sweeping rate of  $0.18 mT/s$  is of 20 s for a linewidth of 3.5 mT. This timescale is similar to what has been observed in previous Electrically Detected FMR experiments<sup>183;184</sup>.

The temperature increase as a function of the sweeping rate is shown in figure 3.5.d. The maximum temperature increase is small, of  $297 \pm 10 mK$  for the slowest sweeping rate, and only of  $75 \pm 10 mK$  for the fastest. The temperature increase is thus found to be strongly dependent on the sweeping time, the thermal equilibrium being not reached after several seconds near resonance. Therefore, any effect originating from a thermal gradient should vary with the sweeping time. The spin signals measured in the configuration of figure 3.4 being totally independent of the sweeping time, we can conclude that in  $SiO_2 \backslash \backslash Pt(10) \backslash \backslash Py(20)$  the Longitudinal Spin Seebeck Effect and anomalous Nernst effects are negligible, and that the observed signals are due to spin pumping and inverse spin Hall effect.

In order to verify this lack of thermal contribution we also performed a combined bolometric and SP-FMR measurements on a  $LSAT \backslash \backslash La_{0.7}Sr_{0.3}MnO_3(13.8) \backslash \backslash Pt(8.2)$  sample, measured along the [100] direction.  $La_{0.7}Sr_{0.3}MnO_3$  (LSMO) possesses a high resistivity compared to Permalloy and Platinum. Moreover the  $LSMO \backslash \backslash Pt$  structure is expected to possess a smaller ANE coefficient but a larger SSE contribution than  $Pt \backslash \backslash Py$ , as demonstrated in Longitudinal Spin Seebeck experiments<sup>208</sup>. Therefore the possible contribution of SSE in this multilayer is expected to be enhanced. In figures 3.6.b and 3.6.c similarly to the case of  $Pt \backslash \backslash Py$  we can see that the thermal equilibrium is still not reached even for the slowest sweeping rate, the total temperature increase is of comparable amplitude and up to  $199 \pm 3 mK$ . As can be seen in figure 3.6.e and 3.6.f, the obtained spin signal is independent on the sweeping rate. Here again, this shows that in this system the ANE and SSE contributions are negligible compared to the spin pumping ISHE signal.

We would like to point out the fact that the NM and FM stacking order is inverted in the  $Pt \backslash \backslash Py$  sample. This leads to a spin signal of opposite sign when compared to  $LSMO \backslash \backslash Pt$  as shown previously in this chapter. The normalized ISHE signal is the ISHE voltage divided by the square of the rf field, the width and the total resistance of the device. The obtained values are of  $0.78 mV.G^{-2}.\Omega^{-1}.m^{-1}$  in  $LSMO \backslash \backslash Pt$  and  $1.11 mV.G^{-2}.\Omega^{-1}.m^{-1}$  in  $Pt \backslash \backslash Py$ , similar to the value of  $0.85 mV.G^{-2}.\Omega^{-1}.m^{-1}$  to  $1.13 mV.G^{-2}.\Omega^{-1}.m^{-1}$  that was previously reported in  $SiO_2 \backslash \backslash Co \backslash \backslash Pt$  of similar thicknesses at X-band<sup>61</sup>. This indicates a similar injected spin currents in these three structures.

### 3.2.4 Differences in the timescale: further evidences

Another control experiment has been done to demonstrate the absence of thermal contribution to the spin pumping signal. The sample was placed in the parallel configuration and the external field was

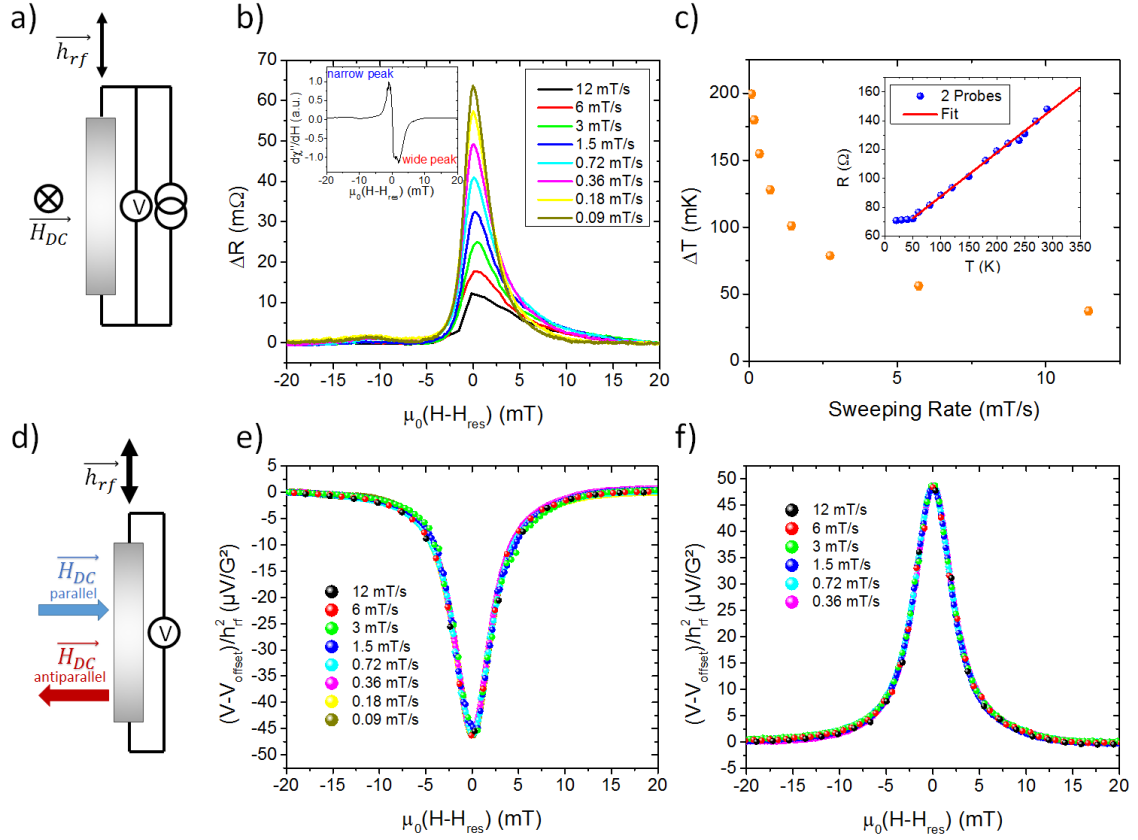


FIG. 3.6: a) Schematic representation of the measurement device used to detect resistance change in the  $LSAT \setminus La_{0.7}Sr_{0.3}MnO_3(13.8) \setminus Pt(8.2)$  sample (top view). b) Change of resistance for various sweeping rate. The inset shows the out of plane FMR response in LSMO, with a narrow and a wide peak c) Temperature change as a function of the sweeping rate. Inset shows the resistance as a function of temperature, and the slope is of  $303 \pm 6 m\Omega/K$ . d) Schematic representation of the measurement device used to detect spin pumping (top view). e) Signal obtained in the in-plane parallel configuration for various sweeping rates, normalized by the squared rf magnetic field  $h_r f^2$  f) Similar measurement in the in-plane antiparallel configuration.

swept as fast as possible from 20 mT below the resonance to the resonance field  $H_{res}$  at a fixed rf power of 100mW. The sweeping rate in this experiments was limited to 1mT/s to avoid a large overshoot of the field when stopping at the resonance field, and thus to allow a fast stabilization of the field, comparable to our time resolution. In a first step, a 5 mA current is applied in the sample, so that the signal variations correspond mostly to resistance variations. The resulting voltage due to Ohm's Law is of  $5\mu V/m\Omega$  using a current of 5mA while the total spin pumping signal is of around  $10\mu V$  at a power of 100mW. The results, shown in figure 3.7, exhibits a resistance increase when reaching the resonance field. The time constant of the temperature increase is of around 10 seconds. In a second step, the same experiment is performed in the open circuit conditions commonly used for spin pumping experiments. In that case, the maximal signal is obtained immediately after reaching the resonance field. This implies that the signal measured in open circuit conditions is not linked to the slow temperature increase at resonance but to the fast dynamical spin injection mechanism. We would like to note that due to the time needed to sweep the field from out of resonance to resonance the rise of the signal in open circuit is not abrupt, but it is constant after reaching the resonance field.

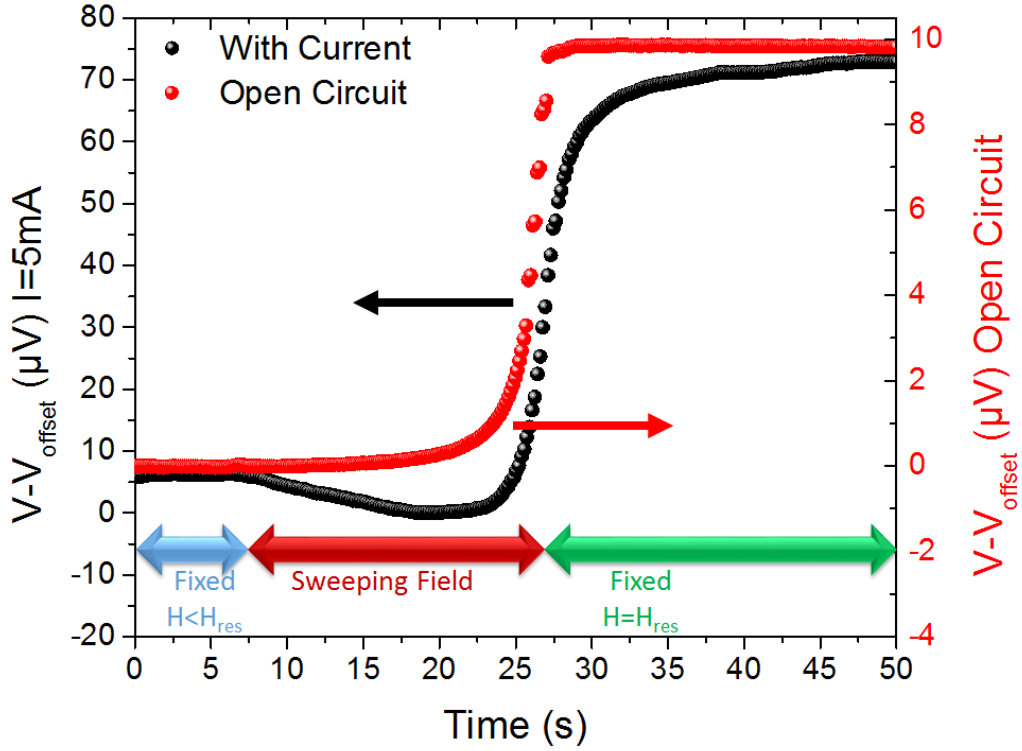


FIG. 3.7: Change in the measured output voltage as a function of time during the sweeping of the field from out of resonance to resonance in the  $\text{SiO}_2 \backslash \backslash \text{Pt}(10) \backslash \text{Py}(20)$  sample for parallel to the plane configuration, for an input current of 5mA (in black) and in open circuit conditions (in red).

We also performed the spin pumping experiment in the parallel and antiparallel configurations in both samples but with a current of 1 mA. This experiment allows to observe both the spin pumping signal and the temperature increase due to power absorption. Using a current of 1mA allows to obtain the sum of spin pumping signal and bolometric effects of comparable intensities. Due to the increase of resistance related to the bolometric effect in  $\text{Pt} \backslash \text{Py}$  and  $\text{LSMO} \backslash \text{Pt}$  the bolometric signal is positive and doesn't change with measurement configuration of the sample and stacking order, contrary to the spin pumping signal that is reversed in both cases. Therefore due to the different stacking orders the absolute value of the signal would increase (decrease) in  $\text{Pt} \backslash \text{Py}$  ( $\text{LSMO} \backslash \text{Pt}$ ) in the parallel direction and decrease in the antiparallel direction for different sweeping rates. This is exactly what is experimentally observed. Note that the signal has been normalized by  $h_{rf}^2$  as different rf field intensity will modify the temperature increase and spin pumping signal. The spin pumping signal measured in open circuit multiplied by 1000 appears to take into account the equivalent resistance change. Interestingly for spin pumping signals opposite to the bolometric signal the obtained signal is asymmetric as observed in figure 3.8.b and 3.8.c while both the bolometric signal and the spin pumping signal are symmetric. This shows that the bolometric lineshape is different from the one of spin pumping signal, due to a delay in the bolometric response with longer timescale it is likely to have a different maximum position. This shows that the maximum of temperature might not be reached exactly at resonance if the sweeping rate is too fast.



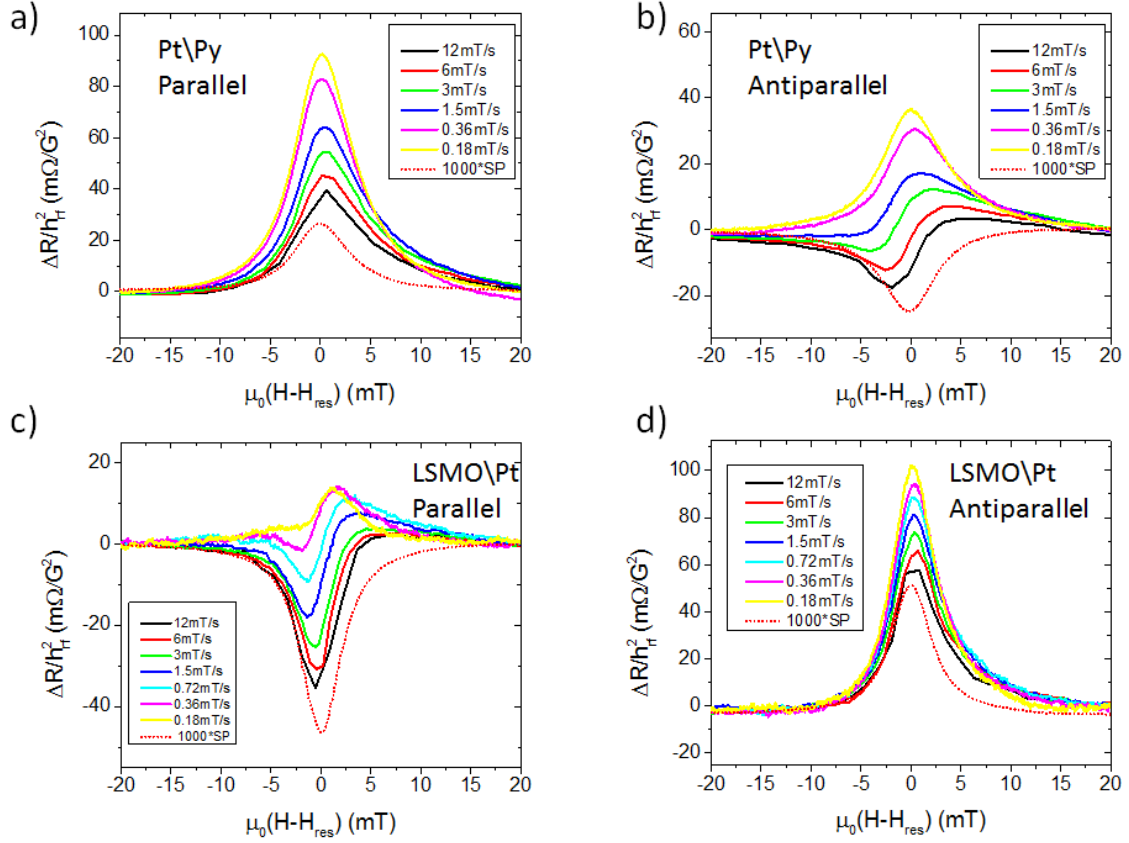


FIG. 3.8: Change of resistance and spin pumping signals for a sweeping field around the resonance field for various sweeping rates in  $SiO_2/Pt(10)/Py(20)$  in a) the parallel and b) the antiparallel configurations and in  $LSAT/La_{0.7}Sr_{0.3}MnO_3(13.8)/Pt(8.2)$  in c) parallel and d) antiparallel configuration with a current of 1mA. In all cases the signal is the sum of a constant spin pumping signal and of a signal varying with time due to the temperature increase.

We observed in SP- FMR experiments in cavity that the temperature increase at resonance is limited to a few hundreds of mK, even at a large rf power of 100 mW, and is further reduced to dozens of mK for our regular field sweeping rate around the resonance. Moreover, regarding the angular dependencies and the absence of link between the detected signal and the temperature increase at resonance, we can conclude that the SSE and ANE are absent in the signals for both  $SiO_2/Pt(10)/Py(20)$  and  $LSAT/La_{0.7}Sr_{0.3}MnO_3(13.8)/Pt(8.2)$  multilayers, and that only the dynamical spin injection described in chapter 2 is involved. The method presented here can be generalized to any multilayer and effect due to thermal gradients in spin pumping experiments. In particular, this method might be very interesting because of the growing interest in Rashba interfaces and topological insulators in spinorbitronics. Indeed, these two groups gather a large number of materials with very high thermoelectric figures of merit<sup>209</sup> such as Bi,  $Bi_2Se_3$ ,  $Bi_2Te_3$  which could possibly give rise to non-negligible thermal signals, unrelated to spin to charge conversion. It might also be useful to evaluate the contribution of the Unidirectional Spin Wave Propagation Induced Seebeck Effect in spin pumping experiments using thick YIG<sup>210</sup>.

We have also observed an heating effect that is occurring when increasing the power entering the

cavity even out of resonance. This increase in temperature is unambiguously associated to the offset signal as seen in appendix B. Moreover in certain specific conditions at large enough power the increase in temperature out of resonance can affect the spin pumping signal at resonance especially in samples sensitive to temperature changes as explained in appendix C.

### 3.3 Spin Hall Effect in Au based alloys

As mentioned previously not only heavy metals as Pt, Ta or W are interesting to obtain large conversion efficiency but also alloys. With intrinsic mechanisms in pure metals the spin Hall angle is typically proportional to the resistivity of the heavy metal. Extrinsic SHE mechanisms associated with the spin dependent scattering on impurities or defects are an alternative to generate transverse spin currents as described by Levy and Fert<sup>88</sup>. Two particular scattering mechanisms have been identified, as mentioned in the first chapter: the skew scattering providing a nondiagonal term of the resistivity tensor proportional to the longitudinal resistivity  $\rho_{xy} \propto \rho_{xx}$ <sup>85</sup> and the side jump for which the nondiagonal term is proportional to the square of the resistivity  $\rho_{xy} \propto \rho_{xx}^2$ <sup>86</sup>. Let's remind the definition of the spin Hall angle  $\theta_{SHE}$  given in chapter 1: it is the ratio of the nondiagonal ( $\rho_{xy}$ ) and diagonal ( $\rho_{xx}$ ) terms of the resistivity tensor. The spin Hall angle can therefore be written as follows:

$$\theta_{SHE} = \frac{\rho_{xy}}{\rho_{xx}} \quad (3.2)$$

The side-jump scattering would therefore offer larger conversion efficiency at lower resistivities as explained in the first chapter. In recent years a wide variety of alloys with large spin hall angle as CuBi<sup>64</sup>, CuIr<sup>87</sup>, AuPt<sup>81</sup>, CuPt<sup>211</sup> were studied. Amongst these materials the large spin hall angle was associated either with skew scattering or intrinsic mechanism. None of them shows evidence of side jump contribution to the SHE.

In this section we will present results of ISHE on Au-based alloys AuW and AuTa and compare spin hall angle and spin diffusion length as a function of concentration of W and Ta in the diluted alloys. The results presented here shows a large side jump contribution in AuTa with a spin Hall angle up to 50% for a resistivity of only  $85\mu\Omega.cm$ . Only an intrinsic contribution was identified in AuW. This work also include comparison with lateral spin valve (LSV) measurements. These measurements on LSV were performed by Piotr Laczkowski and the spin-pumping FMR measurements on AuTa and AuW were performed by Yu Fu, Carlos Rojas Sanchez and I. These results were published in Physical Review B rapid communication, publication is entitled "Large enhancement of the spin Hall effect in Au by side-jump scattering on Ta impurities"<sup>90</sup>. I will mostly present this manuscript in the following but also focus on some results on the determination of  $\lambda_s$  in low resistivity AuW alloys.

#### 3.3.1 Sample fabrication

The alloys were fabricated by DC magnetron sputtering by codeposition of the two pure materials. The concentrations in atomic percent were determined by chemical analyses (proton or electron induced x-ray emission) and from the deposition rate of each species. We control the alloying through the increase of the resistivity as the concentration is increased. We found an almost linear relationship



as seen in figure 3.9, for both AuW and AuTa alloys, as expected for diluted alloys<sup>91</sup>. We note that care has to be taken with heat treatment to avoid eventual clustering of the impurities, which can be detected through the eventual drop of the nominal resistivity.

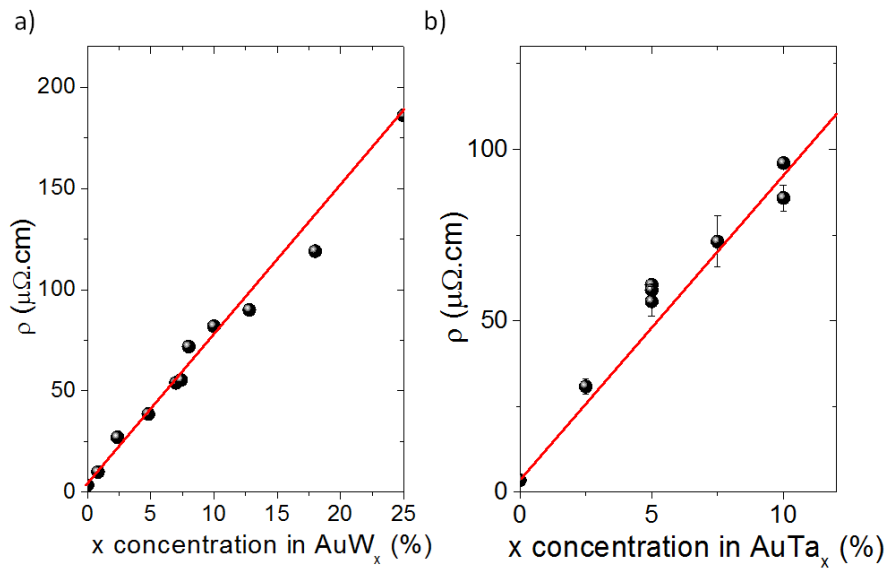


FIG. 3.9: Resistivity of a) AuW and b) AuTa as a function of the concentration  $x$  of W and Ta in Au.

### 3.3.2 Methods

Experimentally, the spin Hall angle has been characterized by the inverse spin Hall effect (ISHE) using both lateral spin valves with inserted SHE materials and spin-pumping ferromagnetic-resonance experiments (SP-FMR). For both types of experiments we follow exactly the same experimental protocols described in previous work of Piotr Laczowski *et al.*<sup>60</sup> and in the previous chapters of this manuscript for the spin pumping. Figure 3.10.a displays a scanning electron microscopy (SEM) image of a typical lateral spin valve used in the experiments. A schematic representation of the nonlocal probe configuration is represented in the insets of figure 3.10.b and c. Nonlocal spin signals recorded for the reference LSV without AuW (blue) and the LSV with spin absorption by the inserted AuW (red) are displayed in figure 3.10.b. These are the typical measurements which are used for spin sink experiments and allowing the extraction of the spin diffusion length in the SHE material<sup>212</sup>. Figure 3.10.c represents the angular variation of the inverse spin Hall effect voltage signal as a function of the external magnetic field for a typical device (the voltage is measured between both sides of the inserted AuW nanowire). With these measurements one has access to the spin diffusion length of a given AuW alloy and its spin Hall angle. The accuracy of SHE measurements with LSVs is, however, limited by current shunting effects<sup>87</sup> for alloys of large resistivity, typically for  $\rho > 100\mu\Omega cm$ . We also performed measurements of ISHE by SP-FMR at room temperature on  $SiO_2/Py/AuX$  bilayers ( $X = W$  or Ta) using the same method and geometry as the one described in chapter 2 that we will shortly summarize here.

At the ferromagnetic resonance, a pure DC spin current  $J_s$  is injected into the Au-based alloy layer along the  $z$  direction with the spin polarization along the  $x$  direction as shown in figure 3.11.b. Due

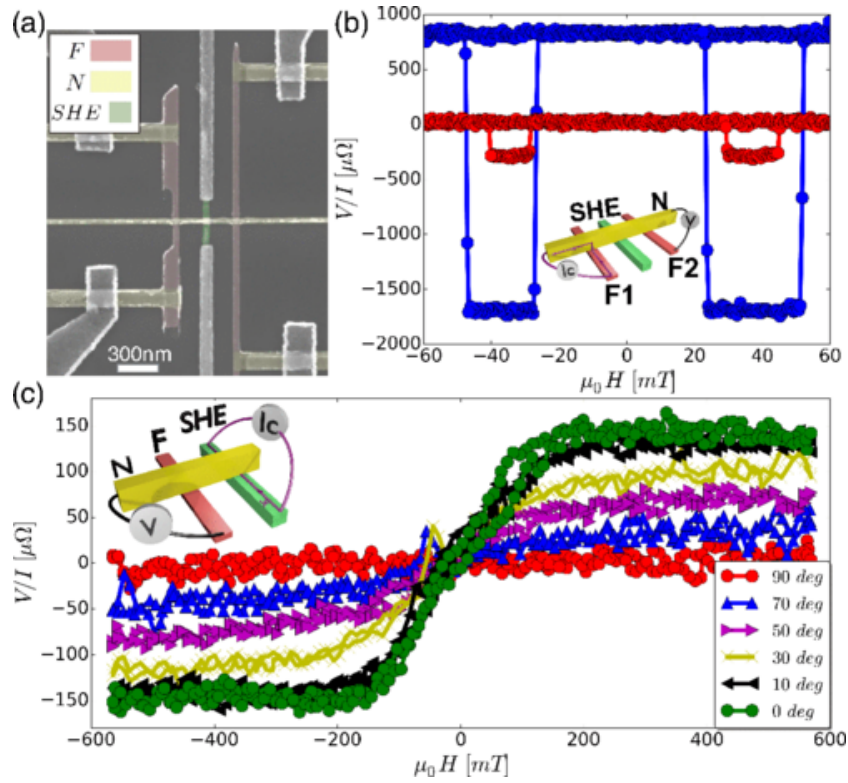


FIG. 3.10: *a)* SEM image of a nonlocal lateral spin valve structure with inserted AuW nanowire. *b)* Typical nonlocal spin signals in experiments of spin absorption by the SHE material (AuW): reference device without AuW (blue) and device with AuW (red). *c)* Field dependence of the signal induced by inverse spin Hall effect at different orientations of the field. The insets in *b)* and *c)* display the respective nonlocal probe configurations.

to the ISHE in Au-based alloy this spin current is then converted into a transversal dc charge current along the y direction, or into a transverse dc voltage in an open circuit measurement. The amplitude of the rf magnetic field was determined by the measurement of the cavity Q factor with the sample placed inside. The derivative of the FMR absorption spectrum is measured at the same time as the voltage taken across the long extremity of the sample as observed in figure 3.11.a. From the stacking order and sign of the signal we can confirm the positive sign of the SHA. We have also carried out a frequency dependence (3 to 24 GHz) of the FMR spectrum in order to determine the effective saturation magnetization  $M_{seff} = 760 \pm 30 \text{ kA/m}$  as well as the damping constant  $\alpha_{NiFe} = 0.0069 \pm 0.0001$ . Here NiFe is 15nm thick and has a damping slightly higher than the 20nm thick NiFe described previously with damping of 0.00636 as usually observed when thickness of the ferromagnetic layer is reduced<sup>213</sup>. This allows us to estimate the effective spin mixing conductance  $g_{eff}$  (of  $6 \pm 1 \text{ nm}^2$  and  $4.5 \pm 0.5 \text{ nm}^2$  for AuW and AuTa, respectively) and thus the spin-current density  $j_s$  injected by SP-FMR.

### 3.3.3 Spin diffusion length and spin Hall angle in AuW

We first focus on our results on SHE in AuW alloys. Figure 3.12.a displays the spin diffusion lengths evaluated using spin-absorption experiments following the protocol described in Laczowski *et al.*<sup>212</sup>. As expected, the spin diffusion length decreases as the resistivity of the AuW increases, changing from 13 nm at low resistivity to 1.2 nm at higher resistivities. One checks that the  $\rho \times \lambda_s$  product

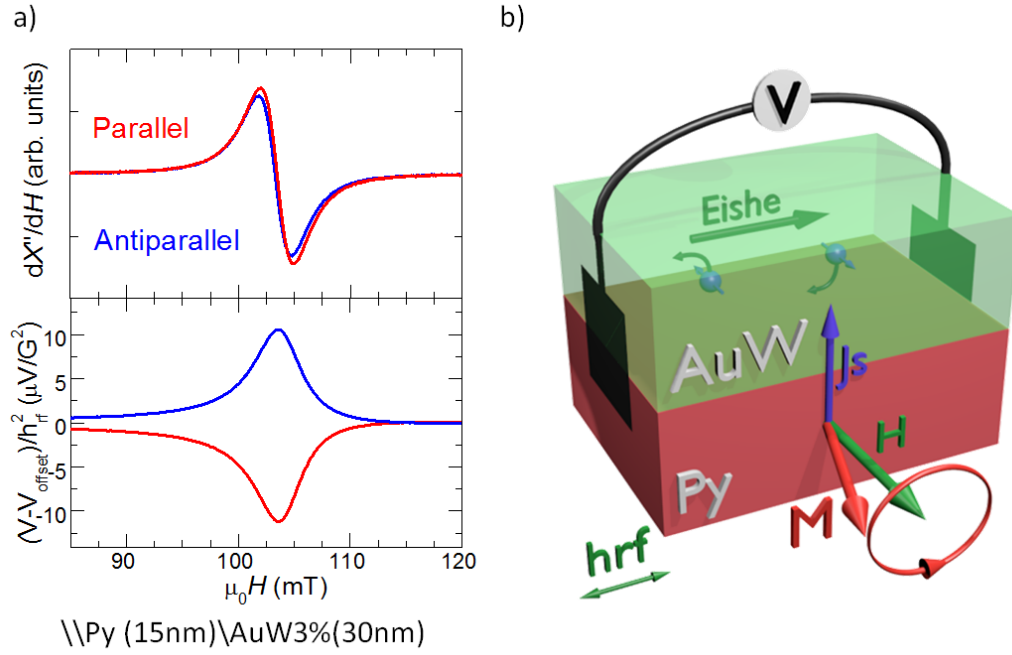


FIG. 3.11: a) Ferromagnetic resonance spectra and inverse spin Hall effect signals of  $Py(15nm)\AuW3\%(30nm)$  sample, measured in parallel and antiparallel positions and normalized by the rf magnetic field. b) Schematic representation of the experiment geometry.

remains constant in the whole explored resistivity range (see the inset of figure 3.12.a), as expected if both the spin and momentum scattering rates  $1/\tau_s$  and  $1/\tau$  increase in the same way with the impurity concentration ( $\rho \times \lambda_s \propto \tau_s/\tau$ ). We have also confirmed the spin diffusion lengths extracted from LSVs by using SP-FMR experiments. For this purpose we have studied the evolution of the measured charge current at resonance  $I_c$  as a function of AuW thicknesses. The curves correspond to a fit to the expression  $I_c = \theta_{SHE} \lambda_s \tanh(t/2\lambda_s) J_s$  (equation 2.47), where  $t$  and  $J_s$  are the thickness of the Au alloys and the injected spin-current density by spin pumping, respectively. The obtained spin diffusion lengths are in very good agreement with those from LSVs, as represented in figure 3.12.a by red squares. Figure 3.12.b summarizes the resistivity dependence of the SHA in the AuW alloys derived from LSVs (green) and SP-FMR (red).

We can see an almost linear initial increase of the SHA up to about 15% followed by a decrease when the AuW resistivity reaches  $90\mu\Omega cm$  for 13% of W. The intrinsic SHE mechanism related to the Berry curvature of the conduction band (independently of extrinsic effects from skew or side-jump scatterings) is expected to give such a linear variation, at least in the limit of small concentration of W and small changes of the bandstructure. Actually, the dashed line in figure 3.12.b represents the intrinsic SHE expected from an average on the data we got on pure gold films or have found in the review on SHE of Hoffmann for films of similar thickness<sup>214</sup>. This line (slope of  $0.1\%/ \mu\Omega.cm$ ) is close to the experimental variation at small concentration for both the data from LSVs and from spin pumping. This indicates that the intrinsic SHE is likely the predominant mechanism of SHE in AuW. The decrease and change of sign of the SHA at concentrations larger than about 13% likely due to the clustering of W in Au is consistent with a change of sign of the intrinsic SHE between a positive sign

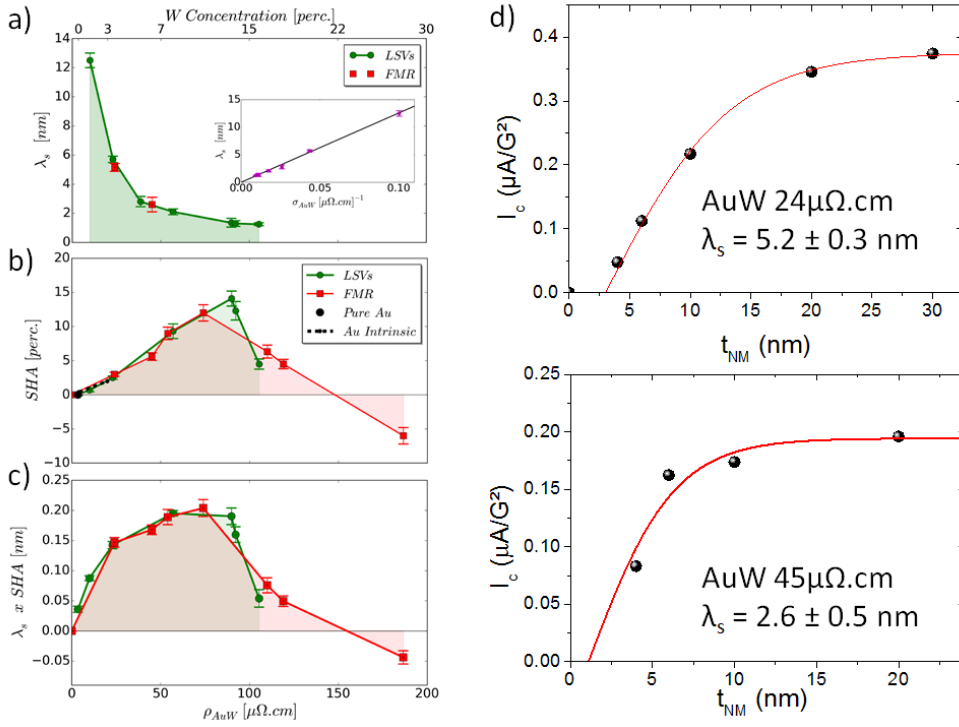


FIG. 3.12: *a)* Spin diffusion lengths extracted using spin-absorption experiments in LSVs (green) or spin-pumping voltage in FMR (red). Inset: The  $\rho \times \lambda_s$  product remains approximately constant in the whole experimental range. *b)* Dependence of the spin Hall angles derived by LSVs and SP-FMR techniques on the AuW concentration/resistivity. The dashed line represents the expected intrinsic contribution derived by averaging data on Au films in the 4 – 19  $\mu\Omega.cm$  resistivity range (see text). *c)* Same as in *b)* for the product of the spin Hall angle and the spin diffusion length characterizing the efficiency of the spin-charge conversion. *d)* AuW thickness dependencies of charge current production by ISHE for W concentrations of 3% and 6% normalized in units of rf field excitation, lines correspond to fits using equation 2.47.

for pure Au and a negative one for pure W. For concentrations above 13%, as the resistivity becomes too high for accurate LSV experiments, we have plotted only the SHA derived from spin pumping. The variation of the length  $\lambda^* = \theta_{SHE} \times \lambda_s$  characterizing the yield of spin to charge conversion<sup>40</sup> as described in chapter 1 is shown in figure 3.12.c. The value of this conversion efficiency figure of merit reaches at most 0.2 nm a value comparable to Pt or Ag\Bi measured using a similar setup<sup>40;61</sup>.

### 3.3.4 Spin diffusion length and spin Hall angle in AuTa

After having established that both lateral spin valves and FMR-ISHE techniques lead to the same spin Hall angles and spin diffusion lengths, we now focus on the results obtained on AuTa alloys by using only spin-pumping by ferromagnetic resonance experiments. The dependence of the charge current induced by conversion in AuTa,  $I_c$  (normalized in units of rf field excitation,  $\mu A/G^2$ ), is displayed in figure 3.13.d for several samples. One can observe the expected first increase of  $I_c$  followed by its saturation as AuTa thickness increases.  $I_c$  levels off at around 0.7 –  $-0.9 \mu A/G^2$ , which is higher than what can be found for pure Pt ( $0.6 \mu A/G^2$ )<sup>61</sup>, or Ta ( $-0.1 \mu A/G^2$ ) under similar experimental

conditions and is a signature of the very high conversion rates for AuTa. The fit of the thickness dependence using equation 2.47 allows us to extract the spin diffusion lengths of the AuTa alloys shown in figure 3.13.a up to 10% of Ta content.

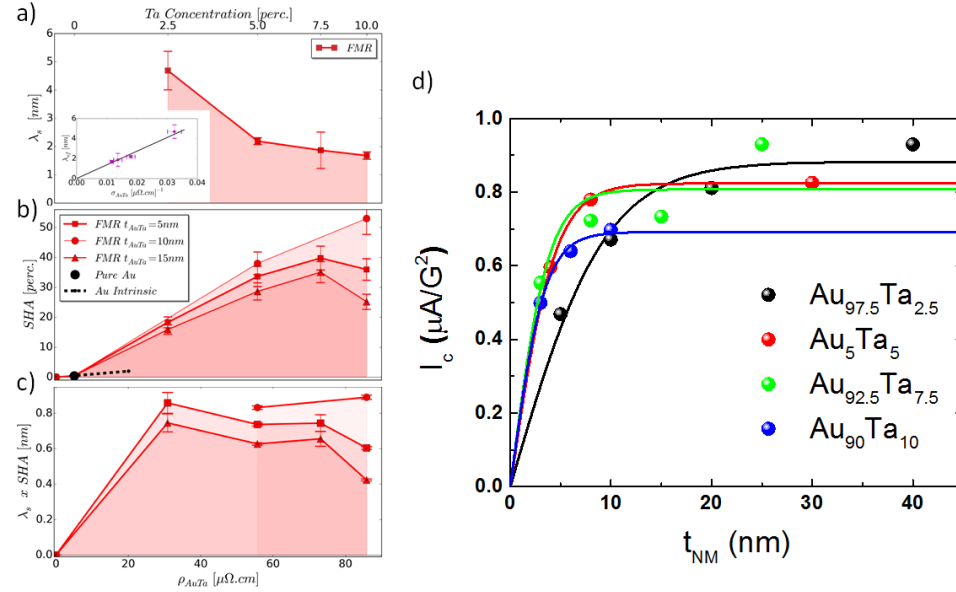


FIG. 3.13: a) Spin diffusion lengths extracted from the thickness dependence of the SP-FMR for the AuTa alloy. Inset evidences that the  $\rho \times \lambda_s$  product remains constant. b) Spin Hall angle of AuTa alloys for different thickness of AuTa as a function of the Ta concentration (or AuTa resistivity). c) Same as in (b) for the product of the spin Hall angle and the spin diffusion length characterizing the efficiency of the spin-charge conversion. d) AuTa thickness dependencies of charge current production by ISHE for Ta concentrations of 2.5%, 5%, 7.5% and 10% normalized in units of rf field excitation, lines correspond to fits using equation 2.47.

As in the AuW alloy, the  $\rho \times \lambda_s$  product in AuTa is found to be constant in this resistivity range. The SHA evaluated using equation 2.47 is reported in figure 3.14.b by taking into account the injected spin-current density estimated by the FMR analysis. The SHA increases almost linearly with the Ta content (and resistivity) and reaches a value as high as 50% for concentrations in the 8% to 10% range. Moreover the  $\lambda^*$  conversion rate is at a large value of 0.8 nm as seen in figure 3.14.c. Note that as the spin memory loss is not included, the SHA values are effective ones, lower bond of the intrinsic value. As the LSV and SP-FMR technique give similar results at least for AuW, the spin memory loss (including interface transparency) is probably small in the used interfaces. As can be seen in figure 3.14.b the slope of the linear dependence of the SHA as a function of the longitudinal resistivity in AuTa is much steeper (by a factor of about 3) than the similar slope for AuW or the slope expected for the intrinsic SHE at small concentration (dashed line in figure 3.14.b).

This additional slope for Au doped with Ta can be attributed to side-jump scattering on Ta impurities that will add up to the intrinsic mechanism to increase the total conversion. The existence of a large side-jump contribution to the SHE is confirmed by calculations performed by Hongxin Yang and Mair Chsiev for alloys of 3%. They used the resonant scattering Fert-Levy model<sup>88</sup> and first-principles cal-

culations to evaluate the spin Hall effect originating from scattering contribution. For both alloys, the skew scattering is found to be negligible, the SHA being of the order of  $10^{-4}$  for 3% content. This is in line with the experiment where the intercept of the SHA slope at zero impurity content is found to be close to zero. On the contrary, for the side-jump contribution, the SHA is found to be small for W but large for Ta. Starting from the side-jump contribution calculated for a concentration of 3% and after linear extrapolation to 10% of Ta, a side-jump SHA equal to 0.33 was obtained. Adding the contribution from the intrinsic SHE estimated for Au at that resistivity, we finally obtain a SHA equal to 0.42 for 10% Ta, in good agreement with our experimental results. The saturation of the increase of SHA at concentration of Ta around 10% anticipates the change of sign of the intrinsic term between Au and Ta. Note also that this concentration is close to the solubility limit for Ta in Au.

To conclude this section we have made measurements of the spin Hall effect (SHE) in AuW and AuTa alloys for a large range of W or Ta concentrations by combining experiments on lateral spin valves and ferromagnetic-resonance/spin-pumping techniques. The main result is the identification of a large enhancement of the spin Hall angle (SHA) by the side-jump mechanism on Ta impurities, with a SHA as high as 50% for about 10% of Ta. The SHA in AuW does not exceed 15% and can be explained by intrinsic SHE of the alloy without significant extrinsic contribution from skew or side-jump scattering by W impurities. The AuTa alloys, as they combine a very large SHA with a moderate resistivity (smaller than  $85\mu\Omega.cm$ ), are promising for spintronic devices exploiting the SHE. These conversion efficiency for a bulk system are particularly high and close to results on AuPt or PtPd obtained at Cornell University [81;215](#).

Finally in this chapter we presented a wide variety of systems containing heavy metals including pure metals and alloys. We showed that spin pumping FMR allows determining accurately the sign of the spin hall effect with a positive sign for Pt and a negative sign for Ta or W, and was free of thermal effects at resonance in the case of  $FM/Pt$  system. Using the spin pumping FMR method we measured both spin diffusion length and spin hall angle of AuW and AuTa, and demonstrated that AuTa alloys has a large spin hall angle with a dominant side jump contribution. To further improve these conversion efficiency as shown in Chapter 1 we might also use Rashba interfaces or topological insulators, the two next chapters focus on the study of these class of materials and more particularly on STO based 2DEG,  $Sb_2Te_3$  and HgTe.



## Rashba Edelstein effect at oxide heterointerfaces

Since the first measurements of the Inverse Edelstein Effect (or spin galvanic effect) in a semiconductor<sup>94;95</sup> the Rashba spin splitting was known to be a key parameter to obtain a large conversion efficiency. The knowledge of the exact bandstructure of the studied material and the amplitude of the spin splitting is thus needed to better understand this phenomenon and possibly to increase or to tune this conversion. Since the report of a conversion efficiency comparable to that of Pt in Ag/Bi interfaces at room temperature<sup>40</sup>, and in a wide variety of interfaces such as Cu/Bi<sup>41</sup>, Ag/Sb<sup>216</sup>,  $Bi_2O_3$ /Cu<sup>217</sup>, the Rashba interfaces have attracted a growing interest in the field of spinorbitronics.

Among these systems, the all oxide two dimensional electron gas (2DEG) obtained at the surface of  $SrTiO_3$  (STO) have shown record high conversion efficiencies and gate tunability<sup>66</sup>. This result was further confirmed by several groups<sup>218;219;220;221</sup>. Nonetheless the exact link between the bandstructure of STO and the high conversion efficiency is still only qualitative. In the following we will present how to obtain a 2DEG on STO, why this system is appealing for spintronics and connect the large conversion efficiency obtained to the STO specific bandstructure. We will also present some recent results on ferroelectricity induced in STO at large electric field and how it could be used to modulate permanently the resistance and spin properties of the 2DEG.

### 4.1 A two dimensional electron gas at the surface of STO

STO is a large bandgap insulator ( $E_{gap} = 3.2eV$ ), and when doped with Nd, Nb or with a high level of oxygen vacancies it becomes a conductive material<sup>222;223</sup>. STO is also particularly well known for its unique dielectric properties, with a dielectric constant of around 300 at room temperature and above 10000 at 4K, accompanied by low dielectric losses<sup>224</sup>. That makes it an extremely useful substrate for back-gating applications for example in graphene and topological insulators-based devices<sup>225;226</sup>. Moreover it also has a nearly perfect lattice matching with a large variety of perovskites and antiperovskites including ferroelectric materials such as  $BaTiO_3$ <sup>227</sup>, ferromagnetic materials such as  $Mn_4N$ <sup>228;229</sup> or  $LSMO$ <sup>230</sup> or high Tc superconductors  $YBaCuO$ <sup>231</sup>.

In recent years another property of STO has yielded a growing interest: the possibility to obtain a two dimensional electron gas (2DEG) at its surface. After a short description of previous results on STO/LAO we will present spin to charge current conversion results in STO/Al. These results are summarized in “Mapping spin-charge conversion to the band structure in a topological oxide two-dimensional electron gas“ and are published in Nature Materials<sup>232</sup>. My coauthors Diogo Vaz grew the samples and performed the XPS measurements, Annika Joansson and Börge Göbel performed the bandstructure and Edelstein tensor calculation. This section can be considered as an extended version of this publication.



### 4.1.1 A 2DEG with appealing properties for spintronics

The first observation of a high mobility two dimensional electron gas at the surface of  $SrTiO_3$  was reported by A. Ohtomo and H. Y. Hwang in 2004<sup>233</sup>. By growing a  $LaAlO_3$  (LAO) layer by pulsed laser deposition (PLD) on a  $TiO_2$  terminated STO they showed that an electron gas was obtained with a mobility as high as  $10000\text{ cm}^2/V.s$  and a high carrier density of some  $10^{13}\text{ cm}^{-2}$  at 4K. The conductivity appears only when the LAO layer was thicker than four unit cells, evidencing an unusual formation mechanism of the 2DEG<sup>234</sup>. Later on similar 2DEGs were obtained with a large variety of interfaces with  $TiO_2$  terminated STO such as  $SrTiO_3\backslash Al_2O_3$ ,  $SrTiO_3\backslash LaTiO_3$ ,  $SrTiO_3\backslash LaVO_3$  etc<sup>235;236;237</sup>. The most studied one remains the STO \LAO interface. This 2DEG is interesting because it is obtained at the interface between two insulating oxides and also due to its numerous properties. This includes superconductivity<sup>238</sup>, magnetism<sup>239</sup>, or quantum transport properties<sup>240;241</sup>. Moreover thanks to the high dielectric constant of STO all these properties can be easily modulated by a back gate voltage at cryogenic temperature<sup>242;243</sup>.

Among these various properties one is particularly appealing for spintronics. Due to inversion symmetry breaking and strong electric field at the interface, a quite large Rashba parameters was extracted by magnetotransport experiments despite a low spin orbit interaction in STO itself. Moreover the magnitude of the Rashba constant can be modulated by a back-gate as can be seen in figure 4.1.a (extracted from Caviglia *et al.*<sup>244</sup>). This property is particularly appealing for the manipulation of the electron spin. Moreover Reyren *et al.* showed that it is possible to perform the spin injection from a ferromagnetic material towards the 2DEG through the LAO layer and to tune it with a backgate voltage leading to possible “Datta-and-Das transistor like“ applications<sup>245</sup>. A large Rashba constant with possible gate modulation paves the way towards efficient and tunable spin-charge interconversion.

An efficient spin to charge current conversion in STO \LAO \NiFe structure was demonstrated in our group by means of spin pumping FMR at 7K, see E. Lesne *et al.*<sup>66</sup>. In figure 4.1.b one can see the gate modulation of the inverse Edelstein length at 7K with a record high inverse Edelstein length value of -6.4 nm. This is quite unexpected due to the moderate effective Rashba SOC in STO compared for example to Ag\Bi (with an inverse Edelstein length of 0.3 nm). Due to the multi-orbital nature of the 2DEG at specific points in the bandstructure the Rashba parameter is enhanced (in the range of  $10^{-12}\text{ eV.m}$ ) especially at the vicinity of the so-called Lifshitz transition. A Lifshitz transition is a change in the topology of a Fermi surface, in the case of STO it corresponds to the transition from a single occupied  $d_{xy}$  band at low electron density to multiple occupied bands with different orbital nature at high density<sup>246</sup>. Moreover a long electron scattering time of 1 ps in the 2DEG, three orders of magnitude larger than in Ag\Bi, and the avoided relaxation channel by a direct contact with a metal, allows to obtain larger spin to charge current conversion efficiencies<sup>117</sup>.

A high conversion efficiency was measured by several other groups at cryogenic temperature in STO \LAO. For example Chauleau *et al.* obtained an inverse Edelstein length up to 2nm at 77K<sup>219</sup> and Ohya *et al.* obtained an inverse Edelstein length of +4nm at 20K<sup>221</sup>. Both groups observed an efficient conversion only at cryogenic temperature and smaller conversion efficiencies at room tempera-

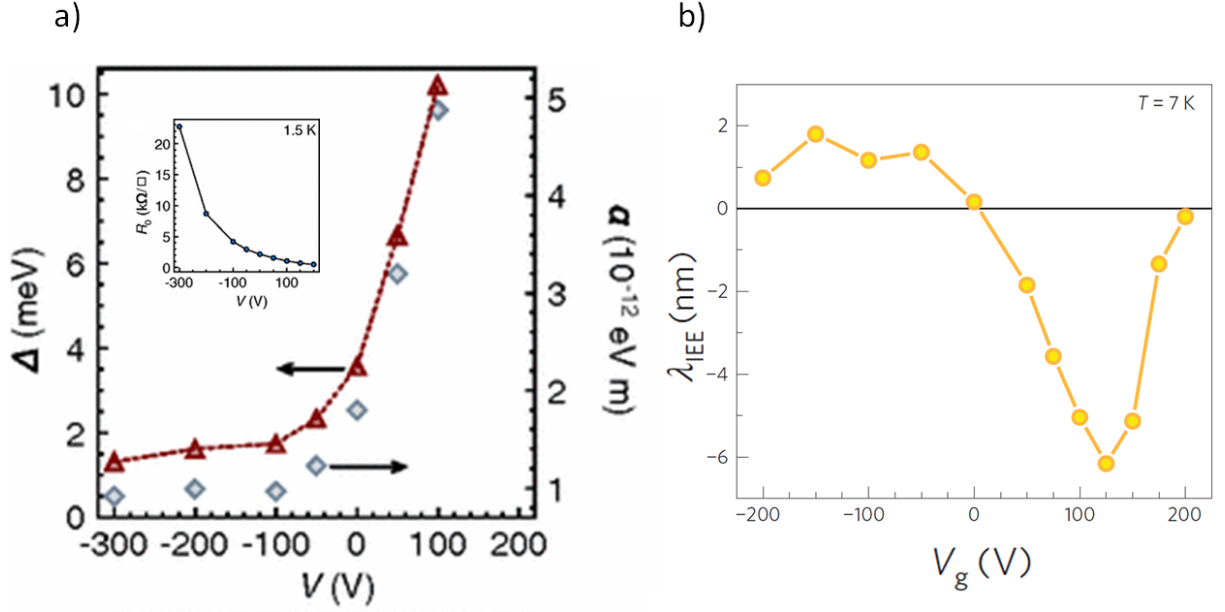


FIG. 4.1: Gate control of the Rashba Spin splitting in the STO/LAO interface a) Left axis, red triangles: field effect modulation of the Rashba spin splitting  $\Delta$ . Right axis, gray diamonds: field effect modulation of the Rashba coupling constant  $\alpha$ . The inset shows the field effect modulation of the 2DEG sheet resistance. This figure is from Caviglia *et al.*<sup>244</sup>. b) Gate dependence of the inverse Edelstein length in STO/LAO (2uc)/NiFe at 7K. This figure is from Lesne *et al.*<sup>66</sup>.

ture. Results of Q. Song *et al.*<sup>218</sup> and Y. Wang *et al.*<sup>220</sup> also showed an efficient conversion but with a strong decrease of the conversion at cryogenic temperature that they associated with a decrease in the spin transmission across the LAO barrier. In general STO based 2DEGs are recognized as a promising system for spintronics. However, a detailed understanding of the system is still lacking, this is especially the case for the link with the  $SrTiO_3$  bandstructure. In the following we will present an alternative method to obtain a 2DEG on STO, and show how it is possible to map the spin to charge current conversion to the bandstructure.

#### 4.1.2 STO/Al: no need of LAO

As mentioned above a 2DEG at the interface between  $SrTiO_3$  (STO) and another insulator,  $LaAlO_3$  (LAO), was first discovered by Ohtomo and Hwang in 2004. Two main mechanisms can give rise to such a 2DEG, the presence of oxygen vacancies in STO or the polar gating (sometimes called “polar catastrophe”). The polar gating postulates that due to the build-up of an internal electrical potential in polar LAO above a critical thickness, electrons accumulate in the surface of the STO<sup>234</sup>. While the exact mechanisms for the 2DEG formation remain debated, it is universally found that a thickness of at least four unit cells of crystalline LAO on a  $TiO_2$  terminated surface of STO is needed for the 2DEG to appear. Nonetheless when oxygen pressure during deposition is reduced/increased the properties of the 2DEG are modified, evidencing the role of oxygen vacancies<sup>247</sup>. As demonstrated by D.C Vaz *et al.*<sup>248;249</sup> and E. Lesne *et al.*<sup>250</sup> the critical thickness of 4 unit cells of LAO can be tuned by changing the capping layer. For metals with a low work-function such as Cobalt or Permalloy the critical thickness can be reduced to 1 to 2 unit cells. On the contrary for noble metals such as Pt or

Au it is increased to 8 unit cells<sup>248</sup>. This phenomenon was associated with the reduction of the STO surface as probed by XPS.

Very recently Rödel *et al.*<sup>251</sup> reported that a 2DEG could also be formed on STO through the deposition of a few Å of Al at room temperature thanks to Al oxidation and STO reduction, which leads to the formation of oxygen vacancies. This approach has several advantages as it alleviates the need for the high temperature growth of crystalline LAO and allows the modulation of the carrier density over a broader range, through the adjustment of the Al thickness or the use of other metals. Following Rödel *et al.* Diogo Vaz prepared STO 2DEGs by depositing an ultra-thin layer of Al (nominal thickness 9 Å) on  $TiO_2$ -terminated STO substrates using magnetron sputtering. For further measurements including transmission electron microscopy (STEM), magnetotransport and spin-pumping experiments, samples with an additional NiFe layer and an AlOx cap (3 nm in thickness) were also grown in the same deposition chamber. The NiFe thickness was 2.5 nm for transport measurements and 20 nm for STEM and spin-pumping experiments.

To evaluate the interaction between Al and the first few layers of STO, in situ X-ray photoelectron spectroscopy (XPS) experiments were performed focusing on the Ti 2p and Al 2p states (figure 4.2.a). The spectrum collected for a bare STO substrate (grey area) corresponds to a  $Ti^{4+}$  valence state, consistent with its insulating character. Upon deposition of the ultrathin Al layer, two peaks associated with  $Ti^{3+}$  and  $Ti^{2+}$  valence states arise, pointing to the reduction of the STO and the generation of an electron-rich layer at its interface with Al. The spectral weight of these peaks is larger than normally observed in STO/LAO heterostructures, indicating a higher electron density. In the inset, we see that the Al 2p signal comprises two spectral features, corresponding to oxidized and metallic Al (high and low binding energies, respectively) and suggesting that the Al is largely oxidized. As previously reported, we conclude that Al is able to react with the surface oxygen and thus induces oxygen vacancies acting as electron donors in the first few layers of STO. We will now refer to these samples as STO/AlOx.

The interface was also characterized by cross sectional Scanning Transmission Electron Microscopy (STEM) analysis by Hanako Okuno. As seen in the Z-contrast in high-angle annular dark field (HAADF) images of figures 4.2.d and 4.2.e, a continuous Al-rich layer can be identified, between the  $TiO_2$ -terminated STO surface and the NiFe layer, with a uniform thickness over all observed areas in the STEM specimen. The AlOx thickness estimated using HAADF Z contrast is  $1.0 \pm 0.1$  nm, consistent with the deposition of 0.9 nm of metallic aluminium and its volume expansion upon oxidation. Sr, Ti, Al and O elemental chemical maps have been acquired using Electron dispersive X-ray spectroscopy (EDX) as seen in figure 4.2.g, and show that oxygen is present in STO but also extends through the Al layer. A tiny amount of Ti also appears to be present in the Al-rich region.

Overall, the STEM analysis corroborates the XPS data and clearly evidences that the Al layer is oxidized at the STO interface. To estimate the spatial distribution of the  $Ti^{3+}$ -rich layer, we performed angle-dependent XPS experiments (cf. figure 4.2.b) and electron energy loss spectroscopy (EELS) at the Ti  $L_{3,2}$  edge (cf. figure 4.2.c). In figure 4.2.b, we plot the ratio between the weights of the  $Ti^{3+}$

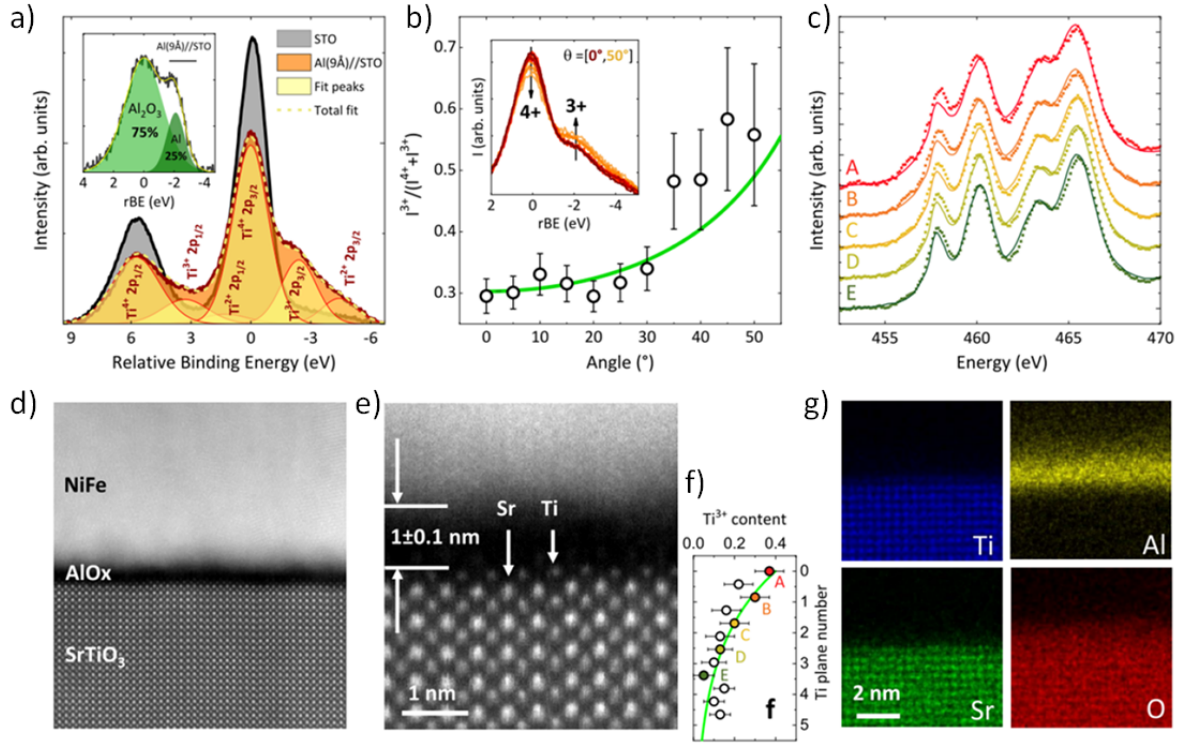


FIG. 4.2: Characterization of the STO/AlOx 2DEGs. a) X-ray photoelectron spectra near the Ti 2p state for a STO single crystal before (black) and after (red) deposition of 9 Å of Al. Inset: spectrum at the Al 2p state after deposition of 9 Å of Al on STO; rBE stands for relative binding energy. b)  $Ti^{3+}$  fraction for different take-off angles. The error bars come from the fitting process using CasaXPS. The experimental spectra are shown in the inset. The green line is a fit using the model of reference<sup>252</sup>. c) EELS spectra at positions indicated in f) in SrTiO<sub>3</sub> (dotted) with simulations (lines) using linear combinations of  $Ti^{3+}$  and  $Ti^{4+}$  spectra corrected for instrumental resolution. d) Scanning transmission electron microscopy image. e) Magnified view of d). f) Variation of the  $Ti^{3+}$  content deduced from simulations shown in c) as a function of position in SrTiO<sub>3</sub>. The green line is an exponential fit. g) EDX maps.

and  $Ti^{4+}$  peaks, that increases exponentially with the XPS electron take-off angle, indicating a larger concentration of  $Ti^{3+}$  closer to the interface. The data are well fitted using a depth-profile model, previously used to estimate the thickness of 2DEG in STO/LAO samples<sup>252</sup>. We extracted a total electron density of  $7.2 \pm 1.0 \times 10^{14} \text{ cm}^{-2}$  and a thickness of  $1.4 \pm 0.4 \text{ nm}$ , confirming the quasi 2D nature of the electron gas. The mixed valence of Ti in STO is also seen in the EELS data presented in figure 4.2.c, that we simulated with linear combinations of  $Ti^{3+}$  and  $Ti^{4+}$  reference signals (taking into account the experimental resolution). The extracted  $Ti^{3+}$  content is plotted in figure 4.2.f, and is found to decrease when going deeper into the STO. The total  $Ti^{3+}$  concentration corresponds to an electron density of  $6.3 \pm 1.0 \times 10^{14} \text{ cm}^{-2}$ , consistent with the XPS analysis.

### 4.1.3 STO 2DEG: a complex bandstructure

We now turn to the transport properties. The temperature dependences of the sheet resistance for a STO\AlO<sub>x</sub>\NiFe\AlO<sub>x</sub> sample and a STO\NiFe\AlO<sub>x</sub> reference sample were measured using the Van der Pauw method<sup>253</sup> and are displayed in figure 4.3.a. Without the Al insertion (brown curve), the resistance shows practically no change over the whole range of temperatures. In contrast, in the full stack (black curve) a drop in resistance is observed below 100 K, signaling an additional conduction path corresponding to the 2DEG. The red curve represents the isolated 2DEG contribution, deduced through a two-channel parallel conduction model<sup>248</sup>. By applying a back-gate voltage  $V_G$  the resistance of the 2DEG is drastically modified as seen in figure 4.3.b. Hall traces of the 2DEG were extracted from Hall measurements at  $T = 7$  K. While a non-linear Hall signal was obtained for large positive gate voltages, decreasing  $V_G$  promoted a more linear dependence, suggesting that a transition between multi-band and single band transport occurs. Fitting the Hall traces in the linear regime and using capacitance measurements we obtained the mobile carrier densities in both regimes. As visible in figure 4.3.c, the carrier density varies from about  $6 - 7 \times 10^{13} \text{ cm}^{-2}$  at  $-175$  V to  $1 \times 10^{14} \text{ cm}^{-2}$  at  $+175$  V. We note that, as often reported in STO 2DEGs, the density of mobile carriers is significantly lower than the total electron concentration inferred from core level spectroscopy<sup>252</sup>, suggesting the existence of a large fraction of localized electrons .

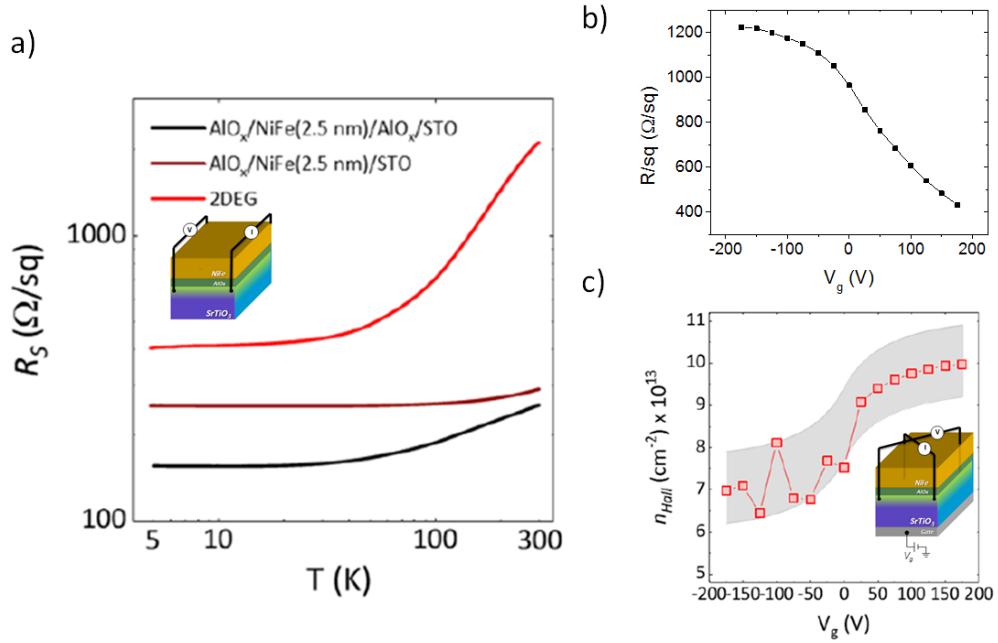


FIG. 4.3: Magnetotransport properties. a) Temperature dependence of the sheet resistance of a STO\AlO<sub>x</sub>\NiFe\AlO<sub>x</sub> sample (black) with a deposited Al thickness of 9 Å and a STO\NiFe\AlO<sub>x</sub> reference sample (brown). The extracted contribution from the 2DEG is shown in red. The inset shows an example of the measurement configuration. b) Sheet resistance of the 2DEG as a function of the back gate voltage. c) Carrier density as a function of gate voltage. The shaded area, derived from the capacitance measurement, corresponds to the uncertainty in the determination of  $n_{Hall}$ . Inset shows the contact configuration used to measure the Hall Effect in the Van der Pauw configuration.



To gain more insight into the electronic structure of STO 2DEGs, we have performed angle-resolved photoemission experiments on STO\AlOx and vacuum cleaved STO samples with integrated carrier densities in the  $10^{13} - 10^{14} \text{ cm}^{-2}$  range (this measurement was performed by the team of Felix Baumberger from University of Geneva). Figure 4.4.a displays the ARPES Fermi surface of a 2DEG stabilized at the (001) surface of STO for a sample with  $n \approx 1.5 \times 10^{14} \text{ cm}^{-2}$ . In bulk STO  $d_{xy}$ ,  $d_{yz}$ , and  $d_{zx}$  bands near the Fermi energy are hybridized due to the spin-orbit interaction. The confinement in the 2DEG leads to the creation of subbands and the emergence of an unconventional Rashba effect with a spin splitting that is enhanced in certain k-space areas due to orbital mixing<sup>254</sup>. We resolve three concentric circular contours centred at the  $\Gamma$  point and two ellipsoidal Fermi surface sheets with major axes along the  $k_x$  and  $k_y$  direction, respectively, giving four inequivalent bands in total (two heavy and two light bands), consistent with previous studies<sup>223;254;251</sup>. The ellipsoidal features have lower intensity due to the light polarization chosen for this experiment. Electronic structure dispersion plots along the high symmetry directions  $\Gamma - X$  [100] and  $\Gamma - M$  [110] are displayed in Figures 4.4.b and 4.4.c respectively. In the dispersion plot along the direction  $\Delta$ , (perpendicular to the [110]) shown in figure 4.4.d, we resolve the lowest lying sub-band that forms the outer Fermi surface sheet. In addition, we observe additional spectral weight at  $k_{\Delta} = 0$  located around 15 meV below the Fermi level.

Next, a model Hamiltonian that reproduces the ARPES measurements was derived. This work has been performed by the group of Ingrid Mertig in Halle Universität, and it was more especially the work of Annika Johansson and Börge Göbel. We take into account the two energetically lowest  $d_{xy}$  bands and one  $d_{yz}$  and  $d_{zx}$  band, respectively. Only these bands were accounted because they are the one contributing to the transport and crossing the Fermi level for typical carrier densities in STO. Accounting for the spin, this results in an eight-band effective Hamiltonian, which reproduces the measured ARPES band structure very well (figures 4.4.a-d). Figure 4.4.e shows the calculated band structure along a  $\Delta$  direction. Because of the interplay between spin orbit coupling and orbital mixing, the band structure shows a band inversion with an avoided crossing at the critical k point  $k_c$  (corresponding to  $k_{\Delta}=0$ ). This band inversion renders the 2DEG topologically non-trivial and gives rise to spin-polarized topological edge states that have been predicted by Vivek *et al.* by means of the  $Z_2$  topological invariant<sup>255</sup>. Figures 4.4.f and 4.4.g show the spin expectation value for all eight bands. The band inversion discussed in figures 4.4.d and 4.4.e leads to strong modulations of the spin expectation values near the Fermi energy. Indeed, as observed in figure 4.4.g, the spin expectation value almost vanishes in the fourth band near  $k_c$ , while it remains considerable in the third band, leading to uncompensated spin textures.

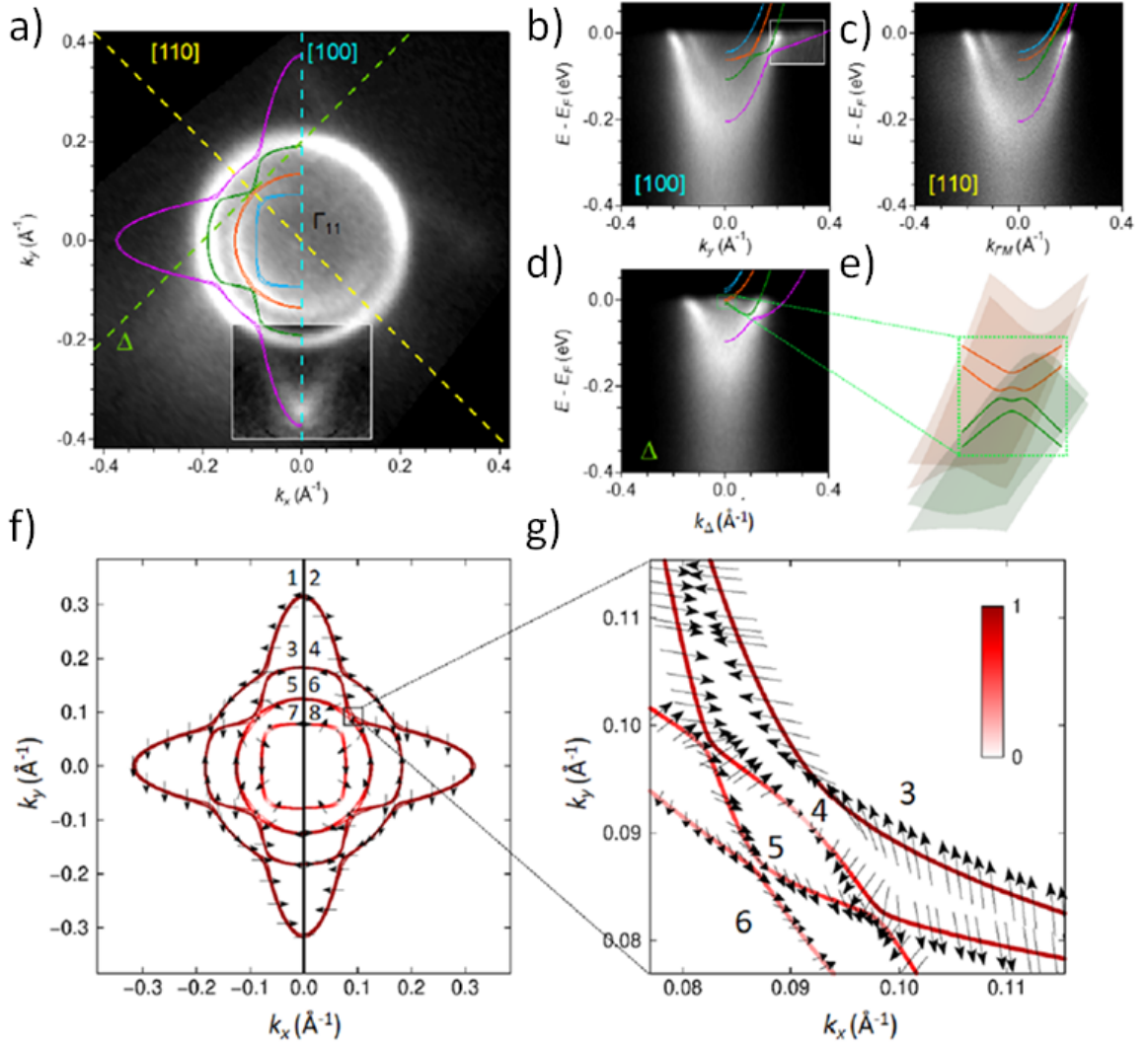


FIG. 4.4: *Electronic and spin structure of the 2DEG. a) Experimental Fermi surface of the 2DEG around the  $\Gamma$  point. (b) Band dispersion along the  $[100]$  direction –cf. cyan dashed line in a)–, with overlaid bands calculated by an eight-band tight-binding model. (c) Same along the  $[110]$  direction –cf. yellow dashed line in a)–. The insets to (a,b) use an enhanced contrast to better visualize the faint heavy bands. d) Same along the  $\Delta$  direction –cf. green dashed line in a)–. e) Calculated band structure along  $\Delta$  near  $k_c$ . f) Calculated Fermi surface and spin expectation values (direction: arrows, absolute value: color scale) at an energy near the band inversion region, where the left (right) panel corresponds to the outer (inner) band of each pair. The numbers denote the band in energetically ascending order. g) is a zoom-in of f) near  $k_c$ .*



## 4.2 Spin to charge conversion in STO\AlPy structure

To characterize the Inverse Edelstein effect (IEE) in our STO\AlOx 2DEGs, we used spin pumping ferromagnetic resonance (FMR) experiments at 15 K on a STO\AlOx (0.9 nm)\NiFe (20 nm)\AlOx sample with a nominal deposited Al thickness of 9Å. A capping layer of 3nm of Al on NiFe was also added to avoid the NiFe oxidation which could cause a strong increase in the damping at low temperature as demonstrated by Frangou *et al.*<sup>256</sup>. This could prevent any accurate measurement of the injected spin current. Figure 4.5.a depicts the layers and geometry used for spin pumping experiments. At the ferromagnetic resonance, a pure spin current is injected in the 2DEG as described in Chapter 2. In the presence of IEE, a transverse DC voltage will be generated. Figure 4.5.b shows FMR signals (top panels) at different gate voltages. The FMR resonance field and the linewidth do not vary, implying that the gate voltage does not affect the properties of the ferromagnet. The bottom panels of figure 4.5.b show the voltage signals produced at resonance, possessing two components: a symmetric one and a much smaller antisymmetric one ( $V_{sym}$  and  $V_{asym}$ , respectively). For all gate voltages shown,  $V_{sym}$  strongly dominates the signal. The out-of-plane angular dependence of the spin signal amplitude at -140V, shown in figure 4.5.c, is in agreement with the theoretical expectations for ISHE or IEE described in chapter 2 (it was also performed at -10V and +100V, confirming the IEE nature of the signal). This evidences the IEE nature of the signal. In addition, the signal was observed to be linear with the rf power, up to a maximum of at least 5 mW. The out-of-plane angular dependences of the ferromagnetic resonance peak-to-peak linewidth  $\Delta H_{pp}$  and the ferromagnetic resonance field  $H_{res}$  allow the extraction of the effective magnetization  $M_{eff} = 833 \text{ kA.m}^{-1}$ , the g-factor  $g = 2.077$  and the damping  $\alpha = 0.0066$  that are typical of a 20 nm thick NiFe film, as previously seen in chapter 2 and 3.

The value of the injected spin current  $J_s^{3D}$  can then be calculated by comparing the value of the damping  $\alpha$  with that of a reference NiFe sample (with a minimum of  $\alpha_{ref} = 0.00636 \pm 0.00003$  for Si\NiFe(20 nm) and a maximum of  $\alpha_{ref} = 0.00645 \pm 0.00002$  for LAO\NiFe (20 nm)); the spin mixing conductance was  $g^{\uparrow\downarrow} = 2.2 \pm 1 \text{ nm}^{-2}$  and  $J_s^{3D}$  is ranging from 1 to 2.4  $MA.m^{-2}.G^{-2}$  using equation 2.40.  $J_c^{2D}$  can then be extracted from the spin signal value and the sample resistivity. From the obtained value of  $J_s^{3D}$  and  $J_c^{2D}$  we calculate the inverse Edelstein length  $\lambda_{IEE}$  and plot its gate dependence in figure 4.5.d. The spin-charge conversion varies strongly in sign and amplitude, with its sign changing several times in the studied range of gate voltages. Moreover, the conversion efficiencies at maximum values are extremely high, for both positive and negative values (+28 nm, -16 nm). These efficiencies are, in absolute value, much higher than those measured in other spin-orbit systems. The conversion efficiency observed here is in particular much higher than what can be obtained in Rashba interfaces (0.3 nm in Ag/Bi<sup>40</sup>), or even in previously studied oxide-based systems (6.4 nm in STO\LAO<sup>66</sup>, and 0.6 nm in Bi2O3\Cu<sup>217</sup>).

### 4.2.1 Mapping to the bandstructure

Although the simple Rashba picture of split parabolic bands is usually used to interpret such experiments, it fails to explain the largest conversion effects and their relation to the actual electronic

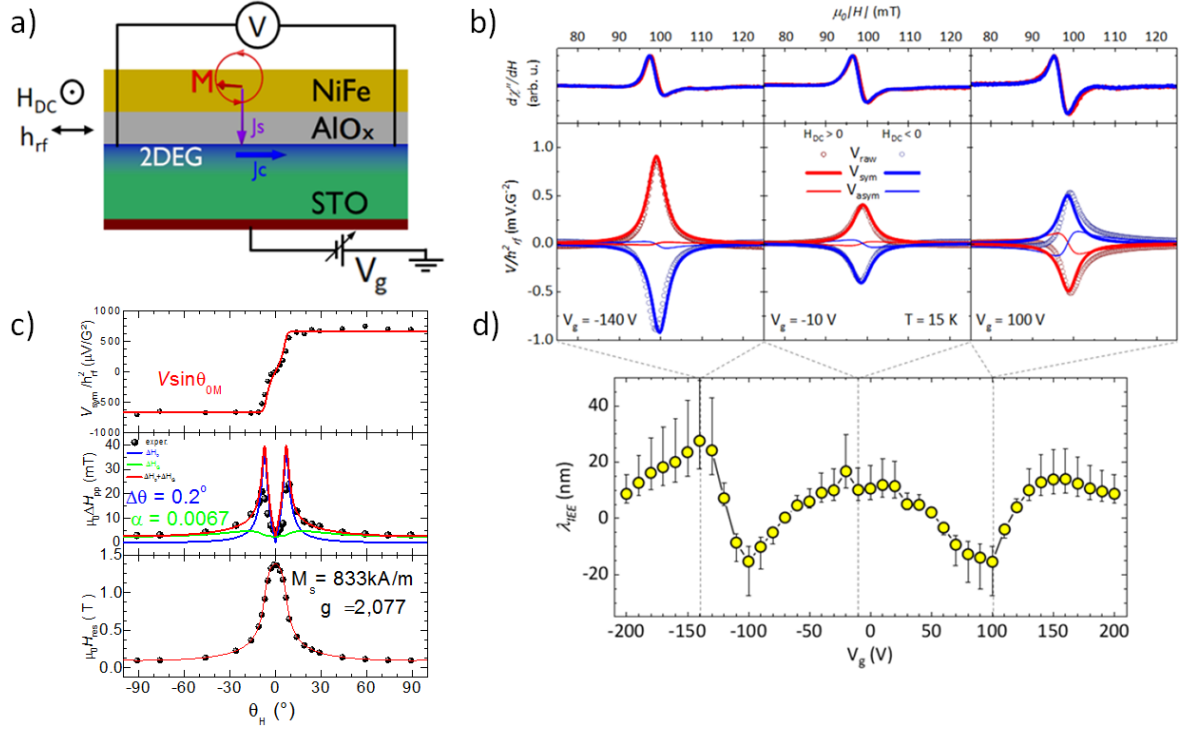


FIG. 4.5: Spin-charge conversion in STO/AlOx (0.9 nm)/NiFe (20 nm)/AlOx. a) Sketch of the spin pumping experiment. b) FMR curves (top) and spin signals (bottom) for different values of the gate voltage, for a positive (red) and negative (blue) applied DC magnetic field. The symmetric  $V_{sym}$  and antisymmetric  $V_{asym}$  components of the raw spin signals  $V_{raw}$  are represented using continuous thick and thin lines, respectively. c) Top panel: angular out-of-plane dependence of the amplitude of the symmetric component of the spin-pumping signal, normalized by the square of the applied rf field. Center panel: angular out-of-plane dependence of the ferromagnetic resonance peak-to-peak linewidth. The fit enables the separation of the contributions of the Gilbert damping ( $\Delta H_G$ ) and the magnetic inhomogeneities in the FM layer ( $\Delta H_\theta$ ), thus allowing the extraction of the damping parameter  $\alpha$ . Bottom panel: angular out-of-plane dependence of the ferromagnetic resonance field. The fit allows the extraction of the magnetization and g-factor. All the fits have been made using the model proposed in chapter 2. d) Spin-charge conversion efficiency  $\lambda_{IEE}$  as a function of gate voltage at 15 K. The error bars come from the uncertainty in the determination of the spin mixing conductance.

structure, especially in STO where the bandstructure differs strongly from the simple Rashba picture with parabolic bands<sup>254</sup>.

Let us now examine how this peculiar band structure produces spin-charge interconversion. We characterize the direct Edelstein effect efficiency by the tensor  $\hat{\kappa}$  that relates the spin  $\vec{s}$  per surface unit cell to the externally applied electric field  $\vec{E}$ :  $\vec{s} = \hat{\kappa} \vec{E}$ . It is calculated using the semi-classical Boltzmann transport theory:

$$\kappa_{ij} = \frac{-eA_0}{A} \sum_k \langle \sigma \rangle_k^i \Lambda_k^j \delta(\epsilon_k - \epsilon_F) \quad (4.1)$$

Here,  $A$  is the total area of the system,  $A_0$  is the area of the surface unit cell,  $e > 0$  is the elementary charge, and  $\langle \sigma \rangle_k$  is the spin expectation value of the state at wave vector  $\vec{k}$  and energy  $\epsilon_k$ . The sum is over all  $k$  points and all bands. The mean free path  $\Lambda_k = \tau_0 v_k$  is approached by the constant relaxation time approximation  $\tau_0 = 1$  ps consistent with the carrier mobility of the 2DEG. At zero temperature, only states at the Fermi level  $\epsilon_F$  contribute to the Edelstein effect. For the 2DEG Hamiltonian, by symmetry only non-zero tensor elements  $\kappa_{xy} = \kappa_{yx}$  are allowed. Thus, an external electric field induces an in-plane spin density perpendicular to the field, as in Rashba systems. Since the EE is the Onsager reciprocal of the inverse Edelstein effect<sup>257</sup>, the experimental data of figure 4.5.d (that we replot in Fig. 4.6.a) can be compared with the theoretical results.

In figure 4.6.b, we plot the direct Edelstein efficiency calculated from the spin expectation values for different Fermi energies (assuming a rigid band shift). At low energy, only the two low-lying  $d_{xy}$  sub-bands (1 in figure 4.6.c) are occupied and  $\kappa_{xy}$  is relatively small, consistent with the modest Rashba-like splitting of these bands. Upon increasing energy, a step occurs corresponding to the population of the next  $d_{xy}$  sub-band pair (2) followed by an extremum signaling the onset of the first heavy sub-band pair (3). Then  $\kappa_{xy}$ , decreases and changes sign, owing to the alternating sign of the spin splitting between the  $d_{xy}$  and the first pair of  $d_{zx,yz}$  bands (as discussed in Seibold *et al.*<sup>258</sup>), reaching a large negative value corresponding to the trivial avoided crossing (4), *i.e.* the first crossing between light  $d_{xy}$  and heavy  $d_{zx,yz}$  bands where orbital mixing enhances Rashba splitting. Another extremum followed by a slope change of  $\kappa_{xy}$  occurs at the band edge of the second pair of  $d_{zx,yz}$  bands, again due to opposite spin splitting compared to the fifth and sixth bands (5), as seen in the light blue curve of figure 4.6.b (top panel). Upon further increasing energy, the topological band inversion is reached (6) where the uncompensated spin texture between the third and fourth bands causes a pronounced maximum in the Edelstein signal. This large spin-charge conversion efficiency is a consequence of the topological order in the system. We point out, however, that it is not caused by topological edge states themselves, whose contributions would compensate at opposite edges of the 2DEG, but due to the uncompensated spin texture.

While the trivial avoided crossing in the [100] direction (4) unlocks only an enhanced Rashba spin splitting due to orbital mixing as previously observed by King *et al.*<sup>254</sup>, the topologically non-trivial avoided crossing in the  $\Delta$  direction adds a large contribution from the uncompensated spin texture (see both insets of figure 4.6.c), which drives the overall Edelstein effect to large values in this re-

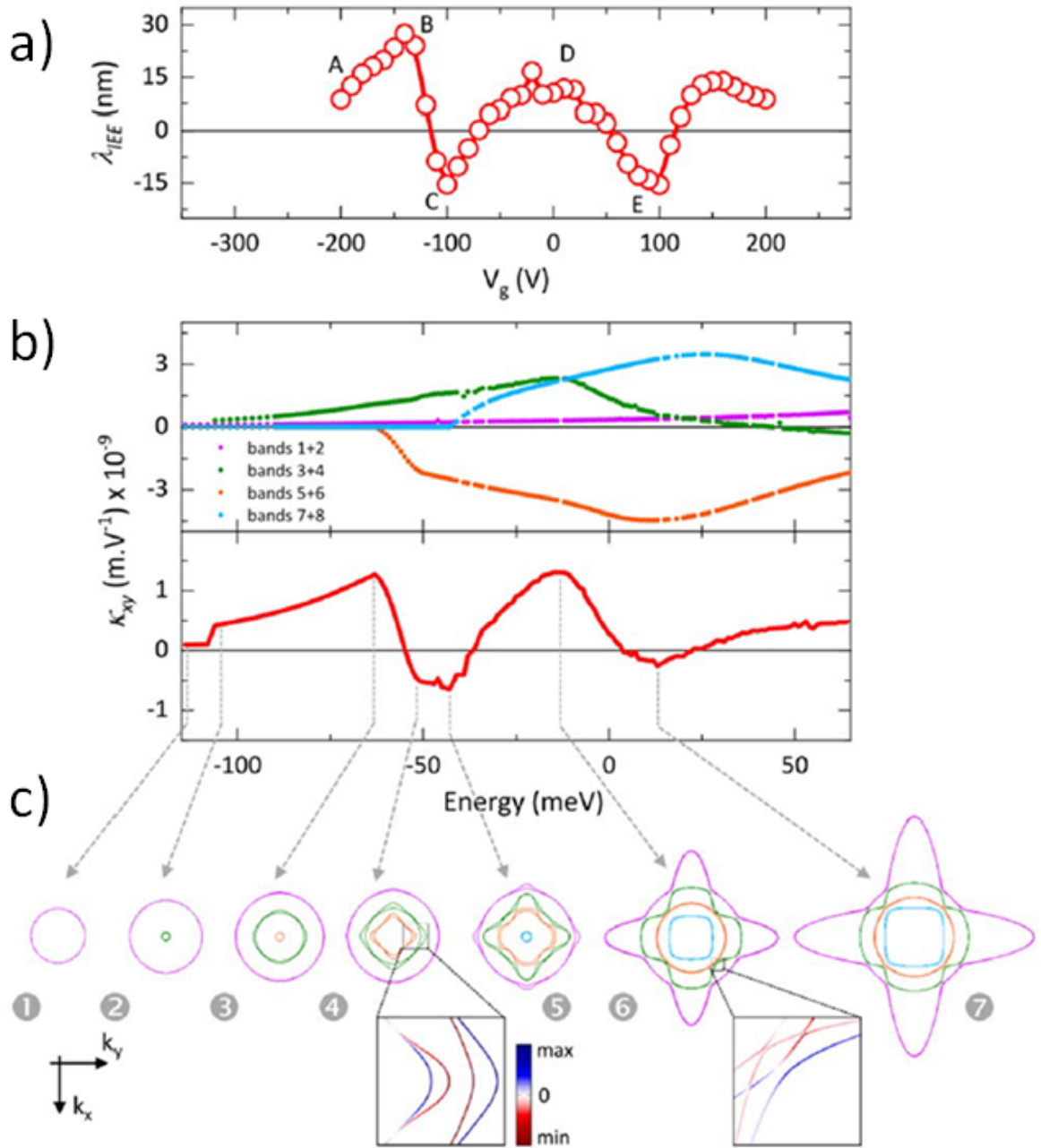


FIG. 4.6: Energy dependence of the spin-charge conversion. (a) Gate dependence of  $\lambda_{IEE}$  at 15 K. (b) Energy dependence of the Edelstein tensor (top: band-resolved; bottom: total). (c) Fermi lines at various energies. (1) Rashba-like bands 1+2. (2) Edge of bands 3+4. (3) Edge of bands 5+6. (4) Trivial avoided crossing. (5) Edge of bands 7+8. (6) Topologically non-trivial avoided crossing (with band inversion). (7) Maximum from multiple bands. The colour scale of the zoom-in regions in (4) and (6) corresponds to the contribution of each state to the Edelstein effect.

gion. This can be better understood by recalling the nature of the Edelstein effect in a Rashba system, where the net spin-charge current produced arises from the inequivalence of the Fermi contours. If the spin splitting between bands is larger, *i.e.* if Fermi contours have very different sizes (large Rashba constant  $\alpha_R$ ) this inequivalence is enhanced. A similar result is intuitively obtained if the spin-split bands have uncompensated spin textures, where the spin current produced through the EE by one contour would be much larger than the one produced by its Rashba-split counterpart. Lastly, for even higher energy, another sign change occurs followed by a negative extremum, resulting from the competing contributions from multiple bands (7).

Remarkably, the calculated  $\kappa_{xy}$  curve qualitatively reproduces the occurrence of extrema and sign changes in the IEE signal. However, the presented energy range cannot be unambiguously related to the depicted gate voltage. To gain more insight into their correspondence, the group of Marc Gabay have performed self-consistent Poisson-Schrödinger calculations<sup>259</sup> of the energy spectrum for an STO interface. These calculations indicate that to shift the Fermi level from the expected energy of the topologically avoided crossing to the trivial avoided crossing, the 2DEG needs to be depleted by  $\Delta n = 2.6 \times 10^{13} \text{ cm}^{-2}$ . By matching these two points in figure 4.6.c (6 and 4) with points D and C in figure 4.6.a, we observe that  $V_G$  was swept between about 0-20 V and -100 V, respectively. According to the transport data in figure 4.3.b, this range of gate voltages is equivalent to a depletion of  $\Delta n = 1.7 \pm 1 \times 10^{13} \text{ cm}^{-2}$ , compatible with the estimation from Poisson-Schrödinger calculations. Although the energy dependence of  $\lambda_{IEE}$  and  $\kappa_{xy}$  are quite comparable and can be related to the spin splitting of the band structure of the STO\AIOx 2DEG, the explanation of the extremely large IEE signal needs another ingredient.

## 4.2.2 Role of the insulating barrier

In the theoretical description scattering is restricted to the 2DEG only. In the experiments, however, the electrons have in principle the possibility to leak out of the 2DEG through a tunneling barrier (in this case, the AlOx layer), and scatter in the metal with very short relaxation times (typically tens of fs). This can be considered as a second scattering channel characterized by an escape time  $\tau_{esc}$  through the tunneling barrier, in addition to the scattering between the STO states with characteristic time  $\tau_{2DEG}$ . The two scattering channels lead to an effective relaxation time  $\tau_{eff} = (\tau_{2DEG}^{-1} + \tau_{esc}^{-1})^{-1}$  that will set the efficiency of the conversion process<sup>119</sup>. The strength of this second scattering channel can modify the IEE signal considerably.

Long escape times would change the IEE signal only slightly and result in an optimal spin-charge conversion signal, while short escape times, as in metallic interfaces such as Ag/Bi, would considerably reduce  $\tau_{eff}$  and consequently the IEE signal. We can use this picture to compare the values found in STO\LAO \NiFe samples<sup>66;219</sup> and here in STO\AIOx \NiFe. We deduce the escape times through 2 uc LAO and  $\approx 1$  nm of AlOx from their estimated resistance area (RA) product ( with  $RA \approx 10 \text{ } \Omega \cdot \mu\text{m}^2$  and  $10^5 \text{ } \Omega \cdot \mu\text{m}^2$ , respectively<sup>261</sup>). The escape time can be expressed as  $\tau_{esc} = \frac{RAe^2m}{2\pi\hbar^2}$ , where  $m$  is the electron effective mass. This leads to escape times in the ps range for 2 uc of LAO and in the ns range for 1 nm of AlOx. We see that for 2 uc of LAO  $\tau_{esc}$  is comparable to the momentum



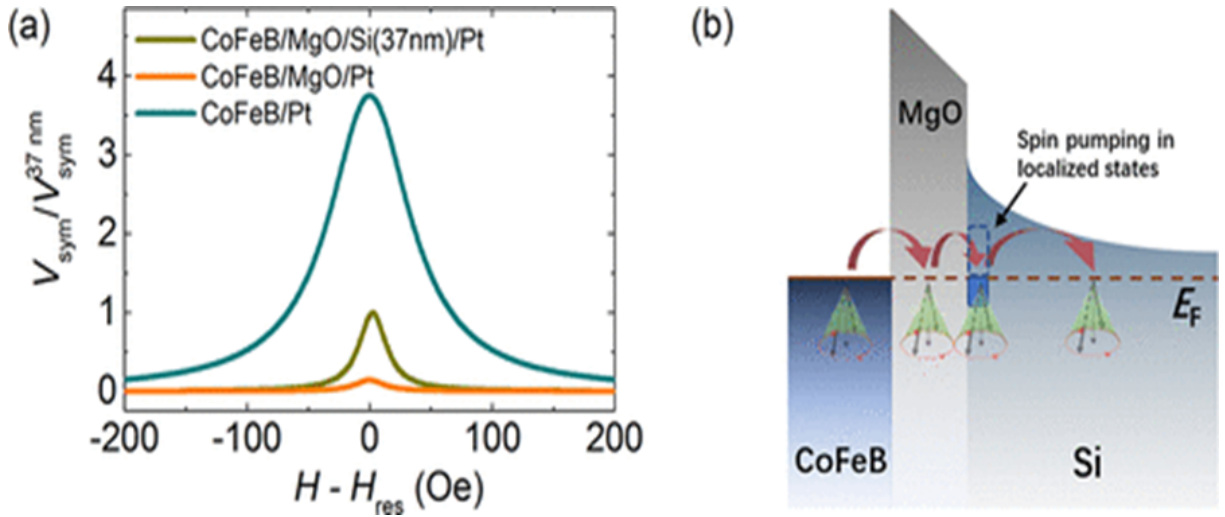


FIG. 4.7: a) Spin pumping FMR signal obtained in a CFB/MgO/Si(37nm)/Pt, CFB/Pt and CFB/MgO/Si/Pt multilayer. Spin signal is considerably larger in CFB/MgO/Si/Pt than CFB/MgO/Pt. b) Possible mechanism for spin injection through MgO barrier into Si associated with localized states. These figures are extracted from Cerqueira *et al.*<sup>260</sup>

relaxation of the 2DEG  $\tau_{2DEG}$ , estimated to be around 1-10 ps from the mobility, which should lead to a reduction of the effective scattering time compared to an isolated 2DEG. On the other hand, for the present STO/AlOx/NiFe samples,  $\tau_{esc}$  is much longer than  $\tau_{2DEG}$ : the electrons will scatter within the 2DEG before having a chance to leak out to the metal. In this case, the 2DEG is well isolated from the metal, and the conversion efficiency can approach its optimum value.

One question still remains, how is it possible to inject spin current through the insulating barrier? It has been observed at Ohio State University, in particular in the work of Du *et al.*<sup>262</sup> and Wang *et al.*<sup>263</sup>, that for non-magnetic barriers the injected spin current and measured ISHE signal decrease exponentially with the thickness of the barrier. They performed ISHE measurements by spin pumping FMR in YIG/Barrier/Pt samples using barriers of various materials and thicknesses. In particular, for barriers with large bandgaps the decay is strong even for thin barriers. In this experiment the spin current is decaying exponentially with the thickness of the barrier and this decay is associated with an exponential decay of the exchange coupling.

If we apply this model to our case, using the barrier height and the thickness of the Alumina in between the NiFe and the 2DEG, we should indeed expect a spin mixing conductance several orders of magnitude smaller than the  $2.2 \times 10^{18} \text{ m}^{-2}$  experimentally observed. This model, although appropriate for heavy metals such as Pt, seems to be irrelevant in the case of STO/AlOx/NiFe. There are several experimental examples of dynamical spin injection in Semiconductors/Barrier/Metal and 2DEG/Barrier/Metal. This is the case of the STO/LAO/NiFe system, studied previously by Edouard Lesne *et al.*<sup>66</sup>, but also notably by Chauleau *et al.*<sup>219</sup>. The measured spin mixing conductance was in both cases of the order of  $8 - 10 \times 10^{18} \text{ m}^{-2}$ , similar to that of NiFe/Heavy metal interfaces. Remarkably, according to Chauleau *et al.* it seems to be independent on the LAO barrier thickness from 4 to 6 uc. They stated that for different LAO barrier thicknesses “the transparency of the inter-

face should in principle vary in a tunneling fashion but this is not observed in our measurements“. Therefore, the model used by the Ohio University group, while effective for Pt based structure, seems to be inadequate here. In previous work on STO/LAO/NiFe, several scenarii have been proposed to explain spin injection through a thick barrier, in particular by exchange coupling via evanescent states or localized states, or hopping through localized states in the barrier.

In a recent experimental and theoretical work of Cerqueira *et al.* on Pt/Si/MgO/CoFeB<sup>260</sup> the proposed model is likely to explain our results. Spin pumping through a 1 nm, 2.2 nm and 3 nm thick MgO barrier towards Si was experimentally demonstrated. The ISHE spin signal detected was considerably higher in CoFeB/MgO (2.2nm)/Si/Pt than in CoFeB/MgO (2.2nm)/Pt as shown in figure 4.7.a extracted from Cerqueira *et al.*. This evidences the role of the semiconductors itself in the spin pumping process and which is not solely determined by the nature of the barrier. Such an effect cannot occur in a YIG/barrier/Pt trilayer (or CoFeB/MgO/Pt trilayer) owing to the lack of localized states at the barrier/Pt interface. In this proposed scenario a weak exchange coupling of some  $\mu eV$  would be sufficient to allow an efficient spin injection through localized states as seen in figure 4.7.b. The RA of 2.2 nm and 3 nm thick MgO barriers is of the order of  $10^4$  to  $10^6 \Omega \cdot \mu m^2$ <sup>264</sup> in this thickness range, and is comparable to the  $10^5 \Omega \cdot \mu m^2$  expected for a 1 nm thick Alumina barrier.

The high RA value did not prevent the spin injection. It is to be noted that defects in the AlOx could also promote such an effect and act as a chain of localized states, such defects are not unexpected owing to the nature of the oxidation. We would like to note here that there exists several other examples of spin injection by spin pumping through a barrier into a semiconductor<sup>59;265;188</sup>, and the exact mechanism still needs clarifications both from a theoretical and experimental point of view.

### 4.2.3 Spin to charge interconversion at room temperature

Finally, we have performed spin pumping experiments at room temperature. Since the inverse Edelstein length is proportional to the momentum relaxation time (and thus to the electron mobility), one expects a strong decrease of  $\lambda_{IEE}$  upon increasing the temperature<sup>117</sup>. As seen in figure 4.7.a this is what we obtained experimentally, with a considerably lower signal and conversion efficiency at room temperature. The conversion efficiency obtained at room temperature would be at maximum of  $0.5 \pm 0.1$  nm, but due to the large contribution of the spin rectification effect evidenced by the angular dependence (figure 4.8.b) it is even lower. This is in line with results of Chauleau *et al.*<sup>219</sup> and Ohya *et al.*<sup>221</sup> where a strong decrease of the signal was observed when increasing the temperature. Moreover, due to the considerably smaller dielectric constant of STO at room temperature, no gate effect was observed. Actually the gate effect disappears already around 80K when the dielectric constant of STO is smaller than 1000<sup>224</sup>.

To sum up this point, we have reported spin to charge conversion in an oxide-based 2DEG formed by the room temperature sputtering deposition of Al on STO. At cryogenic temperatures an efficiency about two orders of magnitude larger than that of the canonical spin-orbit coupling material Pt is found. We have related the amplitude of the effect and its strong gate dependence to the band structure of the



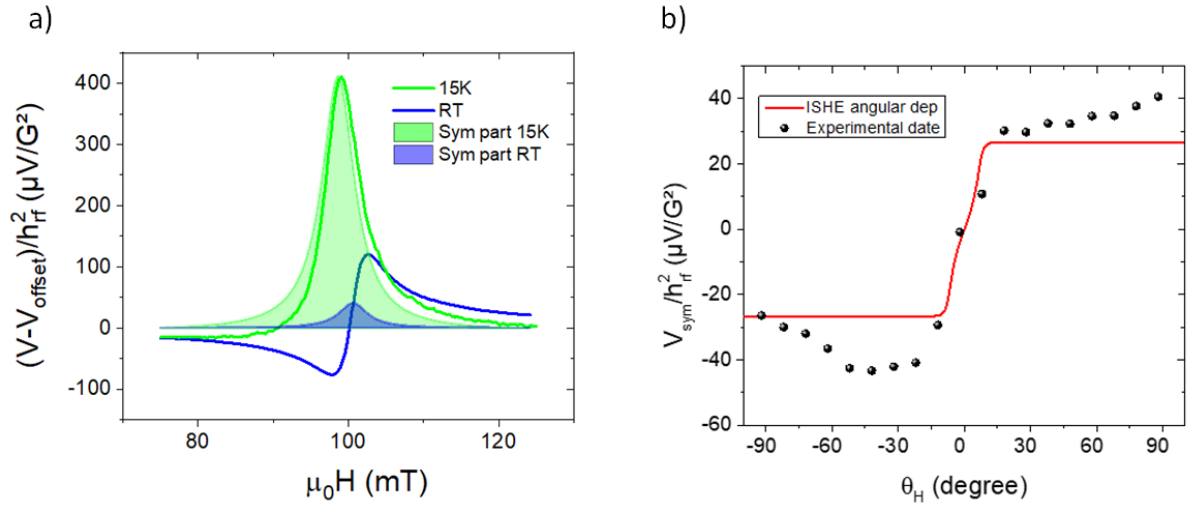


FIG. 4.8: Spin charge conversion at room temperature a) Spin signal obtained with zero gate voltage at 15K and 300K with fit of the symmetric part. b) Angular dependence of the symmetric signal, evidencing that a part of the signal is not due to ISHE/IEE.

2DEG, possessing trivial and topological avoided crossings, and to the high tunnel resistance of the Al oxide layer. Highly-doped STO-based oxide interfaces thus emerge as new members of the family of topological two dimensional materials, able to realize specific functions for spintronics devices.

### 4.3 Ferroelectricity in STO: non volatile switching of the IEE

In spintronics the ferromagnetism usually provides non-volatility, but magnetization reversal by spin torques is power consuming. Another route to achieve low-power non-volatile spin current generation and detection is to use polarization switching in ferroelectrics. This is driving research on multiferroics<sup>266;267;268;269;270</sup>, but practical materials are scarce, and magnetoelectric switching remains difficult to control<sup>270</sup>. Here, we demonstrate an alternative approach to achieve electric-field-controlled spin detection in a non-magnetic system. We use electric-field induced ferroelectricity in STO to manipulate the spin-orbit properties of a two-dimensional electron gas, and efficiently convert spin currents into positive or negative charge currents, depending on the polarization direction. This non-volatile effect opens the way to electric-field controlled spin currents, and to ultralow-power, ferromagnet-free spintronics for beyond-CMOS logic.

This effect can be achieved with the same sample as the one described in the previous section by tuning STO in its ferroelectric phase. The sections below are an extended version of a manuscript entitled “Ferroelectric control of spin-charge conversion using a  $SrTiO_3$  two-dimensional electron gas” by P. Noël *et al.*, and currently under review in Nature, resulting from a collaborative work performed with CNRS Thalès on ferroelectric STO.

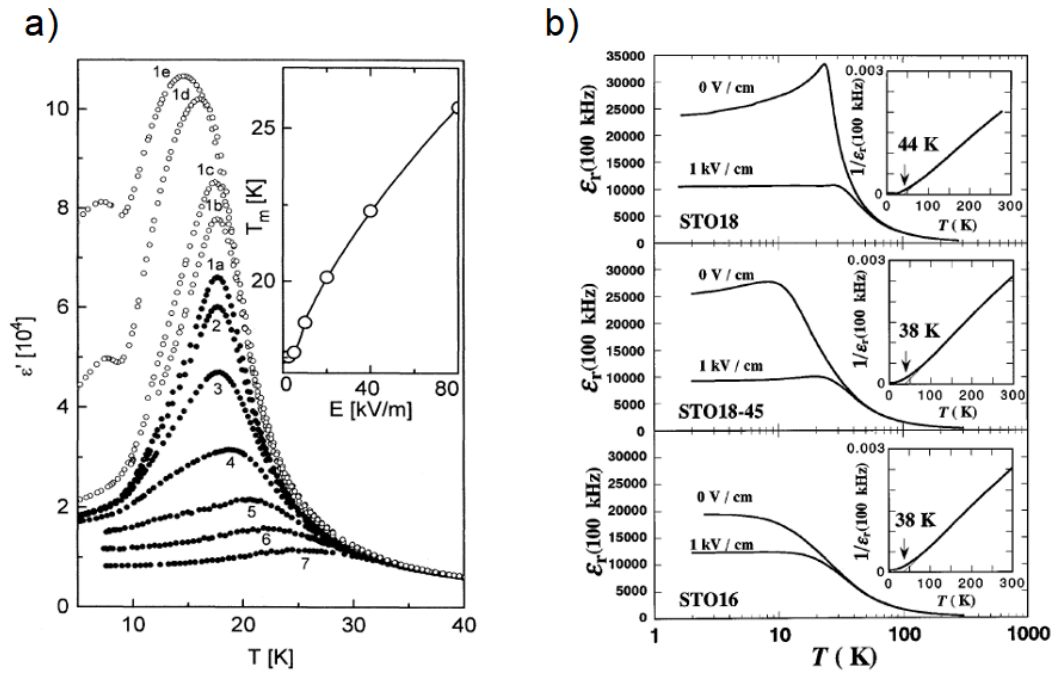


FIG. 4.9: Ferroelectricity induced in STO by a) Calcium cation doping and b) Oxygen isotope exchange. In both cases the transition is associated with a peak in the dielectric constant at finite temperature. These figures are extracted from Bianchi *et al.*<sup>276</sup> and Itoh *et al.*<sup>277</sup>

### 4.3.1 Ferroelectric STO?

A priori, bulk  $SrTiO_3$  is not ferroelectric. However, it is close to be ferroelectric: its dielectric constant follows a Curie Weiss law down to approximately 50K<sup>271;272</sup> but due to quantum fluctuations it is never ferroelectric at finite temperature. That's why STO is usually referred as a quantum paraelectric material *i.e.* it remains paraelectric due to quantum fluctuations<sup>273</sup>. To clarify this point in this section we would like to show how, according to previously published results, ferroelectricity can be obtained in bulk STO. In this part Here we are using bulk STO without any doping or substitution (STO single crystal substrates from Crystec GmbH). It is known that due to tensile strain STO thin films can be ferroelectric as reported for example by Haeni *et al.*<sup>274</sup>. But in bulk STO it is usually assumed that no ferroelectric transition occurs. At room temperature STO is cubic and its crystal symmetry group is  $m-3m$ , it is centrosymmetric and can thus certainly not be ferroelectric. At 105K occurs the well-known antiferrodistorsive cubic to tetragonal transition of STO which adopts a tetragonal structure<sup>275</sup>. The tetragonal structure is in the  $4/mmm$  symmetry group, which is also centrosymmetric, therefore it can not be ferroelectric either. There is no clear experimental evidence of a new phase transition where STO crystal symmetry is reduced at lower temperature and where STO could become ferroelectric.

However the quantum paraelectric state is weak, and any small change in the  $SrTiO_3$  crystal can lead to the appearance of a ferroelectric transition at cryogenic temperature. It was observed in 1984 by Berdnorz and Müller that a paraelectric to ferroelectric phase transition in STO can be induced by replacing 0.18% Sr by Ca in  $Sr_{0.9982}Ca_{0.0018}TiO_3$  alloy<sup>278</sup>, and further confirmed by Bianchi *et al.* with higher Ca concentrations<sup>276</sup>. These Calcium ions are off-center polar impurities, and at low

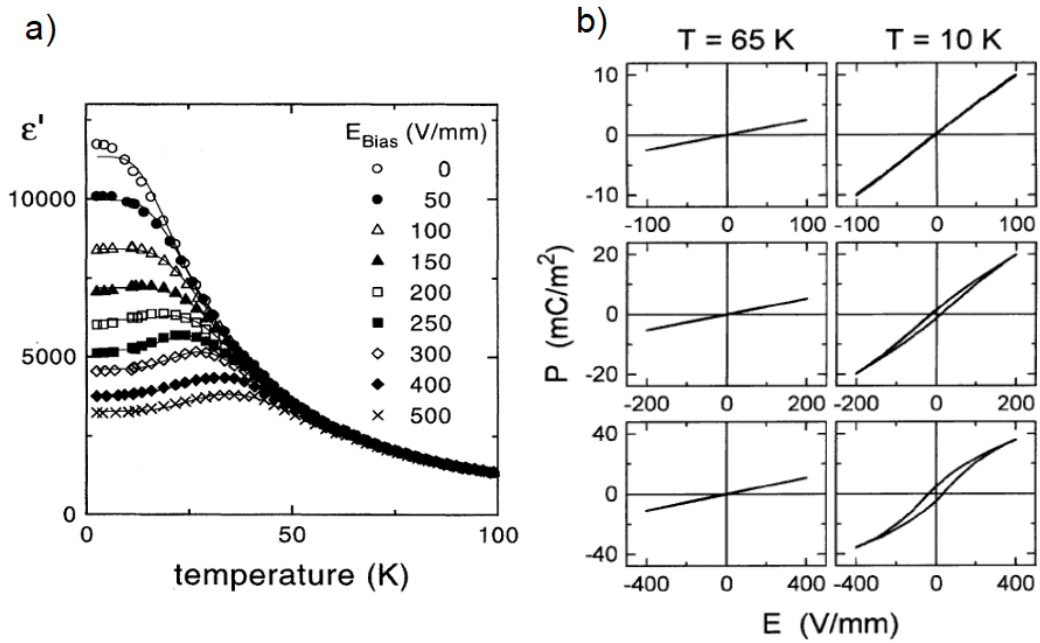


FIG. 4.10: Ferroelectricity induced in STO by Electric field. a) Dielectric constant of a STO single crystal as a function of temperature for different electric fields. b) P-E loop at 65K and 10K for different maximum applied electric fields. These figures are extracted from Hemberger *et al.*<sup>282</sup>

temperature acts as dipoles that will leads to the appearance of polar reorientation (random electric field) and ultimately ferroelectricity at finite temperature. Associated to this ferroelectric transition, a maximum in the dielectric constant of Ca-doped STO can be observed<sup>276</sup>(cf. figure 4.9.a).

Another well-known method to obtain ferroelectricity in STO is by isotope exchange from  $O^{16}$  to  $O^{18}$ , as shown by Itoh and coworkers in 1999<sup>277</sup>. In  $ATiO_3$  perovskite the relative weight of  $A$  and  $TiO_3$  is important to obtain a ferroelectric transition. This ratio is close to 1 in STO, but for atomic weight larger than Sr  $ATiO_3$  perovskite are usually ferroelectric, for instance  $BaTiO_3$  or  $PbTiO_3$ <sup>279</sup>, and quantum paraelectric for lighter ones such as  $CaTiO_3$ <sup>280</sup>. Another important mass ratio is the one between  $Ti$  and  $O_3$ , which is also close to 1. Deviation of this ratio from unity, which can be obtained by oxygen isotope substitution, leads to an enhanced non linear response of the crystal, and to the appearance of a ferroelectric transition in oxygen-substituted crystals<sup>281</sup>. This is also confirmed by dielectric constant measurements shown in figure 4.9.b with a clear maximum at around 23K in a 93 % oxygen-substituted crystal. In both cases a small modification of the crystal leads to the transition.

These doped samples are extremely useful to control well the critical temperature or the dielectric properties. Nonetheless there is an easier way to obtain such a phase transition, known as electric field induced ferroelectricity. If a large enough electric field is applied, a paraelectric to ferroelectric transition occurs. This has been for instance observed by Hemberger *et al.*<sup>282;283</sup>. As seen in figure 4.10.a, for high enough electric field and at temperatures below 40K, there is a maximum in the dielectric constant of STO. This maximum evidences that an electric-field-induced transition occurs. This is further confirmed by the Polarization-Electric field (P-E) loops in figure 4.10.b: when the electric field is above a certain threshold at 10K, the P-E loops are hysteretic and show a remanent polariza-

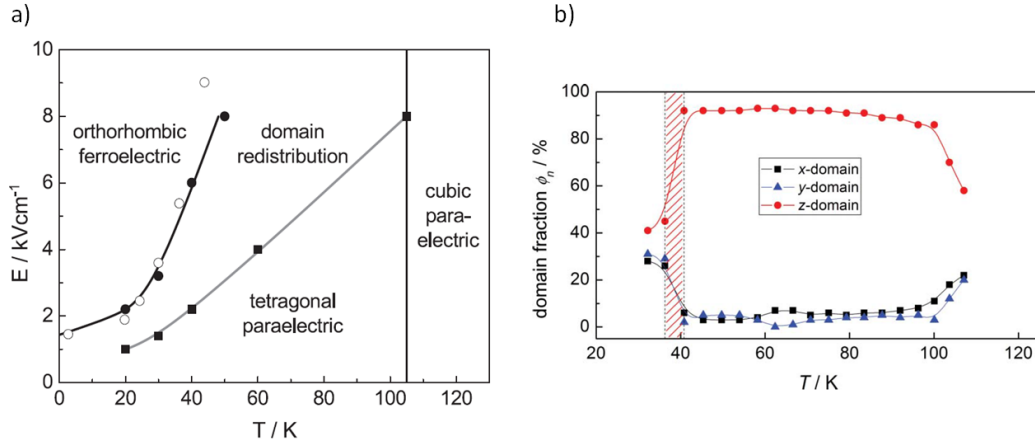


FIG. 4.11: Phase diagram of the STO. a) Temperature dependence of the critical fields: squares and full circles correspond to the threshold for domain redistribution and saturation fields respectively. Open symbols characterize the phase transition into the ferroelectric phase according to the dielectric data of Hegenbarth<sup>272</sup>. b) Temperature dependence of the domain distribution at zero electric field, after having entered the ferroelectric phase at 30 K. These figures are extracted from Sidoruk *et al.*<sup>284</sup>

tion. This effect is not observed at 65K as no transition occur at such a high temperature. It is also not observed for too low electric fields below the phase transition at 10K. Note that similar results has already been obtained in the 50's and 60's by Weaver<sup>271</sup> and Hegenbarth<sup>272</sup>.

It is noteworthy that the transition can be obtained by inducing a mechanical stress in a STO single crystal as observed by Fujii *et al.*<sup>285</sup>. That is why STO is sometimes referred as a flexoelectric material, with a spontaneous electrical polarization induced by a strain. This transition is actually similar to the electric field induced transition, as in STO a high enough electric field induces a tetragonal domain redistribution which leads to a mechanical stress. This allows to study the transition either by dielectric constant measurements as shown above or by structural characterizations, as performed by Sidoruk *et al.*<sup>286</sup>. From these two measurements a similar phase diagram of  $SrTiO_3$  is obtained, this phase diagram is shown in figure 4.11.a. For electric fields larger than a given threshold and at temperatures below 40K a ferroelectric phase transition can be induced in STO, which becomes orthorhombic with a  $P2mm$  symmetry. At higher temperatures only a partial domains redistribution can occur, and ferroelectricity can not be induced anymore. This phase transition can also be studied as a function of the temperature. After inducing the ferroelectric transition at 30K, as observed by the relative fractions of the tetragonal domains in figure 4.11.b, when temperature is increased above 40K all the domains are redistributed and a ferroelectric to paraelectric phase transition occurs<sup>284</sup>.

From both the phase diagram and the domain redistribution in Figure 4.11 one can expect a ferroelectric control of the 2DEG to be possible below 40K, if large enough electric fields can be applied. Therefore a remanent control of spin-charge interconversion should be possible, by combining ferroelectric control of the 2DEG and the drastic changes of the spin charge interconversion with the 2DEG properties seen in the previous section. To obtain such a control it is necessary to apply a larger electric field than in our previous study. We tried to achieve this by thinning down the 500  $\mu m$ -thick

STO substrates down to 200-250  $\mu\text{m}$ .

### 4.3.2 Remanent modulation of the spin to charge conversion

The idea of controlling the spin–charge conversion using ferroelectricity has already been proposed in other systems: the last few years have seen increasing efforts to identify single-phase Rashba ferroelectrics and integrate them into spintronics devices. Most research has been focused on GeTe, a low bandgap semiconductor, predicted to be a bulk Rashba material<sup>287</sup>, in which polarization switching causes a full reversal of the spin texture of the Rashba-split Fermi contours<sup>288;99</sup>. However, because of high leakage due to the Si (111) substrate, indications of ferroelectricity have only been reported in thin films using piezoresponse force microscopy<sup>99</sup>, and spin-charge conversion experiments in GeTe-based structures have yielded only a moderate efficiency<sup>289</sup>. Note that resistance switching were performed recently in GeTe structures (Sara Varotto private communication). Resorting to interface systems combining Rashba SOC and ferroelectricity as in STO\Al should allow to achieve a non-volatile electrical control of a highly efficient spin-charge conversion.

#### Concept of the ferroelectric controled spin-charge interconversion

The general concept of ferroelectrically-controlled spin-charge conversion is described in figure 4.12. At the interface between a ferroelectric and an ultrathin SOC system (a heavy metal, a Weyl semi-metal, a Rashba 2DEG, etc.), electrons are accumulated or depleted depending on the polarization direction (figure 4.12.a). This modifies the electric field in the interface region, and in the ideal case changes its sign. Indeed, if a Rashba state is present at the interface between the ferroelectric and the SOC system, reversing the sign of the local electric field is expected to reverse the chirality of the spin textures in both split Fermi contours (figure 4.12.b). Through the inverse Edelstein effect, the injection of a spin current into the Rashba state will produce a charge current  $J_c$ , the sign of which will depend on the polarization state (figure 4.12.c). This mechanism offers the possibility to design a wealth of devices, such as ferroelectric spin field-effect transistors<sup>287</sup>, or the bipolar memory device proposed in figure 4.12.d: depending on the ferroelectric polarization direction, the spin current injected from a ferromagnet with a fixed magnetization results in a positive or negative charge current. It can also be the basis of logic devices somehow analogous to the magnetoelectric spin-orbit (MESO) device proposed by Intel<sup>48</sup> for beyond-CMOS attojoule nanoelectronics, but without resorting to a multiferroic to switch the ferromagnet.

#### Effect on the spin charge interconversion in STO \Al

To experimentally demonstrate the concept of ferroelectrically-controlled spin-charge conversion, we use a similar sample as the one described previously in a STO\AlNiFe heterostructure. As previously shown in this chapter this 2DEG exhibits a sizeable Rashba SOC, which can be harnessed to achieve spin-charge conversion with a very high efficiency. In addition, as described before STO, is a quantum paraelectric, that possesses an instability towards a ferroelectric state at low temperature when a large electric field is applied. The coexistence of these features in the same material makes it an ideal platform to explore the phenomena described in figure 4.12.

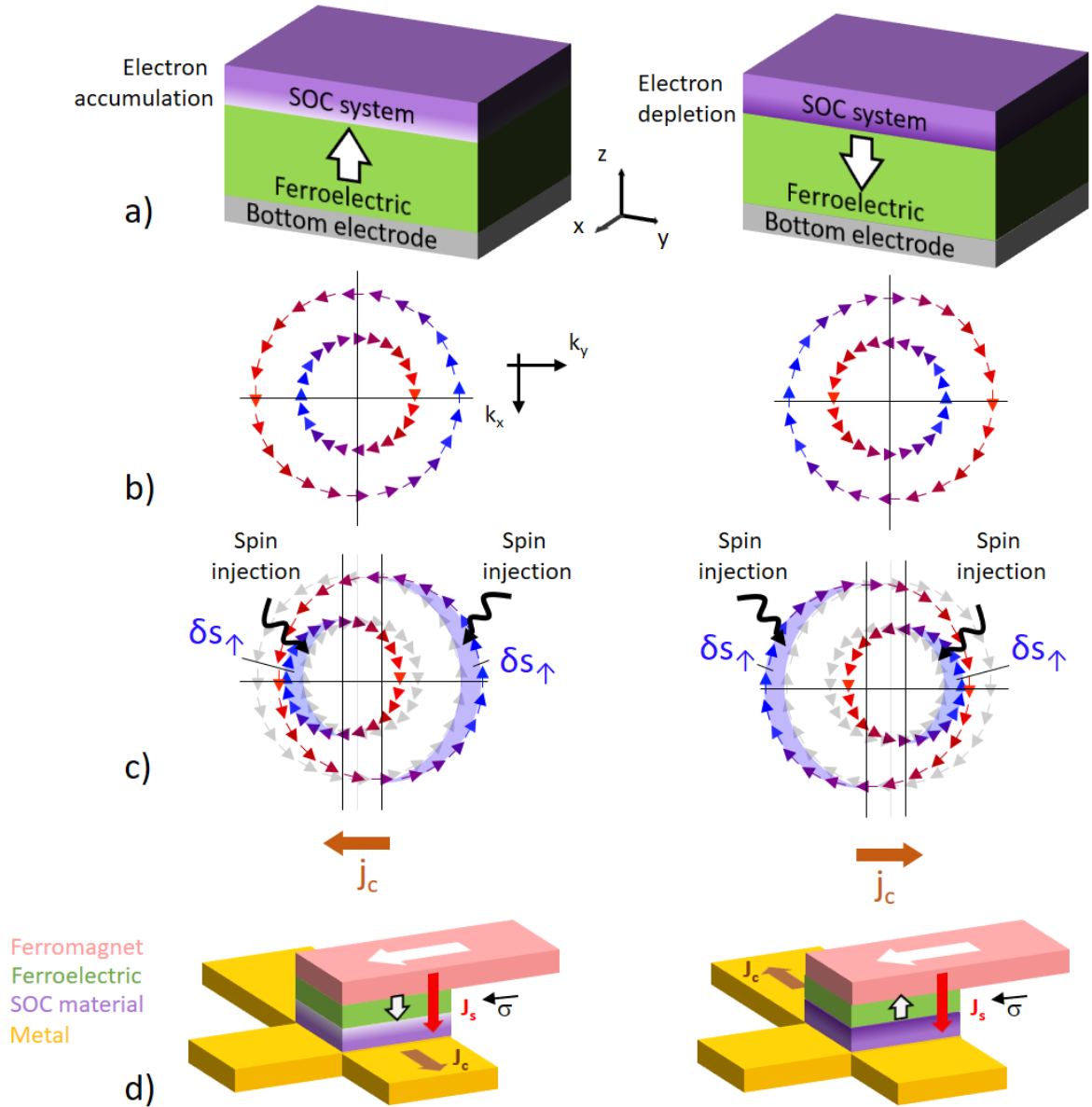


FIG. 4.12: Concept of the ferroelectric-control of spin-charge conversion. a) Sketch of a ferroelectric Rashba architecture combining a ferroelectric material (green) and a material with spin-orbit coupling (purple). Upon switching the polarization, electrons are accumulated (left) or depleted (right) in the SOC material, creating an electric field whose sign depends on the polarization direction. b) Corresponding Rashba-split chiral Fermi contours with spin-momentum locking. The chirality of the contours switches upon switching the ferroelectric polarization. c) Inverse Edelstein effect in a Rashba interface. When a spin current is injected (e.g. by spin pumping) with a spin polarization along the  $y$  axis, the spin population is altered, causing a displacement in momentum space of the two inequivalent Fermi surfaces (red and blue lines) by  $\pm\Delta k$ . This results in a net charge current, generated perpendicularly to the spin current and to its spin polarization. The sign of the generated current depends on the chirality of the Fermi contours, and is thus reversed upon switching ferroelectric polarization. d) Non-volatile device operated by ferroelectricity and Rashba SOC. A charge current  $J_c$  is generated by the conversion of a spin current  $J_s$  through the inverse Edelstein effect. The sign of  $J_c$  changes with the direction of the ferroelectric polarization.



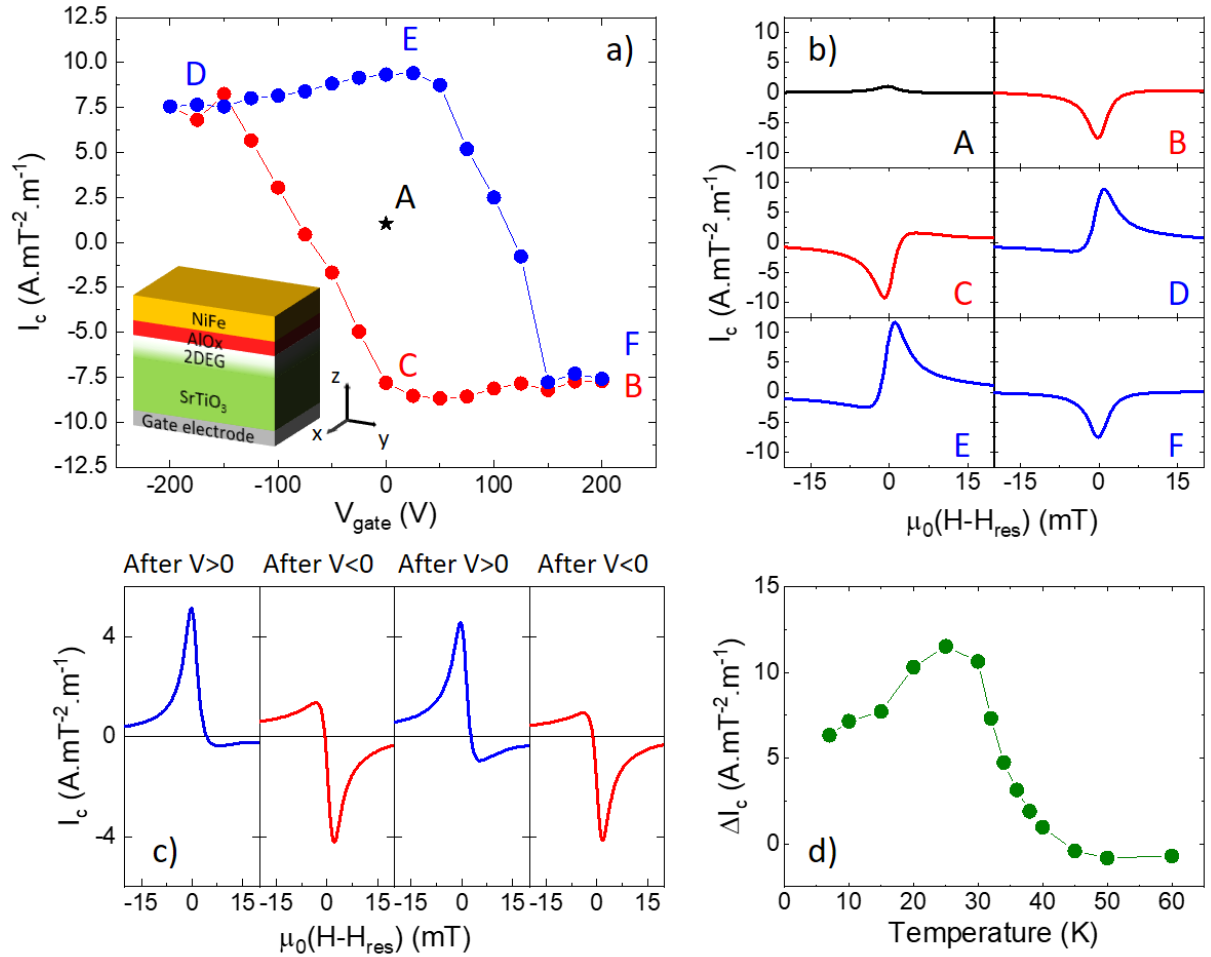


FIG. 4.13: Electric-field dependent spin-charge conversion experiments. a) Gate voltage dependence of the current produced by inverse Edelstein effect. The inset shows a sketch of the heterostructure. b) Dependence of the charge current produced by spin pumping with the magnetic field, for different back-gate voltages (cf. panel a)). c) Produced charge current at electrical remanence, after applying positive or negative 200 V voltage pulses. All data have been measured at 7 K. d) Temperature dependence of the difference between the currents produced at remanence, after the application of a large positive and negative back-gate voltage.



The spin-to-charge conversion was measured using spin pumping by ferromagnetic resonance (cf. sketch in the inset of figure 4.13.a). The nominally 500  $\mu\text{m}$  thick STO substrate was thinned down to  $250 \pm 20 \mu\text{m}$  by mechanical polishing on diamond pads under a deionized water flow. This process allows the application of higher electric fields, in order to reach the electric-field-induced ferroelectric transition of STO described in the previous section. Then, the spin pumping by ferromagnetic resonance experiments were performed. In the pristine, ungated state, the spin pumping signal obtained at resonance corresponds to a positive produced current of  $1.2 \text{ A}\cdot\text{m}^{-1}\cdot\text{mT}^{-2}$ , as displayed in Fig. 4.13.b (top left panel). We then applied back-gate voltages up to  $\pm 200\text{V}$ , corresponding to electric fields up to  $\pm 8\text{kV}/\text{cm}$ , high enough to induce the ferroelectric transition of STO<sup>282;284</sup>. After a first initialization cycle [+200 V; -200 V; +200 V], the gate voltage dependence of the spin pumping signal shows the hysteresis-like behavior seen in Fig. 4.13.a. The charge current produced at ferromagnetic resonance has opposite signs for +200 V and -200 V gate voltages, as seen in points B, F and D of figure 4.13.a and 4.13.b. After applying the maximum voltage, the spin signal reaches a very high amplitude of  $\pm 8.8 \text{ A}\cdot\text{m}^{-1}\cdot\text{mT}^{-2}$ , beyond the record values shown in the previous chapter in STO\AlOx samples (around  $5 \text{ A}\cdot\text{m}^{-1}\cdot\text{mT}^{-2}$ ). Here, we estimate the inverse Edelstein length  $\lambda_{IEE}$  to be around 60 nm.

Remarkably, the spin signal and thus the spin-charge conversion efficiency is remanent at  $V_{gate} = 0\text{V}$ , as seen in C and E. The non-volatile control of the spin-charge conversion process is further evidenced by figure 4.13.c, which displays the produced charge current at 0 V after the application of 500 ms pulses of  $\pm 200\text{V}$  gate voltage. The effect is clearly non-volatile and reproducible. Figure 4.13.d shows the temperature dependence of the difference  $\Delta I_c$  in the produced current obtained at remanence after applying pulses of +200 V and -200 V at 7 K.  $\Delta I_c$  is large below 30 K, but vanishes above 45-50 K, suggesting a transition of STO into the paraelectric phase similar to the one observed by Sidoruk *et al.*<sup>284</sup> and described in figure 4.11.b. A similar hysteretic behavior has been obtained on several thinned-down samples of STO\AlOx \NiFe of different batch as seen in figure 4.14. However it is not observed when studying a 500  $\mu\text{m}$ -thick STO substrate within the same voltage range, which indicates the existence of a critical electric field for the hysteresis to appear.

We show that a  $\pm 200\text{V}$  gate voltage application at 7K allows controlling the spin-charge conversion in a remanent way. To demonstrate the non-volatility associated to this remanence, we performed spin pumping measurements hours after applying a gate voltage of either +200V or -200V during 500ms in sample 2. As seen in figure 4.15.a, the spin signal is preserved, remaining unmodified after several hours. This evidences that if any relaxation of the ferroelectric state occurs it is particularly slow. We have also performed several cooldowns on the same sample. After performing a first cooldown and gate dependence measurements at low temperature, it is possible to recover the initial state by heating up the sample at room temperature. As can be seen in figure 4.15.b (measured on sample 2), the remanent ferroelectric state is lost after heating up to room temperature. When going back to 7K the sample recovers the initial state prior to the ferroelectric transition, with a positive spin signal. After heating the sample at room temperature, it is only after an initialization loop [+200 V; -200 V; +200 V] performed at low temperature that the hysteretic behavior is retrieved. This evidences that the remanence is not preserved upon heating.

One might wonder why this ferroelectric transition has apparently no effect on the Ferromagnetic

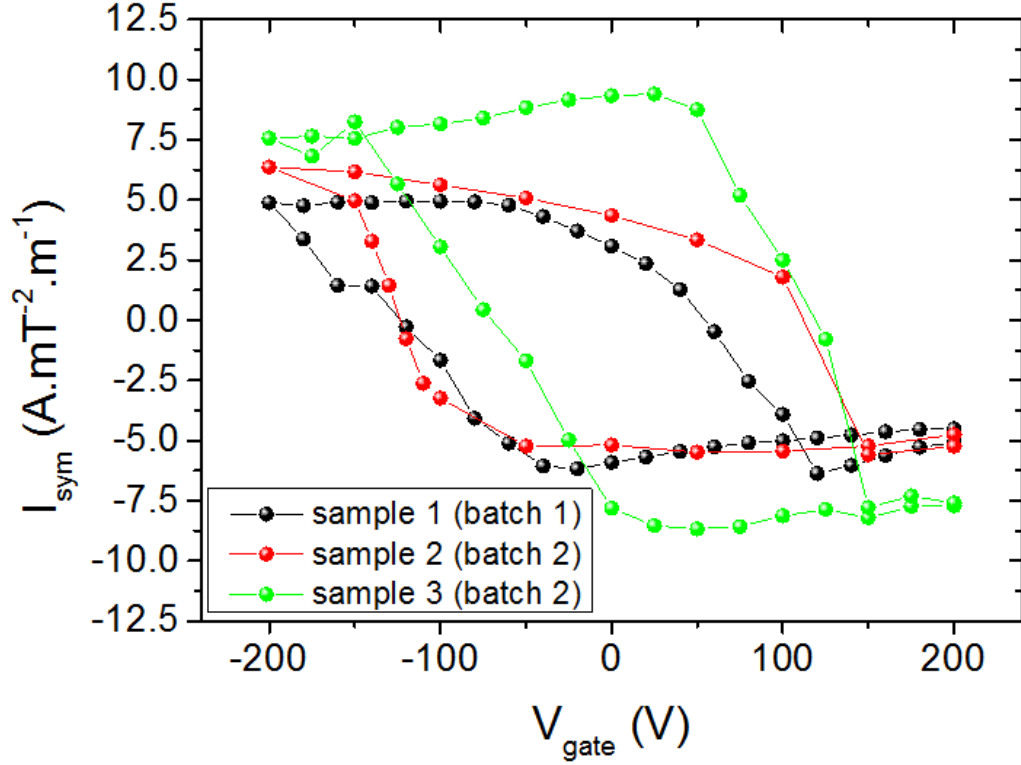


FIG. 4.14: Gate voltage dependence of the produced charge current in three different samples of  $\text{STO}(250\mu\text{m})\backslash\text{Al}(0.9\text{nm})\backslash\text{NiFe}(20\text{nm})$ . Sample 3 is shown in figure 4.13

Resonance Properties of NiFe. If STO is ferroelectric and similarly to what has been observed in other ferroelectric materials such as in  $\text{PZT}\backslash\text{FeGaB}$ <sup>290</sup>, the deformation of the crystal associated to the ferroelectric transition should affect the magnetic properties of the adjacent magnetic layer via a strain mediated magnetoelectric coupling. Nonetheless the NiFe film with Permalloy stoichiometry has a low magnetostriction (ideally no magnetostriction<sup>291</sup>) and is therefore not sensitive to such effect. As shown in annex D, if  $\text{Co}_{40}\text{Fe}_{40}\text{B}_{20}$  with large magnetostriction coefficient is deposited directly on STO, a strong modifications of the FMR lineshape of CoFeB with the gate voltage can be observed evidencing the strain induced by the deformation of the STO crystal.

### 4.3.3 Modulation of the 2DEG by ferroelectricity

To explore further the possible ferroelectric origin of the hysteretic spin-charge conversion effect, we have performed polarization measurements on an  $\text{STO}\backslash\text{Al}$  (1.8 nm) 2DEG sample with a STO thickness of  $200 \pm 20 \mu\text{m}$ . In these experiments, a triangular waveform was applied at a frequency of 1 kHz across the STO, between the 2DEG and a bottom electrode of  $\text{Ti}\backslash\text{Au}$ , and the current  $I$  was measured in real time. Integrating the current with time and normalizing by the sample area yields the polarization<sup>292</sup>. As visible in figure 4.16.b, the application of an electric field up to  $2.5\text{kV}/\text{cm}$  (green curve) yields a linear dependence of the polarization with the electric field, as expected for a dielectric material. However, when the voltage exceeds about  $7.2\text{kV}/\text{cm}$ , a clear hysteresis loop develops, associated with switching current peaks in the  $I$  vs.  $E$  data shown in figure 4.16.a. The sa-

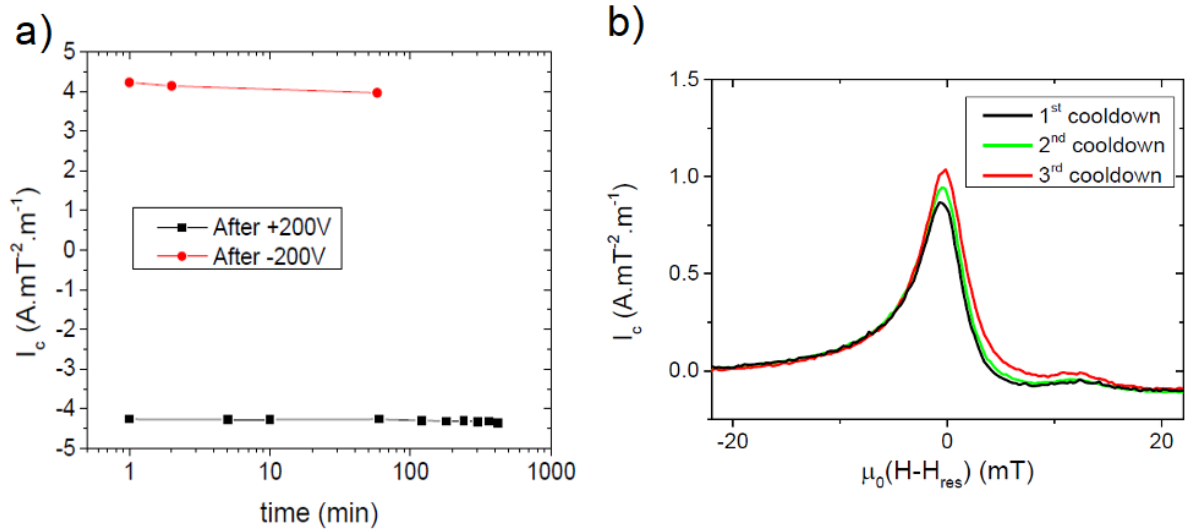


FIG. 4.15: Time and temperature stability of the remanent spin signal. a) Dependence of the produced current with the time spent after application of a positive (black) or negative (red) gate voltage. The measurements were performed at 7K on sample 1. b) Spin pumping signals obtained at 7K, for three different cooldowns from room temperature. After each cooldown, the signal was measured before any gate voltage application.

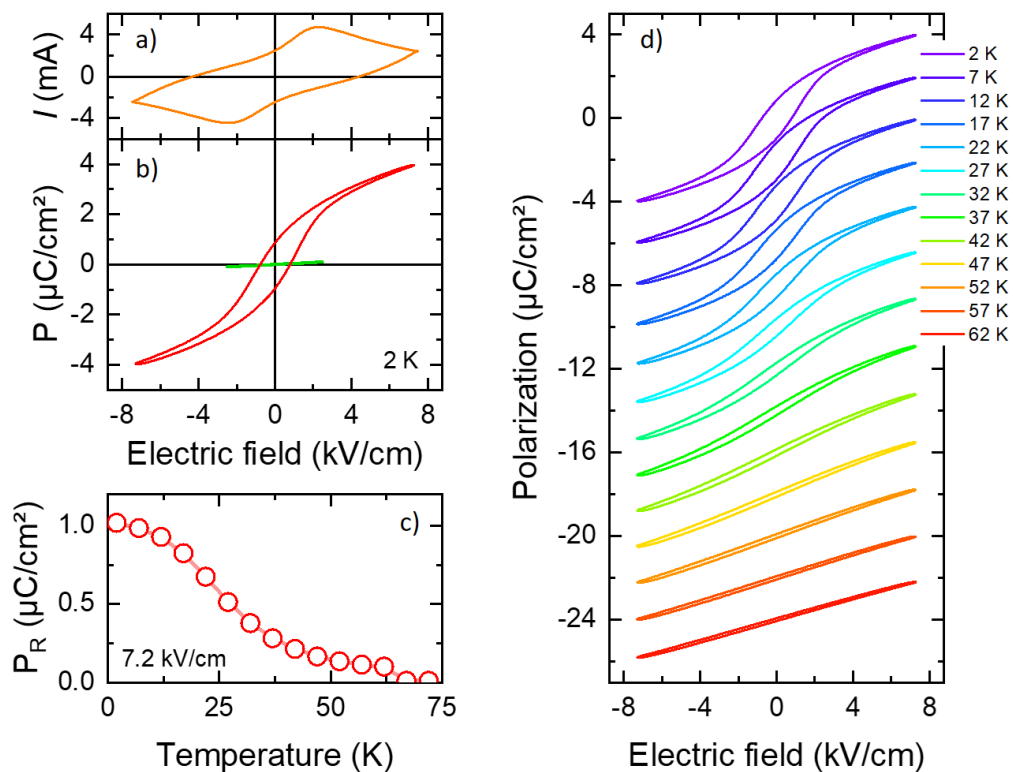


FIG. 4.16: Ferroelectric properties. a) Current vs voltage curves measured on a  $\text{STOAl}(1.8 \text{ nm})$  sample. b) Corresponding polarization loop (red curve). The green curve corresponds to the polarization loop measured with a maximum field of  $2.5 \text{ kV/cm}$ . c) Temperature dependence of the remanent polarization. d) Polarization loops at different temperatures. The curves are shifted by  $2 \mu\text{C/cm}^2$  for clarity.

turation polarization is about  $4\mu\text{C}/\text{cm}^2$ , in agreement with earlier reports<sup>282;272</sup>. As can be seen in figure 4.16.d upon increasing the temperature, the loop progressively closes, and the hysteresis is lost around 50-60 K. Figure 4.16.c displays the temperature dependence of the remanent polarization  $P_R$ , indicating a Curie temperature close to 50 K. These results - which are consistent with earlier data shown in the previous sections - confirm that the application of a large electric field induces a ferroelectric state in STO. Remarkably, this Curie temperature almost coincides with the temperature at which the remanent spin-charge conversion effect vanishes, bringing strong support to ferroelectricity as the origin of the hysteretic inverse Edelstein effect.

Once the ferroelectric state has been initialized, reducing the electric field to below the critical value still yields hysteretic polarization loops, albeit with a lower remanent polarization. This is visible in figure 4.17.a, where loops collected for different maximum electric fields are displayed (and shifted vertically for clarity). The combination of ferroelectricity with the presence of a 2DEG in the same sample brings about the appealing possibility to achieve a non-volatile electrical control of the 2DEG electronic properties using a ferroelectric field effect<sup>293</sup>. Indeed, the strong gate voltage dependence of the sheet resistance  $R_s$  is one of the hallmark features of STO 2DEGs. However, after a first gate initialization sweep, the gate dependence of  $R_s$  is usually non hysteretic, in line with the dielectric nature of STO at relatively low electric fields. As visible in figure 4.17.b, here we observe a different behavior.  $R_s$  is indeed found to vary systematically with the gate voltage, increasing as carriers are removed from the 2DEG at large negative voltage, and decreasing as carriers are added at high positive voltage. However, this dependence also exhibits a clear hysteresis. Remarkably, the amplitude of the hysteresis increases upon increasing the maximum gate electric field, so that the  $R_s$  vs. electric field loops mimic the polarization loops of figure 4.17.a. Hall measurements made at remanence after the application of positive and negative large gate voltages yield carrier densities of  $n_s = 8.37 \times 10^{12}$  and  $n_s = 1.37 \times 10^{13} \text{ cm}^{-2}$ , respectively, *i.e.*, a difference  $\Delta n_s = 5.45 \times 10^{12} \text{ cm}^{-2}$ . This has to be compared with the charge density theoretically accumulated and depleted into the 2DEG by the ferroelectric STO, *i.e.*,  $\Delta n_s = 2P_R/e$  ( $e$  is the electron charge) using  $P_R = 0.9 \mu\text{C}/\text{cm}^2$  we obtain  $\Delta n_s = 1.13 \times 10^{13} \text{ cm}^{-2}$ . The ferroelectric field effect on the 2DEG thus has an efficiency of 48%, a remarkably high value compared to the literature<sup>293;294;295</sup>. The ferroelectric character of the STO can thus be used to achieve a non-volatile hysteretic control of its sheet resistance and carrier density.

Several mechanisms may be invoked to explain our observation of an hysteretic inverse Edelstein effect. One can be related to the description of figure 4.12.a, namely a local inversion of the electric field in the SOC material (here the 2DEG) promoting polarization-direction-dependent Rashba SOC and spin-charge conversion. Additionally, electronic structure effects may be at play as seen in the previous section 4.3.2, depending on the position of the Fermi level in STO the sign of the spin to charge current conversion can change. Moreover, the presence of ferroelectricity may significantly modify the band structure compared to the non-ferroelectric case, as predicted in  $\text{KTO}_3$ <sup>296</sup>. The ferroelectric transition could generate additional (avoided) band crossings, thus leading to super-efficient spin-charge conversion. Theoretical calculations are clearly needed to gain more insight onto the origin of this remarkable phenomenon. I would also like to point out here that there is no example of ferroelectric control of the 2DEG using the STO as a ferroelectric back-gate in the widely studied

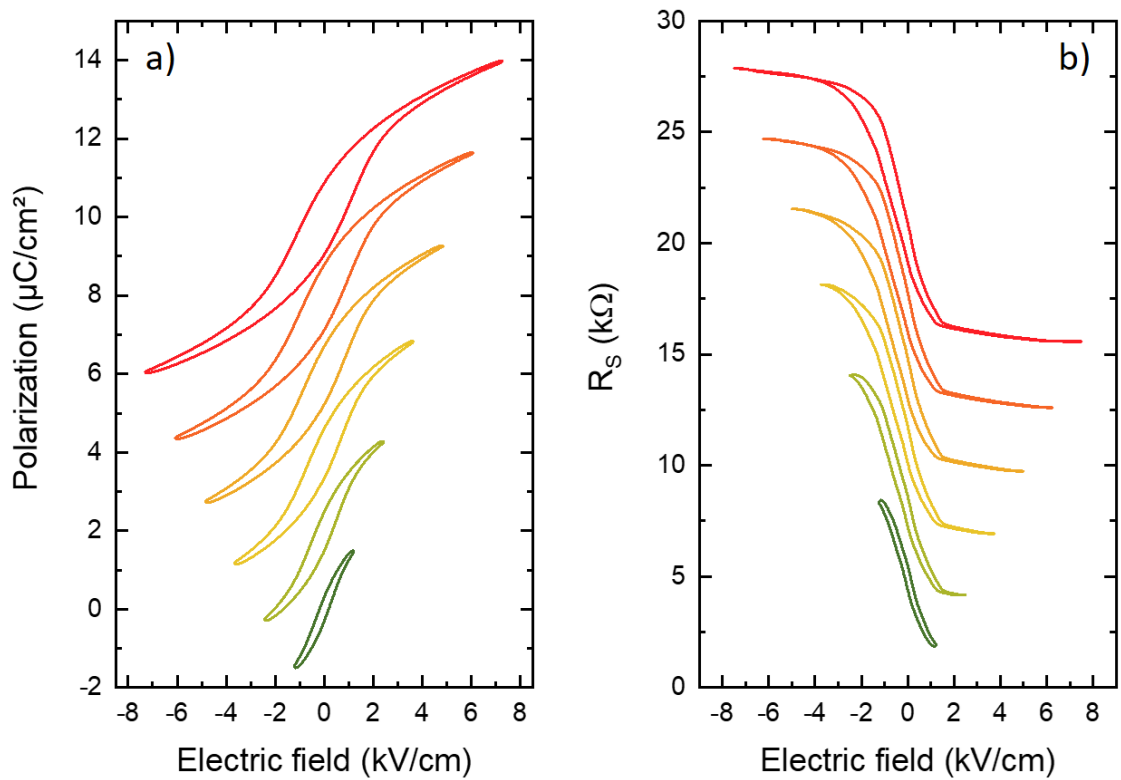


FIG. 4.17: Ferroelectric control of the 2DEG resistance. a) Polarization loops at 7 K measured in the ferroelectric state for decreasing maximum electric fields. The curves are shifted by  $2 \mu\text{C}/\text{cm}^2$  for clarity. b) Gate dependence of the 2DEG sheet resistance, for different maximum electric fields at 2 K. The curves are shifted up by  $3 \text{k}\Omega$  for clarity.

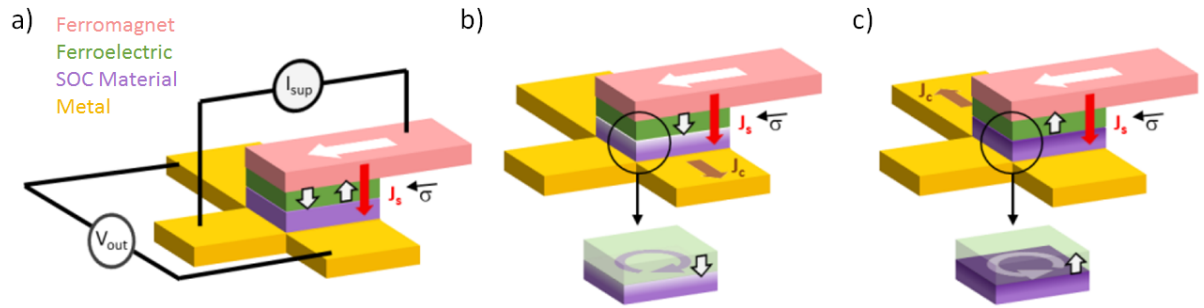


FIG. 4.18: Schematic representation of the ferroelectric spin-orbit memory. a) Configuration of the memory device. The polarized current  $I_{sup}$  is injected from the top to the left contact and the charge current production is detected through  $V_{out}$ . Depending on the polarization direction of the ferroelectric (in b) down polarization and c) up polarization) the sign of the produced charge current is of opposite sign.

crystalline STO/LAO heterostructure.

#### 4.3.4 Possible memory and logic applications

These results open the way to a whole new class of ultralow-power spin-orbitronic devices, where the polarity of the generated and detected spin currents will be controlled ferroelectrically. The devices presented in this section are part of a patent deposited with UMR CNRS Thalès on the ferroelectric spin-orbit logic.

The ferroelectric control of the inverse Edelstein effect demonstrated here could be used to develop memory devices based on the ferroelectric switching of the spin to charge current efficiency. Similarly to the device shown in figure 4.12.d and reproduced in figure 4.18 it is possible to obtain a switchable current production from the injection of a charge current in a Ferromagnetic/Ferroelectric/SOC Material (or 2DEG)/Metal heterostructure. There is no need to switch the magnetization of the ferromagnetic layer that is fixed, as seen in figure 4.18.a the supply current  $I_{sup}$  is injected from the ferromagnetic layer to the bottom left contact, this current is spin polarized and allows to obtain spin to charge current conversion in the SOC material or Rashba 2DEG below it. Depending on the sign of the spin to charge current conversion associated with the polarization of the ferroelectric material, the measured output signal is either positive or negative due to opposite direction of the charge current production (reading of the memory bit). The two possible configurations are shown in figure 4.18.b and 4.18.c. In this device the ferroelectric polarization can be switched using the same contacts as the supply current (writing memory bit). The device can therefore operate as a non-volatile ferroelectric memory device.

An improved version of this device is shown in figure 4.19 can be used as a MESO-like logic device with the low operating power necessary to develop attojoule electronics. The main advantage of this device is that it can be cascaded, as the output signal can be used as an input signal for another device. It works similarly to the MESO-logic presented in the introduction. An input current entering the left arm of the device starts charging the capacitor (metal \dielectric-ferroelectric \Ferromagnet).

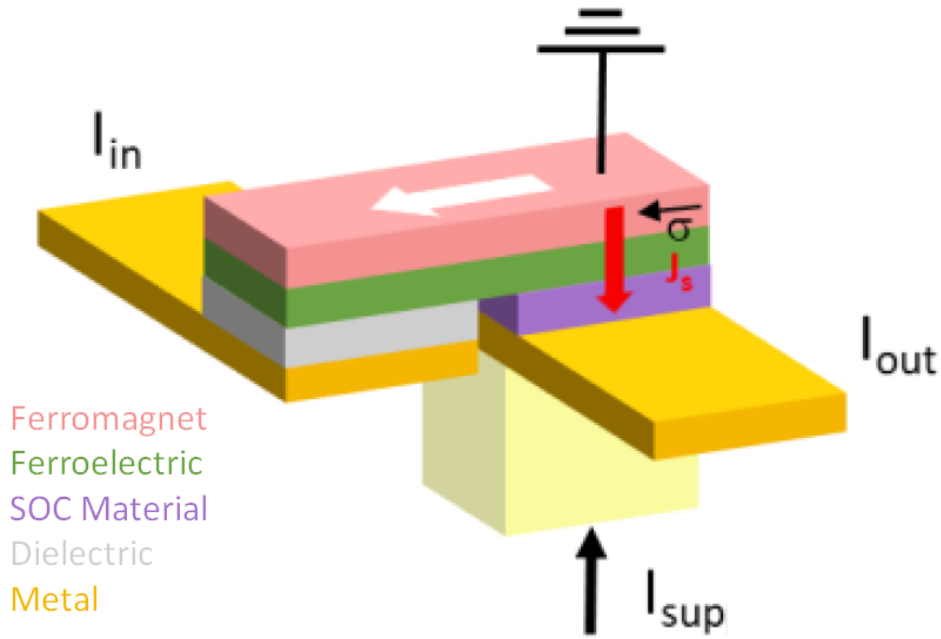


FIG. 4.19: Schematic representation of the ferroelectric spin-orbit logic device.

When a high enough voltage is reached, the left part of the ferroelectric polarization is switched, and this switching will then propagate towards the right arm through ferroelectric domain motion. This will therefore switch the Polarization of the ferroelectric layer at the ferroelectric \Spin Orbit material interface, and thus the output signal in the right arm. This switching can be performed at ultra-low power, thanks to the high resistance of the dielectric-ferroelectric stack. We would like to emphasize that contrary to the MESO-logic device it does not require the magnetization switching of the ferromagnet by magnetoelectric coupling with a multiferroic material. This switching of the magnetization is complex, as it requires a coupling of the magnetization with the ferroelectric order of the multiferroic layer. Moreover it has a lower endurance of some dozens of cycles compared to  $10^{15}$  cycles for a single ferroelectric layer obtained in Ferroelectric RAM<sup>297</sup>.

To conclude this chapter we demonstrated a highly efficient spin to charge current conversion in STO-based two dimensional electron gases. The 2DEG was obtained using the sputtering deposition of Aluminum on STO, a simpler method than the usual deposition of crystalline LAO on STO by pulsed laser deposition. In this STO \Al system the high tunability of the conversion was associated with some specific features of the STO bandstructure. By thinning down the substrate we could also turn the system in a ferroelectric phase that allows to tune the conversion in a remanent way in association with the remanence of the ferroelectric behavior of STO. We have thus demonstrated the ferroelectric control of the spin-charge conversion in STO 2DEGs, with the possibility to obtain conversions with opposite signs at electrical remanence. The hysteretic conversion proceeds by means of the inverse Edelstein effect in the 2DEG, and has a very large efficiency. Ferroelectricity is induced in STO by applying an electric field of a few  $kV/cm$ , and the remanent polarization is around  $1\mu C/cm^2$ . Remarkably, the hysteretic inverse Edelstein effect vanishes at the ferroelectric Curie temperature. This could pave the way to new spintronic devices relying on the remanence of the ferroelectric layer



instead of the ferromagnetic one. The next challenge is to obtain a large conversion efficiency and a ferroelectric control at room temperature. Several ways can be envisioned such as using oxide systems with higher spin-orbit coupling or to obtain 2DEGs on ferroelectric substrates for example in  $KTaO_3$  or  $BaTiO_3$ .

2DEGs at oxide interfaces are thus good candidates for spintronics applications based on the spin to charge current conversion by the inverse Edelstein effect. In the next chapter, we will study the potential of systems belonging to another class of materials: topological insulators.

## Edelstein effect in topological insulators

A rising interest for topological insulators (TIs) recently appeared in the field of spinorbitronics after reports of record charge to spin current conversion efficiency in Bismuth-based topological insulators such as  $Bi_2Se_3$ <sup>43;298</sup>,  $Bi_2Te_3$ <sup>299</sup> or  $BiSbTe$ <sup>116</sup>. Reports of spin Hall angles larger than unity are common in literature on the charge to spin conversion in TIs, even if the physical meaning of such values remains unclear<sup>300</sup>. More recently magnetization switching at low current densities was also demonstrated, evidencing possible future applications of topological insulators<sup>301;302;303</sup>. The conversion is sometimes associated to the Spin Hall Effect in the bulk of the TIs<sup>304</sup> or the Edelstein Effect in the surface states<sup>305</sup>. Nonetheless the spin to charge current in Bi-based TIs shows generally a limited conversion efficiency as measured by means of spin pumping<sup>304;306;193</sup> or spin Seebeck effect<sup>67</sup>, with conversion at most comparable to that of heavy metals such as Pt. Beyond surface states, this conversion could be associated to large amounts of bulk defects in these materials.

While they are the most studied, Bi-based TIs are not the only kind of topological insulators. Strained Mercury Telluride (HgTe) is one of the first discovered topological insulator. This system benefits from a better control of the material quality, associated with a lower density of defects and a larger mobility than in any other TI<sup>307</sup>. As a consequence, it could possibly allow obtaining larger spin to charge current conversion efficiencies at room temperature. In this chapter we will describe results on the spin to charge conversion obtained in HgTe-based heterostructures deposited by molecular beam epitaxy (MBE). We will also shortly present results on  $Sb_2Te_3$  samples deposited by sputtering on silicon dioxide using an industry compatible process on 300 mm wafers.

### 5.1 An efficient spin to charge conversion in strained HgTe

The main advantage of HgTe compared to Bi-based systems is its high material quality. For example  $Bi_2Se_3$  or  $Bi_2Te_3$  have a large number of defects including Se or Te vacancies<sup>308;309;310</sup>, or twin defects<sup>311</sup>. Therefore in thin films the carrier density in these samples is high, usually above  $10^{18} \text{ cm}^{-3}$ , with the Fermi level crossing bulk bands, and the mobility is usually below  $500 \text{ cm}^2/\text{V.s}$ <sup>312</sup>. In these materials the transport properties are far from optimal and closer to a bad metal than an ideal topological insulator. In HgTe epitaxially grown on CdTe the carrier density is smaller with the Fermi level lying close to the charge neutrality point, and the mobility can be up to several  $10^5 \text{ cm}^2/\text{V.s}$ <sup>307;313</sup>, which evidences the higher quality of the samples and the smaller bulk contribution to the conductivity. From this very simple statement one can expect better transport and spin transport properties in HgTe than in Bi-based system, in particular a more efficient spin to charge current conversion.

After some explanations on how topological surface states arise at the surface of HgTe we will describe spin pumping FMR results obtained in HgTe/HgCdTe/NiFe trilayers. In particular we will show

how the use of a protective HgCdTe layer allows increasing the conversion efficiency. We will also show that the dependence of the conversion with the HgTe thickness differs from the usual dependence observed in spin Hall materials. These results have been published in Physical Review Letters in a paper entitled “Highly efficient spin-to-charge current conversion in strained HgTe surface states protected by a HgCdTe layer”<sup>68</sup>. This section can be considered as an extended version of this work.

### 5.1.1 Tensile strained HgTe on CdTe: a 3D topological insulator

In 2006 Bernevig, Hughes and Zhang identified, CdTe \HgTe \CdTe quantum well as a 2D topological insulator with insulating surfaces and conductive sides<sup>314</sup>. The experimental evidence of Quantum Spin Hall Effect associated with the quantized spin dependent conduction in the edges of the sample in a 2D topological insulator were later on demonstrated by König and coworkers in 2007<sup>315</sup>. Since then several theoretical works predicted the expansion of topological properties to three dimensions as mentioned in the first chapter of the manuscript that will results in structures that combine both an insulating bulk and conductive surface states - topological surface states- with spin momentum locking. Among these works Fu and Kane predicted that HgTe when under strain was a 3D topological insulator<sup>102</sup>.

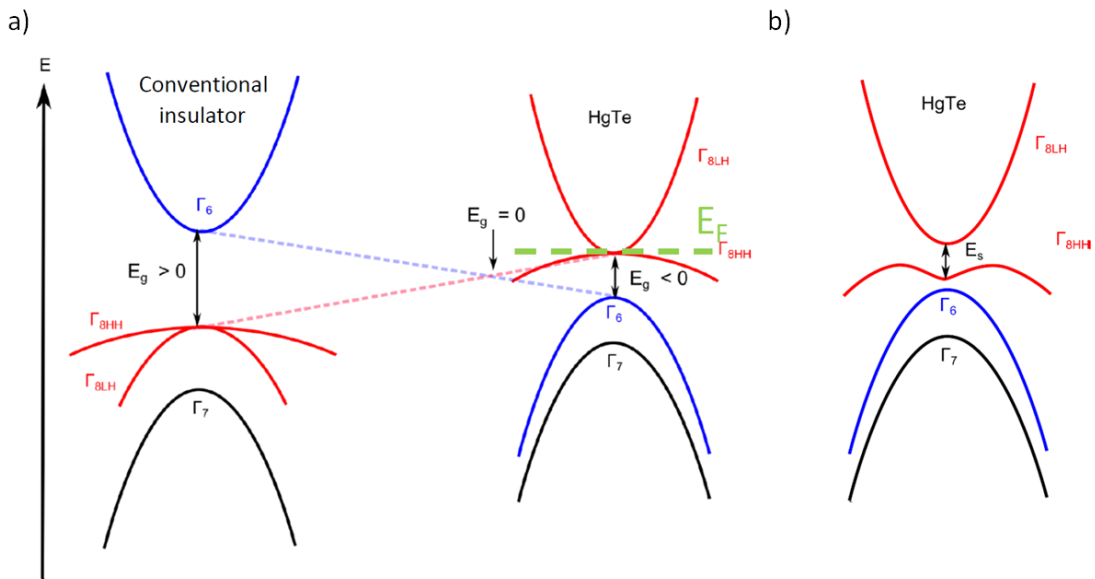


FIG. 5.1: Band inversion and gap opening in HgTe. a) Schematic representation of an insulator with normal band structure as CdTe and inverted band structure as HgTe. Gapless surface states arise at the interface between CdTe normal band structure and HgTe inverted one due to band continuity. b) Bandstructure of HgTe when deposited on CdTe, due to tensile strain the degeneracy at the  $\Gamma$  point is lifted and a gap is opened. Figures are adapted from the Thesis of Candice Thomas<sup>316</sup>.

Mercury Telluride is a semimetal due to the band inversion at the  $\Gamma$  point. The  $\Gamma_8$  band with a hole-like character lies 0.3eV above the electron-like  $\Gamma_6$  band, so it has a negative/inverted bandgap. This band inversion is due to the addition of both the mass velocity correction and the strong spin orbit coupling in HgTe that lift the  $\Gamma_8$  band above the  $\Gamma_6$  one<sup>317</sup>. This is not occurring in CdTe due to the weaker mass velocity correction related to the presence of a lighter atom Cd ( $Z=48$ ) instead of Hg

( $Z=80$ ) that preserves a normal bandstructure with a positive bandgap of 1.6eV as shown in figure 5.1.a. Therefore, at the interface between these two materials, the gap is forced to close to ensure band continuity, leading to the appearance of surface states. However in this picture HgTe is still not a topological insulator due to the lack of bandgap, it remains semimetallic.

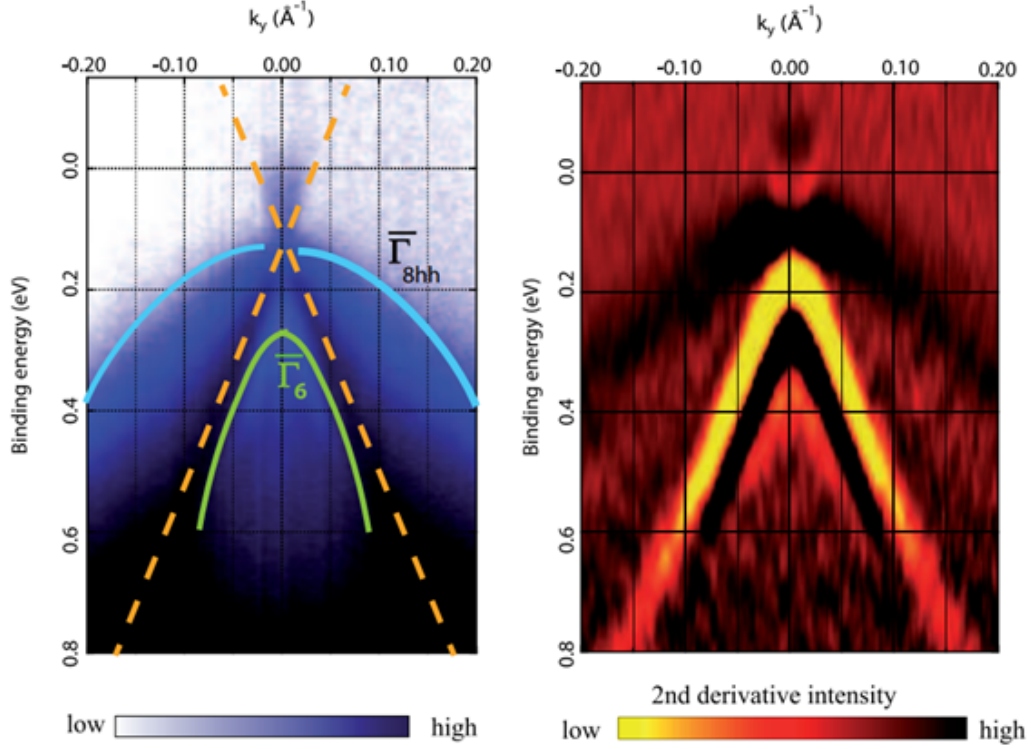


FIG. 5.2: ARPES intensity spectrum and second derivative intensity of the energy-momentum at the HgTe/vacuum interface of a 100nm thick HgTe film deposited on CdTe. Figure adapted from Crauste *et al.*<sup>318</sup>

It is possible to promote a bandgap in HgTe by applying a tensile strain, the deformation of the crystalline network breaks the cubic symmetry, which leads to modifications of the bandstructure and in particular to the gap opening. This is experimentally obtained by depositing HgTe on CdTe. They both have the same zinc-blende structure but a different lattice parameter:  $a_{CdTe} = 0.64815$  and  $a_{HgTe} = 0.64615$  nm. When growing epitaxially HgTe on top of CdTe, the HgTe lattice constant expands to match the CdTe lattice, which leads to a tensile strain of around 0.3%. This strain lift the degeneracy at the  $\Gamma$  point and opens a strain gap  $E_s$  between the  $\Gamma_{8LH}$  light hole band and  $\Gamma_{8HH}$  heavy hole band of around 25 meV, as shown in figure 5.1.b<sup>208</sup>. This turn HgTe into a 3D topological insulator.

As long as HgTe thickness is kept below 130 nm, no plastic relaxation occurs as shown by Ballet *et al.* on similar samples<sup>319</sup> so that the gap is preserved. One might note here that the method to obtain a gap is similar to the case of semimetallic  $\alpha$ -Sn deposited on InSb or CdTe<sup>320</sup>. In these conditions, the existence of a Dirac Cone at the free surface of a 100nm thick HgTe deposited on CdTe has been

confirmed by ARPES measurements shown in figure 5.2<sup>318</sup>. One might note here that the spatial extension of the topological surface states of HgTe is of around 5nm<sup>321</sup> compared to 1nm in  $Bi_2Se_3$ , therefore the complete Dirac cone can be obtained only for thicknesses above 20-30nm, below these thickness it is in a 2D-3D transition regime with a Dirac-gap opening.

### 5.1.2 Sample preparation

The growth of HgTe on CdTe has been done by molecular beam epitaxy by Philippe Ballet at CEA-Leti. The development of ultra-high quality HgCdTe based microstructure for optronics and photonics as infrared detectors allows to obtain samples of high quality thanks to years of both fundamental and industrial development of the growth process. The exact growth conditions (temperature, deposition rates, flux...) are detailed in the following references<sup>319;322;321</sup>. After the deposition of a 200 nm thick CdTe buffer layer on a prepared CdTe (001) substrate, a strained HgTe layer (from nominally 10 nm to 80 nm thick) has been grown, immediately capped with a nominally 5nm thick  $Hg_{0.3}Cd_{0.7}Te$  layer to avoid any Hg desorption at the surface. After deposition, the thicknesses of both the HgTe and HgCdTe layers have been measured by X-Ray Reflectivity (XRR), as seen in figure 5.3.a., and fitted using the software GenX<sup>323</sup>. The estimated roughnesses for the HgTe layer and HgCdTe capping were below 0.5 nm for all samples. The crystallographic quality of the heterostructure and the sharpness of the HgTe\HgCdTe interface have also been controlled by High-Angle Annular Dark-Field (HAADF) imaging in a scanning transmission electron microscope (cf. Figure 5.3.b). The associated intensity profile allows for the marking of the interface chemical boundaries between HgTe and  $Hg_{0.3}Cd_{0.7}Te$ . The interface width of 1.4nm has to be considered as an upper bound as the intensity profile is averaged over the 50-100nm thickness of the focused-ion-beam-prepared TEM lamellae. This evidences the abrupt interface between HgTe and HgCdTe, with an interface width kept lower than the surface states extension.

To perform spin pumping experiments, a 20 nm thick NiFe layer has been deposited ex-situ by evaporation. A soft argon ion etching (240V) has been performed prior to the NiFe deposition, in order to remove the oxide layer, and eventually to modulate the thickness of the HgCdTe barrier. After the deposition of the NiFe layer, the thicknesses of the NiFe and HgCdTe films have been measured by XRR. The samples have then been cut into 0.4 mm wide and 2.4 mm long stripes, before being measured by spin pumping ferromagnetic resonance experiments. Due to the use of very brittle CdTe substrate, the contacts were made using small droplets of silver print instead of wire-bonding.

### 5.1.3 Spin to charge conversion: role of the HgCdTe barrier

To study the spin to charge conversion we have performed the spin pumping FMR measurement as described in the previous chapters in the HgTe\HgCdTe\NiFe multilayer shown in figure 5.4.a.

The damping coefficient of NiFe is higher when deposited on HgTe than on Si (c.f. figure 5.4.b) evidencing that there is spin injection through the HgCdTe barrier. The damping  $\alpha_{ref}$  of NiFe deposited on Si is of ( $\alpha_{ref} = 0.00636 \pm 0.00003$ ) compared to a damping of the trilayer of  $\alpha =$

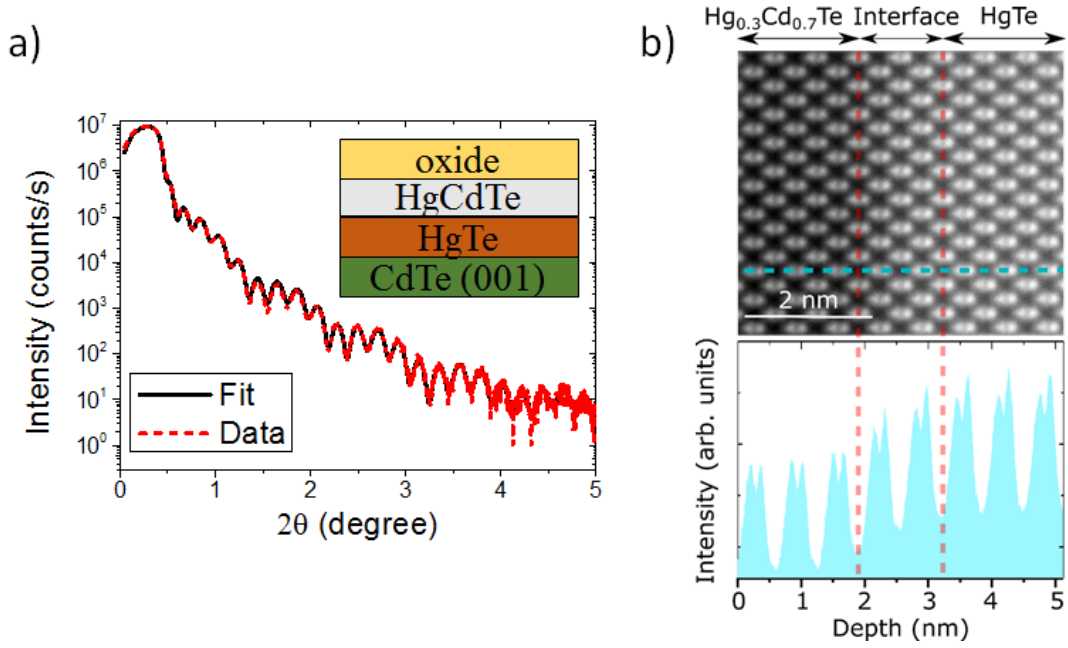


FIG. 5.3: a) X-Ray Reflectivity spectrum of a HgTe(18.5nm)/HgCdTe(5.5nm) sample. The structure used for the fit is represented in the inset. The red dashed curve represents the experimental data, the black curve is the fit. b) Scanning tunnelling electron microscopy HAADF image of HgCdTe/HgTe/HgCdTe structure and corresponding chemical profile. As the electrons cross the whole sample, each pixel corresponds to a value averaged over an atomic column. Thus, the apparent interface thickness, of around 1.4nm, has to be taken as an upper bound of the interdiffusion length.

$0.00750 \pm 0.00007$ ). For a rf field of 0.1 mT (*i.e.* 1 Gauss), and using the other magnetic properties extracted from broadband FMR, the spin pumping theory leads to an injected pure spin current at resonance of  $J_s = 7.6 \pm 0.2 \text{ MA/m}^2$ . For all the studied samples we determined an extra damping value  $\Delta\alpha$  that is in the range of  $1 \times 10^{-4}$  to  $2 \times 10^{-3}$ , depending on the thickness of the HgTe layer and of the barrier. This extra damping value is about ten times smaller than the extra damping induced by Pt but remains larger than the one for STO \Al, which indicates an efficient spin injection.

Figure 5.4.c presents the ferromagnetic resonance signal, together with the spin pumping signal, for a 18.5 nm thick HgTe sample covered by a 1.6 nm thick HgCdTe layer. As can be seen in figs. 5.4.c and 5.4.d, the signal is mostly symmetrical with respect to the resonance field, and its sign is well reversed when turning the sample from the parallel to the antiparallel configuration. The most striking result is the appearance of a large spin signal indicating an efficient spin to charge conversion at room temperature: the produced 2D charge current density  $J_c^{2D} = I_c/w$ , with  $w$  the width of the sample is found to be much larger than what can be obtained with heavy metals. It is up to 4.25 mA/m versus 1.25 mA/m in thick Platinum samples<sup>61</sup> The current production is thus similar to the 5 mA/m reported in  $\alpha$ -Sn<sup>62</sup>.

Let us now focus on the role of the HgCdTe barrier. The direct contact from a metal with a TI is expected to be detrimental to the conversion efficiency, because of the decrease of the carrier lifetime<sup>117</sup>, of Fermi level modifications<sup>324</sup> or of the modification of the interface chemistry<sup>325</sup>. Thus, several theo-



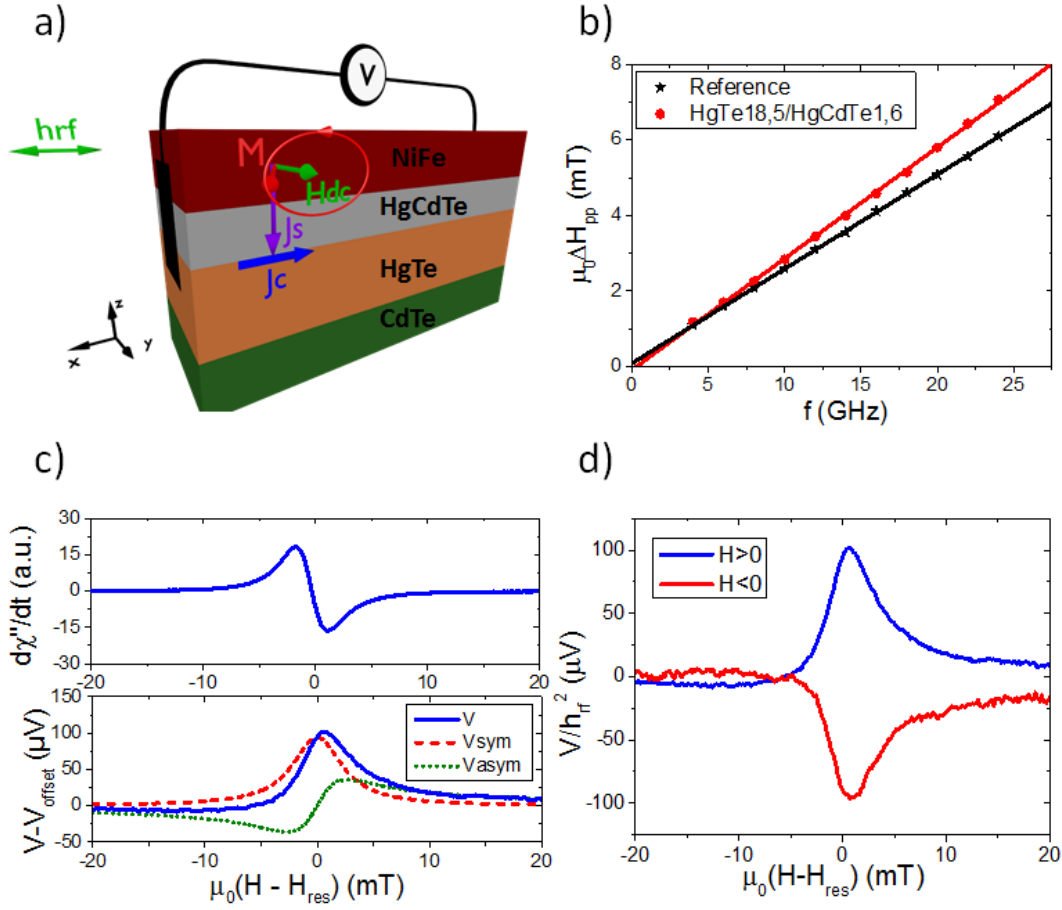


FIG. 5.4: a) Schematic representation of the structure used for the spin pumping by ferromagnetic resonance measurements. b) Broadband frequency dependence of the peak-to-peak FMR linewidth of the reference Si/NiFe (20nm) sample, and of a HgTe (18.5nm)/HgCdTe (1.6nm)/NiFe (20nm) sample. c) FMR and DC voltages, measured by spin pumping FMR on the same sample. The symmetric (red) and antisymmetric (green) contributions have been extracted from the measured signal (in blue). d) Spin-pumping signals obtained for a positive and a negative DC field, on the same sample. The signal amplitude leads to a produced charge current  $I_c = 1.35 \mu A/G^2$ .

retical studies underlined the necessity to protect the surface states with a very thin insulating layer to increase the conversion efficiency<sup>117;119</sup>, but without experimental demonstration yet. To confirm this we studied the dependence of the charge current with the HgCdTe barrier thickness (cf. figs. 5.5.a and 5.5.b). The measurements were all performed on HgTe layers of the same thickness (18.5nm), the thicknesses being measured by XRR after a soft Ar etching to reduce the HgCdTe barrier thickness. As expected, the produced currents are higher than in the case of the direct contact between NiFe and HgTe, for barriers from 0.6 nm to 3 nm. As the barrier thickness is increased the signal decreases due to a decreased spin current injection. A control sample with a 17 nm thick HgCdTe barrier has been deposited, showing a symmetric signal two orders of magnitude smaller than the one for a 0.6nm thick barrier ( $J_c/J_{cmax} = 0.03$ ). This extinction confirms that the observed conversion does not occur at the NiFe/HgCdTe interface and that the observed signal is not due to spin rectification effects. The decrease of the signal with the barrier points toward a decrease of the electronic coupling through the thick semiconducting/insulating HgCdTe layer<sup>262</sup>.



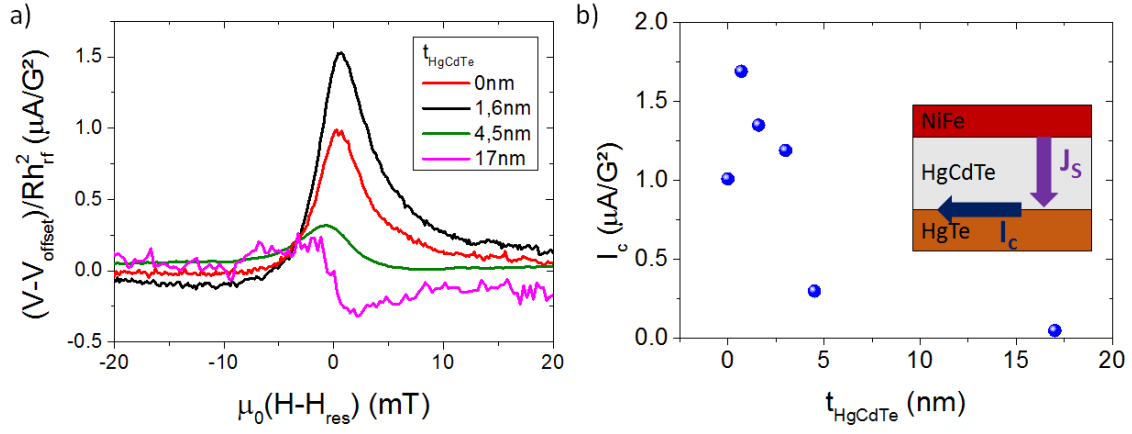


FIG. 5.5: Spin signal as a function of the HgCdTe interlayer thickness a) Spin pumping signals obtained for different thicknesses of HgCdTe barriers, normalized by the sample resistance. b) HgCdTe thickness dependence of the normalized charge current production. Inset: scheme of the stacking.

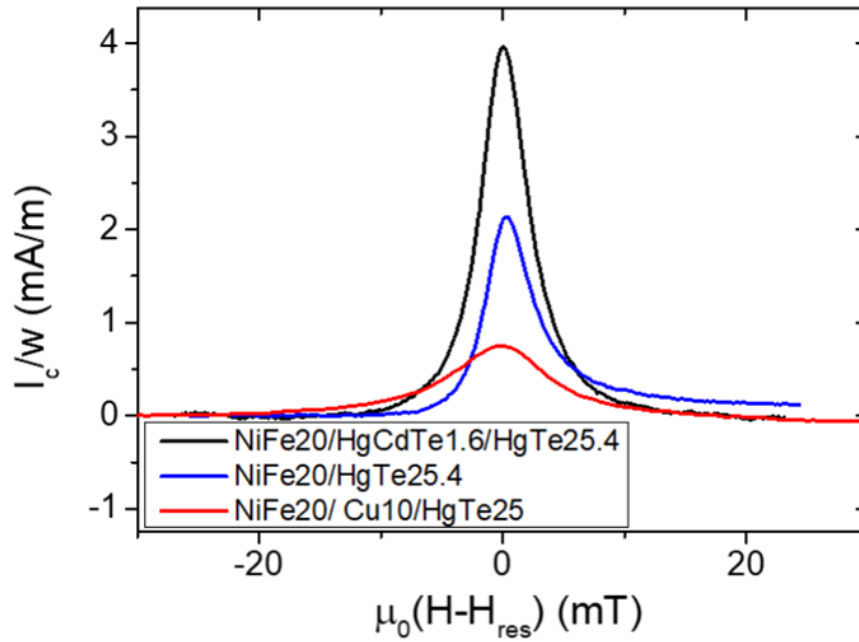


FIG. 5.6: Spin pumping signals obtained for different spacer layers, normalized by the sample resistance and width

Measurements with a Cu spacer layer instead of HgCdTe have also been performed. They exhibit a larger damping parameter and considerably smaller conversion efficiencies, even in comparison with NiFe in direct contact and even when accounting for the decrease in the precession cone angle due to the larger damping. These results shown in figure 5.6 suggest that the conversion efficiency is highly dependent on the material in contact with the TI and that a careful choice of the interlayer is needed to obtain an optimum spin to charge current conversion efficiency. Zhang and Fert predicted that the relaxation times involved are not the same for spin to charge conversion -scattering time- and charge to spin conversion -spin flip time and transfer time across the interface-<sup>117</sup>. Therefore the interlayer

that promotes an optimal conversion can be different for effects related to the direct Edelstein effect (as SOT) and Inverse Edelstein effect (as spin pumping or spin seebeck effect). Apart from a decrease of the electron scattering time due to the direct contact with a metal, the fact that Cu reacts easily with Tellurides could also modify the interface chemistry and destroy the surface properties of HgTe<sup>326</sup>.

### 5.1.4 Spin to charge conversion: role of the HgTe thickness

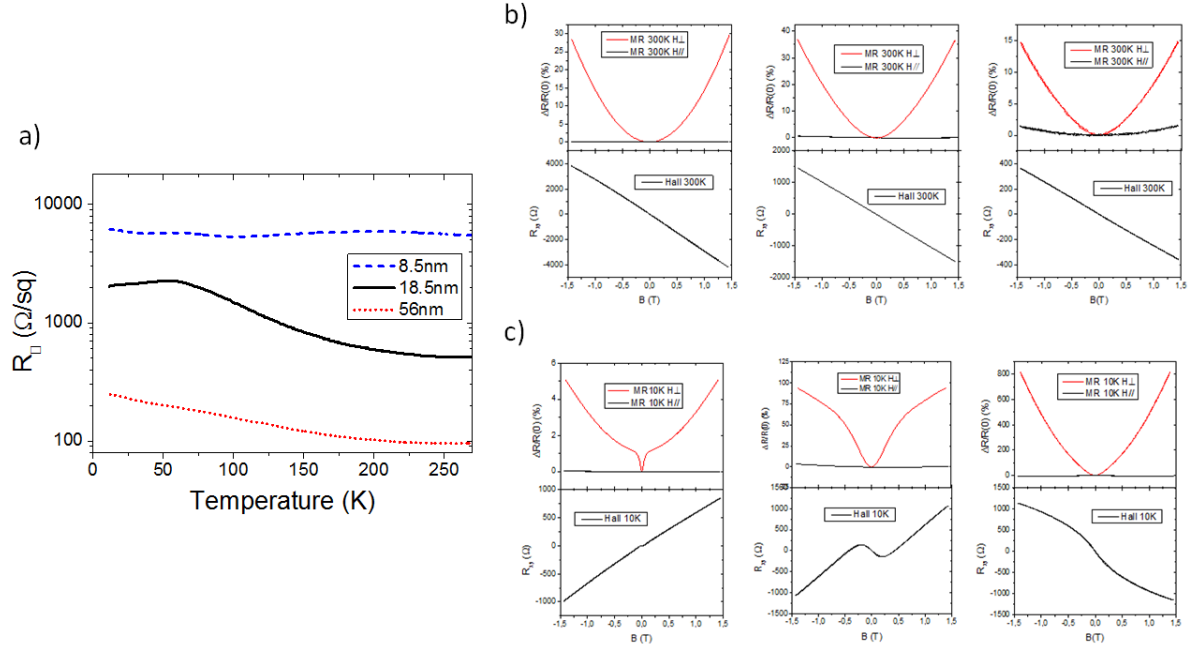


FIG. 5.7: Magnetotransport in HgTe thin films a) Sheet resistance as a function of the temperature, for three samples of different HgTe thicknesses: 8.5 nm, 18.5 nm and 56 nm. Magnetoresistances in perpendicular (red) and parallel (black) configuration, and Hall measurements, for the three different HgTe thicknesses at b) room temperature and c) 10K. From left to right HgTe thickness of 8.5 nm, 18.5 nm and 56 nm.

To understand the exact role of the bulk and surface states we have studied the temperature dependence of the sheet resistance as well as the Hall and magnetoresistance for different HgTe thicknesses (see figure 5.7.a). A resistance maximum is observed at around 50 K for the 18.5 nm thick HgTe layer. Its existence suggests the presence of two parallel channels of conduction, the first one corresponding to the insulating bulk of HgTe, with a resistivity decrease when increasing the temperature, the second one corresponding to the topological surface states, dominating the conductivity at low temperature<sup>307;327</sup>. When increasing the HgTe thickness to 56 nm, the bulk contribution dominates down to 10K: the resistance keeps increasing at low temperature, without any signature of a metallic-like behavior. For a thinner (8.5 nm) sample, where the bulk contribution is expected to be reduced, there is no overall increase of the sheet resistance when decreasing temperature. This presence of both bulk and surface state conduction is supported by Hall measurements shown in figure 5.7.b and c. At 300K, the transport is dominated by an n-type contribution usually associated to thermally activated bulk charge carriers, whereas at 10K both bulk p-type and n-type surface states contribution are observed. In both cases a strong Lorentz magnetoresistance associated with the large carrier mobility can be observed.

Note that while it resembles a weak antilocalization signature the measured MR at low temperature is the sum of a Lorentz contribution associated with highly mobile electrons at low magnetic field and less mobile holes at larger magnetic field. For all samples the carrier mobility is of the order of  $10^4 \text{ cm}^2/\text{V.s}$  at RT.

Let us now estimate the inverse Edelstein Length  $J_c^{2D}/J_s = \lambda_{IEE}$  with the HgTe thickness at a fixed HgCdTe thickness of 1.6 nm. One can possibly expect a thickness dependence associated to a spin to charge conversion occurring in the bulk of HgTe due to ISHE with  $J_c^{2D}/J_s \propto \tanh(2t/\lambda_s)$ . One can also expect an effect occurring at the HgTe \setminus HgCdTe interface associated with a Rashba effect that would exhibit no thickness dependence. But the observed dependence is very different as seen in figure 5.8, with a large increase of  $\lambda_{IEE}$  from  $t = 8.5 \text{ nm}$  to  $26 \text{ nm}$ , where the largest Inverse Edelstein length is obtained, and after which the efficiency drops. The error bars take into account the standard deviation from three measurements on  $J_c^{2D}$  and error bars on  $J_s$ . The large error bars for the 26 nm and 84 nm thick samples are due to a relatively large uncertainty on the extra damping.

Another interesting feature of the spin pumping method is its ability to determine the chirality of the Fermi circle. According to Hall and ARPES measurements<sup>318</sup>, in ungated samples the Fermi level is expected to be above the Dirac point. As the inverse Edelstein length is positive (same sign as Pt) this indicates that the helical fermi contour is counter-clockwise in the upper part of the cone, in accordance with predictions in HgTe<sup>328</sup>. Beyond its sign, the amplitude of the conversion rate is noteworthy. The conversion rate  $\lambda_{IEE}$  can reach a value of  $2.0 \pm 0.5 \text{ nm}$ , comparable to that of alpha-Sn ( $\lambda_{IEE} = 2.1 \text{ nm}$  according to Rojas Sanchez *et al*)<sup>62</sup>, i.e., the highest value recorded up to now at room temperature. This value is one to two orders of magnitude larger than the obtained value for spin charge conversion in Bi-based systems<sup>193;304;67</sup>, and can be ascribed to the higher value of the mobility and mean free path in HgTe.

In the following we will give a possible explanation to this conversion efficiency peak occurring around 25-30 nm thick HgTe. In an ideal topological insulator, the inverse Edelstein length is equal to the Fermi velocity  $v_f$  multiplied by the electron scattering time  $\tau$ ,  $\lambda_{IEE} = v_f \tau$  as shown in chapter 1, for a spin texture with 100% in plane spin polarization  $P$ . As the Fermi velocity of Dirac Fermions is constant as a function of the Fermi energy (linear dispersion), a decrease in the conversion efficiency can originate from a decrease in the scattering time or in a modification of the spin texture.

The calculation performed in chapter 1, but also by Zhang and Fert<sup>117</sup>, take into account only the Topological surface states while other scattering can occur. The hybridization of the Surface states with the bulk band of HgTe but also any other layer in contact with the topological insulator could significantly contribute to a decrease in the conversion efficiency. The exact role of the bulk on the scattering mechanisms is not trivial but we can use the simple empirical model of Yamamoto *et al.*<sup>329</sup> to account for the existence of two relaxation channels, a bulk channel and a surface channel we have:

$$\lambda_{IEE} \propto \frac{R_{bulk}}{R_{bulk} + R_{surf}} \quad (5.1)$$

with  $R_{bulk}$  and  $R_{surf}$  the respective sheet resistance of the bulk and surface. While very simple this

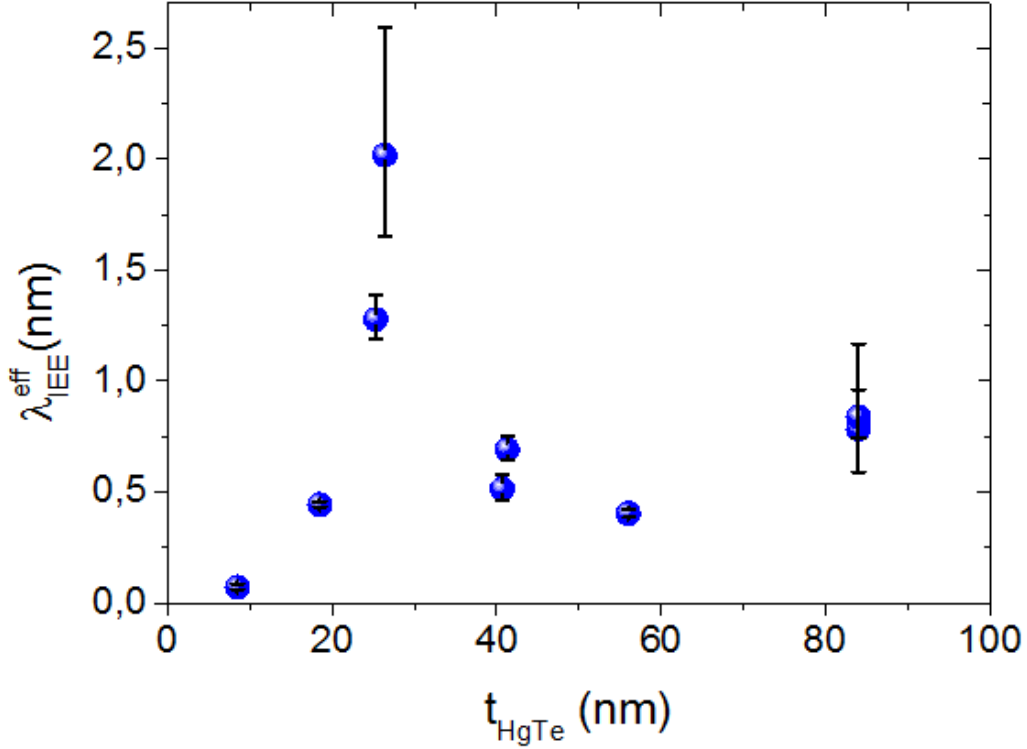


FIG. 5.8: *HgTe* thickness dependence of the inverse Edelstein length. The *HgCdTe* barrier thickness is the same for all the samples  $t_{\text{HgCdTe}} = 1.6\text{nm}$ .

empirical model emphasize the fact that not only surface contribute and that the scattering can occur in the bulk states. The existence of a larger bulk contribution explains the decrease of the conversion efficiency for thick *HgTe* layers as observed in figure 5.8.

But with this simple model the inverse Edelstein length should be maximum in ultra-thin film where the bulk contribution is minimum. This is not in agreement with our experimental observation of a maximum conversion in a 26 nm thin film and an almost zero conversion in a 8.5nm film. The origin of this decrease is likely to be the hybridization of the upper and lower *HgTe* surface states. Due to the overlap of the two surfaces wavefunctions, an electronic transport through states delocalized between the surfaces can be observed, where the spin degeneracy is restored<sup>330</sup>. As a consequence, the spin-momentum locking properties, and thus the polarization  $P$  and the spin-to-charge conversion efficiency are expected to progressively disappear as the thickness of the TI shrinks<sup>331</sup>. Interestingly, the maximum conversion efficiency is obtained close to the 2D-3D topological insulator transition. The decrease observed below this value is consistent with the hypothesis that the main origin of the decrease is the hybridization, as the wavefunction extension is predicted to be of the order of 5 nm<sup>321;332</sup>. This emphasize the importance to optimize both the top-bottom surface hybridization and the surface-bulk hybridization to obtain an efficient conversion in topological insulators. One can extend the empirical model above to account for the top-bottom surface hybridization in the conversion efficiency:

$$\lambda_{IEE} \propto P(t_{TI}) \times \frac{R_{bulk}}{R_{bulk} + R_{surf}} \quad (5.2)$$

This accounts for the thickness dependent spin polarization of the topological surface states  $P(t_{TI})$ . Although the analogy with Bi-based TIs has to be taken cautiously, recent measurements on Bi<sub>2</sub>Se<sub>3</sub> also suggest that the maximal conversion efficiency is reached when surface states are still hybridized, and reduced at larger thicknesses due to larger bulk states contribution<sup>333</sup>.

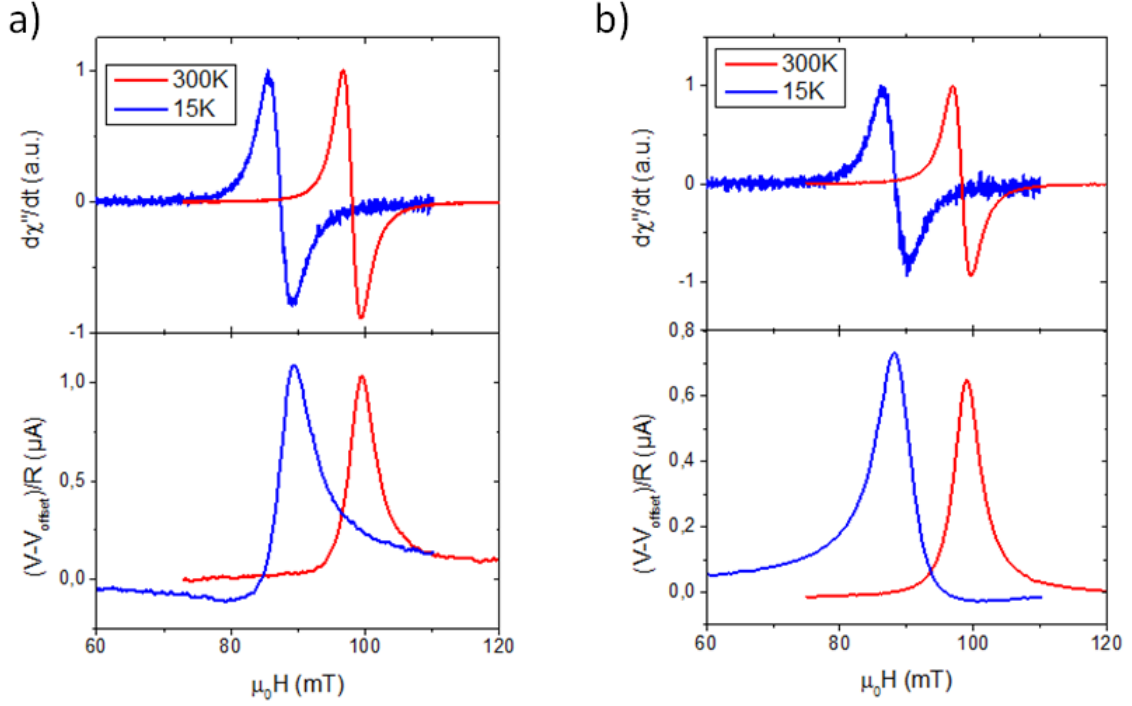


FIG. 5.9: FMR and DC voltages measured by spin pumping FMR on two different samples: a) HgTe (26.4 nm) \HgCdTe (1.6 nm) \NiFe (20 nm) and b) HgTe (56 nm) \HgCdTe (1.6 nm) \NiFe (20 nm), at 15K and 300K.

Note that the conversion remains large at low temperature as seen in figure 5.9. In a 26.4nm and 56nm thick HgTe samples measured at 15K, the current production is comparable or even larger than the one at room temperature while the bulk states are expected to be partially frozen. Unfortunately the evaluation of the conversion efficiency at low temperature is difficult due to modification of NiFe FMR lineshape in particular the linewidth at low temperature. This is either due to its natural oxidation (here NiFe is uncapped) or to a strong strain on CdTe at low temperature. We even observed several CdTe samples that broke when cooled-down.

To conclude we observed at room temperature the spin-to-charge current conversion in the topological surface states of strained HgTe, with a counter-clockwise direction of the spin rotation, and very high conversion rates. As expected theoretically, the conversion can be optimized using a HgCdTe barrier. To obtain the highest conversion rate, it seems that the HgTe layer thickness has to be thick enough to decouple the top and bottom surface, but thin enough to avoid the relaxation within the bulk. These

results show that HgTe has very attractive properties for spintronics and especially to obtain a better understanding of the mechanisms involved in the spin-charge current interconversion. Following these results I am now working with Yu Fu, post-doc at Spintec, and Jules Papin, PhD student in Leti on magnetotransport measurements in HgTe based heterostructures.

## 5.2 $Sb_2Te_3$ : a sputtered deposited topological insulator material

HgTe is an ultraclean system that should allow to better understand the physics of spin to charge interconversion phenomenon. Nonetheless it suffers from the same problem as plenty of other topological insulator or Rashba interfaces it is limited to a given substrate -CdTe- and relies on MBE deposition. Even if the conversion efficiency is not as large, heavy metals as Pt, Ta and W can be deposited by sputtering on 300 mm Silicon wafers which makes them compatible with mainstream electronics and industrial facilities at lower cost. Even if particularly exciting phenomena can be observed in TIs and Rashba interfaces from a physicist point of view, the fact that the growth is difficult to perform, costly and on non-Silicon wafers immediately makes them less appealing for industry.

We would like to note here that there have already been attempts to deposit  $Bi_2Se_3$  on Silicon dioxide ( $SiO_2$ ) by magnetron-sputtering but the quality of the film was way poorer than the one deposited by MBE with small grain size of only few nanometres<sup>334;303</sup>, poor stoichiometry<sup>303</sup> or even amorphous films<sup>335</sup>. Interestingly this strong disorder didn't affect much the conversion efficiency, and very high charge to spin conversion was demonstrated<sup>303;335</sup> as well as relatively high spin to charge conversion<sup>193</sup>. While topological insulators are usually considered to be insensitive to disorder<sup>103</sup>, it is not true for any level of disorder<sup>336</sup>. It is thus unclear if amorphous or nearly amorphous layers with lack of periodicity and strong disorder preserve topological insulators properties. For example only crystalline  $Sb_2Te_3$  shows transport signature of topological surface states<sup>337</sup>. As a consequence thin film of high crystalline quality are needed to be sure to have topological surface states. It would therefore be highly desirable to grow a topological insulator on large  $SiO_2$  wafers and preserve a high enough sample quality to be comparable to MBE deposited samples. This is a possibility offers by Antimony Telluride  $Sb_2Te_3$ .

### 5.2.1 Sputtering: an industry compatible process

Among the large number of topological insulators  $Sb_2Te_3$  is interesting for three reasons: it has been largely understudied, especially when compared to  $Bi_2Se_3$ , with only some reports of spin-charge interconversion<sup>338;339;116</sup> while it is one of the first discovered topological insulator<sup>107</sup>. Second, the reports comparing it to other BiSbTe systems shows a higher or similar conversion efficiency<sup>116;339</sup> while having a larger bulk contribution which is quite intriguing. Third, and maybe the most interesting, compared to other topological insulator it is already widely used in industry either as a parent compound of GeSbTe based phase-change memory or in  $GeTe/Sb_2Te_3$  phase change superlattices<sup>340;341</sup>. Therefore several industrial actors have developed industry compatible deposition technique for this material.

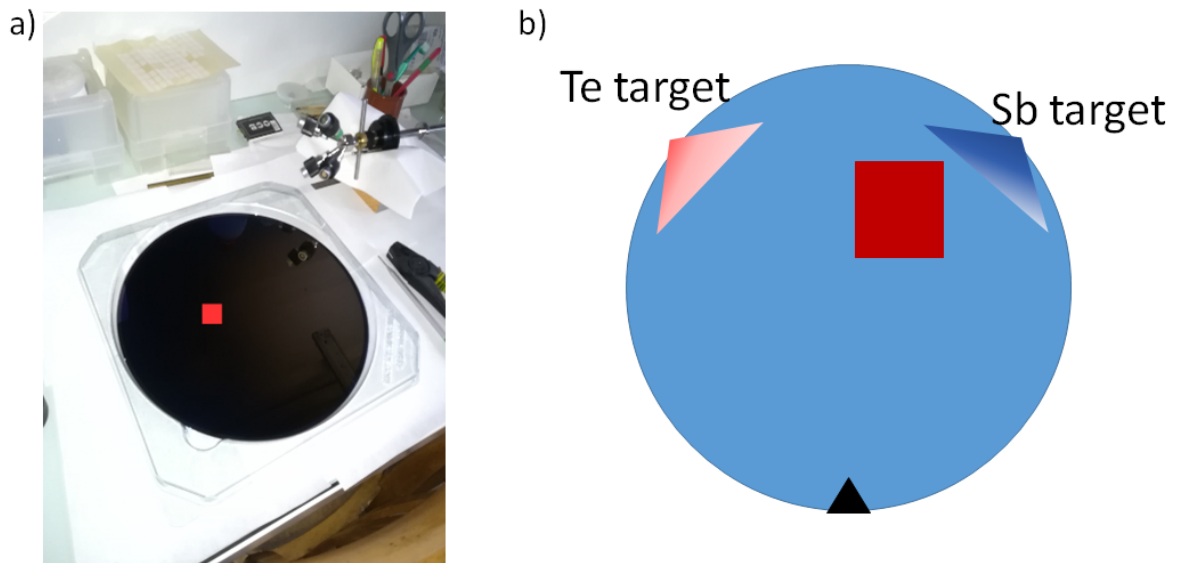


FIG. 5.10: Thanks to the sputtering technique it is possible to obtain large size topological insulator materials. a) 300 mm (12 inches) Silicon wafer with SbTe sputtered on top, in red the typical size of 1 inch substrate deposited by MBE. b) The co-sputtering of Sb and Te allows to obtain a gradient of composition and thickness, in this manuscript we will focus on the area in red with an 2:3 stoichiometry.

In particular Leti and their industrial partners have developed a sputtering technique based on co-deposition of Sb and Te at high temperature to obtain high quality  $Sb_2Te_3$  samples<sup>341</sup> deposited on  $SiO_2$ . This deposition is made on 300 mm (12 inches) thermally oxidized silicon wafers as shown in figure 5.10.a with sample size considerably larger than the usual 1 inch or 2 inches wafers that we are generally using in the lab. This makes the deposition of high quality topological insulator already industry compatible, on  $SiO_2$  which offers possibility to integrate a back-gate<sup>342</sup>. Nonetheless as they are sputtered instead of MBE deposited they might still have different properties. It is therefore necessary to study some of the materials and transport properties as well as the conversion efficiency in these thin films. The wafer was kept static during sputtering process leading to a position dependent thickness and stoichiometry allowing to study several scenario on a single wafer. In this study we will focus on a particular position on the wafer depicted in figure 5.10.b. In this region a 10 nm thin film of  $Sb_2Te_3$  stoichiometry is expected, we also measured other regions of the wafer with thinner films (7 nm and 4 nm). It is of course possible to deposit uniformly a  $Sb_2Te_3$  thin film by making the codeposition on a spinning wafer but without the possibility to study thickness or stoichiometry dependence on a single wafer.

## 5.2.2 High quality thin films

Before studying the sample transport and spin transport properties we should first verify that it is a  $Sb_2Te_3$  thin film with the possibility to show comparable properties to MBE deposited thin films. The first step it to confirm that it possesses a good (001) orientation along the c-direction as well as the



$Sb_2Te_3$  stoichiometry similarly to MBE deposited films.

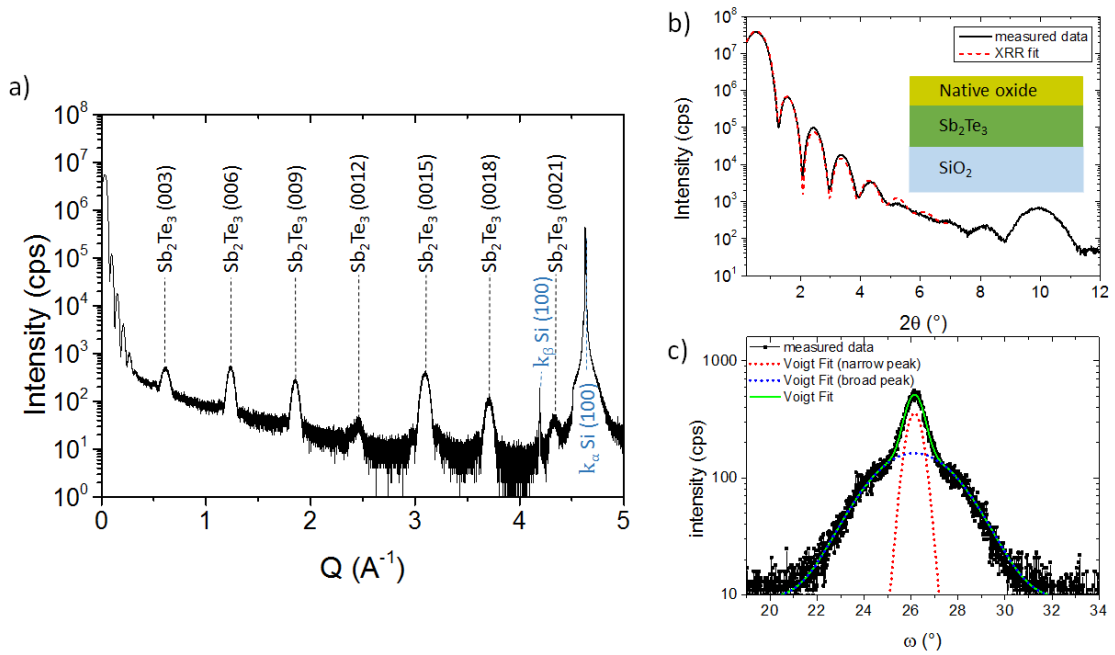


FIG. 5.11: X-ray diffraction and reflectivity measurements. a) X-Ray Diffraction  $\theta - 2\theta$  spectrum for a  $Sb_2Te_3$  10nm-thick film deposited on thermally oxidized  $SiO_2$ . The peaks corresponding to  $Sb_2Te_3$  (00l) are represented in black, the blue color corresponding to the substrate peaks. b) Corresponding X-Ray Reflectivity spectrum. The black curve represents the experimental data, the red dashed curve corresponds to the fit. The structure used for the fit is represented in the inset. The optimal fit is obtained for thicknesses of 9.6 nm for the  $Sb_2Te_3$  film, 1 nm for the oxide layer with a 0.7 nm roughness. The first (003) peak prevents an optimal fitting of the XRR. c) Rocking curve ( $\omega$  - scan) around the (0015) peak, composed of the sum of a broad peak and of a narrow one, with two different mosaic spread. The fit, represented in green, is done using the sum of two Voigt functions with respective FWHM of  $0.860 \pm 0.006^\circ$  and  $4.156 \pm 0.034^\circ$ .

To check the crystal orientation, X-Ray Diffraction measurements were performed in out-of-plane  $\theta - 2\theta$  configuration, using a Panalytical Empyrean diffractometer equipped with a cobalt source, ( $K_\alpha=0.179\text{nm}$ ) operated at 35 kV and 50 mA and equipped with a  $K\beta$  filter on the diffracted beam. Figure 5.11.a shows the out-of-plane  $\theta - 2\theta$  diffraction spectra along the Si (h00) reciprocal direction. In addition to the substrate Si (100) peak, we can observe several other peaks associated with the sputtered  $Sb_xTe_y$  layer. From the positions and spacing of these peaks we can confirm a  $Sb_2Te_3$  stoichiometry with a (001) crystal orientation<sup>343;344</sup>. In particular these peaks are different from the  $Sb_8Te_9$  ones, that can be obtained in strong Tellurium defective films<sup>341</sup>. The attribution of the different peaks is shown in figure 5.11.a, from this we can clearly see that the most intense peaks are the (006) and (0015) peaks whereas the (0012) peak is particularly weak in agreement with MBE deposited  $Sb_2Te_3$ <sup>345;346</sup>. Around the most intense (006) and (0015) Bragg peaks it is even possible to see side fringes -Laue Oscillations- evidencing the high quality and low roughness of the thin film<sup>347</sup>. X-ray diffraction measurement of 4nm and 7nm thin films has also been performed. For these very

thin film the (001) crystal orientation and  $Sb_2Te_3$  stoichiometry were confirmed, evidencing the possibility to obtain ultra-thin topological insulator materials with sputtering on  $SiO_2$ . These results are shown in appendix E as well as how to differentiate the  $Sb_2Te_3$  from the  $Sb_8Te_9$ .

From the full-width at half maximum of the XRD peak  $\Delta Q$  in the out of plane  $\theta - 2\theta$  configuration we can evaluate the grain size  $D_{thickness}$  in the out of plane direction and dispersion of the lattice parameter  $\Delta a$  using the following formula<sup>348</sup>

$$\Delta Q_{\theta-2\theta}^2 = \left( \frac{2\pi}{D_{thickness}} \right)^2 + Q^2 \left( \frac{\Delta a}{a} \right)^2 \quad (5.3)$$

We obtain a grain size/thickness of 10.2 nm as well as the dispersion of the lattice parameter of less than 1%. This thickness is confirmed through X-ray reflectivity (XRR) measurements shown in figure 5.11.b. The optimal fitting is obtained for a 9.6 nm film and a roughness of 0.7 nm. From XRR we can also estimate that a thin native oxide layer of 1 nm forms on top of the deposited film. Note that the thickness of this oxide didn't change with time for several XRR measurements evidencing a fast oxidation of the surface after the sample is taken out of the deposition chamber followed by a considerably slower oxidation process in the volume.

The good crystal orientation is also confirmed by XRD rocking curves measurements  $\omega$  - scan. As can be seen in figure 5.11.c the rocking curve is composed of two different peaks a narrow one with a fullwidth at half maximum of  $0.86^\circ$  and a wide one with a larger width of  $4.15^\circ$ . This evidence the good orientation of the crystals even in 10 nm thin films. This is comparable to MBE deposited thin films on amorphous layers<sup>349</sup> or on Ge(111)<sup>346</sup> but not as good as lattice matched substrate<sup>345</sup>. The double peak nature of the rocking curve is common in SbTe and GeSbTe thin film<sup>350</sup> and is still not fully understood with different possible scenario including difference of crystallite size among the films as proposed by Hilmi *et al.*<sup>351</sup>. From the rocking curve we can also evaluate the crystal size in plane  $D_{plane}$  as well as the mosaicity  $\Delta\xi$ <sup>348</sup>

$$\Delta Q_{\omega}^2 = \left( \frac{2\pi}{D_{plane}} \right)^2 + Q^2 \Delta\xi^2 \quad (5.4)$$

From the fit of the narrow peak we obtained a mosaicity of  $0.9^\circ$ . The crystal size is expected to be large but can not be determined accurately as the position of the intercept is close to zero.

To better characterize the sample quality we have also performed microscopy measurements including Transmission electron microscopy (TEM) and Atomic Force Microscopy (AFM). From the high resolution HAADF-TEM image we can see the  $Sb_2Te_3$  layer with characteristic Te-Sb-Te-Sb-Te Quintuple layer stacking. The thickness from TEM image is of 9 Quintuple Layers which is around 9.15 nm<sup>344</sup> a result compatible with the previously determined thickness by XRR and XRD of  $\approx 10$  nm. This TEM image confirms the large crystal size and the general high quality of the thin film with a well ordered crystal. From this TEM image we can see a blurry region between the Au top layer and the  $Sb_2Te_3$ . It is unlikely to be Au reacting with Sb or Te or due to a thin oxide layer. In both scenario due to the presence of heavy atoms the contrast should have been more intense in dark field. Furthermore before deposition of Au a soft Argon ion etch was performed to eliminate the thin

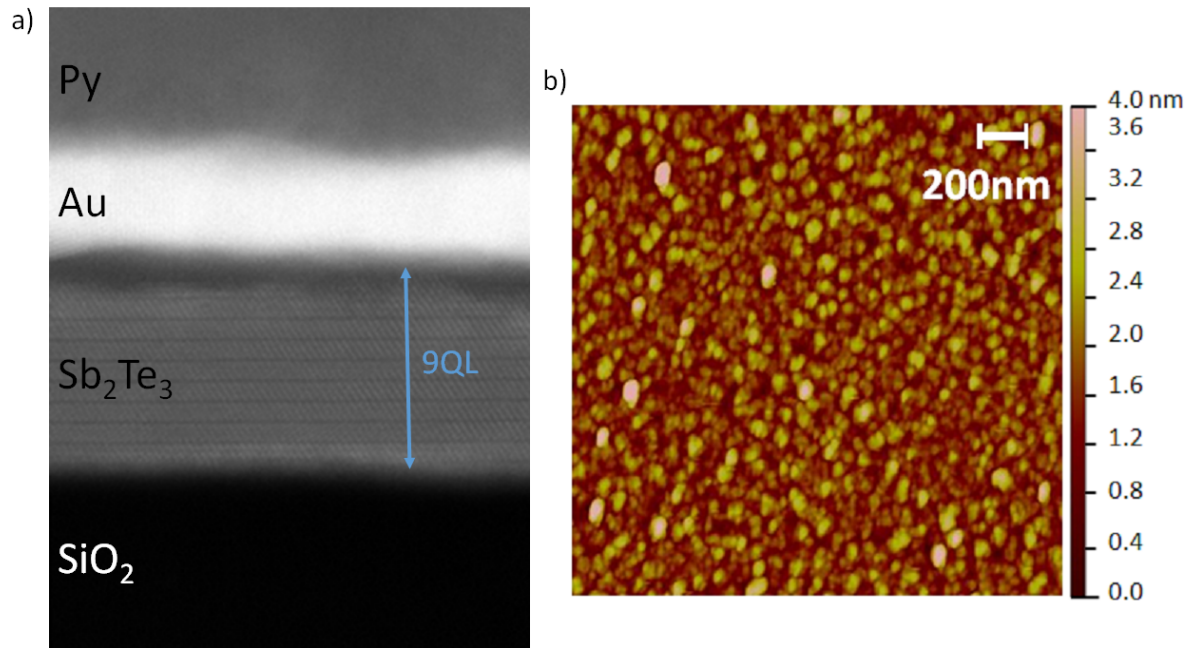


FIG. 5.12: a) TEM image of a  $Sb_2Te_3(10nm)\backslash Au(5nm)\backslash Py(20nm)$  heterostructure. The Quintuple layers and van der Waals gap are clearly visible, the layer thickness is estimated to be 9 Quintuple layers. b) Atomic Force Microscopy image of a 10 nm-thick  $Sb_2Te_3$  film. The mean grain size is 100 nm, and the RMS roughness is of 0.6 nm.

oxide layer thinning it down well below the 1 nm thickness of the blurry region. In fact the observed region appears to be vacuum. It is likely to be associated with the FIB lamellae preparation that have disattached the Au layer associated with easy delamination of Van der Waals thin films. While this observation is not fully understood this TEM image evidence the negligible modification of the  $Sb_2Te_3$  surface with Au deposition and the extremely high crystal quality.

The AFM observation of the thin films shown in figure 5.13.b confirms the low roughness of the thin film with a measured RMS roughness of only 0.6 nm compatible with X-Ray Reflectivity fitting. The main difference between MBE deposited films on lattice matched substrate and sputtered film on  $SiO_2$  as well as MBE deposition on amorphous substrate<sup>349</sup> is visible here: the absence of any preferred in-plane orientation that is usually associated with the presence of triangular grains<sup>311;348</sup>. When deposited on amorphous layers the  $Sb_2Te_3$  has a fiber texture with no in plane order. We can deduce an average grain size of 100 nm from this AFM image evidencing the polycrystalline nature of the film with large grain and moderate disorder of the structure. Especially when compared with other results reporting deposition of TIs on  $SiO_2$  with a lack of orientation and particularly low crystal size of some nm<sup>303</sup>, or even nearly amorphous films<sup>335</sup>. All these characterizations evidence the high sample quality.

### 5.2.3 Magnetotransport: Weak Antilocalization

Following the structural characterization we have performed transport measurements on this 10 nm sputtered  $Sb_2Te_3$  thin film. In particular we have performed magnetotransport measurements at low

temperature to observe effects associated to strong spin orbit interactions in 2D materials known as 2D weak antilocalization (WAL). It is not a demonstration of the existence of TSS at the surface of  $Sb_2Te_3$  but it is a good clue that strong spin orbit coupling and 2D transport is at play in the thin film. We will not describe extensively the physics of the WAL here but compare the results to expectations and previous observations in TIs. All the measurements performed here were done in Van der Pauw configuration<sup>253</sup> to avoid any damage to the structure that can occur in Van der Waals thin films during patterning.

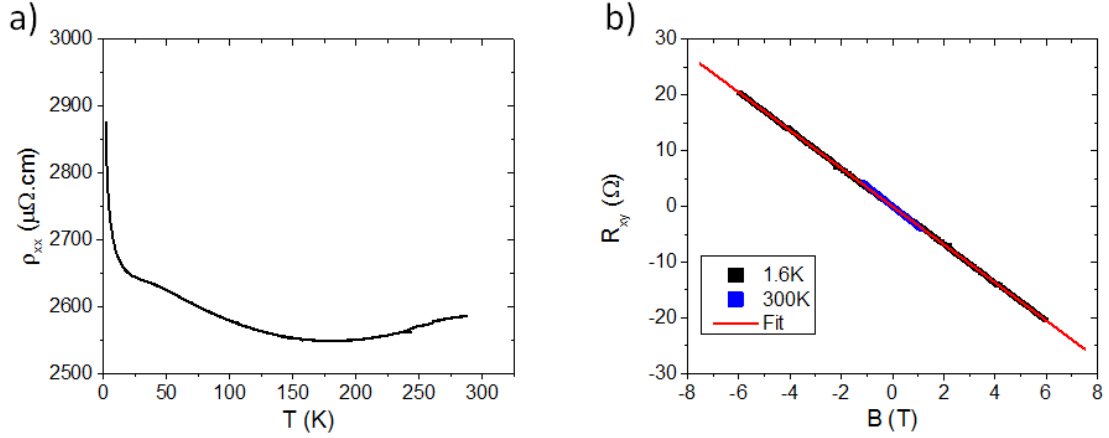


FIG. 5.13: a) Resistivity as a function of temperature in a 10 nm  $Sb_2Te_3$  thin film. b) Hall measurements at 1.6 K and 300 K evidencing no change in the carrier concentration. These measurements were performed in Van der Pauw configuration

Prior to the weak antilocalization measurements we have performed conventional magnetotransport measurements including a resistivity measurement and a Hall measurement shown in figure 5.13. The resistivity is almost constant with temperature showing some evidence of metallic like transport above 150K. But below 100K it is increasing suggesting a hopping mechanism and electron-electron interaction below 10K. This indicates a weakly disordered system which is common in  $Sb_2Te_3$ ,  $Bi_2Te_3$  or  $Bi_2Se_3$  with similar resistivity dependence as seen for example in Park *et al.*<sup>352</sup> or Kim *et al.*<sup>353</sup>. There is no signature of insulating bulk states or surface transport in the temperature vs resistivity. It is to be noted that it is similar for most of the TIs as they are not insulators in the Mott sense<sup>312</sup> due to high density of intrinsic defects. Similarly to many other TIs as  $Sb_2Te_3$ ,  $Bi_2Te_3$  or  $Bi_2Se_3$  deposited by MBE unavoidable defects as Tellurium or Selenium vacancies<sup>308</sup> lead the Fermi level to cross a bulk-band and to be far from the charge neutrality point. Only compensated topological insulators as BiSbTe or BiSnSe have an insulating behavior.

This is also the case in the sputtered deposited samples where similar kind of defects are expected and as confirmed by the Hall measurement. The transport is p-type, as usually observed in  $Sb_2Te_3$ . The carrier density is of  $n_{3D} = 1.82 \pm 0.1 \times 10^{20} \text{ cm}^{-3}$  with almost no temperature change. The mobility is also nearly unaltered with temperature and is  $\mu = 14.4 \pm 1 \text{ cm}^2/\text{V.s}$ . The carrier density measured in the 7 nm film was of  $4.2 \times 10^{20} \text{ cm}^{-3}$  evidencing the role of thickness in the density of defects. This relatively large carrier density (low mobility) is around 5 times higher (lower) than

MBE deposited films of similar thicknesses<sup>116</sup>. This evidence the higher level of disorder in our thin films compared to MBE deposited ones on lattice matched substrate, this is not unexpected due to the absence of in-plane order and is in line with the obtained  $\rho(T)$  curve. In sputtered  $Bi_2Se_3$  DC *et al.*<sup>303</sup> obtained a carrier density of  $1.2 \times 10^{21} \text{ cm}^{-3}$  in 16 nm films, while MBE deposited films of  $Bi_2Se_3$  have a typical carrier density of  $4 \times 10^{19} \text{ cm}^{-3}$ <sup>348</sup>. This is a clear evidence that our samples transport properties are closer to MBE films than previous attempts but still have a larger disorder.

The nearly metallic behaviour of our film and their high crystalline quality indicate that the sample still remain in a low disorder regime. The level of disorder is usually defined using the Ioffe Regel criterion<sup>312</sup>, the limit of low to high disorder is obtained for  $k_F\lambda = 1$  with  $k_F$  the k-vector at the Fermi energy and  $\lambda$  the mean free path. Assuming a 3D isotropic Fermi surface  $k_F = (3\pi^2 n_{3D})^{1/3}$  and  $\lambda = \frac{\hbar\mu}{e}(3\pi^2 n_{3D})^{1/3}$ . In our case  $k_F\lambda \approx 9$ , and the mean free path  $\lambda$  is of 15 nm. In this sample we have  $k_F\lambda \gg 1$ , this evidence a low level of disorder, low enough to preserve the existence of topological surface states and avoid any localization<sup>337;354;312</sup>.

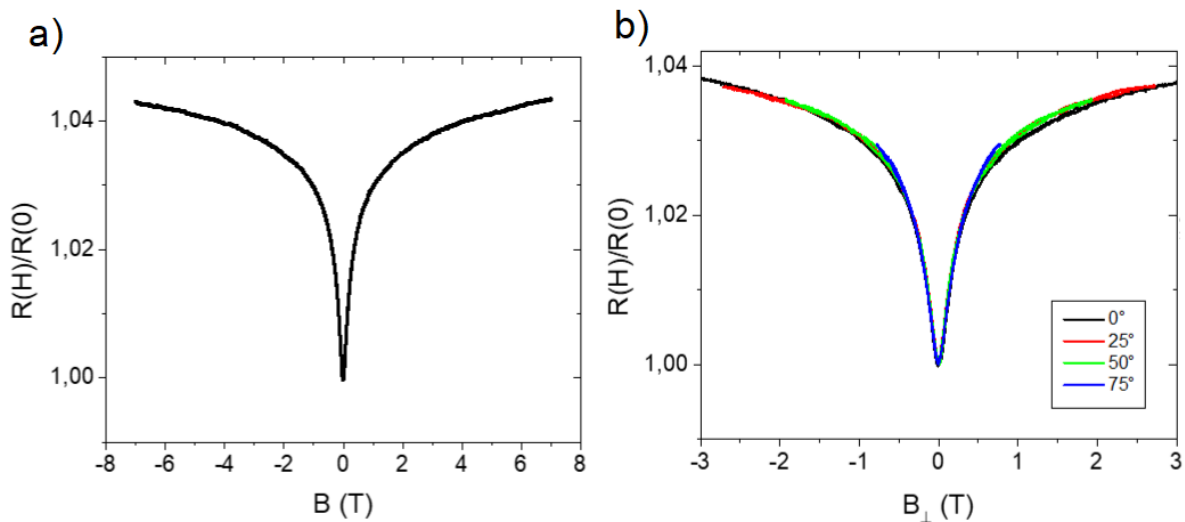


FIG. 5.14: a) Magnetoconductance at 1.6 K with magnetic field out of plane. A Weak AntiLocalization cusp is observed at low fields. Above 2T, the resistance evolves linearly with the magnetic field. b) Dependence of the magnetoconductance with the normal component of the magnetic field, for various angles between the magnetic field and the out-of-plane direction.

One of the common signature to predict the presence of topological surface states in Topological insulators is to measure a magnetoconductance effect occurring at low temperature and known as Weak antilocalization (WAL). WAL is due to quantum interference between electrons executing forward and time reversed paths in a loop. In presence of strong spin-orbit coupling with spin momentum locking this leads to a destructive interference in absence of an external magnetic field. The application of an external magnetic fi

eld perpendicular to the loop will lead to an increase of the resistivity<sup>355</sup>. Weak antilocalization can exist in non-topological materials and can be observed in Ag, Au<sup>356</sup> or InAs<sup>357</sup> for example . In topological insulators due to both the strong spin orbit coupling and spin momentum locking WAL has been observed by several groups with some examples given in Brahlek *et al.*<sup>312</sup>. One of the specific



feature of WAL in topological surface states is its two dimensional nature and the number of conduction channels of one per surface. As can be seen in figure 5.14.a a positive magnetoresistance typical of WAL cusp is observed in 10 nm thick  $Sb_2Te_3$  under high magnetic field at 1.6 K . To confirm the two dimensional nature of the magnetoresistance an angular dependence of the magnetoresistance have been performed, as expected for 2D-WAL a dependence upon the out of plane magnetic field was obtained (figure 5.14.b). Note that we also observed 2D-WAL in the 7 nm film.

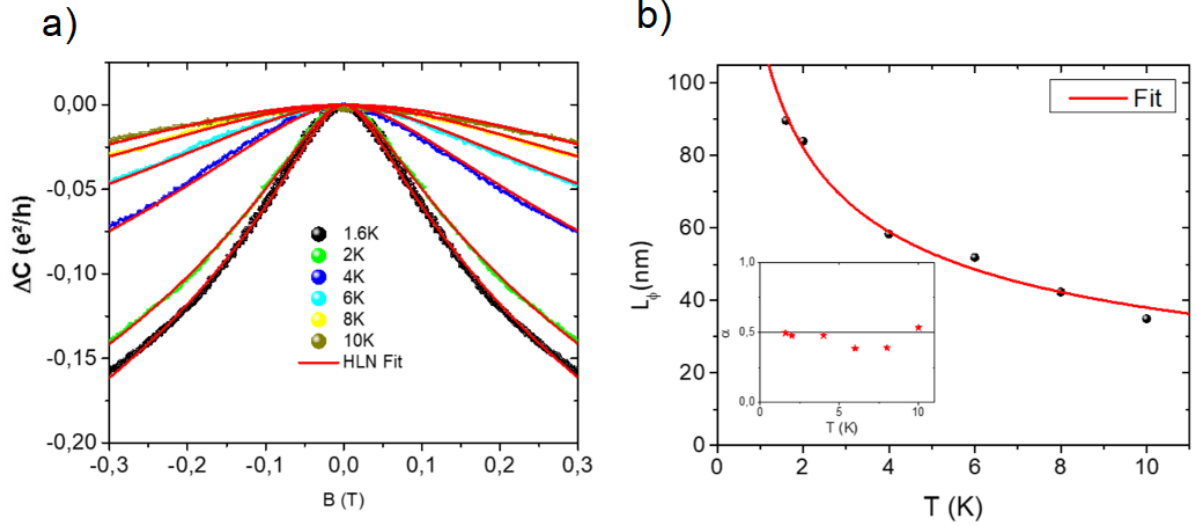


FIG. 5.15: a) Low field magnetoconductance at various temperatures from 1.6K to 10K fitted using the HLN model. b) Phase coherence length  $L_\phi$  and characteristic parameter  $\alpha$  (inset) extracted from the HLN fitting, represented as a function of the temperature.

The corresponding change of conductance under a perpendicular magnetic field can be analyzed with the simplified Hikami, Larkin, Nagaoka (HLN) equation<sup>358</sup>

$$\Delta C = -\frac{\alpha e^2}{2\pi^2 \hbar} \left[ \Psi \left( \frac{\hbar}{4eBL_\phi^2} + \frac{1}{2} \right) - \ln \left( \frac{\hbar}{4eBL_\phi^2} \right) \right] \quad (5.5)$$

Here,  $\Psi(x)$  is the digamma function,  $L_\phi$  is the phase coherence length and  $\alpha$  is a prefactor that is determined by the number of independent coherent channels. A single surface channel gives  $\alpha = 0.5$ , while two independent surface channels give  $\alpha = 1$ . The HLN equation is valid if the magnetic length  $l_B = \sqrt{\frac{\hbar}{eB}}$  is much longer than the mean free path<sup>352;359</sup>. Previously we estimated that the mean free path is of 15 nm in this sample. Therefore the fitting of the HLN function is performed in the  $[-0.3 \text{ T}; 0.3 \text{ T}]$  range so that  $l_B$  is at least three times the mean free paths. The temperature dependence of the WAL as well as the fittings are shown in figure 5.15.a with results of the fitting shown in figure 5.15.b. The phase coherence length is close to 100 nm at 1.6 K and varies as  $T^{-0.48 \pm 0.03}$  which is close to the  $T^{-0.5}$  predicted for the electron-electron interaction (EEI) as the main decoherence channel<sup>360</sup>. This is also compatible with the temperature dependence of the resistivity at very low temperature that it typical for EEI. The fitting gives an  $\alpha$  value close to 0.5 *i.e.* only one 2D conduction channel in the  $Sb_2Te_3$  instead of the two independent surface channels that are expected. In fact the  $\alpha$  value in TIs is usually close to 0.5 and it is only under some specific conditions that requires further engineering

of the material as induced disorder via annealing<sup>352</sup> or band-bending engineering<sup>312</sup> that a value of 1 can be reached. The value of 0.5 indicates that a coupling is allowed between the two surfaces either through bulk conduction or through tunnelling in the ultrathin regime. As the thickness of the  $Sb_2Te_3$  is above the tunnelling limit of 4QL (4nm)<sup>361;362</sup> it is likely to be an effect associated with bulk.

## 5.2.4 Spin to charge interconversion

Now that we have demonstrated that our  $Sb_2Te_3$  thin films are comparable both in material and transport quality to MBE deposited films, we turn onto the spin pumping FMR measurements. As the  $Sb_2Te_3$  is deposited in a specialized sputtering setup dedicated to phase change materials or semiconductors, we can not deposit in situ a ferromagnetic layer or a metallic layer directly on it. To perform the spin pumping measurements we have therefore etched the  $Sb_2Te_3$  layer prior to the deposition to suppress the thin oxide layer and deposited an Au buffer layer of 5nm followed by a 20 nm Permalloy film by evaporation. The stacking is shown in the TEM image of figure 5.12.a. Au has a large spin diffusion length around 40 nm<sup>363</sup> thus allowing spin injection from the NiFe in the  $Sb_2Te_3$ . More importantly it is unreactive with tellurides allowing to avoid any strong modification of the interface chemistry. As observed by Lee Walsh *et al.* in  $Bi_2Se_3$ /NiFe the direct deposition of a ferromagnetic metal in direct contact with a Se and likely Te rich TI is detrimental<sup>325</sup>.

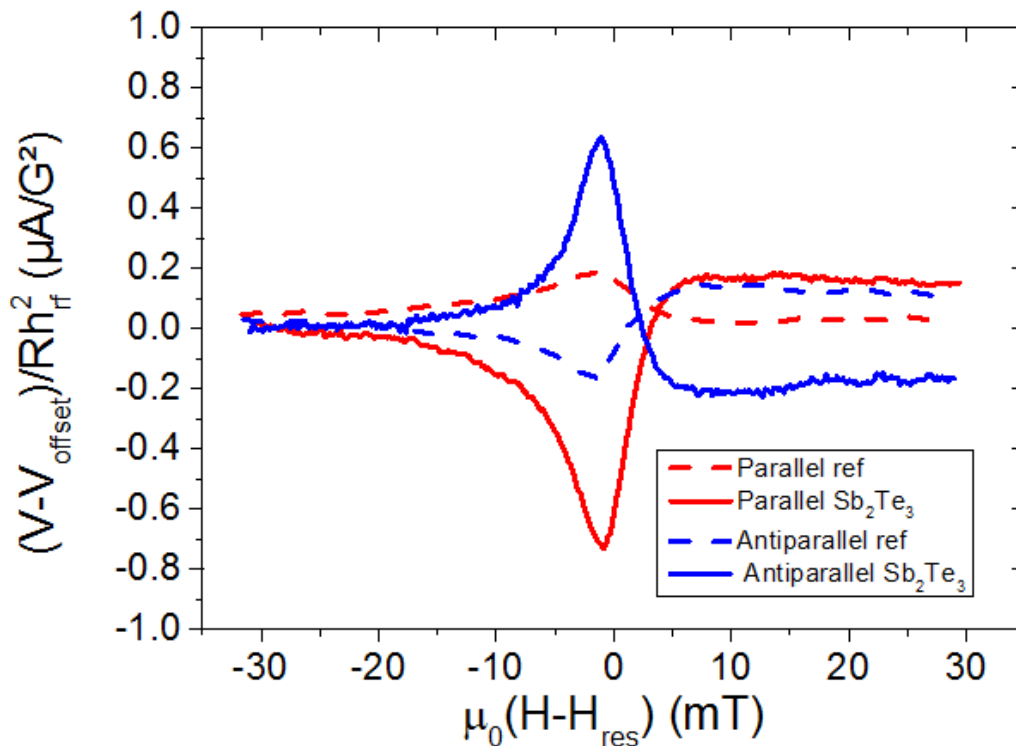


FIG. 5.16: Spin pumping signal obtained in a reference layer of Au/NiFe and of a  $Sb_2Te_3$ /Au/NiFe in parallel and antiparallel configurations.

We have measured spin pumping FMR in two samples deposited at the same time with the same Ar+



etching, 5 nm Au deposition and 20 nm NiFe deposition. The difference between the two samples is that one is deposited directly on a Si wafer and is the reference sample and the other is on a 10 nm  $Sb_2Te_3$  film. The spin pumping FMR results are shown in figure 5.16. There are two striking results, the signal in the sample with antimony telluride is considerably larger than the one with Au only and it is of opposite sign. The larger signal is expected due to the small spin Hall angle of Au, but the sign is opposed to what was previously observed in  $Sb_2Te_3$ . The sign obtained in Au is the same as in Pt, consistent with the positive spin Hall angle of Au. That indicates a negative sign of the conversion in  $Sb_2Te_3$ , same sign as Tantalum or Tungsten. As our samples are more holes doped than MBE deposited ones it is possible that the Fermi level is crossing a band with a spin polarization different from the Topological surface states<sup>364</sup> or that conversion occurs directly in bulk states by ISHE. Alternatively thanks to the Au deposited on top of  $Sb_2Te_3$  and the absence of strong modification of the interface chemistry allow to probe  $Sb_2Te_3$  itself instead of an interlayer forming at the interface. The exact mechanism is unclear and needs further experimental and theoretical background to identify the reason for such an unexpected sign change, the negative sign was also observed in the 4 nm and 7 nm film. Nonetheless the large spin pumping signal observed evidence a large conversion efficiency. Note that it is not a signal of thermal nature, as the signal is insensitive to the sweeping rate.

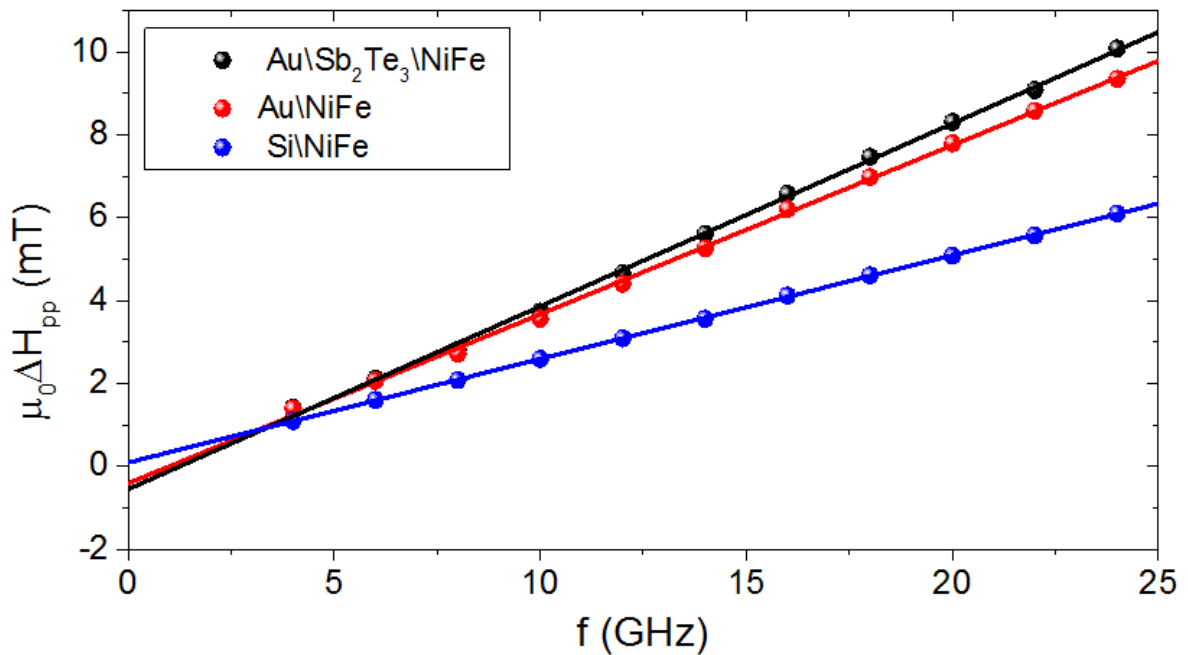


FIG. 5.17: Broadband measurement of the peak-to-peak linewidth in the Si \ NiFe, Au \ NiFe and of a  $Sb_2Te_3$  \ Au \ NiFe.

In order to estimate the conversion efficiency we also performed broadband FMR measurements on these samples. As can be seen in figure 5.17 an enhancement of the damping is observed compared to the deposition on Si with a respective damping of  $0.01123 \pm 0.0001$  for  $Sb_2Te_3$  \ Au \ NiFe and of  $0.01038 \pm 0.00012$  for Au \ NiFe compared to a damping of Si \ NiFe of  $0.00636 \pm 0.00003$ . The exact role of each layer in the extra damping is for now unclear as a trilayer model with loss in Au needs to be accounted. Moreover the deposition of NiFe on thin Au could lead to damping related to roughness of the bottom layer. So we have made the calculation of the conversion efficiency assuming the worst

case scenario, where all the extra damping in  $Sb_2Te_3/Au/NiFe$  is due to spin pumping in  $Sb_2Te_3$ . This leads to a conversion length (either  $\lambda_{IEE}$  or  $\theta_{SHE}\lambda_s$ ) of  $-127 \pm 12$  pm. This is comparable to results previously published on MBE deposited  $Bi_2Se_3$ <sup>304;305</sup> or  $BiSbTe$ <sup>67</sup> and sputtered deposited  $Bi_2Se_3$ <sup>193</sup> with conversion efficiency of the order of 100 pm but of opposite sign. In the best case scenario, Au is completely transparent and extra damping is due mostly to Au, we obtain an efficiency of  $-702 \pm 176$  pm, this efficiency is probably largely overestimated. The exact role of the Au layer as well as the thickness dependence still needs to be understood to conclude on the exact conversion efficiency and conversion mechanism in this system, especially the growth quality of NiFe on Au that can strongly affect the damping property needs to be further studied, but these results show that  $Sb_2Te_3$  is still very promising.

Here we demonstrated that it is possible to obtain topological insulators on large surfaces with structural and transport properties comparable to MBE thin films deposited on lattice matched substrate. Moreover the conversion efficiency in this film while still moderate and below the one obtained in the best heavy metals as Pt, W or Ta is comparable to previously reported spin to charge current conversion in Bi based topological insulator. This demonstrates the possibility to transfer topological insulator materials to industry without the need of a complex and costly MBE deposition in materials already widely used in phase-change materials. One can expect this quality to be preserved in other sputtered tellurides as  $BiSbTe$  or  $Bi_2Te_3$  thin films to extend the possibilities offered by the sputtering deposition of topological insulators. Thanks to the high resistivity of 10 nm thick  $Sb_2Te_3$  of  $2500\mu\Omega.cm$  compared with that of Pt that is around  $20\mu\Omega.cm$  the output signal is expected to be higher in a MESO like logic configuration<sup>48</sup>. This can also allow to obtain large output signals in cross-shaped nanostructure<sup>47</sup>. As mentioned before the large resistivity might still be detrimental for torque applications and more generally torque measurements are needed to conclude on the possibility to use these samples to do efficient magnetization switching. The deposition on thermally oxidized Silicon also paves the way to tune the topological insulator properties with a back-gate voltage.

To conclude, in this chapter we demonstrated that topological insulators could also be used to obtain an efficient spin to charge current conversion efficiency. A record high conversion was obtained in HgTe films at room temperature in particular when the films were protected by a thin HgCdTe layer. The study on these ultra-high quality topological insulator films is now followed by a study that concerns the current dependent magnetoresistive effects occurring in presence of spin momentum locking. We also demonstrated the potential of topological insulator materials deposited on silicon dioxide by sputtering with a quality similar to MBE deposited films. While only a moderate conversion efficiency is obtained in these films, this shows that the new physical phenomenon associated with the properties of topological insulators might not be limited to fundamental physics but could also be extended to industry in the near future.

## Conclusion

The main results obtained during my thesis concern the spin to charge current conversion in oxide interfaces and topological insulators measured by spin pumping by ferromagnetic resonance.

In **Chapter 1**, I gave details on the spin–charge current interconversion mechanisms at stake in materials with high spin orbit coupling, including heavy metals and 2DEGs. Then, in **Chapter 2**, I described the ferromagnetic resonance and the spin pumping by ferromagnetic resonance method. In the next chapters I used this theoretical background in order to analyse the experimental data.

While the experimental work during my thesis was mostly focused on Oxide heterointerfaces and Topological insulators, I also studied the spin to charge conversion in heavy metals. Especially, in **Chapter 3** I presented a method that allows to eliminate possible thermal effects to the spin signal, and thus improving the metrology of the spin to charge current conversion. I also presented results on the inverse spin Hall effect in different heavy metals and in particular gold–based alloys. This work evidenced the large side jump contribution in AuTa alloys, with spin Hall angles up to 50% for 10% of Ta impurities and smaller spin Hall angles in AuW alloys, associated with an intrinsic contribution only.

In **Chapter 4** I evidenced the large spin to charge current conversion in STO based heterostructures. While previous results on the inverse Edelstein effect in these structures focused on STO/LAO, in collaboration with UMR CNRS Thalès we have decided to study the 2DEG forming at the STO/Al interface. This allow obtaining a record high spin–to–charge conversion efficiency at cryogenic temperatures with inverse Edelstein length up to 30 nm. Moreover I evidenced the possibility to strongly tune this effect with gate voltages. Thanks to calculations performed at Halle Universität we linked the gate tunability to the bandstructure of STO. In a thinned–down sample I also demonstrated the possibility to induce ferroelectricity in STO. While this field–induced ferroelectricity has been previously described I evidenced its effect on the 2DEG, and especially on the spin to charge current conversion. I could demonstrate the possibility to switch and maintain a remanent state for the spin–to–charge current conversion using ferroelectricity. This new degree of freedom has for now been unexplored and could offer new possibilities to manipulate spin information.

I also studied the spin–to–charge current conversion efficiency in topological insulators. In **Chapter 5** I presented results on the highly efficient spin to charge current conversion in  $HgTe/HgCdTe/NiFe$  heterostructures. I showed that the thickness dependence of the conversion efficiency was different from that of SHE materials, with a maximum conversion efficiency obtained in a 26 nm thick  $HgTe$  layer. I also demonstrated the need to have a thin protective  $HgCdTe$  layer to improve the conversion efficiency. In the last part of this chapter, I also showed that it was possible to obtain topological insulators deposited by magnetron sputtering on 300 mm  $SiO_2$  wafers. These sample possess properties

close to MBE–deposited samples, with promising spin to charge current conversion efficiency.

## Perspectives

The highly efficient spin to charge conversion in the 2DEG at the surface of oxides or in topological insulators evidence the interest of these structures for spinorbitronics applications. In my thesis, and particularly in **Chapter 4** I evidenced that STO based oxide heterostructures offer large spin to charge current conversion efficiency. Such a large efficiency can possibly be obtained in other oxides in particular  $KTaO_3$  (KTO), that possess a larger spin orbit coupling than STO, thanks to the presence of a heavy Ta atom. It could lead to the increase of the conversion efficiency in these oxide systems and possibly bring it to room temperature. The demonstration of the possibility to switch the conversion sign using ferroelectricity in these oxides structures also paves the way towards new spintronics devices. Moreover, this effect could be extended to other ferroelectric or multiferroic systems such as  $SrCaTiO_3$ , a system that is ferroelectric and comparable to STO, but also  $GeTe$  or more common ferroelectric systems as  $BaTiO_3$ . The effect of the ferroelectric transition in  $SrCaTiO_3$  on the 2DEG forming at its surface after sputtering of Al is now under study at UMR CNRS Thalès. Spin pumping measurements on  $GeTe$  that is ferroelectric up to room temperature, are now being handled in our laboratory by Sara Varotto, from Politecnico di Milano. Studying the conversion from charge to spin is also a key point in these structures, as recent reports mention that oxides do not only give large spin to charge conversion but also promote efficient charge to spin conversion<sup>42</sup>.

Apart from using oxides as materials to promote spin–to–charge current conversion, ferromagnetic oxides such as LSMO are also appealing for spintronics application. Thanks to their small Gilbert damping and high resistivity (compared to ferromagnetic metals) and high magnetization at room temperature (compared to YIG) they could be useful for magnonics applications. LSMO can be used in all oxide systems that allows to obtain larger output voltages thanks to the high resistivity of the structure. The magnetic properties of these oxides, especially their dynamical properties, are studied in collaboration with Victor Haspot in UMR CNRS Thalès. The reader of this manuscript would have also noted that we mentioned some results on the spin to charge conversion in NiCu. While NiCu has a very low spin orbit coupling due to the light atoms that it is made of, recent results mentioned a near unity spin Hall ratio in this alloy<sup>164</sup>, evidencing that not only alloys with large spin orbit coupling impurities such as the AuTa and AuW alloys studied in the **Chapter 3** but also alloys with small spin orbit coupling could offer large conversion efficiencies. While this result is quite unexpected, we indeed observe in NiCu a conversion efficiency comparable to Pt using spin pumping FMR, these measurements being now performed by Sara Varotto and Maxen Cosset-Chesneau in Spintec.

The results on the highly efficient spin to charge current conversion in HgTe show that HgTe is an interesting material for spintronics, not only at ultra low temperature and high magnetic field, where HgTe shows signature of Quantum Hall Effect<sup>313</sup>, but at moderate fields and up to the room temperature. Following these results I am now working with Yu Fu, post-doc at Spintec, Jing Li, Post doc in Leti and Jules Papin, PhD student in Leti on novel magnetoresistance effects associated with helical Fermi contours, in particular on the bilinear magnetoelectric resistance (BMER)<sup>365:366</sup>. These ongoing

experiments in CdTe \HgTe microstructures show promising results, evidencing a large magnetoresistance associated with topological surface states when the Fermi level is tuned in the gap. These results, combined with a theoretical model, should allow a better understanding of the link between the HgTe bandstructure and its spintronics properties.

## Open questions

In my thesis I studied spin to charge conversion in oxide-based 2DEGs and topological insulators and I showed that they could offer higher spin to charge current conversion efficiencies than heavy metals. However there are still open questions that I would like to briefly mention here. As previously described in the manuscript, Zhang and Fert predicted that for the Edelstein Effect the characteristic times involved are not the same for spin to charge conversion –scattering time– and charge to spin conversion –spin flip time and transfer time across the interface–<sup>117</sup>. Therefore the optimal conversion might not be obtained in the same conditions in spin pumping and for spin-orbit torques. It is still unclear how to link the charge to spin to the spin to charge conversion in these systems. For example in the case of STO the thin oxide layer allows to obtain long scattering times that leads to larger spin accumulations, but also increases the transfer time from the 2DEG to the adjacent layer. Therefore it is possible, in SOTs experiments, that a large spin accumulation exists but that such accumulation is not easy to take advantage of because of the poor coupling between the 2DEG and the magnetic layer.

Thanks to their high resistivity, topological insulators and Rashba interfaces are interesting to obtain larger output voltages and power from spin to charge conversion. For materials with similar conversion efficiencies but a higher resistivity, the output voltage would increase, as well as the output power. These materials are therefore appealing for the recently proposed Magneto Electric Spin Orbit (MESO) logic by Intel<sup>48</sup> or for spin caloritronic applications<sup>367</sup>.

Having a high conversion efficiency allows obtaining a high spin accumulation per current density unit flowing in the active SOC layer. Nevertheless the high resistivity of this layer might also be detrimental for low power SOT MRAMs applications. Topological insulators and most 2DEGs have larger resistivities compared to heavy metals, of one to two orders of magnitude at room temperature. Due to these high resistivities, a large part of the current would leak through the ferromagnet and only a small part of it would contribute to the switching. Therefore the total power needed to switch an adjacent ferromagnet remains high, and heavy metals with low resistivity and moderate charge to spin conversion efficiency might be more appealing for SOT applications than Rashba interfaces of Topological insulators<sup>81</sup>. Recent reports of low power switching using topological insulators<sup>368</sup> and Rashba interfaces<sup>44</sup> shows that these materials could still offer improvements for SOT applications in terms of both power consumptions and current densities.

## Personal contribution

During my thesis I have studied various systems and experimental techniques, which allowed me to develop my knowledge in experimental physics. I have been trained to perform electrically detected ferromagnetic resonance measurements in cavity down to helium temperature, and broadband stripline measurements by Juan Carlos Rojas Sanchez and Serge Gambarelli. These two experimental techniques are extensively presented in this manuscript in **Chapter 2** and have been performed to study the spin to charge interconversion in **Chapter 3, 4 and 5**. I also had the opportunity to improve the spin pumping technique by performing time dependent measurements, current dependence measurements shown in **Chapter 3** and automated gate voltage measurements shown in **Chapter 4**. With Nicolas Thiery I could also demonstrate the possibility to perform spin pumping FMR measurements in cavity on Platinum nanowires. I have also characterized more conventional magnetotransport properties of thin films and micro/nano structures down to low temperature including *HgTe* thin films and Hall bars as seen for example in **Chapter 5** and *Sb<sub>2</sub>Te<sub>3</sub>* as presented in **Chapter 5**.

Apart from magnetotransport measurements I was also trained to use several characterization techniques, including X-ray diffraction and reflectivity within the “Service General des rayons X“. I also performed atomic force microscopy, scanning electron microscopy and electron dispersive X-ray spectroscopy to characterize the quality of my samples. I was also trained to use deposition techniques and etching process in “Plate Forme Technologique Amont“. I used these techniques in particular for the work described in **Chapter 5** on *HgTe* and *Sb<sub>2</sub>Te<sub>3</sub>*. The growth of these films were performed by our collaborators Philippe Ballet (*HgTe*) and Pierre Noé (*Sb<sub>2</sub>Te<sub>3</sub>*) in DOPT Leti. I also used a mechanical polishing setup to thin down oxides samples, this process was mandatory to observe the field induced ferroelectricity in *SrTiO<sub>3</sub>* presented in **Chapter 4**. While *SrTiO<sub>3</sub>* is usually considered to be paraelectric I proposed the possibility to obtain a ferroelectric phase transition in thinned down samples. During all this work I was greatly helped by Laurent Vila and Jean-Philippe Attané and all the permanent and non-permanent researchers of Spintec.

A part of the work presented in this thesis has been already published:

- The results on the spin to charge current conversion in Au-based alloys were published in Physical Review B Rapid Communication<sup>90</sup>
- The mapping of the spin to charge conversion to the bandstructure in *SrTiO<sub>3</sub>\Al* was published in Nature Materials<sup>232</sup>
- The demonstration of an highly efficient spin to charge current conversion in strained *HgTe* was published in Physical Review letters<sup>68</sup>

The other results presented in this manuscript are expected to be published, some of these results are now under review:

- A publication on the possibility to tune the spin to charge current conversion using ferroelectricity in *SrTiO<sub>3</sub>* has been submitted to Nature and is now under review. I am also co-inventor of the associated patent.
- The lack of thermal effect in the spin pumping signal studied using bolometric measurements

has been submitted to Physical Review Applied and is now under review. This work is also available on arXiv<sup>205</sup>

- The crystal characterization, magnetotransport and spin to charge current conversion in  $Sb_2Te_3$  is in the course of writing. We still need to understand the cause of the damping enhancement in Au\NiFe, it is unclear if this is a recent problem of the NiFe target or of the growth on Au, and a new batch will be grown soon. A k-PEEM measurement should also be performed in order to better understand the bandstructure of the sputtered deposited  $Sb_2Te_3$ .
- The effect of temperature increase out of resonance on the spin signal presented in annex will also be submitted, as it has important implications for spin pumping measurements using ferromagnets with temperature sensitive properties, or at large power.

In order to obtain a clear manuscript I didn't present all the experimental results obtained during my PhD in particular:

- The possibility to measure spin to charge current conversion in Pt nanostripes deposited on YIG and to increase the spin pumping signal with current annealing. This work is part of a larger study by Nicolas Thiery on the spin transfert properties of the YIG\Pt interface after current annealing, this work will soon be submitted.
- The spin to charge current conversion in NiCu alloys, especially its thickness and temperature dependence. We are now writing a manuscript with Sara Varotto on this study.
- The temperature dependence of the damping and spin pumping signal in LSMO, from cryogenic temperature to room temperature. This work using cavity FMR confirmed previous work on broadband FMR performed by Victor Haspot of UMR CNRS Thalès, who also grow the high quality LSMO samples.

I have also contributed to other experimental works during my internship and PhD that eventually lead to several publications as a coauthor:

- I performed broadband measurements on Fe thin films that were part of the manuscript on the spin to charge conversion in Ge(111)\Fe of Simons Oyarzun published in Nature Communications<sup>188</sup>
- I helped Thomas Guillet to perform the weak antilocalization measurements and give advices on the HLN fitting of  $Bi_2Se_3$  thin films grown on Ge(111). These results were published in AIP Advances<sup>348</sup>
- I had the opportunity to help Pham Van Tuong during his work on the measurements of spin-charge interconversion using cross shaped nanostructures that lead to two publications in Applied physics Letters<sup>47:56</sup>

Finally I have also participated in several conferences including local and international conferences. In particular I had the opportunity to have two invited talks at SPIE Spintronics X and XII in San Diego. I also received a poster prize in Intermag 2017 in Dublin and during Journées de la Matière Condensée 2018 in Grenoble.



## Acknowledgment

Je voudrai remercier un certain nombres de personnes, qui m'ont aidé et soutenu tout au long de ce travail de thèse.

Je tiens d'abord à remercier Jean-Philippe et Laurent mes directeurs/co-directeurs de thèse sans qui ce travail de thèse aurait été impossible. A l'exception de leur tentative de me perdre sur les pistes de Chamrousse ils ont été d'un grand soutien tant dans le travail que dans la vie de tous les jours. Aller au bureau et travailler avec eux a toujours été un grand plaisir. Les colloques Louis Néel, la conférence sur les isolants topologiques à Nancy, ou la rencontre CNRS-CSIC à Madrid resteront d'excellents souvenirs. Les sorties au restaurant vietnamien ou au bureau aussi.

J'aimerais remercier les stagiaires, thésards et post-docs avec qui j'ai eu la chance de travailler durant ma thèse, et qui ne sont pas que des collègues mais sont aussi devenus des amis. Tout d'abord Fabien, Gilles, Chloé et Tuong que j'ai eu la chance de cotoyer pendant mon stage de Master 2 puis ma première année de thèse et qui m'ont grandement aidé dans mon travail. J'espère tous vous recroiser sur Grenoble, Paris ou au Japon qui sait. Une pensée pour Antoine qui a partagé mon bureau pendant tout mon stage et bien évidemment son remplaçant Nicolas que j'ai eu la chance d'avoir dans mon bureau pendant mes trois années de thèse. Malheureusement je n'ai pas pu assister à sa soutenance, j'espère qu'il en fera une rien que pour moi. Je tiens aussi à remercier tout particulièrement Thomas pour nos longues discussions au labo ou plus tard dans la soirée autour d'un verre, et Marie qui revient toujours nous voir avec un grand sourire et est toujours là quand on a besoin d'elle, je leur souhaite le meilleur pour leur dernière année de thèse, et j'espère les recroiser très vite. Cela commence à faire beaucoup de monde mais il ne faut surtout pas que j'oublie Maxen avec qui j'ai eu plaisir à travailler durant ma dernière année, je lui souhaite le meilleur pour sa thèse qui je suis sûr sera couronnée de succès. Bien évidemment je n'oublie pas non plus Yu et son mari Jing qui forment une paire drôlement efficace, mais aussi Sambit et Toshiki que j'espère recroiser bientôt, en espérant pouvoir me déplacer aussi vite que leurs parois de domaines pour aller les voir rapidement au Japon. J'ai aussi une pensée pour Tuan, avec qui je prenais souvent le tram de 20h30 à Presqu'île, j'espère le croiser sur la promenade des anglais lors de ma prochaine balade en moto avec mon ami Christian. Sans oublier évidemment Emilio grâce à qui j'ai pu aller faire la fête dans le parc d'un grand chateau au Nord de Paris.

Parmi les gens qui m'ont été d'une grande aide durant cette thèse je tiens à exprimer ma profonde gratitude pour Matthieu, Céline et Alain. Matthieu pour ses conseils toujours avisés, de même pour Céline qui a toujours été là pour me conseiller sur des points techniques, et Alain qui m'a aidé pour tant de choses. Je n'oublie pas évidemment les autres personnes de Spintec C5 (dit canal historique) notamment Ariel pour sa présence et son aide technique de tous les instants en particulier lors du déménagement et Patrick pour ses dépôts et son humour sans pareil. Une petite pensée pour Lucien

parti en retraite pendant ma thèse et qui je l'espère profite bien de son potager et de ses petits enfants, et Cyrille qui en Californie profite des vagues et de températures plus clémentes. De façon générale je tiens à remercier tous les membres de Spintec qui ont de près ou de loin travaillé avec moi. Je pense en particulier aux Oliviers, à Ursula, Vincent, Fred, Mair, Lucian, Vladimir, Olga, Lamprini, Rafael, Guillaume, Kyongmo, Arnaud, Roméo, Steven, Marco, Jay, Daniel, Haozhe et tous les autres... J'aimerai aussi remercier le personnel administratif et la direction de Spintec, sans leur grande réactivité et leur gentillesse je me serai arraché les cheveux tant de fois sur mes demandes de remboursements, de logiciel et autres documents divers. Un grand merci donc à Sabrina, Léa, Rachel, Céline et Catherine qui m'ont évité bien des déboires administratifs. J'aimerai aussi ici avoir une petite pensée pour Jérôme.

Tout ce travail aurait été impossible sans l'aide d'un nombre important de personnes extérieures au laboratoire. J'aimerai tout d'abord remercier Carlos qui m'a appris énormément de choses sur les mesures de résonance ferromagnétiques, sur comment effectuer de bonnes mesures et travailler le plus efficacement possible. Sans son aide au début de mon stage puis au cours de ma thèse je n'aurai jamais pu accomplir autant. Je n'oublie évidemment pas les personnes du laboratoire de Conception d'architectures moléculaires et processus électroniques (CAMPE) qui ont eu la gentillesse de nous permettre d'utiliser leur spectro de résonance paramagnétique électronique et de les maintenir en état de fonctionnement pour moi ainsi que d'autres personnes faisant des mesures FMR. En particulier je tiens à remercier Serge et Vincent qui ont toujours été là pour répondre à mes questions, ainsi que Christian qui a toujours maintenu le spectromètre dans un état de fonctionnement irréprochable et sans qui ma thèse aurait eu des points d'arrêt à bien des moments. Et bien sûr, Jean-François qui a conçu et fabriqué à la microfraiseuse l'intégralité de mes portes échantillons, la grande qualité de son travail m'a permis d'avancer très vite. En tous les cas sans eux une grande partie de mon travail de thèse n'aurait pu être fait, ils ont en plus fait preuve d'une grande patience et ont toujours été à l'écoute de mes interrogations.

Au sein du CEA Grenoble j'ai aussi reçu l'aide précieuse des permanents et non permanents du service général des rayons X pour mes mesures de réflectivité et de diffraction des rayons X en particulier de Stéphanie et Asma qui m'ont énormément aidé à dompter le Philips couches minces, et Stéphane pour ma formation à la réflectivité rayons X. J'ai aussi eu la chance de recevoir des échantillons de très grande qualité notamment aux échantillons du tellure d'antimoine de Pierre Noé ou de tellure de Mercure dont la croissance et la fabrications des microstructures ont été réalisés par Philippe Ballet, Candice Thomas et Jules Papin. Je n'oublie évidemment pas Tristan Meunier lui aussi très impliqué dans mon travail sur le HgTe et avec qui j'ai eu grand plaisir à travailler. J'ai eu aussi la chance de travailler avec un grand nombre de personnes à CNRS Thalès avec le financement de l'ANR Toprise et OISO. Une grande partie des résultats présentés dans ce manuscrit ne seraient pas présents sans eux. Je pense en particulier au groupe Oxitronique, à Manu, Agnès, Diogo, Felix et Victor qui ont toujours été d'une grande gentillesse et d'une grande aide et m'ont toujours poussé à me surpasser. Et au groupe Isolants topologiques autour de Jean-Marie Georges en particulier notre Breton Quentin qui conduira j'en suis sûr Guiguamp en Champion's League, Nicolas, et Henri avec qui j'ai beaucoup apprécié travailler.

Travailler avec toutes ces personnes a été un plaisir de tous les instants et en même temps un véritable

défi.

Une pensée pour tous mes amis de longue date ou rencontrés plus récemment qui m'ont soutenu pendant ma thèse. La liste est bien trop longue pour tous les citer, pour éviter les listes à la Prévert je me limiterai donc à mes colocataires Olivier et Louise qui m'ont supporté pendant ma période de rédaction. J'ai aussi une petite pensée pour Antoine en écrivant ces lignes. Je remercie mes parents et mon frère qui ont été à mes côtés durant ces trois années de thèse et m'ont toujours soutenu de façon inconditionnelle, mais aussi mon oncle et ma tante Chantal et François qui m'ont toujours accueilli chez eux lorsque je rentrais revoir mes parents.

Pour finir j'aimerais remercier les membres du jury d'avoir accepté de participer à ma soutenance de thèse: Michel Viret, Pietro Gambardella, Abdelmadjid Anane, Dafiné Ravelosona, ainsi que la présidente de jury Stefania Pizzini et le membre invité Manuel Bibès. Je les remercie pour leurs questions d'une grande sagacité, et je m'excuse pour les retards de train au retour vers Paris, je ne suis pas responsable des chutes de neige. Je tiens à remercier Philippe Sabon qui a permis à la vidéo conférence de fonctionner parfaitement durant toute la durée de la soutenance.

Pour finir je remercie évidemment Lanef (ANR-10-LABX51-01) pour avoir financé ma thèse.

# Bibliography

- [1] M. T. Bohr and I. A. Young. CMOS Scaling Trends and Beyond. *IEEE Micro*, 37(6):20–29, November 2017.
- [2] Gordon E. Moore. Cramming more components onto integrated circuits. *Electronics*, 38, 1965.
- [3] M. Mitchell Waldrop. The chips are down for Moores law. *Nature News*, 530(7589):144, February 2016.
- [4] ICT Energy. Ict energy strategic research agenda. 611004, 2016.
- [5] D. E. Nikonov, G. I. Bourianoff, and T. Ghani. Proposal of a Spin Torque Majority Gate Logic. *IEEE Electron Device Letters*, 32(8):1128–1130, August 2011.
- [6] Z. Liang, M. G. Mankalale, J. Hu, Z. Zhao, J. Wang, and S. S. Sapatnekar. Performance Characterization and Majority Gate Design for MESO-Based Circuits. *IEEE Journal on Exploratory Solid-State Computational Devices and Circuits*, 4(2):51–59, December 2018.
- [7] Naoto Nagaosa, Jairo Sinova, Shigeki Onoda, A. H. MacDonald, and N. P. Ong. Anomalous Hall effect. *Reviews of Modern Physics*, 82(2):1539–1592, 2010.
- [8] M. N. Baibich, J. M. Broto, A. Fert, F. Nguyen Van Dau, F. Petroff, P. Etienne, G. Creuzet, A. Friederich, and J. Chazelas. Giant Magnetoresistance of (001)Fe/(001)Cr Magnetic Superlattices. *Physical Review Letters*, 61(21):2472–2475, 1988.
- [9] G. Binasch, P. Grünberg, F. Saurenbach, and W. Zinn. Enhanced magnetoresistance in layered magnetic structures with antiferromagnetic interlayer exchange. *Physical Review B*, 39(7):4828–4830, 1989.
- [10] B. Dieny. Giant magnetoresistance in spin-valve multilayers. *Journal of Magnetism and Magnetic Materials*, 136(3):335–359, September 1994.
- [11] J. S. Moodera, Lisa R. Kinder, Terrilyn M. Wong, and R. Meservey. Large Magnetoresistance at Room Temperature in Ferromagnetic Thin Film Tunnel Junctions. *Physical Review Letters*, 74(16):3273–3276, 1995.
- [12] F. Bonell, T. Hauet, S. Andrieu, F. Bertran, P. Le Fèvre, L. Calmels, A. Tejada, F. Montaigne, B. Warot-Fonrose, B. Belhadji, A. Nicolaou, and A. Taleb-Ibrahimi. Spin-Polarized Electron Tunneling in bcc  $\text{FeCo}/\text{MgO}/\text{FeCo}(001)$  Magnetic Tunnel Junctions. *Physical Review Letters*, 108(17):176602, April 2012.
- [13] Roger Wood. Future hard disk drive systems. *Journal of Magnetism and Magnetic Materials*, 321(6):555–561, March 2009.
- [14] J. C. Slonczewski. Current-driven excitation of magnetic multilayers. *Journal of Magnetism and Magnetic Materials*, 159(1):L1–L7, 1996.
- [15] L. Berger. Emission of spin waves by a magnetic multilayer traversed by a current. *Physical Review B*, 54(13):9353–9358, October 1996.
- [16] S. I. Kiselev, J. C. Sankey, I. N. Krivorotov, N. C. Emley, R. J. Schoelkopf, R. A. Buhrman, and D. C. Ralph. Microwave oscillations of a nanomagnet driven by a spin-polarized current. *Nature*, 425(6956):380–383, September 2003.
- [17] G. S. D. Beach, M. Tsoi, and J. L. Erskine. Current-induced domain wall motion. *Journal of Magnetism and Magnetic Materials*, 320(7):1272–1281, April 2008.
- [18] J. Grollier, V. Cros, A. Hamzic, J. M. George, H. Jaffrès, A. Fert, G. Faini, J. Ben Youssef, and H. Legall. Spin-polarized current induced switching in Co/Cu/Co pillars. *Applied Physics Letters*, 78(23):3663–3665, May 2001.
- [19] Zhitao Diao, Zhanjie Li, Shengyuang Wang, Yunfei Ding, Alex Panchula, Eugene Chen, Lien-Chang Wang, and Yiming Huai. Spin-transfer torque switching in magnetic tunnel junctions and spin-transfer torque random access memory. *Journal of Physics: Condensed Matter*, 19(16):165209, April 2007.
- [20] A. Driskill-Smith, D. Apalkov, V. Nikitin, X. Tang, S. Watts, D. Lottis, K. Moon, A. Khvalkovskiy, R. Kawakami, X. Luo, A. Ong, E. Chen, and M. Krounbi. Latest Advances and Roadmap for In-Plane and Perpendicular STT-RAM. In *2011 3rd IEEE International Memory Workshop (IMW)*, pages 1–3, 2011.

- [21] J. C. Sankey, P. M. Braganca, A. G. F. Garcia, I. N. Krivorotov, R. A. Buhrman, and D. C. Ralph. Spin-Transfer-Driven Ferromagnetic Resonance of Individual Nanomagnets. *Physical Review Letters*, 96(22):227601, June 2006.
- [22] M. I. Dyakonov and V. I. Perel. Current-induced spin orientation of electrons in semiconductors. *Physics Letters A*, 35(6):459–460, 1971.
- [23] A. A. Bakun, B. P. Zakharchenya, A. A. Rogachev, M. N. Tkachuk, and V. G. Fleisher. Observation of a surface photocurrent caused by optical orientation of electrons in a semiconductor. *JETP Lett*, 40, 1984.
- [24] M. N. Tkachuk, B. P. Zakharchenya, and V. G. Fleisher. Resonant photovoltaic effect in the nmr of nuclei in a semiconductor lattice. *Sov. Phys. JETP Lett.*, 44(1), 1986.
- [25] Y. K. Kato, R. C. Myers, A. C. Gossard, and D. D. Awschalom. Observation of the Spin Hall Effect in Semiconductors. *Science*, 306(5703):1910–1913, 2004.
- [26] E. Saitoh, M. Ueda, H. Miyajima, and G. Tatara. Conversion of spin current into charge current at room temperature: Inverse spin-Hall effect. *Applied Physics Letters*, 88(18):182509, 2006.
- [27] S. O. Valenzuela and M. Tinkham. Direct electronic measurement of the spin Hall effect. *Nature*, 442(7099):176, 2006.
- [28] J. E. Hirsch. Spin Hall Effect. *Physical Review Letters*, 83(9):1834–1837, 1999.
- [29] V. M. Edelstein. Spin polarization of conduction electrons induced by electric current in two-dimensional asymmetric electron systems. *Solid State Communications*, 73(3):233–235, 1990.
- [30] M. I. Dyakonov. Spin Hall Effect. *arXiv:1210.3200 [cond-mat, physics:physics, physics:quant-ph]*, 2012. arXiv:1210.3200.
- [31] Ioan Mihai Miron, Kevin Garello, Gilles Gaudin, Pierre-Jean Zermatten, Marius V. Costache, Stéphane Auffret, Sébastien Bandiera, Bernard Rodmacq, Alain Schuhl, and Pietro Gambardella. Perpendicular switching of a single ferromagnetic layer induced by in-plane current injection. *Nature*, 476(7359):189–193, 2011.
- [32] Luqiao Liu, Chi-Feng Pai, Y. Li, H. W. Tseng, D. C. Ralph, and R. A. Buhrman. Spin-Torque Switching with the Giant Spin Hall Effect of Tantalum. *Science*, 336(6081):555–558, 2012.
- [33] M. Collet, X. de Milly, O. dAllivy Kelly, V. V. Naletov, R. Bernard, P. Bortolotti, J. Ben Youssef, V. E. Demidov, S. O. Demokritov, J. L. Prieto, M. Muñoz, V. Cros, A. Anane, G. de Loubens, and O. Klein. Generation of coherent spin-wave modes in yttrium iron garnet microdiscs by spinorbit torque. *Nature Communications*, 7:10377, January 2016.
- [34] Ioan Mihai Miron, Thomas Moore, Helga Szambolics, Liliana Daniela Buda-Prejbeanu, Stéphane Auffret, Bernard Rodmacq, Stefania Pizzini, Jan Vogel, Marlio Bonfim, Alain Schuhl, and Gilles Gaudin. Fast current-induced domain-wall motion controlled by the Rashba effect. *Nature Materials*, 10(6):419–423, June 2011.
- [35] Olivier Boulle, Jan Vogel, Hongxin Yang, Stefania Pizzini, Dayane de Souza Chaves, Andrea Locatelli, Tevfik Onur Mente, Alessandro Sala, Liliana D. Buda-Prejbeanu, Olivier Klein, Mohamed Belmeguenai, Yves Roussigné, Andrey Stashkevich, Salim Mourad Chérif, Lucia Aballe, Michael Foerster, Mairbek Chshiev, Stéphane Auffret, Ioan Mihai Miron, and Gilles Gaudin. Room-temperature chiral magnetic skyrmions in ultrathin magnetic nanostructures. *Nature Nanotechnology*, 11(5):449–454, May 2016.
- [36] William Legrand, Davide Maccariello, Nicolas Reyren, Karin Garcia, Christoforos Moutafis, Constance Moreau-Luchaire, Sophie Collin, Karim Bouzehouane, Vincent Cros, and Albert Fert. Room-Temperature Current-Induced Generation and Motion of sub-100 nm Skyrmions. *Nano Letters*, 17(4):2703–2712, April 2017.
- [37] Kevin Garello, Can Onur Avci, Ioan Mihai Miron, Manuel Baumgartner, Abhijit Ghosh, Stéphane Auffret, Olivier Boulle, Gilles Gaudin, and Pietro Gambardella. Ultrafast magnetization switching by spin-orbit torques. *Applied Physics Letters*, 105(21):212402, November 2014.
- [38] Guoqiang Yu, Pramey Upadhyaya, Yabin Fan, Juan G. Alzate, Wanjun Jiang, Kin L. Wong, So Takei, Scott A. Bender, Li-Te Chang, Ying Jiang, Murong Lang, Jianshi Tang, Yong Wang, Yaroslav Tserkovnyak, Pedram Khalili Amiri, and Kang L. Wang. Switching of perpendicular magnetization by spinorbit torques in the absence of external magnetic fields. *Nature Nanotechnology*, 9(7):548–554, 2014.
- [39] Qiang Hao, Wenzhe Chen, and Gang Xiao. Beta tungsten thin films: Structure, electron transport, and giant spin Hall effect. *Applied Physics Letters*, 106(18):182403, 2015.

- [40] J. C. Rojas Sánchez, L. Vila, G. Desfonds, S. Gambarelli, J. P. Attané, J. M. De Teresa, C. Magén, and A. Fert. Spin-to-charge conversion using Rashba coupling at the interface between non-magnetic materials. *Nature Communications*, 4:2944, 2013.
- [41] Miren Isasa, M. Carmen Martínez-Velarte, Estitxu Villamor, César Magén, Luis Morellón, José M. De Teresa, M. Ricardo Ibarra, Giovanni Vignale, Evgueni V. Chulkov, Eugene E. Krasovskii, Luis E. Hueso, and Fèlix Casanova. Origin of inverse Rashba-Edelstein effect detected at the Cu/Bi interface using lateral spin valves. *Physical Review B*, 93(1):014420, January 2016.
- [42] Huaiwen Yang, Boyu Zhang, Xueying Zhang, Xi Yan, Wenlong Cai, Yinglin Zhao, Jirong Sun, Kang L. Wang, Dapeng Zhu, and Weisheng Zhao. Giant Charge-to-Spin Conversion Efficiency in  $\text{SrTiO}_3$ -Based Electron Gas Interface. *Physical Review Applied*, 12(3):034004, September 2019.
- [43] A. R. Mellnik, J. S. Lee, A. Richardella, J. L. Grab, P. J. Mintun, M. H. Fischer, A. Vaezi, A. Manchon, E.-A. Kim, N. Samarth, and D. C. Ralph. Spin-transfer torque generated by a topological insulator. *Nature*, 511(7510):449–451, 2014.
- [44] Shuyuan Shi, Aizhu Wang, Yi Wang, Rajagopalan Ramaswamy, Lei Shen, Jisoo Moon, Dapeng Zhu, Jiawei Yu, Seongshik Oh, Yuanping Feng, and Hyunsoo Yang. Efficient charge-spin conversion and magnetization switching through the Rashba effect at topological-insulator/Ag interfaces. *Physical Review B*, 97(4):041115, 2018.
- [45] K. Garello, F. Yasin, S. Couet, L. Souriau, J. Swerts, S. Rao, S. Van Beek, W. Kim, E. Liu, S. Kundu, D. Tsvetanova, K. Croes, N. Jossart, E. Grimaldi, M. Baumgartner, D. Crotti, A. Fumémont, P. Gambardella, and G. S. Kar. SOT-MRAM 300nm Integration for Low Power and Ultrafast Embedded Memories. In *2018 IEEE Symposium on VLSI Circuits*, pages 81–82, 2018.
- [46] T. Kampfrath, M. Battiato, P. Maldonado, G. Eilers, J. Nötzold, S. Mährlein, V. Zbarsky, F. Freimuth, Y. Mokrousov, S. Blügel, M. Wolf, I. Radu, P. M. Oppeneer, and M. Münzenberg. Terahertz spin current pulses controlled by magnetic heterostructures. *Nature Nanotechnology*, 8(4):256–260, 2013.
- [47] V. T. Pham, L. Vila, G. Zahnd, P. Noël, A. Marty, and J. P. Attané. Cross-shaped nanostructures for the study of spin to charge inter-conversion using spin-orbit coupling in non-magnetic materials. *Applied Physics Letters*, 114(22):222401, June 2019.
- [48] Sasikanth Manipatruni, Dmitri E. Nikonov, Chia-Ching Lin, Tanay A. Gosavi, Huichu Liu, Bhagwati Prasad, Yen-Lin Huang, Everton Bonturim, Ramamoorthy Ramesh, and Ian A. Young. Scalable energy-efficient magnetoelectric spinorbit logic. *Nature*, 565(7737):35, 2019.
- [49] W. S. Zhao, T. Devolder, Y. Lakys, J. O. Klein, C. Chappert, and P. Mazoyer. Design considerations and strategies for high-reliable STT-MRAM. *Microelectronics Reliability*, 51(9):1454–1458, 2011.
- [50] W. S. Zhao, Y. Zhang, T. Devolder, J. O. Klein, D. Ravelosona, C. Chappert, and P. Mazoyer. Failure and reliability analysis of STT-MRAM. *Microelectronics Reliability*, 52(9):1848–1852, 2012.
- [51] M. Cubukcu, O. Boulle, N. Mikuszeit, C. Hamelin, T. Brächer, N. Lamard, M. Cyrille, L. Buda-Prejbeanu, K. Garello, I. M. Miron, O. Klein, G. de Loubens, V. V. Naletov, J. Langer, B. Ocker, P. Gambardella, and G. Gaudin. Ultra-Fast Perpendicular SpinOrbit Torque MRAM. *IEEE Transactions on Magnetics*, 54(4):1–4, 2018.
- [52] G. Prenat, K. Jabeur, P. Vanhauwaert, G. D. Pendina, F. Oboril, R. Bishnoi, M. Ebrahimi, N. Lamard, O. Boulle, K. Garello, J. Langer, B. Ocker, M. Cyrille, P. Gambardella, M. Tahoori, and G. Gaudin. Ultra-Fast and High-Reliability SOT-MRAM: From Cache Replacement to Normally-Off Computing. *IEEE Transactions on Multi-Scale Computing Systems*, 2(1):49–60, 2016.
- [53] Shunsuke Fukami, Chaoliang Zhang, Samik DuttaGupta, Aleksandr Kurenkov, and Hideo Ohno. Magnetization switching by spinorbit torque in an antiferromagnet/ferromagnet bilayer system. *Nature Materials*, 15(5):535–541, 2016.
- [54] Luqiao Liu, Takahiro Moriyama, D. C. Ralph, and R. A. Buhrman. Spin-Torque Ferromagnetic Resonance Induced by the Spin Hall Effect. *Physical Review Letters*, 106(3):036601, January 2011.
- [55] C. Stamm, C. Murer, M. Berritta, J. Feng, M. Gabureac, P.M. Oppeneer, and P. Gambardella. Magneto-Optical Detection of the Spin Hall Effect in Pt and W Thin Films. *Physical Review Letters*, 119(8):087203, August 2017.

- [56] V. T. Pham, G. Zahnd, A. Marty, W. Savero Torres, M. Jamet, P. Noël, L. Vila, and J. P. Attané. Electrical detection of magnetic domain walls by inverse and direct spin Hall effect. *Applied Physics Letters*, 109(19):192401, November 2016.
- [57] T. Kimura, Y. Otani, T. Sato, S. Takahashi, and S. Maekawa. Room-Temperature Reversible Spin Hall Effect. *Physical Review Letters*, 98(15):156601, 2007.
- [58] Kevin Garello, Ioan Mihai Miron, Can Onur Avci, Frank Freimuth, Yuriy Mokrousov, Stefan Blügel, Stéphane Auffret, Olivier Boulle, Gilles Gaudin, and Pietro Gambardella. Symmetry and magnitude of spinorbit torques in ferromagnetic heterostructures. *Nature Nanotechnology*, 8(8):587–593, August 2013.
- [59] J.-C. Rojas-Sánchez, M. Cubukcu, A. Jain, C. Vergnaud, C. Portemont, C. Ducruet, A. Barski, A. Marty, L. Vila, J.-P. Attané, E. Augendre, G. Desfonds, S. Gambarelli, H. Jaffrès, J.-M. George, and M. Jamet. Spin pumping and inverse spin Hall effect in germanium. *Physical Review B*, 88(6):064403, August 2013.
- [60] P. Laczkowski, J.-C. Rojas-Sánchez, W. Savero-Torres, H. Jaffrès, N. Reyren, C. Deranlot, L. Notin, C. Beigné, A. Marty, J.-P. Attané, L. Vila, J.-M. George, and A. Fert. Experimental evidences of a large extrinsic spin Hall effect in AuW alloy. *Applied Physics Letters*, 104(14):142403, 2014.
- [61] J.-C. Rojas-Sánchez, N. Reyren, P. Laczkowski, W. Savero, J.-P. Attané, C. Deranlot, M. Jamet, J.-M. George, L. Vila, and H. Jaffrès. Spin Pumping and Inverse Spin Hall Effect in Platinum: The Essential Role of Spin-Memory Loss at Metallic Interfaces. *Physical Review Letters*, 112(10):106602, 2014.
- [62] J.-C. Rojas-Sánchez, S. Oyarzún, Y. Fu, A. Marty, C. Vergnaud, S. Gambarelli, L. Vila, M. Jamet, Y. Ohtsubo, A. Taleb-Ibrahimi, P. Le Fèvre, F. Bertran, N. Reyren, J.-M. George, and A. Fert. Spin to Charge Conversion at Room Temperature by Spin Pumping into a New Type of Topological Insulator:  $\alpha$ -Sn Films. *Physical Review Letters*, 116(9):096602, March 2016.
- [63] A. V. Khvalkovskiy, D. Apalkov, S. Watts, R. Chepulskii, R. S. Beach, A. Ong, X. Tang, A. Driskill-Smith, W. H. Butler, P. B. Visscher, D. Lottis, E. Chen, V. Nikitin, and M. Krounbi. Basic principles of STT-MRAM cell operation in memory arrays. *Journal of Physics D: Applied Physics*, 46(7):074001, 2013.
- [64] Y. Niimi, Y. Kawanishi, D. H. Wei, C. Deranlot, H. X. Yang, M. Chshiev, T. Valet, A. Fert, and Y. Otani. Giant Spin Hall Effect Induced by Skew Scattering from Bismuth Impurities inside Thin Film CuBi Alloys. *Physical Review Letters*, 109(15):156602, 2012.
- [65] H.L. Wang, C.H. Du, Y. Pu, R. Adur, P.C. Hammel, and F.Y. Yang. Scaling of Spin Hall Angle in 3d, 4d, and 5d Metals from  $\text{Y}_3\text{Fe}_5\text{O}_{12}$ /Metal Spin Pumping. *Physical Review Letters*, 112(19):197201, 2014.
- [66] E. Lesne, Yu Fu, S. Oyarzun, J. C. Rojas-Sánchez, D. C. Vaz, H. Naganuma, G. Sicoli, J.-P. Attané, M. Jamet, E. Jacquet, J.-M. George, A. Barthélémy, H. Jaffrès, A. Fert, M. Bibes, and L. Vila. Highly efficient and tunable spin-to-charge conversion through Rashba coupling at oxide interfaces. *Nature Materials*, 15(12):1261–1266, 2016.
- [67] J. B. S. Mendes, O. Alves Santos, J. Holanda, R. P. Loreto, C. I. L. de Araujo, Cui-Zu Chang, J. S. Moodera, A. Azevedo, and S. M. Rezende. Dirac-surface-state-dominated spin to charge current conversion in the topological insulator  $(\text{Bi}_{0.22}\text{Sb}_{0.78})_2\text{Te}_3$  films at room temperature. *Physical Review B*, 96(18):180415, 2017.
- [68] P. Noel, C. Thomas, Y. Fu, L. Vila, B. Haas, P-H. Jouneau, S. Gambarelli, T. Meunier, P. Ballet, and J.P. Attané. Highly Efficient Spin-to-Charge Current Conversion in Strained HgTe Surface States Protected by a HgCdTe Layer. *Physical Review Letters*, 120(16):167201, 2018.
- [69] R. J. Elliott. Theory of the Effect of Spin-Orbit Coupling on Magnetic Resonance in Some Semiconductors. *Physical Review*, 96(2):266–279, October 1954.
- [70] Y. Yafet. g Factors and Spin-Lattice Relaxation of Conduction Electrons\*\*Part of the work connected with the preparation of this article, in particular the work on spin-lattice relaxation, was done while the author was at the Westinghouse Research Laboratories, Pittsburgh, Pennsylvania. In Frederick Seitz and David Turnbull, editors, *Solid State Physics*, volume 14, pages 1–98. Academic Press, January 1963.
- [71] Eurne Sagasta, Yasutomo Omori, Miren Isasa, Martin Gradhand, Luis E. Hueso, Yasuhiro Niimi, YoshiChika Otani, and Fèlix Casanova. Tuning the spin Hall effect of Pt from the moderately dirty to the superclean regime. *Physical Review B*, 94(6):060412, 2016.



- [72] Jack Bass and William P. Pratt. Spin-diffusion lengths in metals and alloys, and spin-flipping at metal/metal interfaces: an experimentalist's critical review. *Journal of Physics: Condensed Matter*, 19(18):183201, 2007.
- [73] P. Laczkowski, M. Cosset-Cheneau, W. Savero-Torres, V. T. Pham, G. Zahnd, H. Jaffrès, N. Reyren, J.-C. Rojas-Sánchez, A. Marty, L. Vila, J.-M. George, and J.-P. Attané. Spin-dependent transport characterization in metallic lateral spin valves using one-dimensional and three-dimensional modeling. *Physical Review B*, 99(13):134436, 2019.
- [74] G. Zahnd, L. Vila, V. T. Pham, M. Cosset-Cheneau, W. Lim, A. Brenac, P. Laczkowski, A. Marty, and J. P. Attané. Spin diffusion length and polarization of ferromagnetic metals measured by the spin-absorption technique in lateral spin valves. *Physical Review B*, 98(17):174414, 2018.
- [75] M. I. D'Yakonov and V. I. Perel'. Possibility of Orienting Electron Spins with Current. *Soviet Journal of Experimental and Theoretical Physics Letters*, 13:467, 1971.
- [76] T. Valet and A. Fert. Theory of the perpendicular magnetoresistance in magnetic multilayers. *Physical Review B*, 48(10):7099–7113, 1993.
- [77] Albert Fert, Thierry Valet, and Jozef Barnas. Perpendicular magnetoresistance in magnetic multilayers: Theoretical model and discussion (invited). *Journal of Applied Physics*, 75(10):6693–6698, 1994.
- [78] J. N. Chazalviel and I. Solomon. Experimental Evidence of the Anomalous Hall Effect in a Nonmagnetic Semiconductor. *Physical Review Letters*, 29(25):1676–1679, 1972.
- [79] A. Jain, J.-C. Rojas-Sanchez, M. Cubukcu, J. Peiro, J. C. Le Breton, E. Prestat, C. Vergnaud, L. Louahadj, C. Portemont, C. Ducruet, V. Baltz, A. Barski, P. Bayle-Guillemaud, L. Vila, J.-P. Attané, E. Augendre, G. Desfonds, S. Gambarelli, H. Jaffrès, J.-M. George, and M. Jamet. Crossover from Spin Accumulation into Interface States to Spin Injection in the Germanium Conduction Band. *Physical Review Letters*, 109(10):106603, 2012.
- [80] Jairo Sinova, Sergio O. Valenzuela, J. Wunderlich, C.H. Back, and T. Jungwirth. Spin Hall effects. *Reviews of Modern Physics*, 87(4):1213–1260, 2015.
- [81] Lijun Zhu, Daniel. C. Ralph, and Robert A. Buhrman. Highly Efficient Spin-Current Generation by the Spin Hall Effect in  $\text{Au}_{1-x}\text{Pt}_x$ . *Physical Review Applied*, 10(3):031001, 2018.
- [82] Shuichi Murakami. Intrinsic Spin Hall Effect. *arXiv:cond-mat/0504353*, 45:197–209, 2005. arXiv: cond-mat/0504353.
- [83] Shuichi Murakami, Naoto Nagaosa, and Shou-Cheng Zhang. Dissipationless Quantum Spin Current at Room Temperature. *Science*, 301(5638):1348–1351, 2003.
- [84] A. Fert, A. Friederich, and A. Hamzic. Hall effect in dilute magnetic alloys. *Journal of Magnetism and Magnetic Materials*, 24(3):231–257, 1981.
- [85] J. Smit. The spontaneous hall effect in ferromagnetics I. *Physica*, 21(6):877–887, 1955.
- [86] L. Berger. Side-Jump Mechanism for the Hall Effect of Ferromagnets. *Physical Review B*, 2(11):4559–4566, 1970.
- [87] Y. Niimi, M. Morota, D. H. Wei, C. Deranlot, M. Basletic, A. Hamzic, A. Fert, and Y. Otani. Extrinsic Spin Hall Effect Induced by Iridium Impurities in Copper. *Physical Review Letters*, 106(12):126601, 2011.
- [88] Albert Fert and Peter M. Levy. Spin Hall Effect Induced by Resonant Scattering on Impurities in Metals. *Physical Review Letters*, 106(15):157208, 2011.
- [89] Yufan Li, Dazhi Hou, Li Ye, Yuan Tian, Jianli Xu, Gang Su, and Xiaofeng Jin. Evidence of the side jump mechanism in the anomalous Hall effect in paramagnets. *EPL (Europhysics Letters)*, 110(2):27002, 2015.
- [90] P. Laczkowski, Y. Fu, H. Yang, J.-C. Rojas-Sánchez, P. Noel, V. T. Pham, G. Zahnd, C. Deranlot, S. Collin, C. Bouard, P. Warin, V. Maurel, M. Chshiev, A. Marty, J.-P. Attané, A. Fert, H. Jaffrès, L. Vila, and J.-M. George. Large enhancement of the spin Hall effect in Au by side-jump scattering on Ta impurities. *Physical Review B*, 96(14):140405, 2017.
- [91] J. Bass. Resistivity/atomic percent impurity in dilute alloys. In *Electrical Resistivity, Thermoelectrical Power and Optical Properties*, Landolt-Börnstein - Group III Condensed Matter, pages 1–12. Berlin, Heidelberg, 1985.
- [92] Yu A. Bychkov and E. I. Rashba. Oscillatory effects and the magnetic susceptibility of carriers in inversion layers. *Journal of Physics C: Solid State Physics*, 17(33):6039–6045, 1984.

- [93] Dyakonov. Spin relaxation of two-dimensional electrons in noncentrosymmetric semiconductors. *Sov. Phys. Semicond.* 20 (1), 110-112, 1986.
- [94] S. D. Ganichev, E. L. Ivchenko, V. V. Bel'kov, S. A. Tarasenko, M. Sollinger, D. Weiss, W. Wegscheider, and W. Prettl. Spin-galvanic effect. *Nature*, 417(6885):153, 2002.
- [95] S. D. Ganichev, V. V. Belkov, L. E. Golub, E. L. Ivchenko, Petra Schneider, S. Giglberger, J. Eroms, J. De Boeck, G. Borghs, W. Wegscheider, D. Weiss, and W. Prettl. Experimental Separation of Rashba and Dresselhaus Spin Splittings in Semiconductor Quantum Wells. *Physical Review Letters*, 92(25):256601, 2004.
- [96] S. Giglberger, L. E. Golub, V. V. Belkov, S. N. Danilov, D. Schuh, C. Gerl, F. Rohlfing, J. Stahl, W. Wegscheider, D. Weiss, W. Prettl, and S. D. Ganichev. Rashba and Dresselhaus spin splittings in semiconductor quantum wells measured by spin photocurrents. *Physical Review B*, 75(3):035327, 2007.
- [97] Seung Ryong Park and Changyoung Kim. Microscopic mechanism for the Rashba spin-band splitting: Perspective from formation of local orbital angular momentum. *Journal of Electron Spectroscopy and Related Phenomena*, 201:6–17, 2015.
- [98] Christian R. Ast, Jürgen Henk, Arthur Ernst, Luca Moreschini, Mihaela C. Falub, Daniela Pacilé, Patrick Bruno, Klaus Kern, and Marco Grioni. Giant Spin Splitting through Surface Alloying. *Physical Review Letters*, 98(18):186807, 2007.
- [99] Christian Rinaldi, Sara Varotto, Marco Asa, Jagoda Sawiska, Jun Fujii, Giovanni Vinai, Stefano Cecchi, Domenico Di Sante, Raffaella Calarco, Ivana Vobornik, Giancarlo Panaccione, Silvia Picozzi, and Riccardo Bertacco. Ferroelectric Control of the Spin Texture in GeTe. *Nano Letters*, 18(5):2751–2758, 2018.
- [100] K. Ishizaka, M. S. Bahramy, H. Murakawa, M. Sakano, T. Shimojima, T. Sonobe, K. Koizumi, S. Shin, H. Miyahara, A. Kimura, K. Miyamoto, T. Okuda, H. Namatame, M. Taniguchi, R. Arita, N. Nagaosa, K. Kobayashi, Y. Murakami, R. Kumai, Y. Kaneko, Y. Onose, and Y. Tokura. Giant Rashba-type spin splitting in bulk BiTeI. *Nature Materials*, 10(7):521–526, 2011.
- [101] Siyuan Zhu, Yukiaki Ishida, Kenta Kuroda, Kazuki Sumida, Mao Ye, Jiajia Wang, Hong Pan, Masaki Taniguchi, Shan Qiao, Shik Shin, and Akio Kimura. Ultrafast electron dynamics at the Dirac node of the topological insulator Sb<sub>2</sub>Te<sub>3</sub>. *Scientific Reports*, 5:13213, 2015.
- [102] Liang Fu and C. L. Kane. Topological insulators with inversion symmetry. *Physical Review B*, 76(4):045302, 2007.
- [103] Liang Fu, C. L. Kane, and E. J. Mele. Topological Insulators in Three Dimensions. *Physical Review Letters*, 98(10):106803, 2007.
- [104] D. Hsieh, D. Qian, L. Wray, Y. Xia, Y. S. Hor, R. J. Cava, and M. Z. Hasan. A topological Dirac insulator in a quantum spin Hall phase. *Nature*, 452(7190):970–974, 2008.
- [105] Y. Xia, D. Qian, D. Hsieh, L. Wray, A. Pal, H. Lin, A. Bansil, D. Grauer, Y. S. Hor, R. J. Cava, and M. Z. Hasan. Observation of a large-gap topological-insulator class with a single Dirac cone on the surface. *Nature Physics*, 5(6):398–402, 2009.
- [106] Y. L. Chen, J. G. Analytis, J.-H. Chu, Z. K. Liu, S.-K. Mo, X. L. Qi, H. J. Zhang, D. H. Lu, X. Dai, Z. Fang, S. C. Zhang, I. R. Fisher, Z. Hussain, and Z.-X. Shen. Experimental Realization of a Three-Dimensional Topological Insulator, Bi<sub>2</sub>Te<sub>3</sub>. *Science*, 325(5937):178–181, 2009.
- [107] D. Hsieh, Y. Xia, D. Qian, L. Wray, F. Meier, J. H. Dil, J. Osterwalder, L. Patthey, A. V. Fedorov, H. Lin, A. Bansil, D. Grauer, Y. S. Hor, R. J. Cava, and M. Z. Hasan. Observation of Time-Reversal-Protected Single-Dirac-Cone Topological-Insulator States in Bi<sub>2</sub>Te<sub>3</sub> and Sb<sub>2</sub>Te<sub>3</sub>. *Physical Review Letters*, 103(14):146401, 2009.
- [108] C. Brüne, C. X. Liu, E. G. Novik, E. M. Hankiewicz, H. Buhmann, Y. L. Chen, X. L. Qi, Z. X. Shen, S. C. Zhang, and L. W. Molenkamp. Quantum Hall Effect from the Topological Surface States of Strained Bulk HgTe. *Physical Review Letters*, 106(12):126803, 2011.
- [109] A. Barfuss, L. Dudy, M. R. Scholz, H. Roth, P. Höpfner, C. Blumenstein, G. Landolt, J. H. Dil, N. C. Plumb, M. Radovic, A. Bostwick, E. Rotenberg, A. Fleszar, G. Bihlmayer, D. Wortmann, G. Li, W. Hanke, R. Claessen, and J. Schäfer. Elemental Topological Insulator with Tunable Fermi Level: Strained  $\alpha$ -Sn on InSb(001). *Physical Review Letters*, 111(15):157205, 2013.
- [110] M. G. Vergniory, L. Elcoro, Claudia Felser, Nicolas Regnault, B. Andrei Bernevig, and Zhijun Wang. A complete catalogue of high-quality topological materials. *Nature*, 566(7745):480, 2019.

- [111] D. Hsieh, Y. Xia, D. Qian, L. Wray, J. H. Dil, F. Meier, J. Osterwalder, L. Patthey, J. G. Checkelsky, N. P. Ong, A. V. Fedorov, H. Lin, A. Bansil, D. Grauer, Y. S. Hor, R. J. Cava, and M. Z. Hasan. A tunable topological insulator in the spin helical Dirac transport regime. *Nature*, 460(7259):1101–1105, 2009.
- [112] A. Bansil, Hsin Lin, and Tanmoy Das. Colloquium: Topological band theory. *Reviews of Modern Physics*, 88(2):021004, June 2016.
- [113] P. D. C. King, R. C. Hatch, M. Bianchi, R. Ovsyannikov, C. Lupulescu, G. Landolt, B. Slomski, J. H. Dil, D. Guan, J. L. Mi, E. D. L. Rienks, J. Fink, A. Lindblad, S. Svensson, S. Bao, G. Balakrishnan, B. B. Iversen, J. Osterwalder, W. Eberhardt, F. Baumberger, and Ph. Hofmann. Large Tunable Rashba Spin Splitting of a Two-Dimensional Electron Gas in  $\text{Bi}_2\text{Se}_3$ . *Physical Review Letters*, 107(9):096802, 2011.
- [114] E.Y.Tsymbal. Physics 927, section 8: Electronic transport. *University of Nebraska, Physics lecture*.
- [115] Gambardella Pietro and Miron Ioan Mihai. Current-induced spinorbit torques. *Philosophical Transactions of the Royal Society A: Mathematical, Physical and Engineering Sciences*, 369(1948):3175–3197, 2011.
- [116] K. Kondou, R. Yoshimi, A. Tsukazaki, Y. Fukuma, J. Matsuno, K. S. Takahashi, M. Kawasaki, Y. Tokura, and Y. Otani. Fermi-level-dependent charge-to-spin current conversion by Dirac surface states of topological insulators. *Nature Physics*, 12(11):1027–1031, 2016.
- [117] S. Zhang and A. Fert. Conversion between spin and charge currents with topological insulators. *Physical Review B*, 94(18):184423, 2016.
- [118] Dong-Xia Qu, Y. S. Hor, Jun Xiong, R. J. Cava, and N. P. Ong. Quantum Oscillations and Hall Anomaly of Surface States in the Topological Insulator  $\text{Bi}_2\text{Te}_3$ . *Science*, 329(5993):821–824, 2010.
- [119] Rik Dey, Nitin Prasad, Leonard F. Register, and Sanjay K. Banerjee. Conversion of spin current into charge current in a topological insulator: Role of the interface. *Physical Review B*, 97(17):174406, 2018.
- [120] Mark Johnson and R. H. Silsbee. Spin-injection experiment. *Physical Review B*, 37(10):5326–5335, April 1988.
- [121] A. Azevedo, L. H. Vilela-Leão, R. L. Rodríguez-Suárez, A. F. Lacerda Santos, and S. M. Rezende. Spin pumping and anisotropic magnetoresistance voltages in magnetic bilayers: Theory and experiment. *Physical Review B*, 83(14):144402, April 2011.
- [122] M. V. Costache, M. Sladkov, S. M. Watts, C. H. van der Wal, and B. J. van Wees. Electrical Detection of Spin Pumping due to the Precessing Magnetization of a Single Ferromagnet. *Physical Review Letters*, 97(21):216603, November 2006.
- [123] O. Mosendz, V. Vlaminck, J. E. Pearson, F. Y. Fradin, G. E. W. Bauer, S. D. Bader, and A. Hoffmann. Detection and quantification of inverse spin Hall effect from spin pumping in permalloy/normal metal bilayers. *Physical Review B*, 82(21):214403, December 2010.
- [124] Yaroslav Tserkovnyak, Arne Brataas, Gerrit E. W. Bauer, and Bertrand I. Halperin. Nonlocal magnetization dynamics in ferromagnetic heterostructures. *Reviews of Modern Physics*, 77(4):1375–1421, December 2005.
- [125] L. Landau and E. Lifshitz. 3 - On the theory of the dispersion of magnetic permeability in ferromagnetic bodies Reprinted from *Physikalische Zeitschrift der Sowjetunion* 8, Part 2, 153, 1935. In L. P. Pitaevski, editor, *Perspectives in Theoretical Physics*, pages 51–65. Pergamon, Amsterdam, January 1992.
- [126] T. L. Gilbert. A phenomenological theory of damping in ferromagnetic materials. *IEEE Transactions on Magnetics*, 40(6):3443–3449, November 2004.
- [127] Alexander G. Gurevich and Gennadii A. Melkov. *Magnetization Oscillations and Waves*. CRC Press, September 1996. Google-Books-ID: YgQtSvFIvFQC.
- [128] Michael Farle. Ferromagnetic resonance of ultrathin metallic layers. *Reports on Progress in Physics*, 61(7):755–826, July 1998.
- [129] D. Polder. VIII. On the theory of ferromagnetic resonance. *The London, Edinburgh, and Dublin Philosophical Magazine and Journal of Science*, 40(300):99–115, January 1949.
- [130] Charles Kittel. On the Theory of Ferromagnetic Resonance Absorption. *Physical Review*, 73(2):155–161, January 1948.
- [131] M. S. Suzuki and Suzuki I.S. Lecture note on solid state physics ac magnetic susceptibility.

- [132] Vegard Flovik, Ferran Macià, Andrew D. Kent, and Erik Wahlström. Eddy current interactions in a ferromagnet-normal metal bilayer structure, and its impact on ferromagnetic resonance lineshapes. *Journal of Applied Physics*, 117(14):143902, April 2015.
- [133] Vegard Flovik, Bjørn Holst Pettersen, and Erik Wahlström. Eddy-current effects on ferromagnetic resonance: Spin wave excitations and microwave screening effects. *Journal of Applied Physics*, 119(16):163903, April 2016.
- [134] O. Gladii, R. L. Seeger, L. Frangou, G. Forestier, U. Ebels, S. Auffret, and V. Baltz. Stacking order-dependent sign-change of microwave phase due to eddy currents in nanometer-scale NiFe/Cu heterostructures. *Applied Physics Letters*, 115(3):032403, July 2019.
- [135] H. Hurdequint. FMR studies of ultrathin permalloy layers sandwiched by Al<sub>2</sub>O<sub>3</sub>. *Journal of Magnetism and Magnetic Materials*, 242-245:521–524, April 2002.
- [136] S. Mercone, M. Belmeguenai, S. Malo, F. Ott, F. Cayrel, M. Golosovsky, B. Leridon, C. Adamo, and P. Monod. Investigation of ferromagnetic heterogeneities in La<sub>0.7</sub>sr<sub>0.3</sub>mno<sub>3</sub> thin films. *Journal of Physics D: Applied Physics*, 50(4):045001, January 2017.
- [137] Martin A. W. Schoen, Danny Thonig, Michael L. Schneider, T. J. Silva, Hans T. Nembach, Olle Eriksson, Olof Karis, and Justin M. Shaw. Ultra-low magnetic damping of a metallic ferromagnet. *Nature Physics*, 12(9):839–842, September 2016.
- [138] G. Woltersdorf, M. Kiessling, G. Meyer, J.-U. Thiele, and C. H. Back. Damping by Slow Relaxing Rare Earth Impurities in  $\{\mathrm{Ni}\}_{80}\{\mathrm{Fe}\}_{20}$ . *Physical Review Letters*, 102(25):257602, June 2009.
- [139] C. L. Jermain, S. V. Aradhya, N. D. Reynolds, R. A. Buhrman, J. T. Brangham, M. R. Page, P. C. Hammel, F. Y. Yang, and D. C. Ralph. Increased low-temperature damping in yttrium iron garnet thin films. *Physical Review B*, 95(17):174411, May 2017.
- [140] Kh. Zakeri, J. Lindner, I. Barsukov, R. Meckenstock, M. Farle, U. von Hörsten, H. Wende, W. Keune, J. Rocker, S. S. Kalarickal, K. Lenz, W. Kuch, K. Baberschke, and Z. Frait. Spin dynamics in ferromagnets: Gilbert damping and two-magnon scattering. *Physical Review B*, 76(10):104416, September 2007.
- [141] K. Lenz, H. Wende, W. Kuch, K. Baberschke, K. Nagy, and A. Jánossy. Two-magnon scattering and viscous Gilbert damping in ultrathin ferromagnets. *Physical Review B*, 73(14):144424, April 2006.
- [142] C. J. Brower and C. E. Patton. Determination of anisotropy field in polycrystalline lithium ferrites from FMR linewidths. *Journal of Applied Physics*, 53(3):2104–2106, March 1982.
- [143] T. Devolder, P.-H. Ducrot, J.-P. Adam, I. Barisic, N. Vernier, Joo-Von Kim, B. Ockert, and D. Ravelosona. Damping of CoFe<sub>80</sub>B<sub>20</sub> ultrathin films with perpendicular magnetic anisotropy. *Applied Physics Letters*, 102(2):022407, January 2013.
- [144] S. Sievers, J. Kurda, N. Liebing, F. Hohls, and H. W. Schumacher. Microwave Interferometry for High Sensitivity VNA-FMR Measurements. *IEEE Transactions on Magnetics*, 53(4):1–4, April 2017.
- [145] G. Counil, T. Devolder, J. Kim, P. Crozat, C. Chappert, S. Zoll, and R. Fournel. Temperature Dependences of the Resistivity and the Ferromagnetic Resonance Linewidth in Permalloy Thin Films. *IEEE Transactions on Magnetics*, 42(10):3323–3325, October 2006.
- [146] J.-M. Beaujour, D. Ravelosona, I. Tudosa, E. E. Fullerton, and A. D. Kent. Ferromagnetic resonance linewidth in ultrathin films with perpendicular magnetic anisotropy. *Physical Review B*, 80(18):180415, November 2009.
- [147] H. Puzkarski and M. Kasperski. On the Interpretation of the Angular Dependence of the Main FMR/SWR Line in Ferromagnetic Thin Films. *Acta Physica Polonica A*, 121(5-6):1165–1168, May 2012.
- [148] P. Landeros, Rodrigo E. Arias, and D. L. Mills. Two magnon scattering in ultrathin ferromagnets: The case where the magnetization is out of plane. *Physical Review B*, 77(21):214405, June 2008.
- [149] Ken-ichi Uchida, Hiroto Adachi, Takeru Ota, Hiroyasu Nakayama, Sadamichi Maekawa, and Eiji Saitoh. Observation of longitudinal spin-Seebeck effect in magnetic insulators. *Applied Physics Letters*, 97(17):172505, October 2010.
- [150] Arne Brataas, Yaroslav Tserkovnyak, Gerrit E. W. Bauer, and Bertrand I. Halperin. Spin battery operated by ferromagnetic resonance. *Physical Review B*, 66(6):060404, August 2002.
- [151] Yaroslav Tserkovnyak, Arne Brataas, and Gerrit E. W. Bauer. Spin pumping and magnetization dynamics in metallic multilayers. *Physical Review B*, 66(22):224403, December 2002.

- [152] Yaroslav Tserkovnyak, Arne Brataas, and Gerrit E. W. Bauer. Enhanced Gilbert Damping in Thin Ferromagnetic Films. *Physical Review Letters*, 88(11):117601, February 2002.
- [153] S. Mizukami, Y. Ando, and T. Miyazaki. Effect of spin diffusion on Gilbert damping for a very thin permalloy layer in Cu/permalloy/Cu/Pt films. *Physical Review B*, 66(10):104413, September 2002.
- [154] R. J. H. Wesselink, K. Gupta, Z. Yuan, and Paul J. Kelly. Calculating spin transport properties from first principles: Spin currents. *Physical Review B*, 99(14):144409, April 2019.
- [155] Yi Liu, Zhe Yuan, R.J.H. Wesselink, Anton A. Starikov, and Paul J. Kelly. Interface Enhancement of Gilbert Damping from First Principles. *Physical Review Letters*, 113(20):207202, November 2014.
- [156] J. Foros, G. Woltersdorf, B. Heinrich, and A. Brataas. Scattering of spin current injected in Pd(001). *Journal of Applied Physics*, 97(10):10A714, April 2005.
- [157] Justin M. Shaw, Hans T. Nembach, and T. J. Silva. Determination of spin pumping as a source of linewidth in sputtered Co<sub>90</sub>Fe<sub>10</sub>/Pd multilayers by use of broadband ferromagnetic resonance spectroscopy. *Physical Review B*, 85(5):054412, February 2012.
- [158] X. D. Tao, Z. Feng, B. F. Miao, L. Sun, B. You, D. Wu, J. Du, W. Zhang, and H. F. Ding. The spin Hall angle and spin diffusion length of Pd measured by spin pumping and microwave photoresistance. *Journal of Applied Physics*, 115(17):17C504, January 2014.
- [159] H. Nakayama, K. Ando, K. Harii, T. Yoshino, R. Takahashi, Y. Kajiwara, K. Uchida, Y. Fujikawa, and E. Saitoh. Geometry dependence on inverse spin Hall effect induced by spin pumping in Ni<sub>81</sub>Fe<sub>19</sub>/Pt films. *Physical Review B*, 85(14):144408, April 2012.
- [160] S Mizukami, Y Ando, and T Miyazaki. Ferromagnetic resonance linewidth for NM/80nife/NM films (NM=Cu, Ta, Pd and Pt). *Journal of Magnetism and Magnetic Materials*, 226-230:1640–1642, May 2001.
- [161] M. Caminale, A. Ghosh, S. Auffret, U. Ebels, K. Ollefs, F. Wilhelm, A. Rogalev, and W. E. Bailey. Spin pumping damping and magnetic proximity effect in Pd and Pt spin-sink layers. *Physical Review B*, 94(1):014414, July 2016.
- [162] Xinde Tao, Qi Liu, Bingfeng Miao, Rui Yu, Zheng Feng, Liang Sun, Biao You, Jun Du, Kai Chen, Shufeng Zhang, Luo Zhang, Zhe Yuan, Di Wu, and Haifeng Ding. Self-consistent determination of spin Hall angle and spin diffusion length in Pt and Pd: The role of the interface spin loss. *Science Advances*, 4(6):eaat1670, June 2018.
- [163] Andrew J. Berger, Eric R. J. Edwards, Hans T. Nembach, Olof Karis, Mathias Weiler, and T. J. Silva. Determination of the spin Hall effect and the spin diffusion length of Pt from self-consistent fitting of damping enhancement and inverse spin-orbit torque measurements. *Physical Review B*, 98(2):024402, July 2018.
- [164] Mark W. Keller, Katy S. Gerace, Monika Arora, Erna Krisztina Delczeg-Czirjak, Justin M. Shaw, and T. J. Silva. Near-unity spin Hall ratio in  $\mathrm{N}_i\mathrm{C}_u$  alloys. *Physical Review B*, 99(21):214411, June 2019.
- [165] M. V. Costache, S. M. Watts, C. H. van der Wal, and B. J. van Wees. Electrical detection of spin pumping: dc voltage generated by ferromagnetic resonance at ferromagnet/nonmagnet contact. *Physical Review B*, 78(6):064423, August 2008.
- [166] K. Ando, S. Takahashi, J. Ieda, H. Kurebayashi, T. Trypiniotis, C. H. W. Barnes, S. Maekawa, and E. Saitoh. Electrically tunable spin injector free from the impedance mismatch problem. *Nature Materials*, 10(9):655–659, September 2011.
- [167] K. Ando, S. Takahashi, J. Ieda, Y. Kajiwara, H. Nakayama, T. Yoshino, K. Harii, Y. Fujikawa, M. Matsuo, S. Maekawa, and E. Saitoh. Inverse spin-Hall effect induced by spin pumping in metallic system. *Journal of Applied Physics*, 109(10):103913, May 2011.
- [168] O. Mosendz, J. E. Pearson, F. Y. Fradin, G. E. W. Bauer, S. D. Bader, and A. Hoffmann. Quantifying Spin Hall Angles from Spin Pumping: Experiments and Theory. *Physical Review Letters*, 104(4):046601, January 2010.
- [169] T. Yoshino, K. Ando, K. Harii, H. Nakayama, Y. Kajiwara, and E. Saitoh. Universality of the spin pumping in metallic bilayer films. *Applied Physics Letters*, 98(13):132503, March 2011.
- [170] HuJun Jiao and Gerrit E. W. Bauer. Spin Backflow and ac Voltage Generation by Spin Pumping and the Inverse Spin Hall Effect. *Physical Review Letters*, 110(21):217602, May 2013.
- [171] Mathias Weiler, Justin M. Shaw, Hans T. Nembach, and Thomas J. Silva. Phase-Sensitive Detection of Spin Pumping via the ac Inverse Spin Hall Effect. *Physical Review Letters*, 113(15):157204, October 2014.

- [172] C. Hahn, G. de Loubens, M. Viret, O. Klein, V. V. Naletov, and J. Ben Youssef. Detection of Microwave Spin Pumping Using the Inverse Spin Hall Effect. *Physical Review Letters*, 111(21):217204, November 2013.
- [173] V. Vlaminck, J. E. Pearson, S. D. Bader, and A. Hoffmann. Dependence of spin-pumping spin Hall effect measurements on layer thicknesses and stacking order. *Physical Review B*, 88(6):064414, August 2013.
- [174] Sang-Il Kim, Dong-Jun Kim, Min-Su Seo, Byong-Guk Park, and Seung-Young Park. Stacking order dependence of inverse spin Hall effect and anomalous Hall effect in spin pumping experiments. *Journal of Applied Physics*, 117(17):17D901, January 2015.
- [175] Z. Feng, J. Hu, L. Sun, B. You, D. Wu, J. Du, W. Zhang, A. Hu, Y. Yang, D. M. Tang, B. S. Zhang, and H. F. Ding. Spin Hall angle quantification from spin pumping and microwave photoresistance. *Physical Review B*, 85(21):214423, June 2012.
- [176] Tianxiang Nan, Satoru Emori, Carl T. Boone, Xinjun Wang, Trevor M. Oxholm, John G. Jones, Brandon M. Howe, Gail J. Brown, and Nian X. Sun. Comparison of spin-orbit torques and spin pumping across NiFe/Pt and NiFe/Cu/Pt interfaces. *Physical Review B*, 91(21):214416, June 2015.
- [177] Ayaka Tsukahara, Yuichiro Ando, Yuta Kitamura, Hiroyuki Emoto, Eiji Shikoh, Michael P. Delmo, Teruya Shinjo, and Masashi Shiraishi. Self-induced inverse spin Hall effect in permalloy at room temperature. *Physical Review B*, 89(23):235317, June 2014.
- [178] Y. S. Gui, S. Holland, N. Mecking, and C. M. Hu. Resonances in Ferromagnetic Gratings Detected by Microwave Photoconductivity. *Physical Review Letters*, 95(5):056807, July 2005.
- [179] Michael Harder, Yongsheng Gui, and Can-Ming Hu. Electrical detection of magnetization dynamics via spin rectification effects. *Physics Reports*, 661:1–59, November 2016.
- [180] Kazuto Yamanoi, Yuki Yokotani, and Takashi Kimura. Dynamical Spin Injection Based on Heating Effect due to Ferromagnetic Resonance. *Physical Review Applied*, 8(5):054031, November 2017.
- [181] K. Kaski, P. Kuivalainen, and T. Stubb. Transport properties of EuO at ferromagnetic resonance. *Journal of Applied Physics*, 49(3):1595–1597, March 1978.
- [182] S. T. B. Goennenwein, S. W. Schink, A. Brandlmaier, A. Boger, M. Opel, R. Gross, R. S. Keizer, T. M. Klapwijk, A. Gupta, H. Huebl, C. Bihler, and M. S. Brandt. Electrically detected ferromagnetic resonance. *Applied Physics Letters*, 90(16):162507, April 2007.
- [183] S. T. B. Goennenwein, S. W. Schink, A. Brandlmaier, A. Boger, M. Opel, R. Gross, R. S. Keizer, T. M. Klapwijk, A. Gupta, H. Huebl, C. Bihler, and M. S. Brandt. Electrically detected ferromagnetic resonance. *Applied Physics Letters*, 90(16):162507, April 2007.
- [184] Y. S. Gui, N. Mecking, A. Wirthmann, L. H. Bai, and C.-M. Hu. Electrical detection of the ferromagnetic resonance: Spin-rectification versus bolometric effect. *Applied Physics Letters*, 91(8):082503, August 2007.
- [185] H. J. Juretschke. Electromagnetic Theory of dc Effects in Ferromagnetic Resonance. *Journal of Applied Physics*, 31(8):1401–1406, August 1960.
- [186] W. G. Egan and H. J. Juretschke. DC Detection of Ferromagnetic Resonance in Thin Nickel Films. *Journal of Applied Physics*, 34(5):1477–1484, May 1963.
- [187] Sang-Il Kim, Min-Su Seo, and Seung-young Park. Resonant cavity mode dependence of anomalous and inverse spin Hall effect. *Journal of Applied Physics*, 115(17):17C501, January 2014.
- [188] S. Oyarzún, A. K. Nandy, F. Rortais, J.-C. Rojas-Sánchez, M.-T. Dau, P. Noël, P. Laczkowski, S. Pouget, H. Okuno, L. Vila, C. Vergnaud, C. Beigné, A. Marty, J.-P. Attané, S. Gambarelli, J.-M. George, H. Jaffrès, S. Blügel, and M. Jamet. Evidence for spin-to-charge conversion by Rashba coupling in metallic states at the Fe/Ge(111) interface. *Nature Communications*, 7:13857, December 2016.
- [189] J. Lustikova, Y. Shiomi, and E. Saitoh. Vector spectroscopy for spin pumping. *Physical Review B*, 92(22):224436, December 2015.
- [190] Ryo Iguchi and Eiji Saitoh. Measurement of Spin Pumping Voltage Separated from Extrinsic Microwave Effects. *Journal of the Physical Society of Japan*, 86(1):011003, November 2016.
- [191] Muhammad Ikhlas, Takahiro Tomita, Takashi Koretsune, Michi-To Suzuki, Daisuke Nishio-Hamane, Ryotaro Arita, Yoshichika Otani, and Satoru Nakatsuji. Large anomalous Nernst effect at room temperature in a chiral antiferromagnet. *Nature Physics*, 13(11):1085–1090, November 2017.

- [192] Weiwei Lin and C. L. Chien. Evidence of pure spin current. March 2018.
- [193] Mahendra DC, Jun-Yang Chen, Thomas Peterson, Protuys Sahu, Bin Ma, Naser Mousavi, Ramesh Harjani, and Jian-Ping Wang. Observation of High Spin-to-Charge Conversion by Sputtered Bismuth Selenide Thin Films at Room Temperature. *Nano Letters*, 19(8):4836–4844, August 2019.
- [194] Kazunari Kanagawa, Yoshio Teki, and Eiji Shikoh. Self-induced inverse spin-Hall effect in an iron and a cobalt single-layer films themselves under the ferromagnetic resonance. *AIP Advances*, 8(5):055910, December 2017.
- [195] S. Bandiera, R. C. Sousa, B. Rodmacq, and B. Dieny. Enhancement of perpendicular magnetic anisotropy through reduction of Co-Pt interdiffusion in (Co/Pt) multilayers. *Applied Physics Letters*, 100(14):142410, April 2012.
- [196] Edurne Sagasta, Yasutomo Omori, Saül Vélez, Roger Llopis, Christopher Tollan, Andrey Chuvilin, Luis E. Hueso, Martin Gradhand, YoshiChika Otani, and Fèlix Casanova. Unveiling the mechanisms of the spin Hall effect in Ta. *Physical Review B*, 98(6):060410, August 2018.
- [197] Michael Schreier, Gerrit E. W. Bauer, Vitaliy I. Vasyuchka, Joost Flipse, Ken-ichi Uchida, Johannes Lotze, Viktor Lauer, Andrii V. Chumak, Alexander A. Serga, Shunsuke Daimon, Takashi Kikkawa, Eiji Saitoh, Bart J. van Wees, Burkard Hillebrands, Rudolf Gross, and Sebastian T. B. Goennenwein. Sign of inverse spin Hall voltages generated by ferromagnetic resonance and temperature gradients in yttrium iron garnet platinum bilayers. *Journal of Physics D: Applied Physics*, 48(2):025001, December 2014.
- [198] C. Hahn, G. de Loubens, O. Klein, M. Viret, V. V. Naletov, and J. Ben Youssef. Comparative measurements of inverse spin Hall effects and magnetoresistance in YIG/Pt and YIG/Ta. *Physical Review B*, 87(17):174417, May 2013.
- [199] Dong-Jun Kim, Sang-Il Kim, Seung-Young Park, Kyeong-Dong Lee, and Byong-Guk Park. Ferromagnetic resonance spin pumping in CoFeB with highly resistive non-magnetic electrodes. *Current Applied Physics*, 14(10):1344–1348, October 2014.
- [200] D. Qu, S. Y. Huang, B. F. Miao, S. X. Huang, and C. L. Chien. Self-consistent determination of spin Hall angles in selected  $d$  metals by thermal spin injection. *Physical Review B*, 89(14):140407, April 2014.
- [201] Can Onur Avci, Kevin Garello, Abhijit Ghosh, Mihai Gabureac, Santos F. Alvarado, and Pietro Gambardella. Unidirectional spin Hall magnetoresistance in ferromagnet/normal metal bilayers. *Nature Physics*, 11(7):570–575, July 2015.
- [202] A. Conca, B. Heinz, M. R. Schweizer, S. Keller, E. Th. Papaioannou, and B. Hillebrands. Lack of correlation between the spin-mixing conductance and the inverse spin Hall effect generated voltages in CoFeB/Pt and CoFeB/Ta bilayers. *Physical Review B*, 95(17):174426, May 2017.
- [203] Y. Huo, F.L. Zeng, C. Zhou, and Y.Z. Wu. Spin Pumping and Thermal Effects in Single-Crystalline  $\text{Fe/Pt}$  Bilayers at the Nonresonant Condition. *Physical Review Applied*, 8(1):014022, July 2017.
- [204] Kazuto Yamanoi, Yuki Yokotani, and Takashi Kimura. Heat dissipation due to ferromagnetic resonance in a ferromagnetic metal monitored by electrical resistance measurement. *Applied Physics Letters*, 107(18):182410, November 2015.
- [205] Paul Noël, Maxen Cosset-Cheneau, Victor Haspot, Vincent Maurel, Christian Lombard, Manuel Bibes, Agnès Barthelemy, Laurent Vila, and Jean-Philippe Attané. Do thermal effects always contribute to spin pumping signals? May 2019.
- [206] Wei Zhang, Vincent Vlamincq, John E. Pearson, Ralu Divan, Samuel D. Bader, and Axel Hoffmann. Determination of the Pt spin diffusion length by spin-pumping and spin Hall effect. *Applied Physics Letters*, 103(24):242414, December 2013.
- [207] J. Holanda, O. Alves Santos, R. O. Cunha, J. B. S. Mendes, R. L. Rodríguez-Suárez, A. Azevedo, and S. M. Rezende. Longitudinal spin Seebeck effect in permalloy separated from the anomalous Nernst effect: Theory and experiment. *Physical Review B*, 95(21):214421, June 2017.
- [208] Shu-Chun Wu, Binghai Yan, and Claudia Felser. Ab initio study of topological surface states of strained HgTe. *EPL (Europhysics Letters)*, 107(5):57006, September 2014.
- [209] H. Julian Goldsmid. Bismuth Telluride and Its Alloys as Materials for Thermoelectric Generation. *Materials*, 7(4):2577–2592, April 2014.



- [210] P. Wang, L.F. Zhou, S.W. Jiang, Z.Z. Luan, D.J. Shu, H.F. Ding, and D. Wu. Unidirectional Spin-Wave-Propagation-Induced Seebeck Voltage in a PEDOT:PSS/YIG Bilayer. *Physical Review Letters*, 120(4):047201, January 2018.
- [211] Rajagopalan Ramaswamy, Yi Wang, Mehrdad Elyasi, M. Motapothula, T. Venkatesan, Xuepeng Qiu, and Hyunsoo Yang. Extrinsic Spin Hall Effect in  $\text{Cu}_{1-x}\text{Pt}_x$ . *Physical Review Applied*, 8(2):024034, August 2017.
- [212] P. Laczkowski, H. Jaffrès, W. Savero-Torres, J.-C. Rojas-Sánchez, Y. Fu, N. Reyren, C. Deranlot, L. Notin, C. Beigné, J.-P. Attané, L. Vila, J.-M. George, and A. Marty. Evaluation of spin diffusion length of AuW alloys using spin absorption experiments in the limit of large spin-orbit interactions. *Physical Review B*, 92(21):214405, 2015.
- [213] Yuele Zhao, Qi Song, See-Hun Yang, Tang Su, Wei Yuan, Stuart S. P. Parkin, Jing Shi, and Wei Han. Experimental Investigation of Temperature-Dependent Gilbert Damping in Permalloy Thin Films. *Scientific Reports*, 6:22890, March 2016.
- [214] A. Hoffmann. Spin Hall Effects in Metals. *IEEE Transactions on Magnetics*, 49(10):5172–5193, October 2013.
- [215] Lijun Zhu, Kemal Sobotkewich, Xin Ma, Xiaoqin Li, Daniel C. Ralph, and Robert A. Buhrman. Strong Damping-Like Spin-Orbit Torque and Tunable Dzyaloshinskii-Moriya Interaction Generated by Low-Resistivity Pd<sub>1-x</sub>Pt<sub>x</sub> Alloys. *Advanced Functional Materials*, 29(16):1805822, 2019.
- [216] Wei Zhang, Matthias B. Jungfleisch, Wanjun Jiang, John E. Pearson, and Axel Hoffmann. Spin pumping and inverse Rashba-Edelstein effect in NiFe/Ag/Bi and NiFe/Ag/Sb. *Journal of Applied Physics*, 117(17):17C727, March 2015.
- [217] Shutaro Karube, Kouta Kondou, and YoshiChika Otani. Experimental observation of spin-to-charge current conversion at non-magnetic metal/Bi<sub>2</sub>O<sub>3</sub> interfaces. *Applied Physics Express*, 9(3):033001, January 2016.
- [218] Qi Song, Hongrui Zhang, Tang Su, Wei Yuan, Yangyang Chen, Wenyu Xing, Jing Shi, Jirong Sun, and Wei Han. Observation of inverse Edelstein effect in Rashba-split 2deg between SrTiO<sub>3</sub> and LaAlO<sub>3</sub> at room temperature. *Science Advances*, 3(3):e1602312, March 2017.
- [219] J.-Y. Chauleau, M. Boselli, S. Gariglio, R. Weil, G. de Loubens, J.-M. Triscone, and M. Viret. Efficient spin-to-charge conversion in the 2d electron liquid at the LAO/STO interface. *EPL (Europhysics Letters)*, 116(1):17006, October 2016.
- [220] Yi Wang, Rajagopalan Ramaswamy, Mallikarjuna Motapothula, Kulothungasagaran Narayanapillai, Dapeng Zhu, Jiawei Yu, Thirumalai Venkatesan, and Hyunsoo Yang. Room-Temperature Giant Charge-to-Spin Conversion at the SrTiO<sub>3</sub>/LaAlO<sub>3</sub> Oxide Interface. *Nano Letters*, 17(12):7659–7664, December 2017.
- [221] Shinobu Ohya, Daisei Araki, Le Duc Anh, Shingo Kaneta, Munetoshi Seki, Hitoshi Tabata, and Masaaki Tanaka. Efficient intrinsic spin-to-charge current conversion in an all-epitaxial single-crystal perovskite-oxide heterostructure of La<sub>0.67</sub>Sr<sub>0.33</sub>MnO<sub>3</sub>/LaAlO<sub>3</sub>/SrTiO<sub>3</sub>. *arXiv:1906.06016 [cond-mat]*, June 2019.
- [222] R. K. Astala and P. D. Bristowe. Ab initio calculations of doping mechanisms in SrTiO<sub>3</sub>. *Modelling and Simulation in Materials Science and Engineering*, 12(1):79–90, November 2003.
- [223] A. F. Santander-Syro, O. Copie, T. Kondo, F. Fortuna, S. Pailhès, R. Weht, X. G. Qiu, F. Bertran, A. Nicolaou, A. Taleb-Ibrahimi, P. Le Fèvre, G. Herranz, M. Bibes, N. Reyren, Y. Apertet, P. Lecoeur, A. Barthélémy, and M. J. Rozenberg. Two-dimensional electron gas with universal subbands at the surface of SrTiO<sub>3</sub>. *Nature*, 469(7329):189–193, January 2011.
- [224] Chen Ang, A. S. Bhalla, Ruyan Guo, and L. E. Cross. Dielectric loss of SrTiO<sub>3</sub> single crystals under direct current bias. *Applied Physics Letters*, 76(14):1929–1931, March 2000.
- [225] Nuno J. G. Couto, Benjamin Sacépé, and Alberto F. Morpurgo. Transport through Graphene on  $\text{SrTiO}_3$ . *Physical Review Letters*, 107(22):225501, November 2011.
- [226] Guanhua Zhang, Huajun Qin, Jun Chen, Xiaoyue He, Li Lu, Yongqing Li, and Kehui Wu. Growth of Topological Insulator Bi<sub>2</sub>Se<sub>3</sub> Thin Films on SrTiO<sub>3</sub> with Large Tunability in Chemical Potential. *Advanced Functional Materials*, 21(12):2351–2355, June 2011.
- [227] W. J. Lin, T. Y. Tseng, H. B. Lu, S. L. Tu, S. J. Yang, and I. N. Lin. Growth and ferroelectricity of epitaxiallike BaTiO<sub>3</sub> films on singlecrystal MgO, SrTiO<sub>3</sub>, and silicon substrates synthesized by pulsed laser deposition. *Journal of Applied Physics*, 77(12):6466–6471, June 1995.

- [228] Yoko Yasutomi, Keita Ito, Tatsunori Sanai, Kaoru Toko, and Takashi Suemasu. Perpendicular magnetic anisotropy of Mn<sub>4n</sub> films on MgO(001) and SrTiO<sub>3</sub>(001) substrates. *Journal of Applied Physics*, 115(17):17A935, March 2014.
- [229] T. Gushi, M. Jovievi Klug, J. Peña Garcia, H. Okuno, J. Vogel, J. P. Attané, T. Suemasu, S. Pizzini, and L. Vila. Mn<sub>4n</sub> ferrimagnetic thin films for sustainable spintronics. January 2019.
- [230] J.-L. Maurice, F. Pailloux, A. Barthélémy, A. Rocher, O. Durand, R. Lyonnet, and J.-P. Contour. Strain and magnetism in (La<sub>0.7</sub>Sr<sub>0.3</sub>)MnO<sub>3</sub> very thin films epitaxially grown on SrTiO<sub>3</sub>. *Applied Surface Science*, 188(1-2):176–181, March 2002.
- [231] C. H. Chen, J. Kwo, and M. Hong. Microstructures of YBa<sub>2</sub>Cu<sub>3</sub>O<sub>7-x</sub> superconducting thin films grown on a SrTiO<sub>3</sub>(100) substrate. *Applied Physics Letters*, 52(10):841–843, March 1988.
- [232] Diogo C. Vaz, Paul Noël, Annika Johansson, Børge Göbel, Flavio Y. Bruno, Gyanendra Singh, Siobhan McKeown-Walker, Felix Trier, Luis M. Vicente-Arche, Anke Sander, Sergio Valencia, Pierre Bruneel, Manali Vivek, Marc Gabay, Nicolas Bergeal, Felix Baumberger, Hanako Okuno, Agnès Barthélémy, Albert Fert, Laurent Vila, Ingrid Mertig, Jean-Philippe Attané, and Manuel Bibes. Mapping spincharge conversion to the band structure in a topological oxide two-dimensional electron gas. *Nature Materials*, pages 1–7, September 2019.
- [233] A. Ohtomo and H. Y. Hwang. A high-mobility electron gas at the LaAlO<sub>3</sub>/SrTiO<sub>3</sub> heterointerface. *Nature*, 427(6973):423–426, January 2004.
- [234] M. L. Reinle-Schmitt, C. Cancellieri, D. Li, D. Fontaine, M. Medarde, E. Pomjakushina, C. W. Schneider, S. Gariglio, Ph Ghosez, J.-M. Triscone, and P. R. Willmott. Tunable conductivity threshold at polar oxide interfaces. *Nature Communications*, 3:932, July 2012.
- [235] Y. Z. Chen, N. Bovet, F. Trier, D. V. Christensen, F. M. Qu, N. H. Andersen, T. Kasama, W. Zhang, R. Giraud, J. Dufouleur, T. S. Jespersen, J. R. Sun, A. Smith, J. Nygård, L. Lu, B. Büchner, B. G. Shen, S. Linderöth, and N. Pryds. A high-mobility two-dimensional electron gas at the spinel/perovskite interface of -Al<sub>2</sub>O<sub>3</sub>/SrTiO<sub>3</sub>. *Nature Communications*, 4:1371, January 2013.
- [236] R. Ohtsuka, M. Matvejeff, K. Nishio, R. Takahashi, and M. Lippmaa. Transport properties of LaTiO<sub>3</sub>/SrTiO<sub>3</sub> heterostructures. *Applied Physics Letters*, 96(19):192111, May 2010.
- [237] Y. Hotta, T. Susaki, and H. Y. Hwang. Polar Discontinuity Doping of the  $\{\mathrm{LaVO}\}_3/\{\mathrm{SrTiO}\}_3$  Interface. *Physical Review Letters*, 99(23):236805, December 2007.
- [238] N. Reyren, S. Thiel, A. D. Caviglia, L. Fitting Kourkoutis, G. Hammerl, C. Richter, C. W. Schneider, T. Kopp, A.-S. Rüetschi, D. Jaccard, M. Gabay, D. A. Muller, J.-M. Triscone, and J. Mannhart. Superconducting Interfaces Between Insulating Oxides. *Science*, 317(5842):1196–1199, August 2007.
- [239] Sumilan Banerjee, Onur Erten, and Mohit Randeria. Ferromagnetic exchange, spinorbit coupling and spiral magnetism at the LaAlO<sub>3</sub>/SrTiO<sub>3</sub> interface. *Nature Physics*, 9(10):626–630, October 2013.
- [240] A. D. Caviglia, S. Gariglio, C. Cancellieri, B. Sacépé, A. Fête, N. Reyren, M. Gabay, A. F. Morpurgo, and J.-M. Triscone. Two-Dimensional Quantum Oscillations of the Conductance at  $\{\mathrm{LaAlO}\}_3/\{\mathrm{SrTiO}\}_3$  Interfaces. *Physical Review Letters*, 105(23):236802, December 2010.
- [241] Felix Trier, Guenevere E.D.K. Prawiroatmodjo, Zhicheng Zhong, Dennis Valbjørn Christensen, Merlin von Soosten, Arghya Bhowmik, Juan Maria García Lastra, Yunzhong Chen, Thomas Sand Jespersen, and Nini Pryds. Quantization of Hall Resistance at the Metallic Interface between an Oxide Insulator and  $\{\mathrm{SrTiO}\}_3$ . *Physical Review Letters*, 117(9):096804, August 2016.
- [242] A. D. Caviglia, S. Gariglio, N. Reyren, D. Jaccard, T. Schneider, M. Gabay, S. Thiel, G. Hammerl, J. Mannhart, and J.-M. Triscone. Electric field control of the LaAlO<sub>3</sub>/SrTiO<sub>3</sub> interface ground state. *Nature*, 456(7222):624–627, December 2008.
- [243] M. Ben Shalom, M. Sachs, D. Rakhmilevitch, A. Palevski, and Y. Dagan. Tuning Spin-Orbit Coupling and Superconductivity at the  $\{\mathrm{SrTiO}\}_3/\{\mathrm{LaAlO}\}_3$  Interface: A Magnetotransport Study. *Physical Review Letters*, 104(12):126802, March 2010.

- [244] A. D. Caviglia, M. Gabay, S. Gariglio, N. Reyren, C. Cancellieri, and J.-M. Triscone. Tunable Rashba Spin-Orbit Interaction at Oxide Interfaces. *Physical Review Letters*, 104(12):126803, March 2010.
- [245] N. Reyren, M. Bibes, E. Lesne, J.-M. George, C. Deranlot, S. Collin, A. Barthélémy, and H. Jaffrès. Gate-Controlled Spin Injection at  $\{\mathrm{LaAlO}\}_3/\{\mathrm{SrTiO}\}_3$  Interfaces. *Physical Review Letters*, 108(18):186802, April 2012.
- [246] Arjun Joshua, S. Pecker, J. Ruhman, E. Altman, and S. Ilani. A universal critical density underlying the physics of electrons at the  $\mathrm{LaAlO}_3/\mathrm{SrTiO}_3$  interface. *Nature Communications*, 3:1129, October 2012.
- [247] G. Herranz, M. Basleti, M. Bibes, C. Carrétéro, E. Tafra, E. Jacquet, K. Bouzehouane, C. Deranlot, A. Hamzi, J.-M. Broto, A. Barthélémy, and A. Fert. High Mobility in  $\{\mathrm{LaAlO}\}_3/\{\mathrm{SrTiO}\}_3$  Heterostructures: Origin, Dimensionality, and Perspectives. *Physical Review Letters*, 98(21):216803, May 2007.
- [248] Diogo Castro Vaz, Edouard Lesne, Anke Sander, Hiroshi Naganuma, Eric Jacquet, Jacobo Santamaria, Agnès Barthélémy, and Manuel Bibes. Tuning Up or Down the Critical Thickness in  $\mathrm{LaAlO}_3/\mathrm{SrTiO}_3$  through In Situ Deposition of Metal Overlayers. *Advanced Materials*, 29(28):1700486, 2017.
- [249] Diogo Castro Vaz, Edouard Lesne, Anke Sander, Hiroshi Naganuma, Eric Jacquet, Jacobo Santamaria, Agnès Barthélémy, and Manuel Bibes. Growth and Electrostatic/chemical Properties of Metal/ $\mathrm{LaAlO}_3/\mathrm{SrTiO}_3$  Heterostructures. *JoVE (Journal of Visualized Experiments)*, (132):e56951, February 2018.
- [250] E. Lesne, N. Reyren, D. Doennig, R. Mattana, H. Jaffrès, V. Cros, F. Petroff, F. Choueikani, P. Ohresser, R. Pentcheva, A. Barthélémy, and M. Bibes. Suppression of the critical thickness threshold for conductivity at the  $\mathrm{LaAlO}_3/\mathrm{SrTiO}_3$  interface. *Nature Communications*, 5:4291, July 2014.
- [251] Tobias Chris Rödel, Franck Fortuna, Shamashis Sengupta, Emmanouil Frantzeskakis, Patrick Le Fèvre, François Bertran, Bernard Mercey, Sylvia Matzen, Guillaume Agnus, Thomas Maroutian, Philippe Lecoeur, and Andrés Felipe Santander-Syro. Universal Fabrication of 2d Electron Systems in Functional Oxides. *Advanced Materials*, 28(10):1976–1980, March 2016.
- [252] M. Sing, G. Berner, K. GoSS, A. Müller, A. Ruff, A. Wetscherek, S. Thiel, J. Mannhart, S. A. Pauli, C. W. Schneider, P. R. Willmott, M. Gorgoi, F. Schäfers, and R. Claessen. Profiling the Interface Electron Gas of  $\{\mathrm{LaAlO}\}_3/\{\mathrm{SrTiO}\}_3$  Heterostructures with Hard X-Ray Photoelectron Spectroscopy. *Physical Review Letters*, 102(17):176805, April 2009.
- [253] A. A. Ramadan, R. D. Gould, and A. Ashour. On the Van der Pauw method of resistivity measurements. *Thin Solid Films*, 239(2):272–275, March 1994.
- [254] P. D. C. King, S. McKeown Walker, A. Tamai, A. de la Torre, T. Eknapakul, P. Buaphet, S.-K. Mo, W. Meevasana, M. S. Bahramy, and F. Baumberger. Quasiparticle dynamics and spinorbital texture of the  $\mathrm{SrTiO}_3$  two-dimensional electron gas. *Nature Communications*, 5:3414, February 2014.
- [255] Manali Vivek, Mark O. Goerbig, and Marc Gabay. Topological states at the (001) surface of  $\{\mathrm{SrTiO}\}_3$ . *Physical Review B*, 95(16):165117, April 2017.
- [256] L. Frangou, G. Forestier, S. Auffret, S. Gambarelli, and V. Baltz. Relaxation mechanism in NiFe thin films driven by spin angular momentum absorption throughout the antiferromagnetic phase transition in native surface oxides. *Physical Review B*, 95(5):054416, February 2017.
- [257] Ka Shen, G. Vignale, and R. Raimondi. Microscopic Theory of the Inverse Edelstein Effect. *Physical Review Letters*, 112(9):096601, March 2014.
- [258] Götz Seibold, Sergio Caprara, Marco Grilli, and Roberto Raimondi. Theory of the Spin Galvanic Effect at Oxide Interfaces. *Physical Review Letters*, 119(25):256801, December 2017.
- [259] A. Janotti, L. Bjaalie, L. Gordon, and C. G. Van de Walle. Controlling the density of the two-dimensional electron gas at the  $\mathrm{SrTiO}_3/\mathrm{LaAlO}_3$  interface. *Physical Review B*, 86(24):241108, December 2012.
- [260] Carolina Cerqueira, Jian Yin Qin, Huong Dang, Abdelhak Djeflal, Jean-Christophe Le Breton, Michel Hehn, Juan-Carlos Rojas-Sanchez, Xavier Devaux, Stéphane Suire, Sylvie Migot, Philippe Schieffer, Jean-Georges Mussot, Piotr aczkowski, Abdelmadjid Anane, Sebastien Petit-Watelot, Mathieu Stoffel, Stéphane Mangin, Zhi Liu, Bu Wen Cheng, Xiu Feng Han, Henri Jaffrès, Jean-Marie George, and Yuan Lu. Evidence of Pure Spin-Current Generated by Spin Pumping in Interface-Localized States in Hybrid Metal/Silicon/Metal Vertical Structures. *Nano Letters*, 19(1):90–99, January 2019.

- [261] B. Dlubak, M.-B. Martin, C. Deranlot, K. Bouzehouane, S. Fusil, R. Mattana, F. Petroff, A. Anane, P. Seneor, and A. Fert. Homogeneous pinhole free 1nm Al<sub>2</sub>O<sub>3</sub> tunnel barriers on graphene. *Applied Physics Letters*, 101(20):203104, November 2012.
- [262] C. H. Du, H. L. Wang, Y. Pu, T. L. Meyer, P. M. Woodward, F. Y. Yang, and P. C. Hammel. Probing the Spin Pumping Mechanism: Exchange Coupling with Exponential Decay in  $\text{Y}_3\text{Fe}_5\text{O}_{12}$  Barrier Pt Heterostructures. *Physical Review Letters*, 111(24):247202, December 2013.
- [263] Hailong Wang, Chunhui Du, P. Chris Hammel, and Fengyuan Yang. Antiferromagnonic Spin Transport from  $\text{Y}_3\text{Fe}_5\text{O}_{12}$  into NiO. *Physical Review Letters*, 113(9):097202, August 2014.
- [264] Shinji Yuasa, Taro Nagahama, Akio Fukushima, Yoshishige Suzuki, and Koji Ando. Giant room-temperature magnetoresistance in single-crystal Fe/MgO/Fe magnetic tunnel junctions. *Nature Materials*, 3(12):868–871, December 2004.
- [265] Y. Pu, P.M. Odenthal, R. Adur, J. Beardsley, A.G. Swartz, D.V. Pelekhov, M.E. Flatté, R.K. Kawakami, J. Pelz, P.C. Hammel, and E. Johnston-Halperin. Ferromagnetic Resonance Spin Pumping and Electrical Spin Injection in Silicon-Based Metal-Oxide-Semiconductor Heterostructures. *Physical Review Letters*, 115(24):246602, December 2015.
- [266] R. Ramesh and Nicola A. Spaldin. Multiferroics: progress and prospects in thin films. *Nature Materials*, 6(1):21–29, January 2007.
- [267] Manuel Bibes and Agnès Barthélémy. Multiferroics: Towards a magnetoelectric memory. *Nature Materials*, 7(6):425–426, June 2008.
- [268] J. T. Heron, J. L. Bosse, Q. He, Y. Gao, M. Trassin, L. Ye, J. D. Clarkson, C. Wang, Jian Liu, S. Salahuddin, D. C. Ralph, D. G. Schlom, J. Íñiguez, B. D. Huey, and R. Ramesh. Deterministic switching of ferromagnetism at room temperature using an electric field. *Nature*, 516(7531):370–373, December 2014.
- [269] I. Gross, W. Akhtar, V. Garcia, L. J. Martínez, S. Chouaieb, K. Garcia, C. Carrétéro, A. Barthélémy, P. Appel, P. Maletinsky, J.-V. Kim, J. Y. Chauleau, N. Jaouen, M. Viret, M. Bibes, S. Fusil, and V. Jacques. Real-space imaging of non-collinear antiferromagnetic order with a single-spin magnetometer. *Nature*, 549(7671):252–256, September 2017.
- [270] Peter B. Meisenheimer, Steve Novakov, Nguyen M. Vu, and John T. Heron. Perspective: Magnetoelectric switching in thin film multiferroic heterostructures. *Journal of Applied Physics*, 123(24):240901, June 2018.
- [271] H.E. Weaver. Dielectric properties of single crystals of SrTiO<sub>3</sub> at low temperatures. *Journal of Physics and Chemistry of Solids*, 11(3-4):274–277, October 1959.
- [272] E. Hegenbarth. Die Feldstärkeabhängigkeit der Dielektrizitätskonstanten von SrTiO<sub>3</sub>-Einkristallen im Temperaturbereich von 15 bis 80 K. *physica status solidi (b)*, 6(2):333–337, January 1964.
- [273] K. A. Müller and H. Burkard. SrTiO<sub>3</sub>: An intrinsic quantum paraelectric below 4 K. *Physical Review B*, 19(7):3593–3602, April 1979.
- [274] J. H. Haeni, P. Irvin, W. Chang, R. Uecker, P. Reiche, Y. L. Li, S. Choudhury, W. Tian, M. E. Hawley, B. Craigo, A. K. Tagantsev, X. Q. Pan, S. K. Streiffer, L. Q. Chen, S. W. Kirchoefer, J. Levy, and D. G. Schlom. Room-temperature ferroelectricity in strained SrTiO<sub>3</sub>. *Nature*, 430(7001):758–761, August 2004.
- [275] T. Riste, E.J. Samuelsen, K. Otnes, and J. Feder. Critical behaviour of SrTiO<sub>3</sub> near the 105K phase transition. *Solid State Communications*, 9(17):1455–1458, September 1971.
- [276] U. Bianchi, J. Dec, W. Kleemann, and J. G. Bednorz. Cluster and domain-state dynamics of ferroelectric  $\text{Sr}_{1-x}\text{Ca}_x\text{TiO}_3$  ( $x=0.007$ ). *Physical Review B*, 51(14):8737–8746, April 1995.
- [277] M. Itoh, R. Wang, Y. Inaguma, T. Yamaguchi, Y.-J. Shan, and T. Nakamura. Ferroelectricity Induced by Oxygen Isotope Exchange in Strontium Titanate Perovskite. *Physical Review Letters*, 82(17):3540–3543, April 1999.
- [278] J. G. Bednorz and K. A. Müller.  $\text{Sr}_{1-x}\text{Ca}_x\text{TiO}_3$

- $\text{Ca}_{1-x}\text{Ti}_x\text{O}_3$ : An  $\text{XY}$  Quantum Ferroelectric with Transition to Randomness. *Physical Review Letters*, 52(25):2289–2292, June 1984.
- [279] V.G. Bhide, K.G. Deshmukh, and M.S. Hegde. Ferroelectric properties of  $\text{PbTiO}_3$ . *Physica*, 28(9):871–876, September 1962.
- [280] V.V. Lemanov, A.V. Sotnikov, E.P. Smirnova, M. Weihnacht, and M.R. Kunze. Perovskite  $\text{CaTiO}_3$  as an incipient ferroelectric. *Solid State Communications*, 110(11):611–614, May 1999.
- [281] Mitsuru Itoh and Ruiping Wang. Quantum ferroelectricity in  $\text{SrTiO}_3$  induced by oxygen isotope exchange. *Applied Physics Letters*, 76(2):221–223, January 2000.
- [282] J. Hemberger, M. Nicklas, R. Viana, P. Lunkenheimer, A. Loidl, and R. Böhmer. Quantum paraelectric and induced ferroelectric states in. *Journal of Physics: Condensed Matter*, 8(25):4673–4690, June 1996.
- [283] J. Hemberger, P. Lunkenheimer, R. Viana, R. Böhmer, and A. Loidl. Electric-field-dependent dielectric constant and nonlinear susceptibility in  $\text{SrTiO}_3$ . *Physical Review B*, 52(18):13159–13162, November 1995.
- [284] Jakob Sidoruk, Jeannis Leist, Holger Gibhardt, Oleg Sobolev, Bachir Ouladdiaf, Richard Mole, and Götz Eckold. Kinetics of domain redistribution in  $\text{SrTiO}_3$  under pulsed electric fields. *Ferroelectrics*, 505(1):200–209, December 2016.
- [285] Yoshimasa Fujii, Hiromoto Uwe, and Tunetaro Sakudo. Stress-Induced Quantum Ferroelectricity in  $\text{SrTiO}_3$ . *Journal of the Physical Society of Japan*, 56(6):1940–1942, June 1987.
- [286] J. Sidoruk, J. Leist, H. Gibhardt, M. Meven, K. Hradil, and G. Eckold. Quantitative determination of domain distribution in  $\text{SrTiO}_3$  competing effects of applied electric field and mechanical stress. *Journal of Physics: Condensed Matter*, 22(23):235903, May 2010.
- [287] Domenico Di Sante, Paolo Barone, Riccardo Bertacco, and Silvia Picozzi. Electric Control of the Giant Rashba Effect in Bulk  $\text{GeTe}$ . *Advanced Materials*, 25(4):509–513, January 2013.
- [288] Silvia Picozzi. Ferroelectric Rashba semiconductors as a novel class of multifunctional materials. *Frontiers in Physics*, 2, 2014.
- [289] C. Rinaldi, J. C. Rojas-Sánchez, R. N. Wang, Y. Fu, S. Oyarzun, L. Vila, S. Bertoli, M. Asa, L. Baldrati, M. Cantoni, J.-M. George, R. Calarco, A. Fert, and R. Bertacco. Evidence for spin to charge conversion in  $\text{GeTe}(111)$ . *APL Materials*, 4(3):032501, February 2016.
- [290] J. Lou, D. Reed, C. Pettiford, M. Liu, P. Han, S. Dong, and N. X. Sun. Giant microwave tunability in  $\text{FeGaB}$ /lead magnesium niobate-lead titanate multiferroic composites. *Applied Physics Letters*, 92(26):262502, June 2008.
- [291] L. W. McKeethan and P. P. Cioffi. Magnetostriction in Permalloy. *Physical Review*, 28(1):146–157, July 1926.
- [292] J. F. Scott. Ferroelectrics go bananas. *Journal of Physics: Condensed Matter*, 20(2):021001, December 2007.
- [293] S. Mathews, R. Ramesh, T. Venkatesan, and J. Benedetto. Ferroelectric Field Effect Transistor Based on Epitaxial Perovskite Heterostructures. *Science*, 276(5310):238–240, April 1997.
- [294] Shin-Ik Kim, Dai-Hong Kim, Yoonjung Kim, Seon Young Moon, Min-Gyu Kang, Jong Kwon Choi, Ho Won Jang, Seong Keun Kim, Ji-Won Choi, Seok-Jin Yoon, Hye Jung Chang, Chong-Yun Kang, Suyoun Lee, Seong-Hyeon Hong, Jin-Sang Kim, and Seung-Hyub Baek. Non-Volatile Control of  $2\text{deg}$  Conductivity at Oxide Interfaces. *Advanced Materials*, 25(33):4612–4617, September 2013.
- [295] Christian Mix, Simone Finizio, Mathias Kläui, and Gerhard Jakob. Conductance control at the  $\text{LaAlO}_3/\text{SrTiO}_3$ -interface by a multiferroic  $\text{BiFeO}_3$  ad-layer. *Applied Physics Letters*, 104(26):262903, June 2014.
- [296] L. L. Tao and J. Wang. Strain-tunable ferroelectricity and its control of Rashba effect in  $\text{KTaO}_3$ . *Journal of Applied Physics*, 120(23):234101, December 2016.
- [297] N. Setter, D. Damjanovic, L. Eng, G. Fox, S. Gevorgian, S. Hong, A. Kingon, H. Kohlstedt, N. Y. Park, G. B. Stephenson, I. Stolitchnov, A. K. TagansteV, D. V. Taylor, T. Yamada, and S. Streiffer. Ferroelectric thin films: Review of materials, properties, and applications. *Journal of Applied Physics*, 100(5):051606, September 2006.
- [298] Yi Wang, Praveen Deorani, Karan Banerjee, Nikesh Koirala, Matthew Brahlek, Seongshik Oh, and Hyunsoo Yang. Topological Surface States Originated Spin-Orbit Torques in  $\text{Bi}_2\text{Se}_3$ . *Physical Review Letters*, 114(25):257202, June 2015.

- [299] Q. Shao, G. Yu, L. Pan, X. Che, Y. Fan, K. Murata, Q. He, T. Nie, X. Kou, and K. L. Wang. Large Room Temperature Charge-to-Spin Conversion Efficiency in Topological Insulator/CoFeB bilayers. In *2018 76th Device Research Conference (DRC)*, pages 1–2, June 2018.
- [300] Axel Hoffmann and Sam D. Bader. Opportunities at the Frontiers of Spintronics. *Physical Review Applied*, 4(4):047001, October 2015.
- [301] Jiahao Han, A. Richardella, Saima A. Siddiqui, Joseph Finley, N. Samarth, and Luqiao Liu. Room-Temperature Spin-Orbit Torque Switching Induced by a Topological Insulator. *Physical Review Letters*, 119(7):077702, August 2017.
- [302] Yabin Fan, Pramey Upadhyaya, Xufeng Kou, Murong Lang, So Takei, Zhenxing Wang, Jianshi Tang, Liang He, Li-Te Chang, Mohammad Montazeri, Guoqiang Yu, Wanjun Jiang, Tianxiao Nie, Robert N. Schwartz, Yaroslav Tserkovnyak, and Kang L. Wang. Magnetization switching through giant spinorbit torque in a magnetically doped topological insulator heterostructure. *Nature Materials*, 13(7):699–704, July 2014.
- [303] Mahendra Dc, Roberto Grassi, Jun-Yang Chen, Mahdi Jamali, Danielle Reifsnyder Hickey, Delin Zhang, Zhengyang Zhao, Hongshi Li, P. Quarterman, Yang Lv, Mo Li, Aurelien Manchon, K. Andre Mkhoyan, Tony Low, and Jian-Ping Wang. Room-temperature high spinorbit torque due to quantum confinement in sputtered Bi x Se (1x) films. *Nature Materials*, 17(9):800–807, September 2018.
- [304] Praveen Deorani, Jaesung Son, Karan Banerjee, Nikesh Koirala, Matthew Brahlek, Seongshik Oh, and Hyunsoo Yang. Observation of inverse spin Hall effect in bismuth selenide. *Physical Review B*, 90(9):094403, September 2014.
- [305] Hailong Wang, James Kally, Joon Sue Lee, Tao Liu, Houchen Chang, Danielle Reifsnyder Hickey, K. Andre Mkhoyan, Mingzhong Wu, Anthony Richardella, and Nitin Samarth. Surface-State-Dominated Spin-Charge Current Conversion in Topological-Insulator–Ferromagnetic-Insulator Heterostructures. *Physical Review Letters*, 117(7):076601, August 2016.
- [306] Mahdi Jamali, Joon Sue Lee, Jong Seok Jeong, Farzad Mahfouzi, Yang Lv, Zhengyang Zhao, Branislav K. Nikoli, K. Andre Mkhoyan, Nitin Samarth, and Jian-Ping Wang. Giant Spin Pumping and Inverse Spin Hall Effect in the Presence of Surface and Bulk SpinOrbit Coupling of Topological Insulator Bi<sub>2</sub>Se<sub>3</sub>. *Nano Letters*, 15(10):7126–7132, October 2015.
- [307] D.A. Kozlov, Z.D. Kvon, E.B. Olshanetsky, N.N. Mikhailov, S.A. Dvoretzky, and D. Weiss. Transport Properties of a 3d Topological Insulator based on a Strained High-Mobility HgTe Film. *Physical Review Letters*, 112(19):196801, May 2014.
- [308] J. Navrátil, J. Horák, T. Plecháek, S. Kamba, P. Loták, J. S. Dyck, W. Chen, and C. Uher. Conduction band splitting and transport properties of Bi<sub>2</sub>Se<sub>3</sub>. *Journal of Solid State Chemistry*, 177(4):1704–1712, April 2004.
- [309] F.-T. Huang, M.-W. Chu, H. H. Kung, W. L. Lee, R. Sankar, S.-C. Liou, K. K. Wu, Y. K. Kuo, and F. C. Chou. Nonstoichiometric doping and Bi antisite defect in single crystal Bi<sub>2-x</sub>Se<sub>3</sub>. *Physical Review B*, 86(8):081104, August 2012.
- [310] Guang Wang, Xie-Gang Zhu, Yi-Yang Sun, Yao-Yi Li, Tong Zhang, Jing Wen, Xi Chen, Ke He, Li-Li Wang, Xu-Cun Ma, Jin-Feng Jia, Shengbai B. Zhang, and Qi-Kun Xue. Topological Insulator Thin Films of Bi<sub>2</sub>Te<sub>3</sub> with Controlled Electronic Structure. *Advanced Materials*, 23(26):2929–2932, 2011.
- [311] Frédéric Bonell, Marc G. Cuxart, Kenan Song, Roberto Robles, Pablo Ordejón, Stephan Roche, Aitor Mugarza, and Sergio O. Valenzuela. Growth of Twin-Free and Low-Doped Topological Insulators on BaF<sub>2</sub>(111). *Crystal Growth & Design*, 17(9):4655–4660, September 2017.
- [312] Matthew Brahlek, Nikesh Koirala, Namrata Bansal, and Seongshik Oh. Transport properties of topological insulators: Band bending, bulk metal-to-insulator transition, and weak anti-localization. *Solid State Communications*, 215-216:54–62, July 2015.
- [313] C. Thomas, O. Crauste, B. Haas, P.-H. Jouneau, C. Bäuerle, L. P. Lévy, E. Orignac, D. Carpentier, P. Ballet, and T. Meunier. Revealing topological Dirac fermions at the surface of strained HgTe thin films via quantum Hall transport spectroscopy. *Physical Review B*, 96(24):245420, December 2017.
- [314] B. Andrei Bernevig, Taylor L. Hughes, and Shou-Cheng Zhang. Quantum Spin Hall Effect and Topological Phase Transition in HgTe Quantum Wells. *Science*, 314(5806):1757–1761, December 2006.

- [315] Markus König, Steffen Wiedmann, Christoph Brüne, Andreas Roth, Hartmut Buhmann, Laurens W. Molenkamp, Xiao-Liang Qi, and Shou-Cheng Zhang. Quantum Spin Hall Insulator State in HgTe Quantum Wells. *Science*, 318(5851):766–770, November 2007.
- [316] Candice Thomas. *Strained HgTe/CdTe topological insulators, toward spintronic applications*. thesis, Grenoble Alpes, December 2016.
- [317] Zhiyong Zhu, Yingchun Cheng, and Udo Schwingenschlögl. Band inversion mechanism in topological insulators: A guideline for materials design. *Physical Review B*, 85(23):235401, June 2012.
- [318] Olivier Crauste, Yoshituki Ohtsubo, Philippe Ballet, Pierre André Louis Delplace, David Carpentier, Clément Bouvier, Tristan Meunier, Amina Taleb-Ibrahimi, and Laurent Lévy. Topological surface states of strained Mercury-Telluride probed by ARPES. July 2013.
- [319] P. Ballet, C. Thomas, X. Baudry, C. Bouvier, O. Crauste, T. Meunier, G. Badano, M. Veillerot, J. P. Barnes, P. H. Jouneau, and L. P. Lévy. MBE Growth of Strained HgTe/CdTe Topological Insulator Structures. *Journal of Electronic Materials*, 43(8):2955–2962, August 2014.
- [320] Quentin Barbedienne, Julien Varignon, Nicolas Reyren, Alain Marty, Céline Vergnaud, Matthieu Jamet, Carmen Gomez-Carbonell, Aristide Lemaître, Patrick Le Fèvre, François Bertran, Amina Taleb-Ibrahimi, Henri Jaffrès, Jean-Marie George, and Albert Fert. Angular-resolved photoemission electron spectroscopy and transport studies of the elemental topological insulator  $\alpha$ -Sn. *Physical Review B*, 98(19):195445, November 2018.
- [321] Benedikt Haas, Candice Thomas, Pierre-Henri Jouneau, Nicolas Bernier, Tristan Meunier, Philippe Ballet, and Jean-Luc Rouvière. High precision strain mapping of topological insulator HgTe/CdTe. *Applied Physics Letters*, 110(26):263102, June 2017.
- [322] C. Thomas, X. Baudry, J. P. Barnes, M. Veillerot, P. H. Jouneau, S. Pouget, O. Crauste, T. Meunier, L. P. Lévy, and P. Ballet. MBE growth and interfaces characterizations of strained HgTe/CdTe topological insulators. *Journal of Crystal Growth*, 425:195–198, September 2015.
- [323] M. Björck and G. Andersson. GenX: an extensible X-ray reflectivity refinement program utilizing differential evolution. *Journal of Applied Crystallography*, 40(6):1174–1178, December 2007.
- [324] Catalin D. Spataru and François Léonard. Fermi-level pinning, charge transfer, and relaxation of spin-momentum locking at metal contacts to topological insulators. *Physical Review B*, 90(8):085115, August 2014.
- [325] Lee A. Walsh, Christopher M. Smyth, Adam T. Barton, Qingxiao Wang, Zifan Che, Ruoyu Yue, Jiyoung Kim, Moon J. Kim, Robert M. Wallace, and Christopher L. Hinkle. Interface Chemistry of Contact Metals and Ferromagnets on the Topological Insulator Bi<sub>2</sub>Se<sub>3</sub>. *The Journal of Physical Chemistry C*, 121(42):23551–23563, October 2017.
- [326] G. D. Davis. Overlayer interactions with (HgCd)Te. *Journal of Vacuum Science & Technology A*, 6(3):1939–1945, May 1988.
- [327] Steffen Wiedmann, Andreas Jost, Cornelius Thienel, Christoph Brüne, Philipp Leubner, Hartmut Buhmann, Laurens W. Molenkamp, J. C. Maan, and Uli Zeitler. Temperature-driven transition from a semiconductor to a topological insulator. *Physical Review B*, 91(20):205311, May 2015.
- [328] Frank Kirtschig, Jeroen van den Brink, and Carmine Ortix. Surface-state spin textures in strained bulk HgTe: Strain-induced topological phase transitions. *Physical Review B*, 94(23):235437, December 2016.
- [329] K. T. Yamamoto, Y. Shiomi, Kouji Segawa, Yoichi Ando, and E. Saitoh. Universal scaling for the spin-electricity conversion on surface states of topological insulators. *Physical Review B*, 94(2):024404, July 2016.
- [330] Madhab Neupane, Anthony Richardella, Jaime Sánchez-Barriga, SuYang Xu, Nasser Alidoust, Ilya Belopolski, Chang Liu, Guang Bian, Duming Zhang, Dmitry Marchenko, Andrei Varykhalov, Oliver Rader, Mats Leandersson, Thiagarajan Balasubramanian, Tay-Rong Chang, Horng-Tay Jeng, Susmita Basak, Hsin Lin, Arun Bansil, Nitin Samarth, and M. Zahid Hasan. Observation of quantum-tunnelling-modulated spin texture in ultrathin topological insulator Bi<sub>2</sub>Se<sub>3</sub> films. *Nature Communications*, 5:3841, May 2014.
- [331] Cong Son Ho, Yi Wang, Zhou Bin Siu, Seng Ghee Tan, Mansoor B. A. Jalil, and Hyunsoo Yang. Effect of surface state hybridization on current-induced spin-orbit torque in thin topological insulator films. *Scientific Reports*, 7(1):1–7, April 2017.



- [332] K.-M. Dantscher, D. A. Kozlov, P. Olbrich, C. Zoth, P. Faltermeier, M. Lindner, G. V. Budkin, S. A. Tarasenko, V. V. Bel'kov, Z. D. Kvon, N. N. Mikhailov, S. A. Dvoretzky, D. Weiss, B. Jenichen, and S. D. Ganichev. Cyclotron-resonance-assisted photocurrents in surface states of a three-dimensional topological insulator based on a strained high-mobility HgTe film. *Physical Review B*, 92(16):165314, October 2015.
- [333] Yi Wang, Dapeng Zhu, Yang Wu, Yumeng Yang, Jiawei Yu, Rajagopalan Ramaswamy, Rahul Mishra, Shuyuan Shi, Mehrdad Elyasi, Kie-Leong Teo, Yihong Wu, and Hyunsoo Yang. Room temperature magnetization switching in topological insulator-ferromagnet heterostructures by spin-orbit torques. *Nature Communications*, 8(1):1–6, November 2017.
- [334] Pratyush Sahu, Jun-Yang Chen, Jason C. Myers, and Jian-Ping Wang. Weak antilocalization and low-temperature characterization of sputtered polycrystalline bismuth selenide. *Applied Physics Letters*, 112(12):122402, March 2018.
- [335] Rajagopalan Ramaswamy, Tanmay Dutta, Shiheng Liang, Guang Yang, M. S. M. Saifullah, and Hyunsoo Yang. Spin orbit torque driven magnetization switching with sputtered Bi<sub>2</sub>Se<sub>3</sub> spin current source. *Journal of Physics D: Applied Physics*, 52(22):224001, March 2019.
- [336] Gerald Schubert, Holger Fehske, Lars Fritz, and Matthias Vojta. Fate of topological-insulator surface states under strong disorder. *Physical Review B*, 85(20):201105, May 2012.
- [337] Inna Korzhovska. Effects of Structural and Electronic Disorder in Topological Insulator Sb<sub>2</sub>Te<sub>3</sub> Thin Films. *All Dissertations, Theses, and Capstone Projects*, February 2018.
- [338] C. H. Li, O. M. J. van t Erve, Y. Y. Li, L. Li, and B. T. Jonker. Electrical Detection of the Helical Spin Texture in a p-type Topological Insulator Sb<sub>2</sub>Te<sub>3</sub>. *Scientific Reports*, 6, July 2016.
- [339] Hailong Wang, James Kally, Cuneyt Sahin, Tao Liu, Wilson Yanez, Eric J. Kamp, Anthony Richardella, Mingzhong Wu, Michael E. Flatte, and Nitin Samarth. Fermi Level Dependent Spin Pumping from a Magnetic Insulator into a Topological Insulator. June 2019.
- [340] R. E. Simpson, P. Fons, A. V. Kolobov, T. Fukaya, M. Krbal, T. Yagi, and J. Tominaga. Interfacial phase-change memory. *Nature Nanotechnology*, 6(8):501–505, August 2011.
- [341] Philippe Kowalczyk, Françoise Hippert, Nicolas Bernier, Cristian Mocuta, Chiara Sabbione, Walter BatistaPessoa, and Pierre Noé. Impact of Stoichiometry on the Structure of van der Waals Layered GeTe/Sb<sub>2</sub>Te<sub>3</sub> Superlattices Used in Interfacial Phase-Change Memory (iPCM) Devices. *Small*, 14(24):1704514, 2018.
- [342] Namrata Bansal, Nimesh Koirala, Matthew Brahlek, Myung-Geun Han, Yimei Zhu, Yue Cao, Justin Waugh, Daniel S. Dessau, and Seongshik Oh. Robust topological surface states of Bi<sub>2</sub>Se<sub>3</sub> thin films on amorphous SiO<sub>2</sub>/Si substrate and a large ambipolar gating effect. *Applied Physics Letters*, 104(24):241606, June 2014.
- [343] Indu Rajput, Sumesh Rana, Rudra Prasad Jena, and Archana Lakhani. Crystal growth and x-ray diffraction characterization of Sb<sub>2</sub>Te<sub>3</sub> single crystal. *AIP Conference Proceedings*, 2100(1):020070, April 2019.
- [344] T. L. Anderson and H. B. Krause. Refinement of the Sb<sub>2</sub>Te<sub>3</sub> and Sb<sub>2</sub>Te<sub>2</sub>Se structures and their relationship to nonstoichiometric Sb<sub>2</sub>Te<sub>3</sub>Se<sub>y</sub> compounds. *Acta Crystallographica Section B: Structural Crystallography and Crystal Chemistry*, 30(5):1307–1310, May 1974.
- [345] Zhaoquan Zeng, Timothy A. Morgan, Dongsheng Fan, Chen Li, Yusuke Hirono, Xian Hu, Yanfei Zhao, Joon Sue Lee, Jian Wang, Zhiming M. Wang, Shuiqing Yu, Michael E. Hawkrige, Mourad Benamara, and Gregory J. Salamo. Molecular beam epitaxial growth of Bi<sub>2</sub>Te<sub>3</sub> and Sb<sub>2</sub>Te<sub>3</sub> topological insulators on GaAs (111) substrates: a potential route to fabricate topological insulator p-n junction. *AIP Advances*, 3(7):072112, July 2013.
- [346] Beining Zheng, Yu Sun, Jie Wu, Mei Han, Xiaofeng Wu, Keke Huang, and Shouhua Feng. Group IV semiconductor Ge integration with topological insulator Sb<sub>2</sub>Te<sub>3</sub> for spintronic application. *Journal of Physics D: Applied Physics*, 50(10):105303, February 2017.
- [347] Paulina Komar and Gerhard Jakob. CADEM: calculate X-ray diffraction of epitaxial multilayers. *Journal of Applied Crystallography*, 50(Pt 1):288–292, February 2017.
- [348] T. Guillet, A. Marty, C. Beigné, C. Vergnaud, M.-T. Dau, P. Noël, J. Frigerio, G. Isella, and M. Jamet. Magnetotransport in Bi<sub>2</sub>Se<sub>3</sub> thin films epitaxially grown on Ge(111). *AIP Advances*, 8(11):115125, November 2018.

- [349] Jos E. Boschker, E. Tisbi, E. Placidi, Jamo Momand, Andrea Redaelli, Bart J. Kooi, Fabrizio Arciprete, and Raffaella Calarco. Textured Sb<sub>2</sub>Te<sub>3</sub> films and GeTe/Sb<sub>2</sub>Te<sub>3</sub> superlattices grown on amorphous substrates by molecular beam epitaxy. *AIP Advances*, 7(1):015106, January 2017.
- [350] Jos E. Boschker and Raffaella Calarco. Growth of crystalline phase change materials by physical deposition methods. *Advances in Physics: X*, 2(3):675–694, May 2017.
- [351] I. Hilmi, E. Thelander, P. Schumacher, J. W. Gerlach, and B. Rauschenbach. Epitaxial Ge<sub>2</sub>Sb<sub>2</sub>Te<sub>5</sub> films on Si(111) prepared by pulsed laser deposition. *Thin Solid Films*, 619:81–85, November 2016.
- [352] Hanbum Park, Jimin Chae, Kwangsik Jeong, Hyejin Choi, Jaehun Jeong, Dasol Kim, and Mann-Ho Cho. Disorder-induced decoupled surface transport channels in thin films of doped topological insulators. *Physical Review B*, 98(4):045411, July 2018.
- [353] Yong Seung Kim, Matthew Brahlek, Namrata Bansal, Eliav Edrey, Gary A. Kapilevich, Keiko Iida, Makoto Tanimura, Yoichi Horibe, Sang-Wook Cheong, and Seongshik Oh. Thickness-dependent bulk properties and weak antilocalization effect in topological insulator Bi<sub>2</sub>Se<sub>3</sub>. *Physical Review B*, 84(7):073109, August 2011.
- [354] Jian Liao, Yunbo Ou, Xiao Feng, Shuo Yang, Chaojing Lin, Wenmin Yang, Kehui Wu, Ke He, Xucun Ma, Qi-Kun Xue, and Yongqing Li. Observation of Anderson Localization in Ultrathin Films of Three-Dimensional Topological Insulators. *Physical Review Letters*, 114(21):216601, May 2015.
- [355] G. Bergmann. Weak anti-localization An experimental proof for the destructive interference of rotated spin 12. *Solid State Communications*, 42(11):815–817, June 1982.
- [356] Gerd Bergmann. Inelastic life-time of the conduction electrons in some noble metal films. *Zeitschrift für Physik B Condensed Matter*, 48(1):5–16, August 1982.
- [357] A. E. Hansen, M. T. Björk, C. Fasth, C. Thelander, and L. Samuelson. Spin relaxation in InAs nanowires studied by tunable weak antilocalization. *Physical Review B*, 71(20):205328, May 2005.
- [358] Shinobu Hikami, Anatoly I. Larkin, and Yosuke Nagaoka. Spin-Orbit Interaction and Magnetoresistance in the Two Dimensional Random System. *Progress of Theoretical Physics*, 63(2):707–710, February 1980.
- [359] Murong Lang, Liang He, Xufeng Kou, Pramey Upadhyaya, Yabin Fan, Hao Chu, Ying Jiang, Jens H. Bardarson, Wanjun Jiang, Eun Sang Choi, Yong Wang, Nai-Chang Yeh, Joel Moore, and Kang L. Wang. Competing Weak Localization and Weak Antilocalization in Ultrathin Topological Insulators. *Nano Letters*, 13(1):48–53, January 2013.
- [360] D. S. Golubev, A. D. Zaikin, and Gerd Schön. On Low-Temperature Dephasing by Electron-Electron Interaction. *Journal of Low Temperature Physics*, 126(3):1355–1376, February 2002.
- [361] Yeping Jiang, Yilin Wang, Mu Chen, Zhi Li, Canli Song, Ke He, Lili Wang, Xi Chen, Xucun Ma, and Qi-Kun Xue. Landau Quantization and the Thickness Limit of Topological Insulator Thin Films of Sb<sub>2</sub>Te<sub>3</sub>. *Physical Review Letters*, 108(1):016401, January 2012.
- [362] Richarj Mondal, Yuta Saito, Yuki Aihara, Paul Fons, Alexander V. Kolobov, Junji Tominaga, Shuichi Murakami, and Muneaki Hase. A cascading nonlinear magneto-optical effect in topological insulators. *Scientific Reports*, 8(1):1–8, March 2018.
- [363] Miren Isasa, Estitxu Villamor, Luis E. Hueso, Martin Gradhand, and Fèlix Casanova. Temperature dependence of spin diffusion length and spin Hall angle in Au and Pt. *Physical Review B*, 91(2):024402, January 2015.
- [364] Christoph Seibel, Henriette Maaß, Hendrik Bentmann, Jürgen Braun, Kazuyuki Sakamoto, Masashi Arita, Kenya Shimada, Jan Minár, Hubert Ebert, and Friedrich Reinert. The Rashba-split surface state of Sb<sub>2</sub>Te<sub>3</sub>(0001) and its interaction with bulk states. *Journal of Electron Spectroscopy and Related Phenomena*, 201:110–114, May 2015.
- [365] Pan He, Steven S.-L. Zhang, Dapeng Zhu, Yang Liu, Yi Wang, Jiawei Yu, Giovanni Vignale, and Hyunsoo Yang. Bilinear magnetoelectric resistance as a probe of three-dimensional spin texture in topological surface states. *Nature Physics*, 14(5):495–499, May 2018.
- [366] T. Guillet, C. Zucchetti, Q. Barbedienne, A. Marty, G. Isella, L. Cagnon, C. Vergnaud, N. Reyren, J.-M. George, A. Fert, and M. Jamet. Observation of Large Unidirectional Rashba Magnetoresistance in Ge(111). June 2019.
- [367] J.-C. Rojas-Sánchez and A. Fert. Compared Efficiencies of Conversions between Charge and Spin Current by Spin-Orbit Interactions in Two- and Three-Dimensional Systems. *Physical Review Applied*, 11(5):054049, 2019.

- [368] Nguyen Huynh Duy Khang, Yugo Ueda, and Pham Nam Hai. A conductive topological insulator with large spin Hall effect for ultralow power spinorbit torque switching. *Nature Materials*, 17(9):808, 2018.
- [369] James S Hyde, W Froncisz, and T Oles. Multipurpose loop-gap resonator. *Journal of Magnetic Resonance (1969)*, 82(2):223–230, April 1989.
- [370] George A. Rinard and Gareth R. Eaton. Loop-Gap Resonators. In Sandra R. Eaton, Gareth R. Eaton, and Lawrence J. Berliner, editors, *Biomedical EPR, Part B: Methodology, Instrumentation, and Dynamics*, Biological Magnetic Resonance, pages 19–52. Springer US, Boston, MA, 2005.
- [371] Bruker Biospin. Epr resonators: User training service course. Chapter 5.
- [372] Bruker Biospin. Epr accessories: The solutions for multiple-choice epr experiments. CW / FT-EPR.
- [373] Konrad Klein, Benedikt Hauer, Benedikt Stoib, Markus Trautwein, Sonja Matich, Hans Huebl, Oleksandr Astakhov, Friedhelm Finger, Robert Bittl, Martin Stutzmann, and Martin S. Brandt. The electrically detected magnetic resonance microscope: Combining conductive atomic force microscopy with electrically detected magnetic resonance. *Review of Scientific Instruments*, 84(10):103911, October 2013.
- [374] V. Garcia, M. Bibes, A. Barthélémy, M. Bowen, E. Jacquet, J.-P. Contour, and A. Fert. Temperature dependence of the interfacial spin polarization of  $\text{La}_{2/3}\text{Sr}_{1/3}\text{MnO}_3$ . *Physical Review B*, 69(5):052403, February 2004.
- [375] G. Y. Luo, C. R. Chang, and J. G. Lin. Influence of damping constant on inverse spin hall voltage of  $\text{La}_{0.7}\text{Sr}_{0.3}\text{MnO}_3/\text{platinum}$  bilayers. *Journal of Applied Physics*, 115(17):17C508, January 2014.
- [376] G. Y. Luo, M. Y. Song, H. Y. Hung, Y. C. Chiu, J. Kwo, S. F. Lee, C. R. Chang, and J. G. Lin. Spin Pumping Induced Inverse Spin-Hall Effects in  $\text{La}_{0.7}\text{Sr}_{0.3}\text{MnO}_3/\text{Platinum}$  Bilayer Film. *IEEE Transactions on Magnetics*, 48(11):3958–3960, November 2012.
- [377] G. Y. Luo, M. Belméguenai, Y. Roussigné, C. R. Chang, J. G. Lin, and S. M. Chérif. Enhanced magnetic damping in  $\text{La}_{0.7}\text{Sr}_{0.3}\text{MnO}_3$  capped by normal metal layer. *AIP Advances*, 5(9):097148, September 2015.
- [378] S. M. Haidar, Y. Shiomi, J. Lustikova, and E. Saitoh. Enhanced inverse spin Hall contribution at high microwave power levels in  $\text{La}_{0.67}\text{Sr}_{0.33}\text{MnO}_3/\text{SrRuO}_3$  epitaxial bilayers. *Applied Physics Letters*, 107(15):152408, October 2015.
- [379] G. Y. Luo, J. G. Lin, Wen-Chung Chiang, and Ching-Ray Chang. Spin pump and probe in lanthanum strontium manganite/platinum bilayers. *Scientific Reports*, 7(1):1–9, July 2017.
- [380] Yi Li, M. Farle, and K. Baberschke. Critical spin fluctuations and Curie temperatures of ultrathin  $\text{Ni}(111)/\text{W}(110)$ : A magnetic-resonance study in ultrahigh vacuum. *Physical Review B*, 41(13):9596–9599, May 1990.
- [381] V. Castel, N. Vlietstra, B. J. van Wees, and J. Ben Youssef. Frequency and power dependence of spin-current emission by spin pumping in a thin-film YIG/Pt system. *Physical Review B*, 86(13):134419, October 2012.
- [382] M. B. Jungfleisch, A. V. Chumak, A. Kehlberger, V. Lauer, D. H. Kim, M. C. Onbasli, C. A. Ross, M. Kläui, and B. Hillebrands. Thickness and power dependence of the spin-pumping effect in  $\text{Y}_3\text{Fe}_5\text{O}_{12}/\text{Pt}$  heterostructures measured by the inverse spin Hall effect. *Physical Review B*, 91(13):134407, April 2015.
- [383] J. Lustikova, Y. Shiomi, Y. Handa, and E. Saitoh. Spectral shape deformation in inverse spin Hall voltage in  $\text{Y}_3\text{Fe}_5\text{O}_{12}/\text{Pt}$  bilayers at high microwave power levels. *Journal of Applied Physics*, 117(7):073901, February 2015.
- [384] Y. S. Chen, J. G. Lin, S. Y. Huang, and C. L. Chien. Incoherent spin pumping from YIG single crystals. *Physical Review B*, 99(22):220402, June 2019.
- [385] Ming Liu, Ogheneyunume Obi, Jing Lou, Yajie Chen, Zhuhua Cai, Stephen Stoute, Mary Espanol, Magnum Lew, Xiaodan Situ, Kate S. Ziemer, Vince G. Harris, and Nian X. Sun. Giant Electric Field Tuning of Magnetic Properties in Multiferroic Ferrite/Ferroelectric Heterostructures. *Advanced Functional Materials*, 19(11):1826–1831, 2009.
- [386] Shandong Li, Ming Liu, J. Lou, Shawn Beguhn, Jianpeng Wu, Jie Qiu, Jianhua Lin, Zhiyi Cai, Yi Hu, Feng Xu, Jenq-Gong Duh, and Nian X. Sun. E-field tuning microwave frequency performance of  $\text{Co}_2\text{FeSi}/\text{lead zinc niobate}$  lead titanate magnetoelectric coupling composites. *Journal of Applied Physics*, 111(7):07C705, February 2012.
- [387] M. Zhu, T. Nan, M. Liu, W. Ren, Z. Zhou, and N. X. Sun. Voltage Tuning of Ferromagnetic Resonance and Linewidth in Spinel Ferrite/Ferroelectric Multiferroic Heterostructures. *IEEE Magnetics Letters*, 6:1–4, 2015.

- [388] Rongxin Xiong, Bin Fang, Gang Li, Yongguang Xiao, Minghua Tang, and Zheng Li. Electric-field tuning of ferromagnetic resonance in CoFeB/MgO magnetic tunnel junction on a piezoelectric PMN-PT substrate. *Applied Physics Letters*, 111(6):062401, August 2017.
- [389] Dexin Wang, Cathy Nordman, Zhenghong Qian, James M. Daughton, and John Myers. Magnetostriction effect of amorphous CoFeB thin films and application in spin-dependent tunnel junctions. *Journal of Applied Physics*, 97(10):10C906, May 2005.
- [390] Blai Casals, Andrea Schiaffino, Arianna Casiraghi, Sampo J. Hämäläinen, Diego López González, Sebastiaan van Dijken, Massimiliano Stengel, and Gervasi Herranz. Low-Temperature Dielectric Anisotropy Driven by an Antiferroelectric Mode in  $\text{SrTiO}_3$ . *Physical Review Letters*, 120(21):217601, May 2018.
- [391] M. Honig, J. A. Sulpizio, J. Drori, A. Joshua, E. Zeldov, and S. Ilani. Local electrostatic imaging of striped domain order in  $\text{LaAlO}_3/\text{SrTiO}_3$ . *Nature Materials*, 12(12):1112–1118, December 2013.
- [392] Daniel E. Grupp and Allen M. Goldman. Giant Piezoelectric Effect in Strontium Titanate at Cryogenic Temperatures. *Science*, 276(5311):392–394, April 1997.

## FMR cavity: Bruker MS5 loop gap

The cavity used for all the spin pumping FMR measurements presented in this manuscript is a ER 4118X-MS-5 loop gap. Strictly speaking, the MS5 shouldn't be referred as a cavity but as a loop-gap resonator<sup>369;370</sup>. A loop-gap resonator serves a similar purpose to the cavity resonator, but they work differently.

A cavity resonator is a closed conductor containing electromagnetic waves reflecting back and forth thus storing energy under the form of an electromagnetic field. Cavity of different shapes and sizes lead to different resonance frequencies and resonant modes. Cavity that are usually available in an EPR setup are circular cavities operating in the TE<sub>011</sub> mode (like the ER 4114HT) and rectangular cavity in the TE<sub>102</sub> mode (like the Bruker ER 4102ST). The direction of the electric and magnetic rf field for these two modes are depicted in figure A.1.

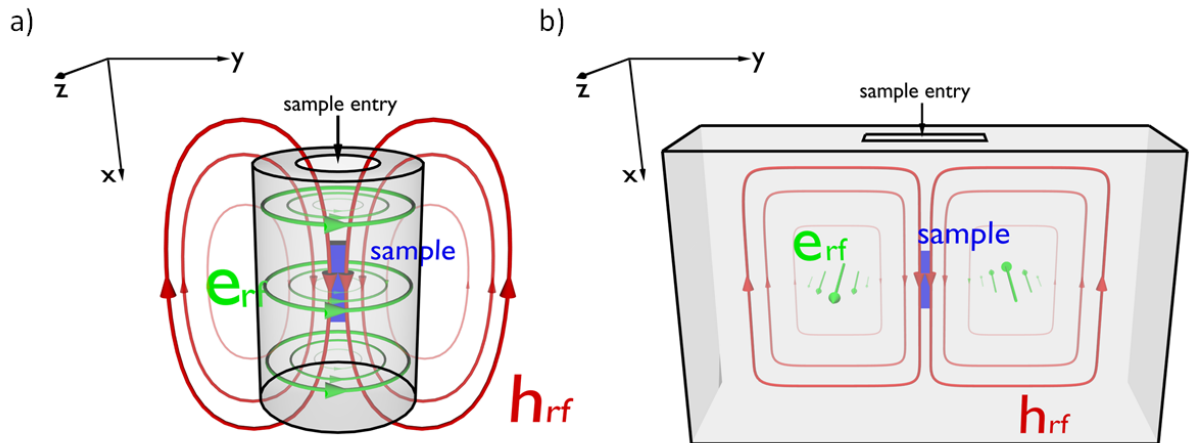


FIG. A.1: Two different EPR cavities: a) a cylindrical cavity operating in the TE<sub>011</sub> mode and b) a rectangular cavity operating in the TE<sub>102</sub> mode. Direction of the electric and magnetic field is depicted in both cases.

For FMR measurements there is no particular difference between these two modes, the direction of the rf magnetic field is the same and in both cases the sample can be placed in the nodal plane where the rf magnetic field is maximum and the electric field is minimum<sup>371</sup>. Nonetheless using a cavity operating in the TE<sub>102</sub> mode is well adapted to the electrical detection of ISHE or IEE compared to a cavity in the TE<sub>011</sub> mode. Let us consider a sample placed in the cavity center at the minimum of electric field. If the sample rotates around the X axis, in the TE<sub>011</sub> cylindrical cavity the electric field is always parallel to the surface and the sample is exposed to electric fields in all directions, while in the TE<sub>102</sub> rectangular cavity it is changing from parallel to perpendicular to the plane.. Therefore the contribution of the signal originating from the radiofrequency electric field and known (spin rectifi-

cation effects) is reduced<sup>187</sup> and have an angular dependence that is different from ISHE or IEE, as shown in the main text (see chapter 2).

We could have used a rectangular cavity for our spin pumping experiment at X-band, nonetheless we used a MS5 3loop–2gap resonator operating in a pseudo TE102 mode<sup>369</sup> instead, because of its several advantages compared with a rectangular cavity. The design of such a resonator is shown in figure A.2, it is composed of three loops and two gaps, is shielded to prevent radiation loss and is coupled using an antenna which position can be modified to obtain critical coupling. The microwave feed line (microwave power input) is positioned just above the antenna.

In a 3loop–2gap resonator the electric field is contained within the gap whereas the magnetic field is within the loop which makes the electric field and magnetic field better separated<sup>370</sup>. This limits the spin rectification effect even for a poor positioning of the sample. The size of the loop gap is also smaller, the section has to be equal to the wavelength  $\lambda$  of the rf field, which is around 3 cm at 10GHz. This makes rectangular cavities particularly big for frequencies at X-band and below compared to loop gap resonators. Moreover the uniformity of the magnetic field along the z direction is better, which makes the excitation of the magnetic field uniform over the whole sample length. And last, but not least the rf magnetic field per watt is also higher, making the measured electrical signal higher using an MS5 cavity. This thus makes the loop-gap resonator the “ultimate“ cavity for spin pumping experiments.

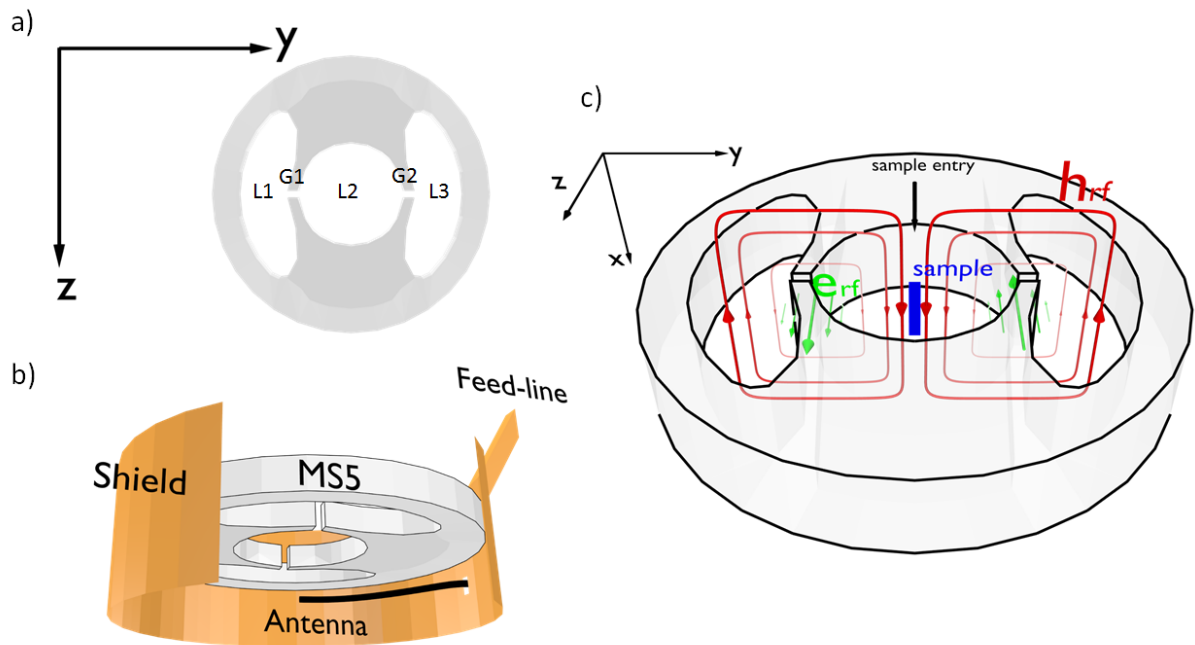


FIG. A.2: MS5 loop gap cavity: a) Model of the 3-loops 2-gaps cavity, the three loops L1, L2, L3 and the 2 gaps G1 and G2 are marked b) Side view of the resonator in its shield with antenna and connected to the microwave feed-line c) A MS5 loop gap cavity operating in a pseudo TE102 mode. The direction of the electric field, magnetic field and position of the sample are depicted.

There are still some disadvantages to use the MS5 resonator. Due to the smaller Q factor, the sensitivity of the EPR spectrometer is reduced. However this is not a strong disadvantage as the larger rf field allows a simplified electrical detection of the resonance. Moreover due to its small thermal mass, heating can occur at large power, and for low temperature measurements. Not only the sample but also the resonator has to be cooled down, this makes the cooldown longer but increase the thermal stability. The advantages and disadvantages of loop-gap resonators compared to a standard cavity are described in a chapter of “biological magnetic resonance“ by Rinard and Eaton<sup>370</sup>.

The properties of the ER 4118X-MS-5 are described in the brucker datasheet<sup>372</sup>. The unloaded cavity resonance frequency is of 9.75 GHz (X-band), the sample access size is of 5 mm, and the width of the resonator is of 40 mm. The conversion factor is 0.2 mT (2 G) per square root Watt at a Q factor of 500. This gives the link between the rf magnetic field  $h_{rf}$  in mT, the Q factor and the microwave power in Watt:

$$h_{rf} = 0.2 \sqrt{\frac{PQ}{500}} \quad (\text{A.1})$$

Such a conversion factor allows to obtain rf magnetic field  $h_{rf}$  of around 0.1mT for a power of 200mW which allows to detect spin signal easily even for small ISHE contributions. It is to be noted that the exact configuration of the rf magnetic field and electric field have been calculated in a similar resonator<sup>373</sup> (cf. figure A.3.)

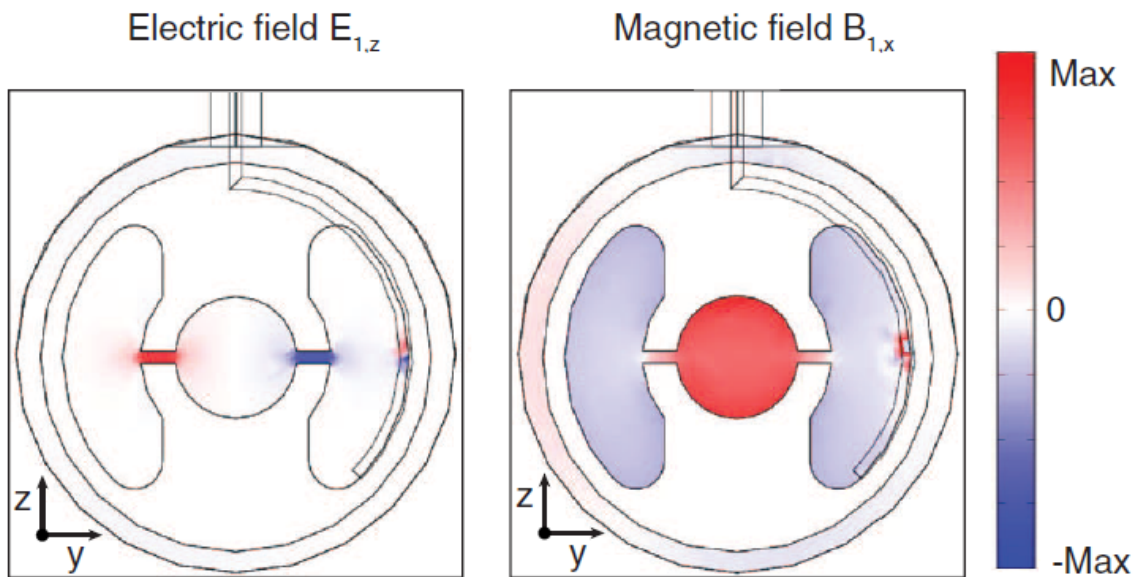


FIG. A.3: FEM simulation of the high frequency mode of the 3loop-2gap resonator  $z$ -component of the electric microwave field  $E_{1,z}$  and  $x$ -component of the microwave magnetic field  $B_{1,x}$ . This simulation is taken from Klein et al.<sup>373</sup>.

Note that there exists cavities with the possibility to change the direction of the rf fields as the Bruker ER 4116DM from TE102 mode to TE012 mode in X-band that allows to study different rf field geometries. This type of cavity should also provide interesting ways to probe the rf field direction dependence of the spin rectification signals.



## Offset signal associated with the temperature increase

In chapter 3 we studied possible thermal effects occurring at resonance, due to the additional dissipation associated with the magnetization precession. There could also be a thermal contribution to the signal appearing at any field, as this heating process occurs also out of resonance. In the following we will call it the out-of-resonance thermal contribution. Due to power entering the cavity two effects might occur: it is possible that the temperature of the whole cavity, including that of the sample increases, and it is also possible that the non-zero eddy currents related to misplacement leads to Joule heating. The temperature of the sample might then be higher than the expected temperature, knowing that this temperature increase can be larger than the temperature increase due to FMR, as it is associated with a considerably larger power. Therefore some thermal gradient could exist out of resonance and lead to modification of the offset signal.

As the offset signal is an out of resonance signal, it is usually subtracted to the total signal to take into account only the voltage drop at resonance, *i.e.*, the voltage drop due to spin pumping. Nonetheless, as previously observed the offset voltage is increasing with power<sup>59</sup>, and more recently it was shown by Huo *et al.* that the offset voltage could include several thermal contributions<sup>203</sup>. To test this hypothesis we can use a similar measurement method based on the time dependence of the signal by measuring both the offset voltage far from resonance field and the resistance of the sample. The sample was purposely misplaced to maximize the rf current flowing into it, showing the worst case scenario when the temperature increase is maximum.

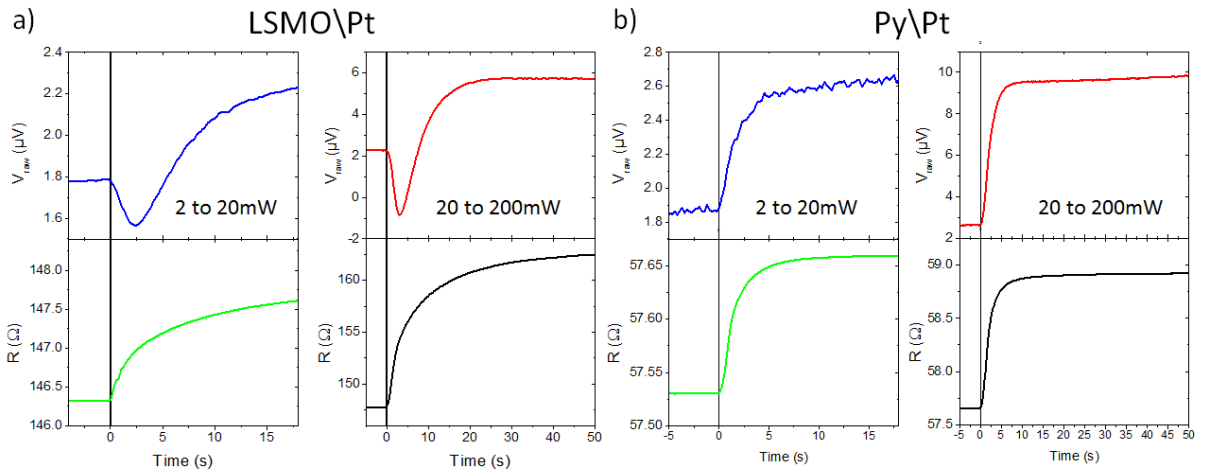


FIG. B.1: Change of offset voltage and resistance out of resonance as a function of the time. The time origin corresponds to an increase of the power entering the cavity. The samples are a) LSMO/Pt and b) Pt/Py.

By measuring the resistance of the sample we can see that it is changing with power, in the case of both  $LSMO/Pt$  and  $Pt/Py$  the higher the power the higher the resistance. This is due to the expected temperature increase associated with higher power absorption. More importantly this temperature/resistance increase is not instantaneous and as seen in figure B.1 it takes several seconds to stabilize from 2 to 20 mW or from 20 to 200 mW. The characteristic time is different in the two samples due to the differences in the thermal conductivity of the layers. More importantly the increase of resistance is very high compared to the one at resonance. Here it is of several  $\Omega$  while it was only of some dozens of  $m\Omega$  at resonance. This increase in temperature is thus two orders of magnitude higher, and non negligible thermal related contributions to the signal might appear.

In open circuit the offset signal is also sensitive to the absorbed power and thus on the rf field intensity. This offset voltage is of some  $\mu V$  at 200 mW. . More importantly, as can be seen in fig B.1 it takes time for the offset voltage to stabilize, with a stabilization time identical to that of the temperature change measured by recording the resistivity. This is an indication that this signal is of thermal origin. In the case of  $LSMO/Pt$  the offset signal first decreases on a short timescale and then increases, contrary to  $Pt/Py$  where it is only increasing. The nature of this jump is still unclear in  $LSMO/Pt$ , but might be associated with the drastic changes of the LSMO properties on a narrow temperature range above room temperature. The temperature increase in  $LSMO/Pt$  is also way larger than  $Pt/Py$ , likely because of the small thermal conductivity of both  $LSMO$  and the substrate  $LSAT$  compared to  $Si$  and  $Py$ .

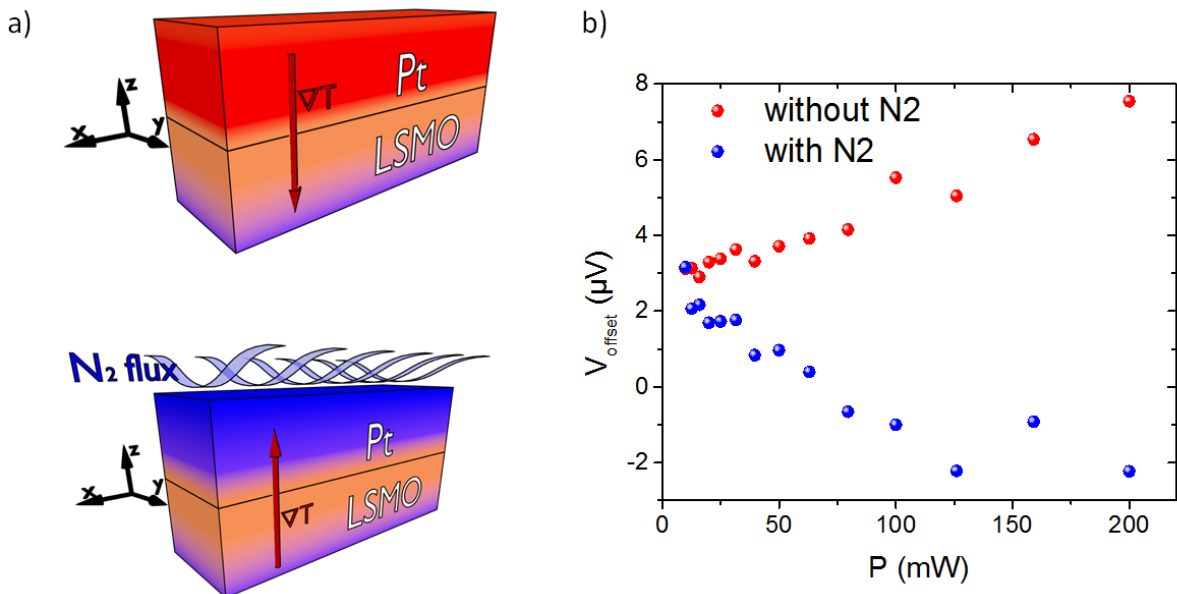


FIG. B.2: a) Schematic representation of the thermal profile out of resonance of the  $LSMO/Pt$  sample with and without  $N_2$  flux and b) change of the offset voltage in presence or absence of  $N_2$ .

To further confirm the thermal nature of the offset signal we have modified the thermal boundary conditions in  $LSMO/Pt$ . It is possible in our cavity setup to add a flow of helium for low temperature measurements but also of gaseous  $N_2$  at room temperature. This allows to have a flow of gas directly on the sample that will modify the thermal gradient profile. The exact thermal gradient profile

is unknown, but to clarify the modification due to flux of  $N_2$  we show the expected change of thermal profile in figure B.2.a. In absence of  $N_2$  flux, most of the rf power is dissipated in Pt (in red) because of the eddy currents, leading to the existence of a thermal gradient while the *LSMO* remains cooler (in orange/blue). By adding a flux of  $N_2$  the temperature of the Pt layer surface decreases, leading to a drastic change in the thermal conductivity profile and thus in a change of the thermal associated effects. It is also likely that the flux of  $N_2$  is not perfectly facing the sample and will give rise to a change of thermal gradient along x, leading to z change of the Seebeck voltage. Whatever the exact nature of the signal, the fact that it changes when using the  $N_2$  flux confirms its thermal origin.

Note that measuring the temperature increase out of resonance could be a good method to obtain an accurate evaluation of the eddy currents amplitude. Indeed the amplitude of the eddy currents are connected to the temperature increase (via the Joule effect). This could be useful to estimate the contribution of the spin rectification effects without the need of an angular dependence.

## Change of the magnetic properties of the ferromagnet with the applied power

The increase of temperature out of resonance is high enough to affect the magnetic properties of ferromagnetic materials with temperature-dependent properties in the studied temperature range. Any spin-charge conversion effect that is sensitive to temperature can also be modified. Therefore it is likely that the spin pumping signal can be affected by the temperature increase out of resonance which is not always accounted. In this part we will evidence the importance to accurately measure the temperature of the sample when performing measurements using materials that have temperature sensitive properties or when performing experiments using a large microwave power. We will verify this effect by using a LSMO/Pt bilayers that have temperature-dependent magnetic properties in a narrow range of temperature, close to 300K.

### Change of magnetic properties of the ferromagnet

In annex B we have clarified that the temperature of the sample can increase, especially when a large power is used and when the sample is poorly centred. In some systems, such a temperature increase could modify the magnetic properties that are important for an accurate estimation of the injected spin current. It is particularly important when using ferromagnets with a Curie temperature  $T_c$  close to the studied temperature range, such as LSMO which has a  $T_c$  of around 360K<sup>374</sup>.

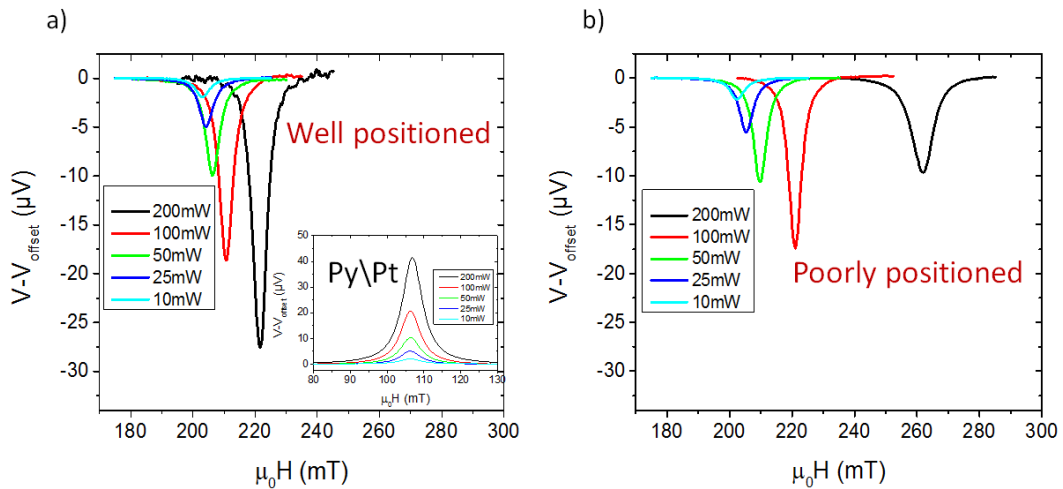


FIG. C.1: Change of resonance field and signal as a function of power in a LSMO/Pt sample, for a field along the 001 direction, in the case of a sample that is a) well positioned, far from the sides of the resonator and for the same sample but b) poorly positioned. The inset of figure a) shows spin pumping FMR results for a well positioned Pt/Py sample.

As can be seen in figure C.1.a and b, when the incident power increases, the resonance field is also

increasing in the  $LSMO/Pt$  bilayer. This has already been observed by several groups and has been either unexplained<sup>375</sup> or associated to various effects including the existence of an internal field within LSMO<sup>376</sup>, an increase of the precession cone angle that reduces the effective magnetization<sup>377</sup> or a microwave heating effect<sup>378;379</sup>. Our interpretation is that this is only due to a temperature increase of the sample at large powers, which leads to a change of the magnetization properties and especially of the saturation magnetization  $M_s$  of  $LSMO$  close to the room temperature. When the sample is well positioned, as in figure C.1.a, the resonance shift between 5mW and 200mW is smaller than when the sample is poorly positioned (figure C.1.b.). This is simply due to the fact that the temperature increase is smaller for a well-positioned sample. As the Q factors are similar, *i.e.*, the rf field amplitudes are similar, and as both experiments are performed using the same sample, this shows the influence of a good positioning on the temperature increase out of resonance. This also evidences the increase of the rf current flowing in the sample for a poorly positioned sample. Using LSMO, which possess a high resistivity compared to the Pt overlayer, allows to avoid large eddy currents flowing in the Ferromagnetic layer when poorly positioned, this is important to avoid an increase of the spin rectification effects that could prevent an accurate measurement.

### **Linearity of the spin pumping signal with power**

We can also see that the signal is non-linear with the power, especially when the sample is poorly positioned. This also originates from the decrease in  $M_s$  when increasing the temperature<sup>374</sup>, which leads to a decrease in the injected spin current according to the equation 2.40. For Permalloy, Cobalt or CoFeB with a considerably larger  $T_c$  the magnetic properties are not modified on a narrow range close to room temperature, especially the resonance field remains unmodified and the signal varies linearly with the power. A typical example can be seen in the inset of figure C.1.a in the case of  $Pt/Py$ . This shows that only a very large heating of the sample can lead to similar effects in usual ferromagnetic metals. In general one should still be careful of the exact temperature of the sample in presence of a nonlinear dependence of the signal with the applied power.

As the change of  $M_s$  and thus of the spin signal is due to the temperature increase, this effect can be easily modified by using the  $N_2$  flux as shown before. We used the same poorly centred  $LSMO/Pt$  bilayer as before to study this effect. As can be seen in figure C.2.a, the temperature decrease using  $N_2$  flux leads to a saturation magnetization increase, and thus to a decrease of the resonance field. This confirms that the heating of the sample can have strong effects on the magnetization properties for ferromagnets with properties sensitive to temperature such as LSMO. The exact sample temperature should be carefully checked before concluding on power or temperature dependences, especially in presence of non-linearities. From the small change of the resonance field it is clear that the cooldown power of the room temperature  $N_2$  flux is not particularly high, but it is still high enough to modify it in a visible way. We can also see in figure C.2.b that the measured spin signal increases at large power when the sample is cooled using the  $N_2$  flux. This is expected because of the larger  $M_s$  value that leads to a larger injected spin current. At low power the  $N_2$  flux does not have any effect on the sample properties because the temperature difference with that of the  $N_2$  flux is too small.

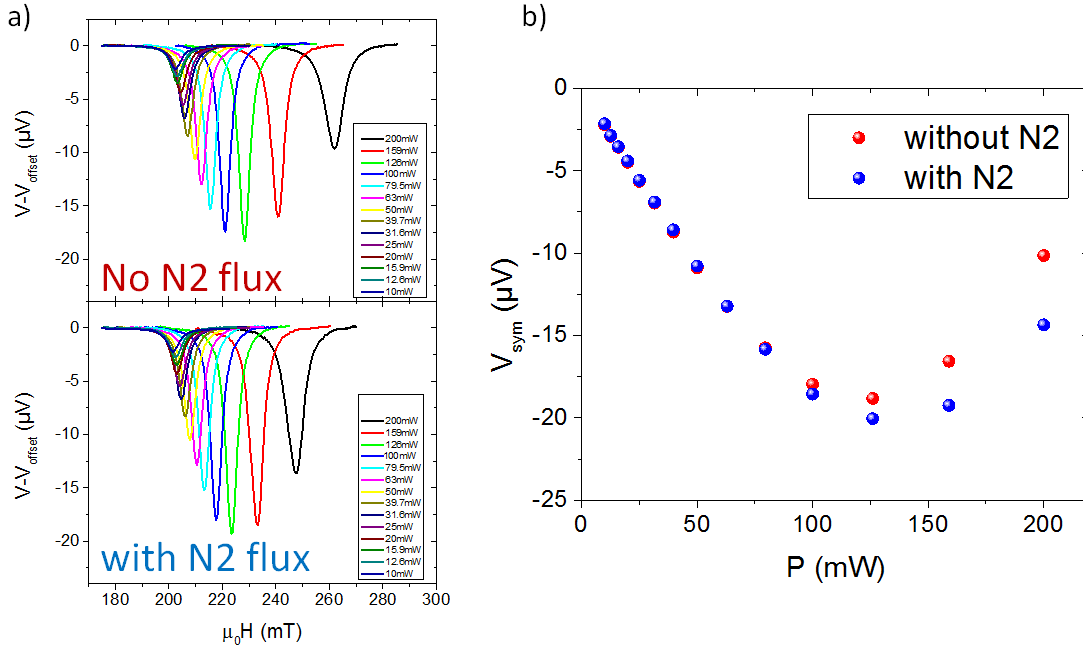


FIG. C.2: Change of the ferromagnetic properties and of the spin signal with the power in presence and absence of a  $N_2$  flux. a) Spin signal (with the offset subtracted) as a function of power for both cases and b) Obtained symmetric signal fitted from these data.

We have performed a complete power dependence of the same  $LSMO/Pt$  sample in both the parallel and antiparallel configurations, with and without  $N_2$  flux to cool down the sample. In the antiparallel configuration the Q factor of the cavity was lower ( $Q = 293$ ) than in the parallel configuration ( $Q = 537$ ). The difference in Q factors is expected, due to the misplacement of the sample in the cavity it is more disturbed in one of the two configuration. The lower Q factor in antiparallel leads to a smaller heating effect at similar power due to smaller rf field, evidencing once again the deep link of the temperature increase with the rf field amplitude. This leads to an increase of the charge current production normalized by the rf field, and of  $M_s$  at a similar power. This also leads to a decrease in the linewidth  $\Delta H_{pp}$  when using powers above 100mW, and in the resistance R out of resonance as seen respectively in figure C.3.a,b,c and d. We extracted  $M_s$  from the resonance field value by using the Kittel formula and by assuming that the anisotropy field  $H_k$  is negligible.

In figure C.3 we can see a clear correlation between the decrease of the temperature, using  $N_2$  flux or due to a smaller cavity Q factor, and the smaller resistance, larger  $M_s$  and increase in the charge current production. This is particularly visible at a power of 200 mW where the signal is multiplied by almost 3 from  $80nA/G^2$  in the parallel configuration without  $N_2$  flux to  $210nA/G^2$  in the antiparallel configuration with the  $N_2$  flux.

In order to understand what is happening here we have to consider the temperature dependence instead of the power dependence. Using the resistance versus power dependence shown in figure C.3.d and the resistance versus temperature dependence shown in the inset of figure C.4.a, we could extract the exact temperature of the sample for all the measurements of figure C.3. The magnetic properties

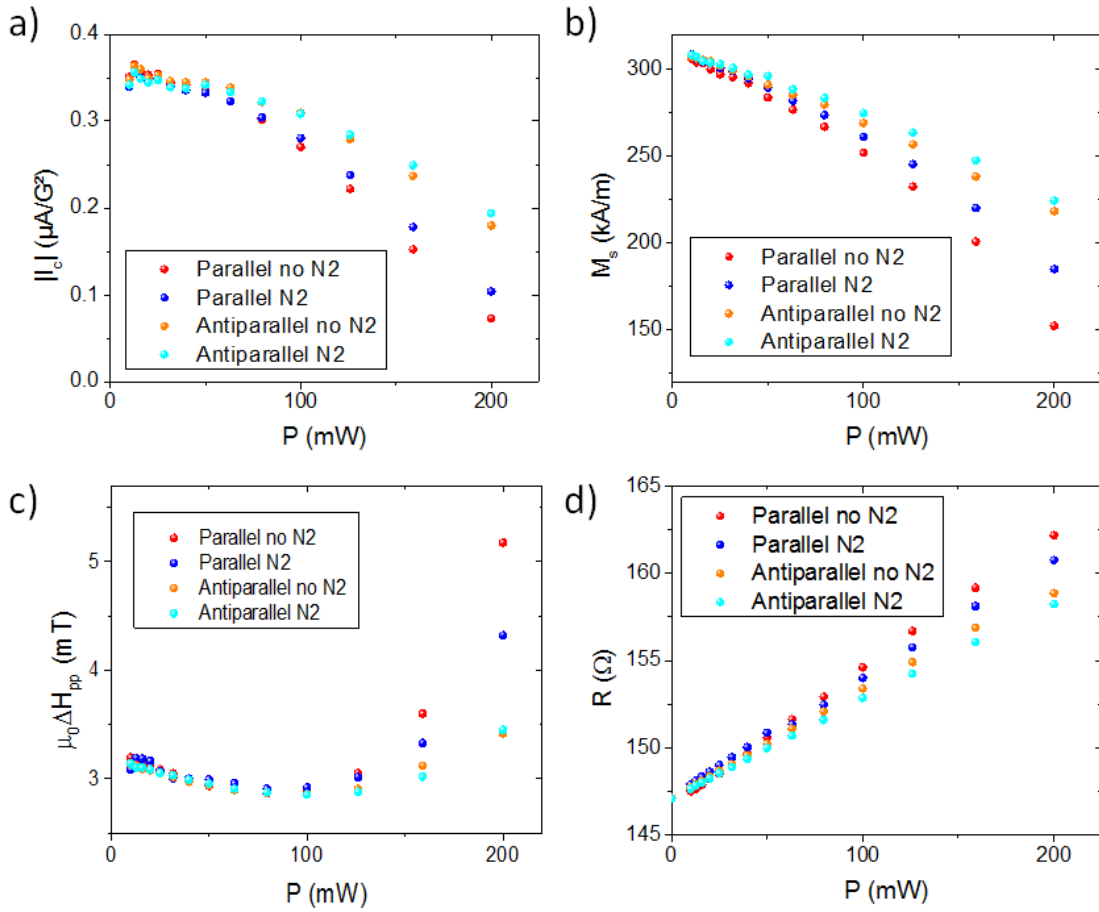


FIG. C.3: Modification of various properties as a function of power extracted from spin pumping FMR data including: a) The charge current production normalized by the rf magnetic field. b) The magnetization  $M_s$ . c) The peak to peak linewidth  $\Delta H_{pp}$ . d) The resistance  $R$  out of resonance. Measurements were performed in the parallel and antiparallel configurations with and without  $N_2$  flux.

of the *LSMO* film were also measured by SQUID by Victor Haspot in CNRS Thalès (who also grows the *LSMO* samples). The values of  $M_s$  obtained from FMR measurements agree very well with the one obtained by SQUID (cf. figure C.4.a) confirming a posteriori the negligible anisotropy at these temperatures and the accurate temperature estimation. As can be seen in figure C.4.b there is also an increase of the linewidth as a function of the temperature above 320 K. This evidences that close to the Curie temperature the magnetization decreases, but also the damping of the *LSMO* thin film increases. An increase of the damping was previously observed in other ferromagnetic materials close to the Curie temperature, associated with enhanced spin fluctuations<sup>128;380</sup>.

The decrease in the spin signal at large power can be explained by the temperature increase and change in the magnetic properties of *LSMO* and especially the damping and the saturation magnetization. By using equations 2.40 and 2.46, which gives the expression of the spin pumping signal previously



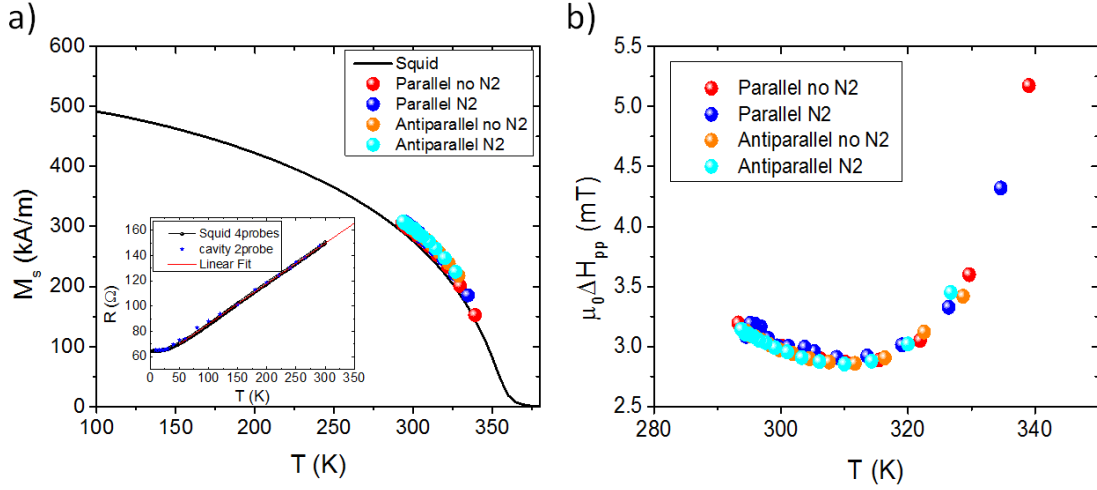


FIG. C.4: Modification of a) magnetization and b) peak to peak linewidth of LSMO/Pt as a function of temperature. The temperature dependence of the resistance was obtained in both 2 probes and 4 probes to obtain an accurate evaluation of the exact temperature of the sample. The magnetization obtained by FMR is plotted alongside SQUID measurements performed by Victor Haspot.

presented in chapter 2, it is possible to fit the data:

$$|I_c| = W\theta_{SHE}\lambda_s J_{s,pump} \tanh\left(\frac{t_N}{2\lambda_s}\right) \quad (C.1)$$

$$J_{s,pump} = \frac{Re(g^{\uparrow\downarrow})\gamma^2\hbar h_{rf}^2}{8\pi\alpha^2} \left( \frac{4\pi M_s\gamma + \sqrt{(4\pi M_s\gamma)^2 + 4\omega^2}}{(4\pi M_s\gamma)^2 + 4\omega^2} \right) \left( \frac{2e}{\hbar} \right)$$

Using equations C.2, and assuming that  $\theta_{SHE}\lambda_s$  is constant in Pt as a function of temperature<sup>71</sup>, and that  $\tanh\left(\frac{t_N}{2\lambda_s}\right)$  is nearly constant when the thickness of the Pt film is larger than  $\lambda_s$ , the only remaining variables that could possibly affect charge current production are the magnetization  $M_s$  and the damping  $\alpha$ . Note that this analysis also includes the variations of the spin mixing conductance  $g^{\uparrow\downarrow}$ , that is proportional to the magnetization. Therefore equations (C.2) can be rewritten as follows:

$$|I_c| = C_{ste} \times \frac{M_s}{\alpha^2} \left( \frac{4\pi M_s\gamma + \sqrt{(4\pi M_s\gamma)^2 + 4\omega^2}}{(4\pi M_s\gamma)^2 + 4\omega^2} \right) \quad (C.2)$$

Due to the decrease of  $M_s$ , and as experimentally observed, the signal is expected to decrease. the signal is expected to decrease, as experimentally observed. But as can be seen in figure C.5 it is not sufficient to explain the decrease at large powers/temperatures above 315 K. At temperatures higher than 315K the increase in the linewidth, associated with an increase in the damping close to the Curie temperature, is likely to be the cause of such a discrepancy. By accounting for the enhanced linewidth above 315K we can obtain an accurate fitting of the data, as seen in the solid curve in figure C.5.

This power dependence demonstrates that the analysis of the spin pumping experiments cannot always be done by assuming a fixed temperature and a simple proportionality of the signal with the power. The dependence of the exact sample temperature with the power can be a key element. The results obtained here can explain non-linearities observed at very large excitation powers in ferromagnetic metals<sup>123</sup> or at temperatures close to the Curie temperature<sup>377</sup>. It also shows that spin pumping

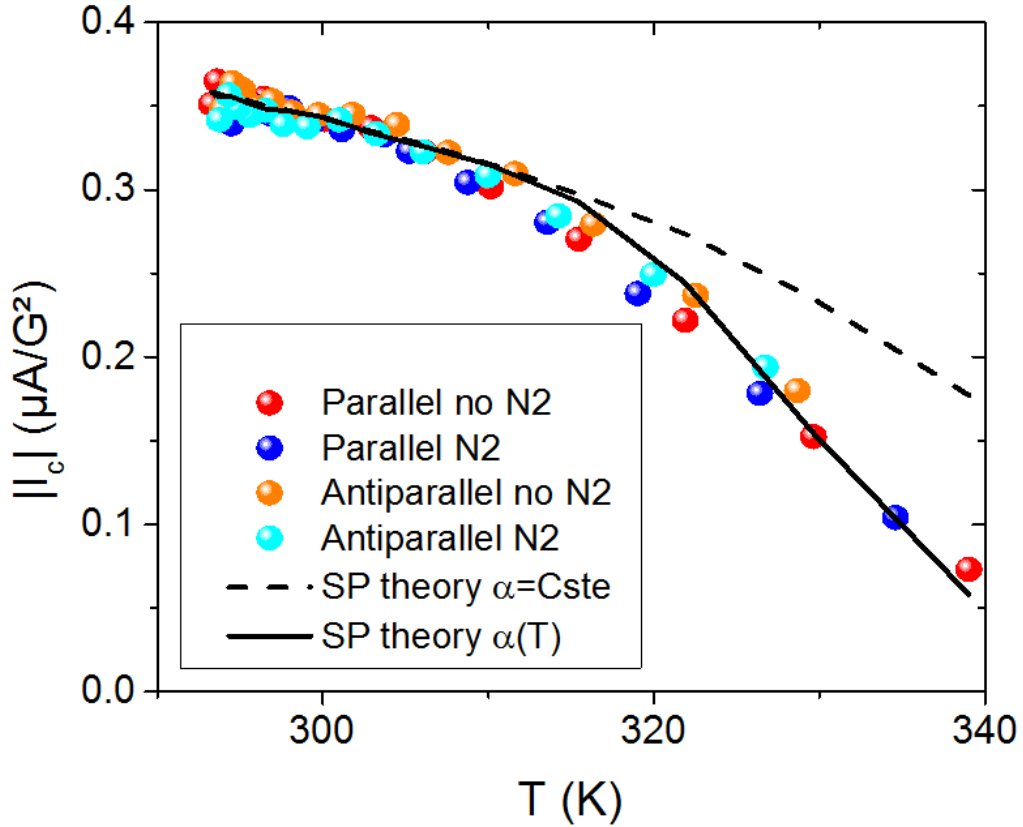


FIG. C.5: Temperature dependence of the spin pumping signal as a function of the temperature for different measurement configurations, fitted using equation 3.3 with fixed damping and varying damping.

signal saturation at large powers is not only due to incoherent spin precession at high precession cone angles<sup>381;382</sup>, large temperature increase at resonance<sup>383</sup>, or spincaloritronics effects at resonance<sup>180</sup> but can simply be due to a temperature increase of the sample with the microwave power out of resonance. More generally it demonstrates that one should always measure the exact temperature of the sample when performing spin pumping FMR measurements, especially when performing measurements sensitive to temperature. Note that in our setup the good centering of the sample allows to avoid large heating effects.

It is also possible to take advantage of this temperature increase out of resonance to perform temperature dependence measurements. In particular it is possible to perform a faster measurement by using power dependence at a fixed cryostat temperature instead of changing the cryostat temperature and use a low power. We developed this technique recently with Sara Varotto to study the spin to charge conversion in NiCu alloys close to the Curie temperature of NiCu. To conclude, the most important message in this annex is that when doing spin pumping FMR measurement we should be careful on the exact temperature of the sample, and its exact magnetic properties including the resistance, the magnetization  $M_s$  and the damping  $\alpha$  (including non-Gilbert damping if important<sup>384</sup>). This is needed to evaluate accurately the conversion efficiency or other properties such as the spin mixing conductance, and to avoid any misinterpretation of the experimental data.

## Gate voltage dependence of the ferromagnetic resonance lineshape in STO \CFB

We have shown in chapter 4 that STO is ferroelectric for high enough electric fields. If it is ferroelectric there is a distortion of the lattice that occurs as a function of electric field and this should induce some strain on the layer on top of the STO crystal: NiFe. It has been shown by various groups that a shift of the resonance field as a function of gate voltage can be obtained in ferroelectric \ferromagnetic bilayers<sup>290;385;386;387;388</sup>. However we do not observe any strong modification of the resonance field or linewidth in NiFe. This is likely due to the fact that these modifications of the resonance field are due to the inverse magnetostriction of the ferromagnetic layer. For NiFe with Permalloy stoichiometry, the magnetostriction coefficient is ideally zero, therefore its magnetic properties should not be modified by the application of strain. These effects should appear if we use a ferromagnet with a large magnetostriction coefficient. To study that case,  $Co_{40}Fe_{40}B_{20}$ , that has a large magnetostriction coefficient<sup>389</sup>, was directly deposited on a TiO<sub>2</sub> terminated STO substrate.

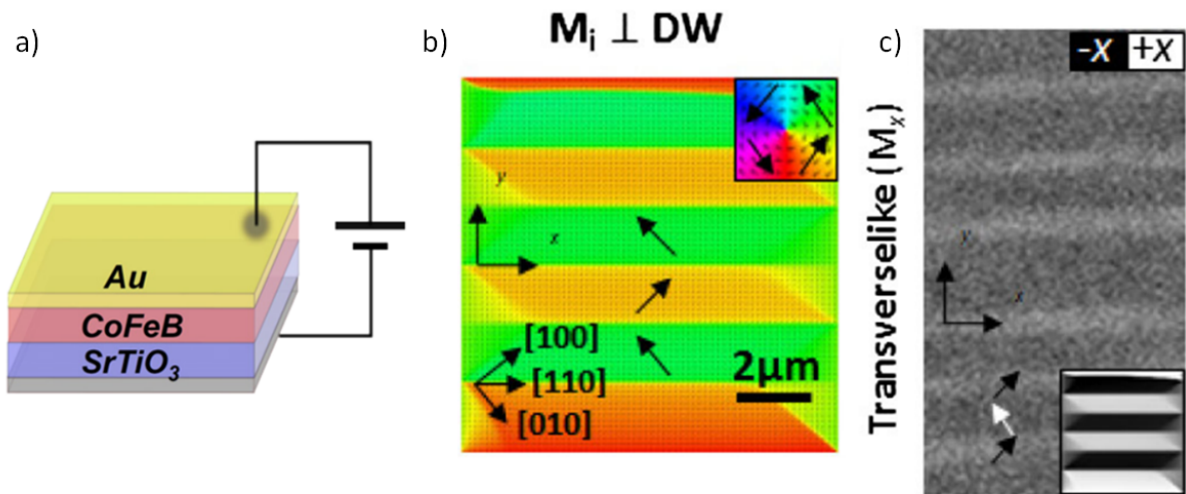


FIG. D.1: MOKE imaging of the ferroelastic domain walls in STO. a) Illustration of the sample b) Micromagnetic simulation of the remanent state for DW. c) Transverse MOKE remanence images for initial magnetic saturated states of the CoFeB layer perpendicular to the ferroelastic domain walls. These figures are extracted from Casals *et al.*<sup>390</sup>

In fact, using CoFeB on top of STO allows to image simply (via MOKE) the evolution of the tetragonal domains below the antiferrodistorsive transition upon application of an electric field. Such a measurement has been performed in a STO \CoFeB \Au heterostructure shown in figure D.1.a by Casals *et al.*<sup>390</sup>. The strain due to the presence of ferroelastic twins in the tetragonal phase is transferred from the STO to the CoFeB and the modification of the CoFeB magnetic properties as shown by micromagnetic simulation in figure D.1.b. It allows to reveal the presence of the twins and of te-

tragonal domains of STO by using MOKE and thus without the use of unconventional detectors such as scanning single-electron transistor microscope<sup>391</sup>. The imaging of the tetragonal domains using MOKE is shown in figure D.1.c and the domain structure can be modified by applying gate voltages. Therefore, in our experiments, a modification of the FMR linewidth of CoFeB with the gate voltage is expected, even in the non-ferroelectric phase.

To confirm this we studied two different STO \CoFeB (20nm) samples, the first one with a substrate thickness of 500  $\mu\text{m}$ , the second one with a substrate thinned down to 250  $\mu\text{m}$ .

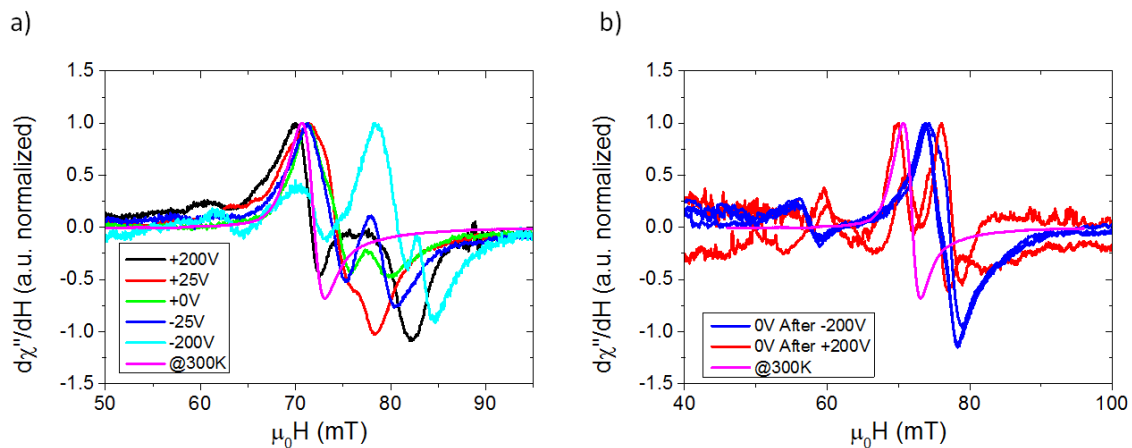


FIG. D.2: a) Modulation of the FMR lineshape in the CoFeB sample with a thick substrate at 7K. b) Modulation of the FMR lineshape in the CoFeB sample with a thinned substrate at 7K. A strong modulation of the lineshape is observed in both cases.

We can see in figure D.2.a the FMR lineshape of the thick sample measured at 7K for different gate voltages. The striking feature is that contrary to the FMR lineshape obtained at 300K there is not only one peak but several peaks. The number and position of these peaks can be tuned with gate voltage and close to +25V it is possible to tune it back to only one peak with a slightly deformed shape. This experimental result confirms the modification of the CoFeB magnetic properties with gate voltage. An enhancement of the linewidth associated with inhomogeneous strain has already been reported before<sup>386;387</sup> but such a fine structure that can be tuned with gate has not been observed. This evidence both the large piezoelectric coefficient of STO<sup>392</sup> at cryogenic temperature and the presence of the tetragonal domains with different orientations that are modified with gate voltage<sup>284;391</sup>. As the size of the tetragonal domains is considerably larger (several  $\mu\text{m}$ ) than the exchange length (some nm) this gives rise to an inhomogeneous modification of the effective magnetization, the ferromagnetic resonance peaks corresponding to a given strain and domain orientation. Such a FMR lineshape with a fine structure is similar to what can be obtained in a sample with large crystallite size and inhomogeneous magnetization properties as can be seen for example in Mercone *et al.* in LSMO thin films<sup>136</sup>. Note that after initialization this effect shows no remanence or hysteresis-like behavior.

For the thinned down sample a similar modification of the lineshape can be obtained, but the effect is remanent. As can be seen in figure D.2.b after applying a negative gate voltage of -200V, at 0V the

lineshape is similar to the one obtained at room temperature with one main resonance peak around 80mT and a smaller subpeak at 60mT. The same lineshape has been obtained for three different measurements at 0V in different cycles. After applying +200V the lineshape is considerably more complex with at least three resonance peaks. This measurement could also be reproduced in three different cycles. This emphasize that the ferroelectricity is intimately related to the displacement of the tetragonal domains<sup>284</sup>. Nonetheless this very unusual pattern is still not well understood. The fact that such a modification can be observed using the FMR lineshape of CoFeB shows that the ferroelectric transition could possibly be studied using MOKE to better understand the tetragonal domains displacements in this phase.

## $Sb_2Te_3$ ultrathin films and stoichiometry

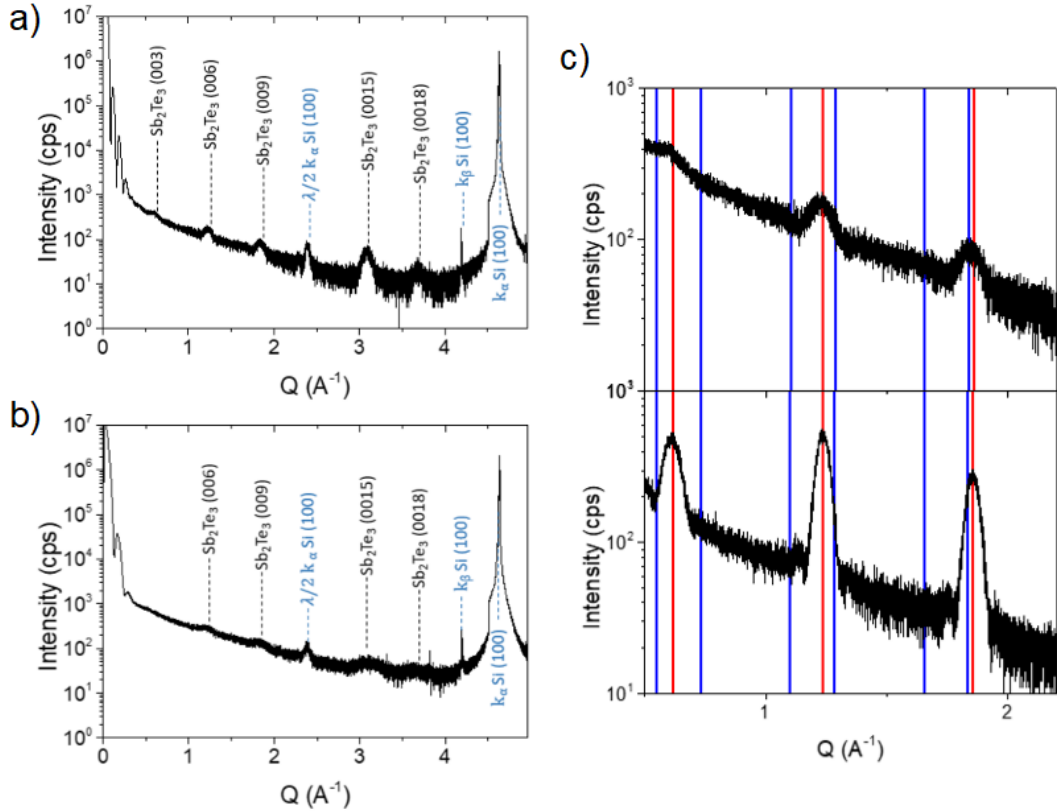


FIG. E.1: X-Ray Diffraction  $\theta - 2\theta$  spectrum for a) 7nm-thick film and b) 4nm-thick film deposited on thermally oxidized  $SiO_2$ . The peaks corresponding to  $Sb_2Te_3$  (00l) are represented in black, the blue color corresponding to the substrate peaks. c) The First peaks of the 7nm and 10nm sample  $\theta - 2\theta$  XRD measurement. In red the expected position of the  $Sb_2Te_3$  peaks, in blue the expected position of the  $Sb_8Te_9$  peaks.

To confirm the possibility to grow topological insulator ultra thin film with good crystalline orientation and stoichiometry we have performed out-of-plane  $\Theta - 2\Theta$  X-ray Diffraction measurements on a 4 nm and 7 nm thick  $Sb_2Te_3$  thin films of the same wafer. These measurements are shown in figure E.1.a and b. We can observe that a nice (00l) orientation is preserved even for the thinnest 4 nm film. As shown by Kowalczyk *et al.* if the conditions of film deposition are not well controlled it is possible to obtain a  $Sb_8Te_9$  film with a large number of tellurium vacancies and with an XRD pattern similar to the  $Sb_2Te_3$  one<sup>341</sup>. We have mentioned in Chapter 5 that the obtained thin films possess the expected 2:3 stoichiometry. As can be seen in figure E.1.c when comparing the peak positions of  $Sb_2Te_3$  and  $Sb_8Te_9$  with our experimentally obtained XRD it is clear that the experiments are compatible only with the  $Sb_2Te_3$  ratio. This is further confirm by EDX measurements with an optimal fitting close to a 2:3 ratio as shown in figure E.2.

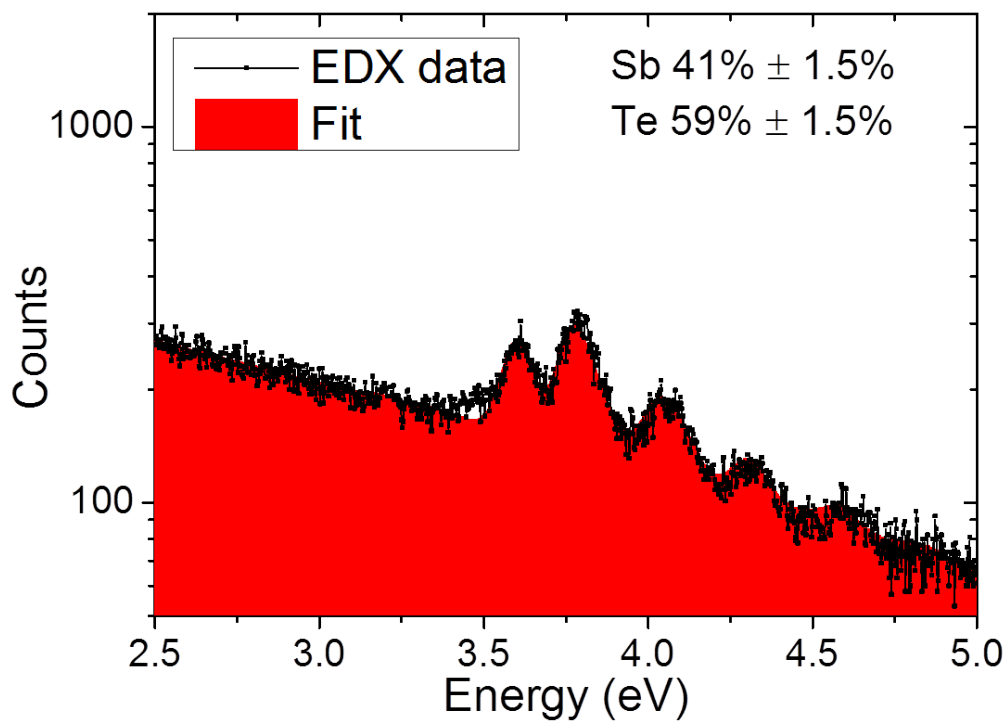


FIG. E.2: EDX spectrum of the 10 nm thick  $Sb_2Te_3$  sample. The optimal fit of the data (in red) is obtained for a ratio of  $41\% \pm 1.5\%$  of Sb and  $59\% \pm 1.5\%$  Te, close to 2:3.



## **Résumé:**

Un champ émergent de la spintronique, appelé spin-orbitronique, s'attelle à l'utilisation du couplage spin orbite pour détecter et produire des courants de spin en l'absence de matériaux ferromagnétiques. Une interconversion efficace entre courant de spin et courant de charge a pu être obtenue à l'aide de l'effet Hall de spin dans les métaux lourds tels que le Platine ou le Tantale. Une telle conversion peut aussi être obtenue en utilisant l'effet Edelstein dans les interfaces Rashba et les isolants topologiques. La conversion de courant de spin à courant de charge par effet Hall de spin et effet Edelstein inverse peut être étudiée par la méthode dite du pompage de spin par résonance ferromagnétique. Ce manuscrit présente l'étude de la conversion dans les métaux, les interfaces Rashba à base d'oxyde et les isolants topologiques. Parmi ces systèmes nous avons montré la possibilité de moduler la conversion avec une grille électrostatique dans le gaz d'électron bidimensionnel à la surface de SrTiO<sub>3</sub>. Nous avons aussi montré qu'une conversion efficace peut être obtenue à température ambiante dans les isolants topologiques HgTe et Sb<sub>2</sub>Te<sub>3</sub>. Ces résultats suggèrent que les gaz d'électrons bidimensionnels aux interfaces d'oxydes et à la surface des isolants topologiques sont des systèmes prometteurs pour la manipulation des courants de spin.

## **Summary:**

An emerging field of spintronics, called spin-orbitronics, is based on the use of spin-orbit coupling to detect and produce spin currents, possibly in the absence of any ferromagnetic material. An effective interconversion between spin current and charge current can be obtained using the spin Hall Effect in heavy metals such as platinum or tantalum. Such a conversion can also be obtained by using the Edelstein effect in Rashba interfaces and topological insulators. This conversion can be studied by the so-called ferromagnetic resonance spin pumping method. This thesis presents the study of this conversion in metals, in oxide-based Rashba interfaces, and in topological insulators. Among these systems we have shown the possibility of modulating with an electrostatic grid the spin charge conversion in a two-dimensional electron gas, at the surface of a SrTiO<sub>3</sub> oxide. We also showed that the topological insulators HgTe and Sb<sub>2</sub>Te<sub>3</sub> exhibit exciting spin-to-charge conversion properties at room temperature. These results suggest that both bidimensional electron gases at oxide interfaces and topological insulators are promising systems for spin currents manipulation.